

**SPATIAL AND TEMPORAL DYNAMICS OF THREE EAST ANTARCTIC
OUTLET GLACIERS AND THEIR FLOATING ICE TONGUES**

DISSERTATION

Presented in Partial Fulfillment of the Requirements for
the Degree Doctor of Philosophy in the
Graduate School of The Ohio State University

By

Jan Wuite, M.S.

* * * * *

The Ohio State University

2006

Dissertation Committee:

Dr. K.C. Jezek , Adviser

Dr. C.J. van der Veen

Dr. G.D. McKenzie

Dr. T.J. Wilson

Approved by:

Adviser

Graduate Program in
Geological Sciences

ABSTRACT

Recent observations show that some outlet glaciers in Greenland and Antarctica undergo rapid changes in flow velocity and ice thickness. There is concern about the implications of this for global sea levels and ocean circulation. At least part of the changes has been ascribed to changes in the dynamics of these glaciers. Measuring ice flow velocity and gradients in velocity are first steps in studying their dynamics and possible response to climatic changes. With the launch of the RADARSAT-1 satellite and the RADARSAT-1 Antarctic Mapping Project (RAMP) a great opportunity arose to derive ice flow velocity of Antarctica's glaciers remotely.

This study uses RAMP imagery to derive ice flow velocity and, in combination with various other datasets, including BEDMAP, VELMAP, OSUDEM, ICESat and InSAR derived velocity, to study spatial and temporal fluctuations in the velocity and stress fields of selected Antarctic glaciers. In particular we focus on the flow regimes of David Glacier, Mertz Glacier and Stancomb-Wills Glacier. These are all major East Antarctic outlet glaciers that have floating termini. We explore the role of these so-called ice tongues on their feeding glaciers. This is relevant especially in the wake of recent evidence that suggests the significant speed up and thinning of some glaciers in the Antarctic Peninsula is triggered by the collapse of a buttressing ice shelf.

The derived high-resolution 2-dimensional surface velocity maps form an important benchmark for gauging possible (future) changes in velocity and dynamics and form one of the major contributions of this study. The maps are derived using pre-established feature tracking techniques that we improved, optimized and streamlined in order to extract as much reliable velocity data as possible from the wealth of data provided by the RAMP project. This included pre-processing of the images by using a speckle reduction filter, the addition of an adaptive window extraction routine and the design and application of a noise removal filter.

To determine the important flow governing forces we use pre-existing force-budget theory. We include a detailed error analysis and investigate the implications of a recently established flow law on derived stresses. The investigations of our study areas suggest that flow has been rather constant over decadal timescales. Based on this we infer that the stress field has not changed significantly either, permitting the combination of various data sets (averaged over different time spans) to optimize the velocity field in order to study dynamics in greater detail than previously possible. We find that the relative contribution of side drag declines along the fjords, but demonstrate that, once they leave the valley walls, the glaciers are not immediately true free floating ice shelves. Measurements show that ice tongues spread faster in the across flow direction than the along flow direction for a considerable length. In addition there appears to be some lateral drag, once a glacier leaves the coast, which could be associated with sub-surface valley walls or an adjacent ice shelf. This could lead to an increase in along flow creep if the ice tongue were to break off. Finally we conclude that ice tongues are important, because they can provide clues to past ice sheet behavior and fluctuations.

Dedicated to Annemarie

ACKNOWLEDGMENTS

I have to express my gratitude to a great many people, without whom I would not have been able to complete this dissertation. First of all I would like to thank my advisor Ken Jezek for his helpful comments and suggestions throughout my studies. I enjoyed our discussions and thank you for the opportunities that you gave me.

Next I have to thank my former advisor Ian Whillans, who sadly passed away in 2001. You convinced me to apply at The Ohio State University and taught me a lot about the fascinating science of glaciology.

Thanks to all my committee members. Kees van der Veen, je boek is mijn bijbel geworden de laatste jaren! Lonnie Thompson, unfortunately you are in Tibet during my defense. Garry McKenzie, thanks for kindly filling the space on such short notice! Terry Wilson, I cannot express how grateful I am for the opportunity you gave me to visit Antarctica, enabling me to see my study area with my own eyes!

Then, of course, I would like to show my appreciation to everyone that worked, or still works, in the remote sensing lab at Byrd Polar Research Center, including Katy, Kee-Tae, Gi-Choul, Leigh, Xiaolan, Jiahong, Tom, Bobbi, Stacy and Trey. Karl, you helped me surmount some long-standing problems I had with feature tracking. Steve, you made the lab an exiting place to be! I enjoyed our presentations for the literally hundreds

and hundreds of kids that visited our lab in recent years! Indrajit, I leave seniorship to you now. I am sure you are capable of the task! I enjoyed our science discussions and wish you good luck with the remainder of your PhD studies. I am now able to pronounce your last name fluently! Other people at BPRC that I am indebted too are Lynn E., Lynn L. and Michele, thanks for all your efforts!

There is a great many other friends that I would like to thank as well. I do not know where to start, in random order: Rahul, Stefan, Yushin, Kyung In, Jason, Andy, Sarah, Brad, Kate, Mike, Jessica, Perry, Janelle, Lingke, Yuri, Sarah, Uwe, Jennifer, Raghu, Alexandra, Andrew, Amanda, Chad, Bob, Marcus, Mohammad and Roman, you all made me feel at home in Columbus, my third hometown (besides Heerlen and Amsterdam). Sandra, bedankt voor je meubels! Josh, Nick, Faezeh and Dave, I enjoyed our climbing trips at the Red River Gorge in Kentucky. You are great rope mates!

Joris, Ron, Remko en Jeroen, ik heb jullie gemist!

Jaap, Toos, Marleen, Tony and Pim, many thanks as well!

Special thanks to my three sisters, Ingrid, Karin and Henriëtte, for their support, interest and their visits to Columbus. Also thanks to Sascha, Jelle, Ryuji, little Bart and big Niels!

I am deeply indebted to my parents for their support throughout the years, you helped me a lot!

Finally, Annemarie, thank you so much for your encouragement, advise and companionship!

This work was supported by a grant from NASA's Polar Oceans and Ice Sheets Program and by NASA Headquarters under the Earth System Science Fellowship Grant NGT5-30533.

VITA

August 24, 1974Born – Heerlen, The Netherlands
1999.....M.S. Physical Geography, University of
Amsterdam
2000-2006Graduate Research Associate and Graduate
Fellow, The Ohio State University

FIELDS OF STUDY

Major field of study: Geology

TABLE OF CONTENTS

Abstract	ii
Dedication	iv
Acknowledgments	v
Vita	viii
List of Figures	xii
List of Tables	xviii
List of Abbreviations	xix
 Chapter 1: Introduction	 1
1.1 Introduction	1
1.2 Problem statement	3
1.3 Glacier Flow and Velocity	5
1.4 Goals	7
1.5 Study Areas	8
1.6 Overview of the study	10
 Chapter 2: Theory	 13
2.1 Introduction	13
2.2 Force budget calculation	14
2.2.1 Driving stress	15
2.2.2 Resistive stresses	17
2.3 Floating glaciers bounded by valley walls	25
2.4 Free floating glaciers	29
2.5 Error propagation	30
2.6 Averaging velocity measurements	33
2.7 Implications of a new flow law	34
2.8 Summary	46
 Chapter 3: Datasets and Methods	 49
3.1 Introduction	49
3.2 Flow velocity measurements	50
3.2.1 Introduction	50
3.2.2 Feature tracking	51
3.2.3 Radarsat missions AMM1 & MAMM data	55

3.2.4 Orthorectification	57
3.2.5 Pre processing: 16 to 8 bits conversion and filtering	58
3.2.6 Co-registration and tie points	60
3.2.7 Image cross-correlation: Imcorr	63
3.2.8 Imcorr settings	67
3.2.9 Imcorr modifications.....	69
3.3 Validation and outlier removal	72
3.3.1 Visual check and vector validation	72
3.3.2 Outlier removal	73
3.3.3 Mean and median filters.....	75
3.3.4 Mask filter.....	75
3.3.5 Inverse distance weighted standard deviation filter	78
3.4 Error estimates	82
3.5 InSAR	84
3.5.1 Theory and applications.....	84
3.5.2 InSAR method	87
3.5.3 InSAR versus feature tracking.....	88
3.6. VELMAP velocity and literature	88
3.7 Additional datasets.....	89
3.7.1 Surface topography	89
3.7.2 BEDMAP ice thickness	91
3.8 Summary	93
Chapter 4: The flow regime of David Glacier and Drygalski Ice Tongue.....	95
4.1 Introduction.....	95
4.2 David Glacier- Drygalski Ice Tongue.....	96
4.3 Previous studies	97
4.4 Velocity.....	98
4.5 Basal Melting.....	108
4.6 Ice margin and calving.....	115
4.7 Resistive stresses.....	117
4.7.1 Driving Stress.....	118
4.7.2 Longitudinal stress gradients	120
4.7.3 Lateral drag	122
4.7.4 Basal Drag.....	125
4.8 Floating part	128
4.8.1 Driving stress	130
4.8.2 Longitudinal stress gradients	133
4.8.3 Lateral Drag	139
4.9 Free floating section.....	143
4.10 Equilibrium profile.....	146
4.11 Summary and conclusions	149

Chapter 5: The flow regime of Stancomb-Wills Ice Tongue.....	152
5.1 Introduction.....	152
5.2 Area description and previous studies	153
5.3 Velocity.....	154
5.4 Velocity comparison	158
5.5 Ice shelf spreading and basal melting	161
5.6 Flow dynamics	167
5.6.1 Driving stress and longitudinal stress gradients	167
5.6.2 Lateral drag	168
5.7 Relict flow stripes	171
5.8 Flow stripe extrapolation	175
5.9 Discussion	179
5.10 Conclusions.....	183
Chapter 6: The flow regime of Mertz Glacier Tongue	184
6.1 Introduction.....	184
6.2 Mertz Glacier Tongue	188
6.3 Velocity.....	189
6.4 Velocity comparison	193
6.5 Ice shelf spreading	198
6.6 Calving.....	202
6.7 Flow dynamics	207
6.7.1 Driving Stress.....	207
6.7.2 Lateral Drag	209
6.7.3 Longitudinal Stress Gradients.....	214
6.8 Summary and Conclusions	217
Chapter 7: the significance of ice tongues	219
7.1 Introduction.....	219
7.2 Significance of ice tongues	219
7.2.1 Glaciological significance of ice tongues	219
7.2.2 Oceanographic significance of ice tongues.....	226
7.3 Temporal changes on ice tongues	228
7.3.1 Pine Island Glacier: a changing glacier	230
7.4 Ice tongues can provide clues to past ice sheet behavior.....	235
7.5 summary and conclusions	235
Chapter 8: Conclusion.....	237
8.1 Summary	237
8.2 Recommendations for future research	240
References.....	241

LIST OF FIGURES

Figure 1.1 Location of the study areas depicted on the RADARSAT-1 Antarctic Mapping Project (RAMP) mosaic.	10
Figure 2.1 Schematic view of the different resistive forces governing glacier flow.	15
Figure 2.2 Lateral spreading in a non-parallel valley.	27
Figure 2.3 Values of log A1 as a function of grain size at three different temperatures. .	38
Figure 2.4 Average crystal (grain) size versus depth for the GRIP ice core.	42
Figure 2.5 Comparison of the relation between effective strain rate and shear stress for ice at -20°C using both Glen’s flow law and the Goldsby-Kohlstedt constitutive equation for a range of grain sizes.	45
Figure 2.6 Comparison of the relation between effective strain rate and longitudinal stress for ice at -20°C using both Glen’s flow law and the Goldsby-Kohlstedt constitutive equation for a range of grain sizes.	46
Figure 3.1 Flowchart detailing the various steps involved in velocity extraction from multilook RADARSAT-1 SAR imagery using feature tracking.	54
Figure 3.2 The AMM-1 mosaic and MAMM mosaic.....	56
Figure 3.3 Two scenes illustrating the difference between an unfiltered image and a filtered image.	60
Figure 3.4 Illustration of the co-registration process.	62
Figure 3.5 Two co-registered RADARSAT-1 scenes of Drygalski Ice Tongue illustrating Imcorr.....	64

Figure 3.6 Two correlation plots derived from comparing a ‘reference window’ with a larger ‘search window’ extracted from two different scenes of the 2000 MAMM mission taken 24 days apart.....	67
Figure 3.7 Two correlation plots derived from comparing a ‘reference window’ with a ‘search window’ for the same test area on Jelbart Ice Shelf and illustrating the effect of the modification of Imcorr developed in this study.	71
Figure 3.8 Velocity vectors projected on a RADARSAT-1 image of David Cauldron, an icefall on David Glacier.	73
Figure 3.9 Ice flow velocity on Brunt Ice Shelf and Stancomb-Wills Ice Tongue.....	77
Figure 3.10 Various examples and stadia of the filtering and interpolation process for a region on Jelbart Ice Shelf.	81
Figure 3.11 Two histograms showing the displacement in x and y direction given by Imcorr using the same image.	83
Figure 3.12 Geometry of an interferometric SAR.	85
Figure 3.13 Hill shaded relief map of the OSUDEM.	90
Figure 3.14 BEDMAP digital ice thickness model of Antarctica.....	92
Figure 3.15 Bedmap thickness error.	93
Figure 4.1 RADARSAT-1 mosaic of David Glacier and Drygalski ice tongue in Victoria Land.	97
Figure 4.2 Ice flow velocity on Drygalski Ice Tongue and David Glacier.....	101
Figure 4.3 Displacements between cycle 2 and cycle 3 subtracted from displacements between cycle 1 and 2 and associated histogram.....	103
Figure 4.4 Displacements between cycle 1 and cycle 3 (48-day averaged velocity) subtracted from displacements between 1997 and 2000 (3-year averaged velocity) and associated histogram.	104
Figure 4.5 Comparison of derived feature tracking and InSAR velocities with velocities from the Velmap database.	106
Figure 4.6 Velocity profiles taken along a flow line derived from feature tracking over different time intervals and InSAR.	107

Figure 4.7 Difference between geoidal height and mean ICESat elevations given for the sea ice region around Drygalski Ice Tongue.....	109
Figure 4.8 Comparison of ice thickness estimates along Drygalski Ice Tongue.	110
Figure 4.9 3-dimensional model of the study area showing the location of flux gates used to calculate basal melt rates.	113
Figure 4.10 Cross section of Drygalski Ice Tongue showing surface elevation from ICESat and derived bottom elevation.	115
Figure 4.11 Optimized velocity field.	118
Figure 4.12 Five surface elevation profiles taken along flow lines.	119
Figure 4.13 Velocity profile and ice thickness profile along the center of the main tributary of David Glacier.	122
Figure 4.14 Several across flow profiles of velocity, strain rate and shear stress used to calculate lateral drag.	124
Figure 4.15 Location plot with flux gates.	129
Figure 4.16 Elevation data between gate 2 and 5 and between gate 5 and 6 which is used to derive ice thickness and surface slope as a function of distance.	131
Figure 4.17 Driving stress between gates 2 and 5 calculated from elevation and derived ice thickness.	133
Figure 4.18 Velocity along a flow line between gate 2 and 5 as a function of distance.	134
Figure 4.19 Y-component of velocity as a function of across flow distance.	135
Figure 4.20 Profile of V_y taken across flow between gate 5 and 6 as a function of across flow distance.	137
Figure 4.21 Velocity along a flowline between gate 5 and 6 as a function of distance..	139
Figure 4.22 Across flow velocity profile used to calculate shear strain rate and shear stress along a section of Drygalski Ice Tongue bounded by valley walls.	140
Figure 4.23 Measured velocity, strain rate and shear stress across several profiles between gates 5 and 6.....	141
Figure 4.24 Values of γ as a function of distance between gate 2 and 6.	143

Figure 4.25 Velocity, elevation, ice thickness and surface gradient along a profile on Drygalski Ice Tongue.....	145
Figure 4.26 Values of longitudinal strain rate, longitudinal stress and driving stress versus distance along the free floating section of Drygalski Ice Tongue.	146
Figure 4.27 Comparison between modeled profiles and profile derived from ICESat data.	148
Figure 4.28 Relative contribution of basal drag , lateral drag and longitudinal stress gradients in opposing the driving stress for the David Glacier- Drygalski Ice Tongue System.....	150
Figure 5.1 Ice flow velocity on Brunt Ice Shelf and Stancomb-Wills Glacier Tongue on the Caird Coast in East Antarctica.	156
Figure 5.2 Two velocity profiles taken from the velocity field	157
Figure 5.3 Longitudinal strain rates determined along two profiles.	158
Figure 5.4 Velocity difference between 3-year averaged feature tracking velocity (1997-2000) and 2000 InSAR velocity.	160
Figure 5.5 Histogram of differences between 3-year averaged feature tracking and InSAR velocities.	161
Figure 5.6 Strain rates in along and across flow direction determined from derived velocity.....	163
Figure 5.7 Velocity profile and thickness profile taken along the center of the Stancomb-Wills Ice Tongue.....	164
Figure 5.8 Basal melting calculated along a profile in the center of SWIT.....	166
Figure 5.9 Driving stress calculated along a profile.	168
Figure 5.10 Across flow profile of velocity, used to calculate shear strain rate and shear stress along the profile.	170
Figure 5.11 RADARSAT image of BIS and SWIT showing flow lines inferred from the velocity field, traced flow stripes, feature tracking and InSAR velocity vectors.	174
Figure 5.12 Velocity profile along a flow line used to calculate the elapsed time since the perturbation.	175

Figure 5.13 Comparison between extrapolated relict flow stripes and actual position of the same flow lines on a 2000 RADARSAT image and a 1986 Landsat image.	177
Figure 5.14 Extrapolated configuration of two relict flow stripes during time of perturbation and position of the stripes on a 1997 image.	178
Figure 5.15 1997 RADARSAT image of BIS and SWIT showing bed topography and ICESat elevation along satellite tracks.	181
Figure 5.16 Three profiles of bed topography underneath SWIT from BEDMAP data.	182
Figure 6.1 Radarsat-1 image of Mertz Glacier Tongue acquired during the MAMM mission in 2000.	187
Figure 6.2 3 year averaged velocity and 48 day averaged velocity depicted on a 1997 RADARSAT-1 scene of Mertz Glacier Tongue.	191
Figure 6.3 Close up of the front of Mertz Glacier Tongue illustrating the advance between 1997 and 2000.	192
Figure 6.4 Difference map calculated by subtracting 3 year averaged velocity (1997-2000) from 48 day averaged velocity (2000) and associated histogram.	193
Figure 6.5 Locations of displacement vectors, derived by Berthier and others (2003), that are used for comparison with velocity derived in this study.	195
Figure 6.6 Scatter plot showing a comparison between velocities from Berthier and others (2003) and 48-day averaged velocities derived in this study and associated histograms of velocity differences.	196
Figure 6.7 Scatter plot showing a comparison between velocities from Berthier and others (2003) and 3-year averaged velocities derived in this study and associated histograms of velocity differences.	197
Figure 6.8 Transect of velocity, elevation and ice thickness along the Mertz Glacier ...	199
Figure 6.9 Values of ϵ_{yy} and ϵ_{xx} along the Mertz Glacier Tongue calculated from derived velocities along several profiles.	201
Figure 6.10 The y component of velocity on MGT	204
Figure 6.11 Driving stress of Mertz Glacier Tongue as a function of distance from the grounding line.	209

Figure 6.12 Velocity, effective strain rate and calculated shear stress along a transect at the point where MGT leaves the fjord.	212
Figure 6.13 Across flow profile of velocity taken 10 km after MGT leaves the valley walls.	213
Figure 6.14 Manual check of displacements of two crevasse intersection points	214
Figure 6.15 Relative contribution of basal drag, lateral drag and longitudinal stress gradients in opposing the driving stress for the Mertz Glacier.	217
Figure 7.1 Across-flow profile of velocity on Drygalski Ice, just after the ice leaves the fjord walls	224
Figure 7.2 Comparison of cross sections and longitudinal velocity in our study areas: Drygalski Ice Tongue, Mertz Glacier Tongue and Stancomb-Wills Ice Tongue.	226
Figure 7.3 3-year averaged feature tracking velocity and 2000 InSAR velocity near the calving front of Pine Island Glacier in the Amundsen Bay region.	232
Figure 7.4 Comparison of velocity data derived in this study with earlier measurements available through VELMAP.	233
Figure 7.5 Comparison between a profile derived from 1997-2000 feature tracking velocity and 2000 InSAR velocity.	234

LIST OF TABLES

Table 2.1 Parameters for the ‘Goldsby’ constitutive equation.	36
Table 4.1 RADARSAT-1 data used in this study	99
Table 4.2 Values used to calculate basal melt rates in this study.	114
Table 4.3 Values for average ice thickness and surface slope used to calculate the driving stress for the 5 sub-areas.	120
Table 4.4 Calculated values for driving stress, longitudinal stress gradients, lateral drag and basal drag.	125
Table 7.1 Averaged velocity values in m a^{-1} near the ice front and grounding line in our study areas.....	229

LIST OF ABBREVIATIONS

AMM-1	- Antarctic Mapping Mission 1 (1997)
BIS	- Brunt Ice Shelf
DEM	- Digital Elevation Model
DN	- Digital Number
EAIS	- East Antarctic Ice Sheet
ERS-1	- European Remote-Sensing Satellite 1
GISP2	- Greenland Ice Sheet Project 2
GRIP	- Greenland Ice Core Project
ICESat	- Ice, Cloud and land Elevation Satellite
InSAR	- Synthetic aperture radar interferometry
MAMM	- Modified Antarctic Mapping Mission (2000)
MGT	- Mertz Glacier Tongue
OSUDEM	- The Ohio State University Digital Elevation Model
RAMP	- RADARSAT-1 Antarctic Mapping Project
RES	- Radio Echo Sounding
SAR	- Synthetic Aperture Radar
SWIT	- Stancomb-Wills Ice Tongue
WAIS	- West Antarctic Ice Sheet

CHAPTER 1

INTRODUCTION

1.1 Introduction

Antarctica has been portrayed as a barometer of climate change. According to the 2001 report of The Intergovernmental Panel on Climate Change (IPCC), although regional responses might vary, Antarctica as a whole is expected to gain mass in the next century and thus moderate observed and expected sea-level rise (IPCC, 2001). This is primarily ascribed to a predicted increase in precipitation. A more recent study, however, finds no significant increase in precipitation in the last 50 years and indicates that this might be too optimistic a view (Monaghan and others, 2006). The mass balance and equilibrium state of an ice sheet is a complex function of external climate forcing and internal dynamical processes.

On the one hand, Holocene changes in ice sheet thickness and extent are attributable to temperature fluctuations and changing precipitation patterns (IPCC, 2001). On the other hand, recent rapid thinning of several major outlet glaciers in both Greenland and Antarctica is partly ascribed to changes in their dynamics (e.g. Zwally and others, 2002; Thomas and others, 2003; Thomas and others, 2004; Rignot and

Kanagaratnam, 2006; Luckman and others, 2006). It has become clear that the relation between climate fluctuations and ice sheet response is complicated and depends on many factors. A better fundamental understanding of glacier dynamics is therefore necessary.

In order to understand the dynamical behavior of an ice sheet and to assess its future behavior it is necessary to identify the dominant forces acting on the ice sheet, and their response to climate changes. A basic element in developing that understanding is to measure ice flow velocities and document changes in velocities and velocity gradients in different flow regimes of the ice sheet. This then can be used, via theory and models, to determine and assess the important flow governing processes. It is, however, very difficult to obtain sufficient velocity data to investigate processes and the stability of the Antarctic ice sheet with conventional glaciological techniques. The dimensions and remoteness of the region make acquiring accurate measurements very complicated, dangerous and expensive. Fortunately, repeat airborne and satellite imagery, together with remote sensing analysis and image processing techniques, have facilitated data collection in recent years. A great opportunity arose for glaciologists with the launch of the Canadian RADARSAT-1 satellite in 1995 and the RADARSAT-1 Antarctic Mapping Project (RAMP), which completed two mapping missions: the Antarctic Mapping Mission-1 (AMM-1) in 1997 and the Modified Antarctic Mapping Mission (MAMM) in 2000. RAMP provided the first complete high-resolution radar mosaic of Antarctica (Jezek, 1998) and allowed for unprecedented detailed velocity measurements of Antarctic ice streams (Joughin and others, 1999).

In this study, ice flow velocity measurements of several large Antarctic outlet glaciers are obtained using AMM-1 and MAMM RADARSAT-1 SAR data. The measurements are used, together with data from previous studies, to analyze spatial and temporal variability of surface velocity and flow governing dynamical processes in order to better comprehend the behavior of ice sheets and assess their (future) stability in response to predicted climate changes. This is important given the rapid changes in the cryosphere that we witness today and their potential consequences.

1.2 Problem statement

Global warming is expected to be amplified in polar regions due to various feedback mechanisms. The mean temperature of Antarctica, based on all Antarctic stations, shows a slight warming trend of 1.2°C over the last decades, however, regional responses vary widely (Vaughan and others, 2001). Records from the Antarctic Peninsula and the Bellingshausen Sea sector indicate a particularly pronounced warming over the last decades that is considerably higher than the Antarctic (and global) average. The magnitude of recent sudden ice shelf collapses, that seem to be associated with this warming trend, has caused concern among scientists and was widely covered by the popular media. The break-ups seem to confirm Mercer's (1978) prediction that the break ups would be early indicators of CO₂-induced global warming. There have been reports that glaciers formerly feeding these ice-shelves are speeding up, thus contributing to sea-level rise (e.g. Rignot and others, 2004; De Angelis and Skvarca, 2003).

Major sea-level changes in the past have been associated with the rise and demise of large continental ice sheets (Lambeck and others, 2002). Substantial melt of ice sheets is also believed to have disrupted ocean circulation patterns and perhaps even to have shutdown the thermo-haline circulation (THC) altogether, which may have led to sudden rapid climate changes in the past of which evidence was first found in Greenland ice cores (Dansgaard and others, 1982, 1989; Oeschger and others, 1984). Antarctica alone contains enough ice to raise global sea-level by about 70 meters, but even a small rise could have considerable societal impact (Alley and others, 2005). Studies show that dynamical responses of ice sheets to warming may play a more important role in the future mass balance of ice sheets than previously thought and future sea-level rise predictions might have to be adjusted upward (Rignot and Kanagaratnam, 2006; Alley and others, 2005). Alley and others (2005, p. 460) state that “a major challenge hereby is to acquire the observations necessary to characterize rapid dynamic changes, and to incorporate those data into improved models, allowing more reliable predictions of ice contribution to sea-level change over the coming decades and centuries.”

A paper by Rignot and Thomas (2002) gives a refined estimate of the balance state of Antarctica, but also indicates, however, that there are still large uncertainties at present and that for the East Antarctic Ice Sheet (EAIS) it is still not possible to evaluate whether there is a net gain or loss of mass without acquiring new data. The West Antarctic Ice Sheet (WAIS) is in all probability currently losing mass; especially the Pine Island region has a considerable deficit (Rignot and Thomas, 2002). Yet other authors report a positive mass balance for the dynamic Ross ice streams (Joughin and Tulaczyk, 2002; Stearns, 2002).

To understand regional variations in mass balance of the Antarctic Ice Sheet and its link to climate change and sea-level we need a fundamental understanding of the processes that are involved and how and why these processes vary within and between different drainage basins. In particular it is necessary to determine what factors contribute to glaciers speeding up or slowing down. Of special interest, after the break up of several large ice shelves the last decade, is what the effects are of removing a floating ice tongue on a glacier that feeds it. Also of interest is how short term fluctuations relate to longer term ice flow behavior. The investigation of these issues is an objective of this study.

1.3 Glacier Flow and Velocity

The massive ice sheet in Antarctica consist of different drainage basins that are drained by numerous fast outlet glaciers and ice streams, which seemingly slide over their bed and transport the majority of ice to the ocean. Some streams reach deep into the interior and others can reach velocities well over 3000 m a^{-1} at their (floating) termini (Rosanova and others, 1998; Joughin and others, 1999). These fast flowing glaciers and ice streams are embedded in a slower moving ice mass that largely moves as a result of internal deformation. To understand the behavior and assess the stability of an ice sheet and possible changes herein it is necessary to quantify the forces that drive glacier flow and resistive forces that oppose it, particularly those of fast outlet glaciers.

Glaciers flow as a result of pressure built up due to their own weight. This is reasonably well understood and can be quantified with some knowledge about their geometry. Resistance to flow is provided by friction at the bed or sides or longitudinal

pulling or pushing from upstream ice. Evaluating the relative roles of these is crucial in assessing the stability of a glacier and in predicting its response to potential perturbations. Because resistance to flow cannot be measured directly, it must be inferred indirectly. For this, detailed velocity measurements are necessary in combination with theoretical models. Although models simplify reality, they have become a vital tool for understanding the behavior of glaciers.

Various models have been proposed that describe glacier flow (e.g. Weertman, 1957; Nye, 1957; Van der Veen and Whillans, 1989; Hughes, 2003). A crucial point in these models is the relationship between stresses and strain rates. The latter can be derived from gradients in velocity. By far the most commonly used ‘law’ that describes this relation is Glen’s flow law (Nye, 1953). A recent study by Goldsby and Kohlstedt (2001) points out, however, that flow of ice cannot be accurately described using a single flow law. Their experiments led them to propose a new constitutive relation. The new flow law enabled Peltier and others (Peltier, 2000) to better explain the aspect ratio of the Greenland ice sheet and the Late Glacial Maximum Laurentide ice sheet simultaneously. For that reason it is necessary to investigate how this flow law can affect calculation of stresses from measured velocity gradients in existing models.

Over the years several techniques have been developed to extract flow velocity from repeat imagery such as automated feature tracking, which measures movement of features that move with the ice such as crevasses, and radar interferometry (InSAR), which measures velocity using phase differences between acquisitions. Although InSAR is a very accurate method to acquire a detailed velocity field, only feature tracking is

capable of measuring velocity on fast moving glaciers over longer time spans. It is important to establish a link between ‘instantaneous’ velocity and longer term velocity. It is difficult to acquire enough trustworthy data from the RADARSAT-1 imagery to initiate a detailed force-budget study without some modifications of existing techniques. This is highly required considering the wealth of information that the RAMP project provides.

1.4 Goals

The primary goal of this study is to improve our understanding of the role of ice tongues on glacier flow and dynamics of several East Antarctic glacier systems that have floating termini, and to investigate spatial and temporal variability in velocity and stress field in an effort to deduce possible trends, causative mechanisms and make predictions for future behavior. The selected study areas and the rationale for choosing these are pointed out in chapter 1.5. Our approach is to make velocity measurements of these areas on various time scales by means of feature tracking and interferometry using RADARSAT-1 imagery, as well as from velocity data culled from the literature and sources such as VELMAP, which is an online database with velocity data for several glaciers (NSIDC, 2000). This allows for calculation of strain rates, and force budget, necessary to investigate flow-governing processes. The different timescales makes it possible to deduce decadal trends and evaluate disparities between short and longer-term averages. Based on literature East Antarctica is believed to be more stable than other parts of Antarctica. Therefore we want to test whether or not our selected study areas in

East Antarctica undergo the same rapid changes, or are susceptible to them, as rapidly changing glaciers found elsewhere. To do this we will try to answer the following questions: (1) Have velocities and stress fields changed over time? (2) What are the dominant forces for different glaciers in Antarctica and how do they vary within and between catchments? (3) Do present day ‘instantaneous’ velocities differ significantly from longer-term (3-year) averages? (4) Are selected areas behaving differently and, if so, what are the responsible mechanisms and how do they affect mass balance? Finally, by studying outlet glaciers and ice flow velocities it will be possible to find answers to questions such as what are the effects of removing an ice shelf or floating ice tongue? Answers to these questions are much needed, especially in the light of recent break ups of several large ice shelves.

1.5 Study Areas

The majority of scientific papers dealing with ice dynamics focus on West Antarctic glaciers, while many East Antarctic glaciers remain understudied. In this study we focus predominantly on several major East Antarctic outlet glaciers. Although the EAIS is believed to be rather stable, the large areas that these glaciers drain warrant a more detailed investigation of their dynamics and potential velocity changes. Furthermore, because they terminate as floating ice tongues and large parts of their drainage areas have beds well below sea-level, they at least have the potential for rapid changes, as demonstrated by rapid changing glaciers in other parts of the polar regions.

In this thesis we focus especially on three areas of interest in East Antarctica. These are David Glacier-Drygalski Ice Tongue in northern Victoria Land, Mertz Glacier Tongue on the George V Coast in Wilkes Land and Brunt Ice Shelf-Stancomb-Wills Ice Tongue on the Caird Coast in Queen Maud Land. All of these glaciers drain large areas of the East Antarctic Ice Sheet (EAIS) and terminate as long floating ice tongues and are therefore relevant to answer the research questions. Investigating similarities and dissimilarities of these glaciers should provide clues to why glaciers behave different. The study areas are indicated on the RAMP mosaic in figure 1.1.

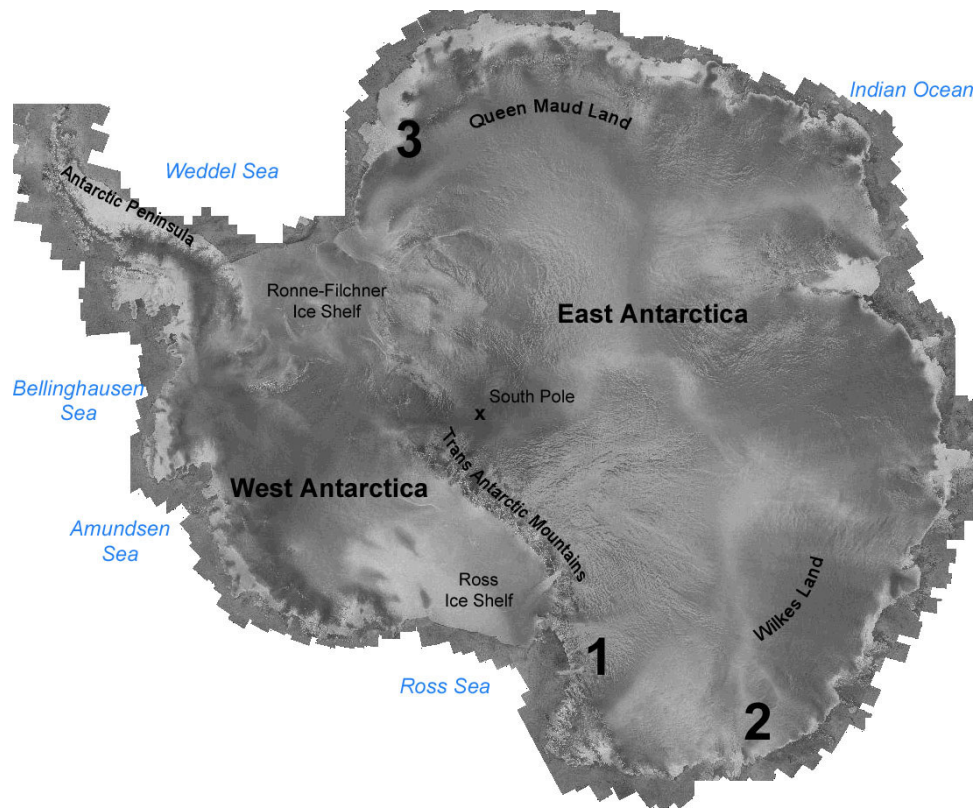


Figure 1.1 Location of the study areas depicted on the RADARSAT-1 Antarctic Mapping Project (RAMP) mosaic, created by the remote sensing lab at The Ohio State University (Noltimier and others, 1999). Numbers depict location of David Glacier-Drygalski Ice Tongue (1), Mertz Glacier Tongue (2) and Brunt Ice Shelf-Stancomb-Wills Ice Tongue (3).

1.6 Overview of the study

In sum, this study is concerned with the behavior of major Antarctic outlet glaciers. It specifically attempts to identify, analyze, and explain the dominant forces that act on the ice sheet and in doing so shed light on its behavior and stability. In order to do

so, we measure ice flow velocities and document changes in velocities and velocity gradients in different areas and over different time spans, since these variables are the most important in modeling ice sheet behavior. We use 1997 AMM-1 and 2000 MAMM RADARSAT-1 SAR data to acquire ice flow velocities and, in combination with other datasets, to analyze the dynamic behavior of the selected study areas with special emphasis on the role of their floating termini in controlling ice flow. The availability of these newly acquired datasets allows for a more detailed assessment than previously possible and fills in data gaps. Most importantly, the remote sensing data record is now becoming sufficiently long to begin an investigation of natural variability for comparison with longer term trends. We focus primarily on several relatively understudied East Antarctic glaciers that drain the largest ice sheet in the world. Studying the dynamic behavior of these outlet glaciers should result in a fuller and more nuanced understanding of ice sheet behavior in Antarctica, which is critical in the context of global warming and its impacts.

This dissertation is organized as follows. Chapter 2 reviews the theoretical framework used in this study. We explain what drives glacier flow and how resistive forces can be estimated from ice flow velocities and gradients in velocities. We expand on existing theory by investigating the result of using a different flow law, describing the stress-strain relation.

Chapter 3 discusses and justifies the various datasets and methods that are used in this study and their associated errors. The principal data source is repeat RADARSAT-1 SAR imagery. This is used to derive ice flow velocities through various techniques. We modify an often used feature tracking algorithm and develop a procedure in order to

optimize velocity extraction from the available data sources. The steps involved in this process are discussed in detail and justified. Other data sources that we use and discuss are VELMAP, OSUDEM, BEDMAP and ICESat.

In chapter 4 we investigate whether changes occurred in the flow regime of David Glacier and Drygalski Ice Tongue. Velocity maps are presented and discussed. Velocity comparisons are made and discussed. We apply the force-budget technique described in chapter 2 and investigate the stress partitioning along the drainage system.

In chapters 5 and 6 we apply a similar approach and investigate the flow regime of Brunt Ice Shelf-Stancomb-Wills Ice Tongue and the flow regime of Mertz Glacier Tongue.

The aim of chapter 7 is to compare the results of the various areas presented in chapters 4-6. We will also look at the rapidly changing Pine Island Glacier. Answers to the research questions discussed in chapter 1 are given.

Chapter 8 concludes the dissertation and in it the main results and conclusions of this study are summarized and recommendations for future research are given.

CHAPTER 2

THEORY

2.1 Introduction

To understand the behavior of glaciers and possible changes therein it is necessary to quantify the forces that drive glacier flow and the resistive forces that oppose it. This chapter describes the derivation of these quantities in terms of measurable velocity components. For this we use existing force-budget theory described in Van der Veen and Whillans (1989) and Van der Veen (1999). Because this method is critical to this study, we review the force-budget technique in this chapter. We go on to discuss the need for a link between short and long term ice flow behavior that is best established using remotely sensed velocity data averaged over various time spans. We do this motivated by recent observations of highly discontinuous ice motion on several West Antarctic ice streams that seems to be associated with tidal cycles. As will be shown in subsequent chapters we find short term velocity to be very similar to longer term velocity for most of our study areas. We contribute to existing theory by carefully assessing how uncertainties in the data propagate into the calculation of resistive stresses. Furthermore, we expand on the force-budget technique by developing an approach to incorporate a new constitutive

relation in the force-budget technique for comparison with the more familiar Glen's flow law. This is important because recent advances in laboratory techniques have revealed an important, newly discovered, creep regime, which is grain size dependent and is not accounted for in Glen's flow law. We find that, using this new flow law, calculated longitudinal and lateral shear stresses can be up to 30 % higher for a range of common grain sizes. For the calculation of lateral drag, this usually has little effect since we use the gradient in shear stress rather than its absolute value and we find the bias to be almost systematic. However, it does affect the calculation of the longitudinal resistance, resulting in smaller values for inferred basal drag.

2.2 Force-budget calculation

To calculate the various resistive forces and their relative role in opposing the driving stress we use the force-budget method (Van de Veen and Whillans, 1989), which is reviewed here. Force-budget calculations can be used to determine the dominant forces acting on the ice sheet, and investigate the important flow governing processes. It is a theoretical method that requires knowledge about the glacier geometry and surface velocity field. With this information the driving stress, which is the result of gravitational forces on the ice, and resistance to it can be calculated. The driving stress, which drives glacier flow, is opposed by lateral drag acting on the sides, longitudinal stress gradients (tension or compression exerted by down or upstream ice) and by basal drag, which is the resistance caused by the bed (figure 2.1).

By using the force-budget technique the relative importance of the resistive forces can be determined, which is necessary to understand the dynamics of a glacier (Van der

Veen, 1999). Since there is no way of doing this directly in the field, the method represents an indirect way to investigate interactions between the ice and the bed, and the ice and its sides. This then can be used to assess the sensitivity of a glacier to perturbations such as the collapse of a buttressing ice shelf.

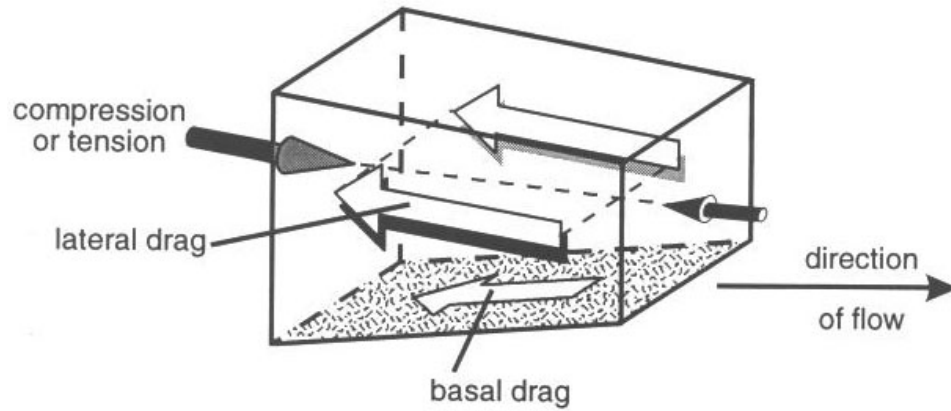


Figure 2.1 Schematic view of the different resistive forces governing glacier flow. The gravitational driving stress is opposed by lateral drag, acting on the sides, basal drag, acting on the bed, and longitudinal compression or tension (adapted from Van der Veen, 1999).

2.2.1 Driving stress

The gravitational pull that acts on glaciers and causes them to move is called the driving stress. The driving stress τ_{dx} is a function of ice density ρ , the acceleration due to gravity g , the ice thickness H and the surface slope of the ice α according to:

$$\tau_{dx} = -\rho g H \alpha \quad (2.1)$$

whereby α is estimated from the difference in elevation (h) between two points x_1 and x_2 :

$$\alpha = \frac{h_2 - h_1}{x_2 - x_1} \quad (2.2)$$

The gravitational driving stress is assumed to be opposed by resistive forces so that there is zero net force acting on the ice. When estimating the driving stress from ice thickness data and a DEM the error can be expressed as (ignoring uncertainties in density):

$$\sigma_{\tau_{dx}} = \left[\left(\frac{\partial \tau_{dx}}{\partial H} \right)^2 \sigma_H^2 + \left(\frac{\partial \tau_{dx}}{\partial \alpha} \right)^2 \sigma_\alpha^2 \right]^{1/2} = \left[(-\rho g \alpha \sigma_H)^2 + (-\rho g H \sigma_\alpha)^2 \right]^{1/2} \quad (2.3)$$

Since both elevation errors are equal, the error in surface slope (ignoring positional errors) is given by:

$$\sigma_\alpha = \sqrt{2} \left(\frac{\sigma_h}{\delta x} \right) \quad (2.4)$$

where δx is the distance over which the surface gradient is calculated. The last term in equation 2.3 (associated with the error in surface slope) is usually dominant.

2.2.2 Resistive stresses

Resistive stresses cannot be measured directly in the field and must be estimated indirectly from gradients in velocity. In this way the lateral and longitudinal resistance to flow can be estimated. Basal resistance is assumed to be the remainder necessary to balance the driving stress. How this is done is explained in this chapter.

To understand glacier flow we need to define the concept of strain. Strain measures the amount of deformation that occurs as a result of stresses on a medium. The strain rate is the amount of strain that occurs per unit time. Nye (1953) suggested a relation between effective strain rates and effective stresses, which are the second invariants of the strain rate and stress tensors respectively. The effective strain rate $\dot{\epsilon}_e$ is related to strain rate $\dot{\epsilon}_{ij}$ according to:

$$2\dot{\epsilon}_e^2 = \dot{\epsilon}_{xx}^2 + \dot{\epsilon}_{yy}^2 + \dot{\epsilon}_{zz}^2 + 2(\dot{\epsilon}_{xy}^2 + \dot{\epsilon}_{xz}^2 + \dot{\epsilon}_{yz}^2) \quad (2.5)$$

Similarly the effective stress τ_e is defined as:

$$2\tau_e^2 = \tau_{xx}^2 + \tau_{yy}^2 + \tau_{zz}^2 + 2(\tau_{xy}^2 + \tau_{xz}^2 + \tau_{yz}^2) \quad (2.6)$$

Here τ_{ij} is called the stress deviator, which is related to the full stress tensor σ_{ij} as follows:

$$\tau_{ij} = \sigma_{ij} - \delta_{ij} \frac{1}{3} P \quad (2.7)$$

where δ_{ij} is the Kronecker delta ($\delta_{ij}=1$ if $i=j$ and $\delta_{ij}=0$ if $i \neq j$) and P is the hydrostatic pressure defined as the sum of the three normal stresses:

$$P = \sigma_{xx} + \sigma_{yy} + \sigma_{zz} \quad (2.8)$$

Experiments have shown that for ice strain rate and stress are related to each other through Glen's flow law (Nye, 1953).

$$\dot{\epsilon}_{ij} = A \tau_e^{n-1} \tau_{ij} \quad (2.9)$$

or written differently:

$$\tau_{ij} = B \dot{\epsilon}_e^{1/n-1} \dot{\epsilon}_{ij} \quad (2.10)$$

where A and B are flow parameters (and $B=A^{-n}$) that are mainly dependent on the temperature of the ice and n is the flow law exponent (usually taken to be 3). Equation 2.10 is important because it allows the calculation of stresses from measurable velocity gradients.

It is assumed here that ice is isotropic and incompressible, therefore the sum of the three strain rate components in the normal direction must equal zero:

$$\dot{\epsilon}_{xx} + \dot{\epsilon}_{yy} + \dot{\epsilon}_{zz} = 0 \quad (2.11)$$

It follows that:

$$\dot{\epsilon}_{zz}^2 = \dot{\epsilon}_{xx}^2 + 2\dot{\epsilon}_{xx}\dot{\epsilon}_{yy} + \dot{\epsilon}_{yy}^2 \quad (2.12)$$

hence we can rewrite equation 2.10 as follows:

$$\tau_{ij} = B[(\dot{\epsilon}_{xx}^2 + \dot{\epsilon}_{yy}^2 + \dot{\epsilon}_{xx}\dot{\epsilon}_{yy} + \dot{\epsilon}_{xy}^2 + \dot{\epsilon}_{xz}^2 + \dot{\epsilon}_{yz}^2)^{1/2}]^{-2/3} \dot{\epsilon}_{ij} \quad (2.13)$$

Full stresses can also be separated in terms of resistive stresses R_{ij} as follows:

$$\sigma_{ij} = R_{ij} + \delta_{ij} L \quad (2.14)$$

L is called the lithostatic stress which is the weight of the ice above a certain level. This only affects the normal stresses and is calculated from:

$$L = -\rho g(h - z) \quad (2.15)$$

where h is the surface elevation. If we substitute full stresses for resistive stress in the stress equilibrium equations we get:

$$\begin{aligned}
\frac{\partial[R_{xx} - \rho g(h - z)]}{\partial x} + \frac{\partial R_{yx}}{\partial y} + \frac{\partial R_{zx}}{\partial z} &= 0 \\
\frac{\partial R_{yx}}{\partial x} + \frac{\partial[R_{yy} - \rho g(h - z)]}{\partial y} + \frac{\partial R_{zy}}{\partial z} &= 0 \\
\frac{\partial R_{xz}}{\partial x} + \frac{\partial R_{yz}}{\partial y} + \frac{\partial[R_{zz} - \rho g(h - z)]}{\partial z} - \rho g &= 0
\end{aligned} \tag{2.16}$$

Integrating the first equation in 2.16 from the base of the ice ($h-H$) to the surface (h), using Leibnitz rule, we find:

$$\begin{aligned}
\frac{\partial}{\partial x} \int_{h-H}^h R_{xx} dz - R_{xx}(h) \frac{\partial h}{\partial x} + R_{xx}(h-H) \frac{\partial(h-H)}{\partial x} - \\
\rho g H \frac{\partial h}{\partial x} + R_{xz}(h) - R_{xz}(h-H) + \frac{\partial}{\partial y} \int_{h-H}^h R_{xy} dz - \\
R_{xy}(h) \frac{\partial h}{\partial y} + R_{xy}(h-H) \frac{\partial(h-H)}{\partial y} = 0
\end{aligned} \tag{2.17}$$

This equation can be simplified since the surface must be stress free and thus:

$$R_{xx}(h) \frac{\partial h}{\partial x} + R_{xy}(h) \frac{\partial h}{\partial y} - R_{xz}(h) = 0 \tag{2.18}$$

Basal drag τ_{bx} and driving stress τ_{dx} can be defined as:

$$\tau_{bx} = R_{xz}(h-H) - R_{xx}(h-H) \frac{\partial(h-H)}{\partial x} - R_{xy}(h-H) \frac{\partial(h-H)}{\partial y} \quad (2.19)$$

$$\tau_{dx} = -\rho g H \frac{\partial h}{\partial x} \quad (2.20)$$

Combining equation 2.17-20 we find the force balance equation for the x-direction:

$$\tau_{dx} = \tau_{bx} - \frac{\partial}{\partial x} \int_{h-H}^h R_{xx} dz - \frac{\partial}{\partial y} \int_{h-H}^h R_{xy} dz \quad (2.21)$$

If we assume that resistive stresses are constant with depth this results in:

$$\tau_{dx} = \tau_{bx} - \frac{\partial}{\partial x} (H R_{xx}) - \frac{\partial}{\partial y} (H R_{xy}) \quad (2.22)$$

The terms in equation 2.22 describe driving stress, basal drag, longitudinal and lateral resistance respectively. From equation 2.7 and 2.14 we find that:

$$R_{ij} = \tau_{ij} + \delta_{ij} \left(\frac{1}{3} P - L \right) \quad (2.24)$$

Thus for $i = j = z$:

$$R_{zz} = \tau_{zz} + \left(\frac{1}{3}P - L \right) \quad (2.25)$$

From equation 2.7 and 2.8 we find that the sum of the three normal deviatoric stresses equals zero, thus:

$$\tau_{zz} = -\tau_{xx} - \tau_{yy} \quad (2.26)$$

It follows that:

$$\left(\frac{1}{3}P - L \right) = R_{zz} + \tau_{xx} + \tau_{yy} \quad (2.27)$$

Using the flow law (equation 2.10) we can now write the resistive stresses in terms of strain rates:

$$\begin{aligned} R_{xx} &= 2\tau_{xx} + \tau_{yy} + R_{zz} = 2(B\dot{\epsilon}_e^{-2/3}\dot{\epsilon}_{xx}) + (B\dot{\epsilon}_e^{-2/3}\dot{\epsilon}_{yy}) + R_{zz} = \\ &B\dot{\epsilon}_e^{-2/3}(2\dot{\epsilon}_{xx} + \dot{\epsilon}_{yy}) + R_{zz} \\ R_{yy} &= 2\tau_{yy} + \tau_{xx} + R_{zz} = B\dot{\epsilon}_e^{-2/3}(2\dot{\epsilon}_{yy} + \dot{\epsilon}_{xx}) + R_{zz} \\ R_{xy} &= \tau_{xy} = B\dot{\epsilon}_e^{-2/3}\dot{\epsilon}_{xy} \\ R_{xz} &= \tau_{xz} = B\dot{\epsilon}_e^{-2/3}\dot{\epsilon}_{xz} \\ R_{yz} &= \tau_{yz} = B\dot{\epsilon}_e^{-2/3}\dot{\epsilon}_{yz}. \end{aligned} \quad (2.28)$$

Resistive stresses can thus be estimated by writing strain rates in terms of velocity components (with u , v and w denoting the velocity components in the x , y and z direction respectively) since by definition:

$$\dot{\epsilon}_{ij} = \frac{1}{2} \left(\frac{\partial u_i}{\partial x_j} + \frac{\partial u_j}{\partial x_i} \right) \quad (2.29)$$

and thus the individual strain rate components are calculated from:

$$\begin{aligned} \dot{\epsilon}_{xx} &= \frac{\partial u}{\partial x} & \dot{\epsilon}_{xz} &= \frac{1}{2} \left(\frac{\partial u}{\partial z} + \frac{\partial w}{\partial x} \right) \\ \dot{\epsilon}_{yy} &= \frac{\partial v}{\partial y} & \dot{\epsilon}_{yz} &= \frac{1}{2} \left(\frac{\partial v}{\partial z} + \frac{\partial w}{\partial y} \right) \\ \dot{\epsilon}_{xy} &= \frac{1}{2} \left(\frac{\partial u}{\partial y} + \frac{\partial v}{\partial x} \right) \end{aligned} \quad (2.30)$$

Using these expressions we can write the resistive stresses, necessary to solve the balance equations, in terms of velocity components:

$$\begin{aligned} R_{xx} = B & \left[\left\{ \left(\frac{\partial u}{\partial x} \right)^2 + \left(\frac{\partial v}{\partial y} \right)^2 + \left(\frac{\partial u}{\partial x} \frac{\partial v}{\partial y} \right) + \left(\frac{1}{2} \left(\frac{\partial u}{\partial y} + \frac{\partial v}{\partial x} \right) \right)^2 + \left(\frac{1}{2} \left(\frac{\partial u}{\partial z} + \frac{\partial w}{\partial x} \right) \right)^2 + \right. \right. \\ & \left. \left. \left(\frac{1}{2} \left(\frac{\partial v}{\partial z} + \frac{\partial w}{\partial y} \right) \right)^2 \right\}^{1/2} \right]^{-2/3} \left(2 \frac{\partial u}{\partial x} + \frac{\partial v}{\partial y} \right) + R_{zz} \end{aligned}$$

$$R_{yy} = B \left[\left\{ \left(\frac{\partial u}{\partial x} \right)^2 + \left(\frac{\partial v}{\partial y} \right)^2 + \left(\frac{\partial u}{\partial x} \frac{\partial v}{\partial y} \right) + \left(\frac{1}{2} \left(\frac{\partial u}{\partial y} + \frac{\partial v}{\partial x} \right) \right)^2 + \left(\frac{1}{2} \left(\frac{\partial u}{\partial z} + \frac{\partial w}{\partial x} \right) \right)^2 + \left(\frac{1}{2} \left(\frac{\partial v}{\partial z} + \frac{\partial w}{\partial y} \right) \right)^2 \right\}^{1/2} \right]^{-2/3} \left(2 \frac{\partial v}{\partial y} + \frac{\partial u}{\partial x} \right) + R_{zz} \quad (2.31)$$

$$R_{xy} = B \left[\left\{ \left(\frac{\partial u}{\partial x} \right)^2 + \left(\frac{\partial v}{\partial y} \right)^2 + \left(\frac{\partial u}{\partial x} \frac{\partial v}{\partial y} \right) + \left(\frac{1}{2} \left(\frac{\partial u}{\partial y} + \frac{\partial v}{\partial x} \right) \right)^2 + \left(\frac{1}{2} \left(\frac{\partial u}{\partial z} + \frac{\partial w}{\partial x} \right) \right)^2 + \left(\frac{1}{2} \left(\frac{\partial v}{\partial z} + \frac{\partial w}{\partial y} \right) \right)^2 \right\}^{1/2} \right]^{-2/3} \frac{1}{2} \left(\frac{\partial u}{\partial y} + \frac{\partial v}{\partial x} \right)$$

These equations can be simplified if we assume R_{zz} , $\frac{\partial u}{\partial z}$, $\frac{\partial v}{\partial z}$, $\frac{\partial w}{\partial x}$ and $\frac{\partial w}{\partial y}$ to be small:

$$R_{xx} = B \left[\left\{ \left(\frac{\partial u}{\partial x} \right)^2 + \left(\frac{\partial v}{\partial y} \right)^2 + \left(\frac{\partial u}{\partial x} \frac{\partial v}{\partial y} \right) + \left(\frac{1}{2} \left(\frac{\partial u}{\partial y} + \frac{\partial v}{\partial x} \right) \right)^2 \right\}^{1/2} \right]^{-2/3} \left(2 \frac{\partial u}{\partial x} + \frac{\partial v}{\partial y} \right)$$

$$R_{yy} = B \left[\left\{ \left(\frac{\partial u}{\partial x} \right)^2 + \left(\frac{\partial v}{\partial y} \right)^2 + \left(\frac{\partial u}{\partial x} \frac{\partial v}{\partial y} \right) + \left(\frac{1}{2} \left(\frac{\partial u}{\partial y} + \frac{\partial v}{\partial x} \right) \right)^2 \right\}^{1/2} \right]^{-2/3} \left(2 \frac{\partial v}{\partial y} + \frac{\partial u}{\partial x} \right) \quad (2.32)$$

$$R_{xy} = B \left[\left\{ \left(\frac{\partial u}{\partial x} \right)^2 + \left(\frac{\partial v}{\partial y} \right)^2 + \left(\frac{\partial u}{\partial x} \frac{\partial v}{\partial y} \right) + \left(\frac{1}{2} \left(\frac{\partial u}{\partial y} + \frac{\partial v}{\partial x} \right) \right)^2 \right\}^{1/2} \right]^{-2/3} \frac{1}{2} \left(\frac{\partial u}{\partial y} + \frac{\partial v}{\partial x} \right)$$

All the terms in these equations, except B , can be calculated from velocity profiles in across and along flow directions, for example:

$$\dot{\epsilon}_{xx}\left(n+\frac{1}{2}\right) = \frac{\partial u}{\partial x}\left(n+\frac{1}{2}\right) \approx \frac{u_{x(n+1)} - u_{x(n)}}{x_{(n+1)} - x_{(n)}} \quad (2.33)$$

2.3 Floating glaciers bounded by valley walls

For a floating glacier or ice tongue, where basal drag can be neglected, resistance to flow is provided by lateral drag, caused by valley walls, and longitudinal stress gradients. The balance equation in the x-direction (2.22) becomes:

$$\tau_{dx} = -\frac{\partial}{\partial x}(HR_{xx}) - \frac{\partial}{\partial y}(HR_{xy}) \quad (2.34)$$

These terms can be calculated from velocity profiles in along and across flow directions and strain rates in a similar way as described in the previous section. Where across flow transects of velocity are not available, a slightly different approach can be used. In this approach the longitudinal stress gradients and driving stress are calculated and it is assumed that the lateral drag is the remainder necessary to balance equation 2.34. Therefore the different approach can also be used as an independent check on the magnitude of lateral drag calculated from across flow gradients only. We can denote the fraction of the driving stress that is supported by lateral drag ψ as follows:

$$\psi = \frac{-\frac{\partial}{\partial y}(HR_{xy})}{\tau_{dx}} \quad (2.35)$$

so that:

$$(1 - \psi)\tau_{dx} = -\frac{\partial}{\partial x}(HR_{xx}) \quad (2.36)$$

or rewriting the equation:

$$\psi = 1 + \frac{1}{\tau_{dx}} \frac{\partial}{\partial x}(HR_{xx}) \quad (2.37)$$

If $\psi = 0$ all resistance comes from longitudinal stress gradients; if $\psi = 1$ all resistance is associated with lateral drag. Any value in between these two extremes indicates that resistance to flow is due to a combination of lateral shear and longitudinal stress gradients.

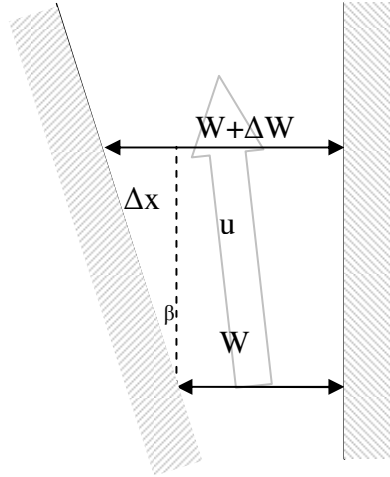


Figure 2.2 Lateral spreading in a non-parallel valley.

If the walls of a fjord where a glacier flows are not exactly parallel, it causes the glacier to spread or converge. The strain rate associated with this can be estimated in two different ways. First it can be estimated by calculating the gradient of the y-component of velocity in the across flow direction. Again, if across flow transects of velocity are not available, or poor, a different approach can be used. This is based on the presumption that the spreading must be fast enough for the glacier to remain in contact with the sides. If at one point the width of a glacier is W and downstream the width of the glacier is $W + \Delta W$ then (figure 2.2):

$$\epsilon_{yy} = \frac{\Delta W}{W} \quad (2.38)$$

and the strain rate is:

$$\dot{\epsilon}_{yy} = \frac{\Delta W}{Wt} \quad (2.39)$$

Where t is time and is calculated from:

$$t = \frac{\Delta x}{u} \quad (2.40)$$

It follows that:

$$\dot{\epsilon}_{yy} = \frac{u}{W} \frac{\partial W}{\partial x} \approx \frac{u}{W} \sin \beta \approx \frac{\partial v}{\partial y} \quad (2.41)$$

The two approaches should theoretically yield similar results but could differ if the fjord walls spread too fast for the ice to maintain contact or if the across flow component of velocity is highly variable, thus making it difficult to determine a gradient. Using equation 2.32 and 2.41 we can estimate R_{xx} along the center line of a glacier, where lateral shearing is usually very small and can be ignored, using:

$$R_{xx} = B \left[\left\{ \left(\frac{\partial u}{\partial x} \right)^2 + \left(\frac{u}{W} \frac{\partial W}{\partial x} \right)^2 + \frac{\partial u}{\partial x} \left(\frac{u}{W} \frac{\partial W}{\partial x} \right) \right\}^{1/2} \right]^{-2/3} \left(2 \frac{\partial u}{\partial x} + \frac{u}{W} \frac{\partial W}{\partial x} \right) \quad (2.42)$$

In this equation the value for R_{xx} is assigned to the midpoint of the transect used to approximate the strain rate (see equation 2.33). This can then be used in equation 2.37 to calculate ψ and, then, lateral drag from:

$$\psi\tau_{dx} = -\frac{\partial}{\partial y}(HR_{xy}) \quad (2.43)$$

2.4 Free floating glaciers

When a glacier is floating freely and is not bounded by fjord walls resistance to flow is provided by longitudinal stress gradients in the direction of flow denoted by x . If we look at the along flow direction the force balance equation (2.22) becomes:

$$\tau_{dx} = \rho g H \frac{\partial h}{\partial x} = \frac{\partial}{\partial x}(HR_{xx}). \quad (2.44)$$

For a floating glacier the ice thickness H is related to the surface elevation h through the floatation criterion:

$$h = \left(1 - \frac{\rho_i}{\rho_w}\right)H \quad (2.45)$$

where ρ_i and ρ_w are the densities of ice and water respectively. Combining equation 2.44 and 2.45 we find:

$$\frac{1}{2}\rho g\left(1-\frac{\rho_i}{\rho_w}\right)\frac{\partial H^2}{\partial x}=\frac{\partial}{\partial x}(HR_{xx}) \quad (2.46)$$

and after integration we can estimate the longitudinal stress from the ice thickness:

$$R_{xx}=\frac{1}{2}\rho_i g\left(1-\frac{\rho_i}{\rho_w}\right)H. \quad (2.47)$$

This solution was first derived by Weertman (1957). A comparison between longitudinal stress gradients derived from ice thickness with that from measured velocity gradients can indicate whether other factors (such as side drag) might still play a role.

2.5 Error propagation

To investigate how uncertainties in the different source datasets propagate in the calculation of the stress partitioning we use the theory of error propagation. This error analysis assumes Glen's flow law with a specific value for the flow law exponent ($n=3$) and a normal distributed error. Since both velocity errors in equation 2.33 are assumed equal, the error in each term can be expressed as (ignoring positional errors):

$$\sigma_{\varepsilon_{ij}}=\left[\left(\frac{\partial \varepsilon_{ij}}{\partial u_2}\right)^2\sigma_{u_2}^2+\left(\frac{\partial \varepsilon_{ij}}{\partial u_1}\right)^2\sigma_{u_1}^2\right]^{\frac{1}{2}}=\left[2\left(\frac{1}{\delta x}\right)^2\sigma_u^2\right]^{\frac{1}{2}}=\left(\frac{\sigma_u}{\delta x}\right)\sqrt{2} \quad (2.48)$$

Where σ denotes the standard error, $\dot{\epsilon}_{ij}$ is the strain rate, u_1 and u_2 are the velocities at two points, δx is the length over which the gradient is calculated. The longer this length, the smaller the error in the calculated strain rate. To calculate the uncertainty in strain rate we assume here that the errors are random, although there might be a systematic bias because of the method of deriving velocity.

The error in lateral shearing (equation 2.28) is determined through error propagation by:

$$\sigma_{R_{xy}} = \left[\left(\frac{\partial R_{xy}}{\partial \dot{\epsilon}_{xy}} \right)^2 \sigma_{\dot{\epsilon}_{xy}}^2 + \left(\frac{\partial R_{xy}}{\partial B} \right)^2 \sigma_B^2 \right]^{\frac{1}{2}} = \left[\left(\frac{1}{3} B \dot{\epsilon}_{xy}^{-\frac{2}{3}} \right)^2 \sigma_{\dot{\epsilon}_{xy}}^2 + \left(\dot{\epsilon}_{xy}^{\frac{1}{3}} \right)^2 \sigma_B^2 \right]^{\frac{1}{2}} \quad (2.49)$$

To find the error in the longitudinal resistive stress it is convenient to first find the derivative of $\dot{\epsilon}_e$ with respect to $\dot{\epsilon}_{xx}$ and $\dot{\epsilon}_{yy}$. From equation 2.5 and the chain rule it follows that:

$$\frac{\partial \dot{\epsilon}_e}{\partial \dot{\epsilon}_{xx}} = \frac{(2\dot{\epsilon}_{xx} + \dot{\epsilon}_{yy})}{2\dot{\epsilon}_e} \quad \frac{\partial \dot{\epsilon}_e}{\partial \dot{\epsilon}_{yy}} = \frac{(2\dot{\epsilon}_{yy} + \dot{\epsilon}_{xx})}{2\dot{\epsilon}_e} \quad (2.50)$$

Next the error in R_{xx} can be expressed as:

$$\sigma_{R_{xx}} = \left[\left(\frac{\partial R_{xx}}{\partial \dot{\epsilon}_{xx}} \right)^2 \sigma_{\dot{\epsilon}_{xx}}^2 + \left(\frac{\partial R_{xx}}{\partial \dot{\epsilon}_{yy}} \right)^2 \sigma_{\dot{\epsilon}_{yy}}^2 + \left(\frac{\partial R_{xx}}{\partial B} \right)^2 \sigma_B^2 \right]^{\frac{1}{2}} \quad (2.51)$$

Taking the first term on the right hand side it follows from equation 2.28:

$$\frac{\partial R_{xx}}{\partial \dot{\epsilon}_{xx}} = 2B\dot{\epsilon}_e^{-\frac{2}{3}} - \frac{4}{3}B\dot{\epsilon}_{xx}\dot{\epsilon}_e^{-\frac{1}{3}}\left(\frac{\partial \dot{\epsilon}_e}{\partial \dot{\epsilon}_{xx}}\right) - \frac{2}{3}B\dot{\epsilon}_{yy}\dot{\epsilon}_e^{-\frac{1}{3}}\left(\frac{\partial \dot{\epsilon}_e}{\partial \dot{\epsilon}_{xx}}\right) \quad (2.52)$$

And almost similarly:

$$\frac{\partial R_{xx}}{\partial \dot{\epsilon}_{yy}} = B\dot{\epsilon}_e^{-\frac{2}{3}} - \frac{4}{3}B\dot{\epsilon}_{xx}\dot{\epsilon}_e^{-\frac{1}{3}}\left(\frac{\partial \dot{\epsilon}_e}{\partial \dot{\epsilon}_{yy}}\right) - \frac{2}{3}B\dot{\epsilon}_{yy}\dot{\epsilon}_e^{-\frac{1}{3}}\left(\frac{\partial \dot{\epsilon}_e}{\partial \dot{\epsilon}_{yy}}\right) \quad (2.53)$$

The derivative in the last term of equation 2.51 becomes:

$$\frac{\partial R_{xx}}{\partial B} = \dot{\epsilon}_e^{-2/3}(2\dot{\epsilon}_{xx} + \dot{\epsilon}_{yy}) \quad (2.54)$$

Finally the error in the terms of the balance equation (equation 2.22) can be determined.

The gradient in longitudinal stress R_L is calculated from:

$$R_L = \frac{\partial}{\partial x}(HR_{xx}) \approx \frac{H_2 R_{xx2}}{\delta x} - \frac{H_1 R_{xx1}}{\delta x} \quad (2.55)$$

The error of R_L is given by:

$$\begin{aligned}
\sigma_{R_L} &= \left[\left(\frac{\partial R_L}{\partial H_2} \right)^2 \sigma_{H_2}^2 + \left(\frac{\partial R_L}{\partial R_{xx2}} \right)^2 \sigma_{R_{xx2}}^2 + \left(\frac{\partial R_L}{\partial H_1} \right)^2 \sigma_{H_1}^2 + \left(\frac{\partial R_L}{\partial R_{xx1}} \right)^2 \sigma_{R_{xx1}}^2 \right]^{\frac{1}{2}} = \\
&\left[\left(\frac{R_{xx2}}{\delta_x} \right)^2 \sigma_{H_2}^2 + \left(\frac{H_2}{\delta_x} \right)^2 \sigma_{R_{xx2}}^2 + \left(\frac{R_{xx1}}{\delta_x} \right)^2 \sigma_{H_1}^2 + \left(\frac{H_1}{\delta_x} \right)^2 \sigma_{R_{xx1}}^2 \right]^{\frac{1}{2}} = \quad (2.56) \\
&\left[\left(\frac{1}{\delta_x} \right)^2 \left(\sigma_H^2 (R_{xx2}^2 + R_{xx1}^2) + \sigma_{R_{xx}}^2 (H_2^2 + H_1^2) \right) \right]^{\frac{1}{2}}
\end{aligned}$$

Since basal drag is calculated indirectly, its error is the largest and is calculated from the errors in the other terms of the balance equation.

2.6 Averaging velocity measurements

The methods described in the previous section strongly rely on accurate and dense surface velocity data that are best obtained from remote sensing. Velocity from satellite imagery is basically derived by measuring the displacement of a point or feature on two images separated by a certain time. This means that averaging takes place, referred to as the temporal resolution. Recent observations from GPS and seismic surveys on the West Antarctic ice streams show highly discontinuous motion of ice on short timescales (less than a day) that seems to be associated with tidal cycles (Bindshadler and others, 2003). The rapid motion events were separated by extended quiescent periods. In addition, the variation in velocity was found to be highest at spring tide and the higher the tidal range, the faster the flow. This tidal forcing was even seen more than 90 km upstream from the grounding line (Anandakrishnan, pers. comm.). Such short term fluctuations cannot be

resolved from velocity measurements derived from repeat satellite imagery as repeat overpasses are usually at the least several days apart. Therefore strain rates and stresses derived from longer term averaging cannot be used to model these short term processes. However, it is important to seek a link between short term, tidal fluctuations and longer term fluctuations to understand long term ice sheet behavior. It is therefore important to make velocity measurements at various time scales. In this study we find that short term ice flow velocity (e.g. averaged over several weeks) is very similar to longer term averaged flow velocity (years to decades) for most of the areas we investigated, as will be shown in subsequent chapters.

2.7 Implications of a new flow law

Various models have been proposed that describe glacier flow (e.g. Weertman, 1957; Nye, 1957; Van der Veen and Whillans, 1989; Hughes, 2003). A crucial point in these models is the relationship between stress and strain. Thus in order to describe the rheological behavior of ice on a macroscopic scale it is necessary to invoke a constitutive relation. This constitutive relation or flow law must describe the amount of deformation of ice when subjected to a force. By far the most commonly used ‘law’ that describes this relation, and used in the force-budget technique, is Glen’s flow law (equation 2.6). This relation was suggested by Nye based on laboratory data from Glen (Nye, 1953). Laboratory experiments have since indicated that ice flows by a number of micromechanical processes. These processes include dislocation creep, sliding on grain boundaries, basal or easy slip and grain boundary diffusion and characterize ice flow over a range of stress, strain rate and temperature (Goldsby and Kohlstedt, 2001). Goldsby and

Kohlstedt (2001) point out that flow of ice cannot accurately be described using a single flow law. They further argue that Glen's flow law oversimplifies ice flow behavior as it is attributed to just a single deformation mechanism (dislocation creep), but based on data in the vicinity of the transition between two different creep regimes, namely dislocation creep and superplastic flow regime. Superplastic flow involves grain boundary sliding that is grain size sensitive (Goldsby and Kohlstedt, 2001). Their experiments led them to propose a new constitutive relation:

$$\dot{\epsilon}_{total} = \dot{\epsilon}_{diff} + \left(\frac{1}{\dot{\epsilon}_{basal}} + \frac{1}{\dot{\epsilon}_{gbs}} \right)^{-1} + \dot{\epsilon}_{disl} \quad (2.57)$$

In this equation the subscripts refer to the different flow regimes, diffusional flow (*diff*), basal slip (*basal*), grain boundary sliding (*gbs*) and dislocation creep (*disl*). According to Goldsby (2006) only dislocation creep and grain boundary sliding occur at, for glacier and ice sheet modeling, important stresses and therefore a simplified form can be used here:

$$\dot{\epsilon}_{total} = \dot{\epsilon}_{gbs} + \dot{\epsilon}_{disl} \quad (2.58)$$

Each individual strain rate term on the right hand side is described by a flow law similar to Glen's flow law:

$$\dot{\epsilon}_e = A \frac{1}{d^p} \sigma^n \exp\left(\frac{-Q}{RT}\right) \quad (2.59)$$

where A is a constant dependent on the type of material, d is grain size, p is the grain size exponent, σ is differential stress, n is the stress exponent, Q is the activation energy for creep, R is the gas constant ($8.3145 \text{ J mol}^{-1} \text{ K}^{-1}$) and T is absolute temperature. Goldsby (2006) gives revised values for the parameters A , n , p and Q (table 2.1). These parameters depend on the creep regime and the absolute temperature of the ice.

Creep Regime	A	n	p	Q (kJ mol ⁻¹)
Disl, T<258 K	$1.2 \times 10^6 \text{ MPa}^{-4.0} \text{ s}^{-1}$	4.0	0	60
Disl, T>258 K	$6.0 \times 10^{28} \text{ MPa}^{-4.0} \text{ s}^{-1}$	4.0	0	181
GBS, T<255 K	$3.9 \times 10^{-3} \text{ MPa}^{-1.8} \text{ m}^{1.4} \text{ s}^{-1}$	1.8	1.4	49
GBS, T>255 K	$3.0 \times 10^{26} \text{ MPa}^{-1.8} \text{ m}^{1.4} \text{ s}^{-1}$	1.8	1.4	192

Table 2.1 Parameters for the ‘Goldsby’ constitutive equation (after Goldsby, 2006).

Using these values the effective strain rate can be determined from the simplified equation:

$$\dot{\epsilon}_e^{tot} = A_1 \tau_e^{n_{gbs}} + A_2 \tau_e^{n_{disl}} \quad (2.60)$$

where A_1 and A_2 are given by:

$$A_1 = A_{gs} \frac{1}{d^{p_{gs}}} \exp\left(\frac{-Q_{gs}}{RT}\right)$$

$$A_2 = A_{disl} \exp\left(\frac{-Q_{disl}}{RT}\right)$$
(2.61)

Here the value for A_1 (associated with grain boundary sliding) is proportional to both temperature and grain size, while A_2 only varies with temperature. Figure 2.3 shows values for $\log A_1$ as a function of grain size for ice of -25°C (248 K), -17°C (256 K) and -5°C (268 K). The figure shows that temperature only has a small effect on its value for cold ice as opposed to grain size. For warmer ice, as might occur near the base of a glacier and where strain rate gradients are highest, the value is significantly higher, although the shape of the curve is similar.

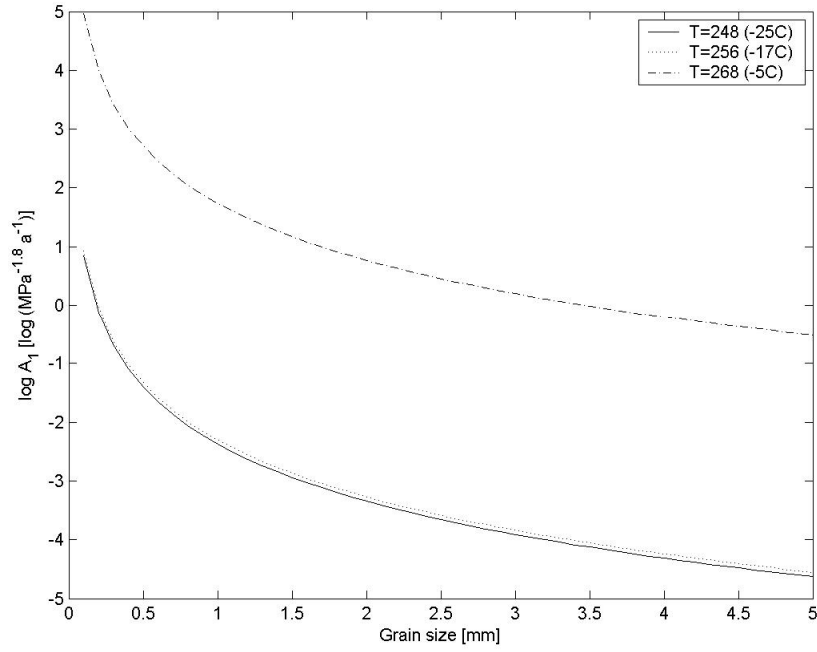


Figure 2.3 Values of log A1 as a function of grain size at three different temperatures.

Because this flow law gives a clearer physical meaning to individual parameters than Glen's flow law, it is imperative to investigate the implications of this new flow law for the derivation of resistive stresses and the stress partitioning. For this purpose we need to determine stress from measured strain rates, rather than to determine the strain rate for a given stress (as can only be done in a lab environment). Therefore we need to invert this relationship as is done in equation 2.10 for Glen's flow law. This cannot be done analytically, but can be done numerically if we define $x = \tau_e^{n_{gbs}}$ and note that the two effective stress components can then be related using:

$$\tau_e^{n_{disl}} = (x)^{n_{disl} / n_{gbs}} \quad (2.62)$$

Therefore we can rewrite equation 2.60 in a form similar as:

$$ax^m + bx - c = 0 \quad (2.63)$$

whereby $x = \tau_e^{n_{gbs}}$, $a = A_2$, $b = A_1$, $c = \dot{\epsilon}_e$ and $m = \frac{n_{disl}}{n_{gbs}}$. For a given effective strain rate

the only unknown in this equation is x , which can be determined numerically using for example Newton's method:

$$x_{n+1} = x_n - \frac{f(x_n)}{f'(x_n)} \quad (2.64)$$

For a starting value x_n the value for x is found after only a few iterations. The effective stress is then simply calculated from:

$$\tau_e = x^{\frac{1}{n_{gbs}}} \quad (2.65)$$

In order to compute resistive stresses we need to determine the individual stress components. Nye (1957) showed that for Glen's flow law the individual stress components are related to the effective stress according to:

$$\tau_{ij} = \frac{\tau_e \dot{\epsilon}_{ij}}{\dot{\epsilon}_e} \quad (2.66)$$

We show here that this is also the case for the Goldsby-Kohlstedt constitutive relation by splitting up the two components of the relation, and treat them the same as with Glen's flow law:

$$\begin{aligned} \dot{\epsilon}_e^{gbs} &= A_1 \tau_e^{n_{gbs}} & \dot{\epsilon}_e^{disl} &= A_2 \tau_e^{n_{disl}} \\ \dot{\epsilon}_{ij}^{gbs} &= A_1 \tau_e^{n_{gbs}-1} \tau_{ij} & \dot{\epsilon}_{ij}^{disl} &= A_2 \tau_e^{n_{disl}-1} \tau_{ij} \end{aligned} \quad (2.67)$$

$$\begin{aligned} \frac{\dot{\epsilon}_{ij}^{gbs}}{\tau_{ij}} &= A_1 \tau_e^{n_{gbs}-1} = \frac{A_1 \tau_e^{n_{gbs}}}{\tau_e} = \frac{\dot{\epsilon}_e^{gbs}}{\tau_e} & \frac{\dot{\epsilon}_{ij}^{disl}}{\tau_{ij}} &= A_2 \tau_e^{n_{disl}-1} = \frac{A_2 \tau_e^{n_{disl}}}{\tau_e} = \frac{\dot{\epsilon}_e^{disl}}{\tau_e} \end{aligned}$$

From this and equation 2.54 it follows that:

$$\frac{\dot{\epsilon}_e^{tot}}{\tau_e} = \frac{\dot{\epsilon}_e^{gbs} + \dot{\epsilon}_e^{disl}}{\tau_e} = \frac{\dot{\epsilon}_{ij}^{gbs} + \dot{\epsilon}_{ij}^{disl}}{\tau_{ij}} = \frac{\dot{\epsilon}_{ij}^{tot}}{\tau_{ij}} \quad (2.68)$$

Equation 2.68 can be rewritten to give equation 2.66. So based on this scheme we can calculate τ_{ij} from measurable quantities. Next the resistive stresses are determined similarly as in equation 2.28 from:

$$\begin{aligned}
R_{ii} &= 2\tau_{ii} + \tau_{jj} + R_{zz} \\
R_{ij} &= \tau_{ij}
\end{aligned}
\tag{2.69}$$

When estimating resistive stresses, careful thought should be given to the depth averaged grain size while using the Goldsby-Kohlstedt constitutive equation. For our purpose here we use grain size values that fall in the range of those observed in the deep ice cores drilled at Byrd, GRIP and GISP2 (Gow, 1970; Thorsteinsson and others, 1997; Gow and others, 1997). In all of these cores, grain sizes first rapidly increase with depth in the upper 200 m, but then seem to be rather constant varying between 2-4 mm along a substantial part of the cores (figure 2.4). Only at the very bottom of the cores grain sizes increase rapidly again to values larger than 1 cm, sometimes even reaching cross sections of 30 cm² (Gow, 1970).

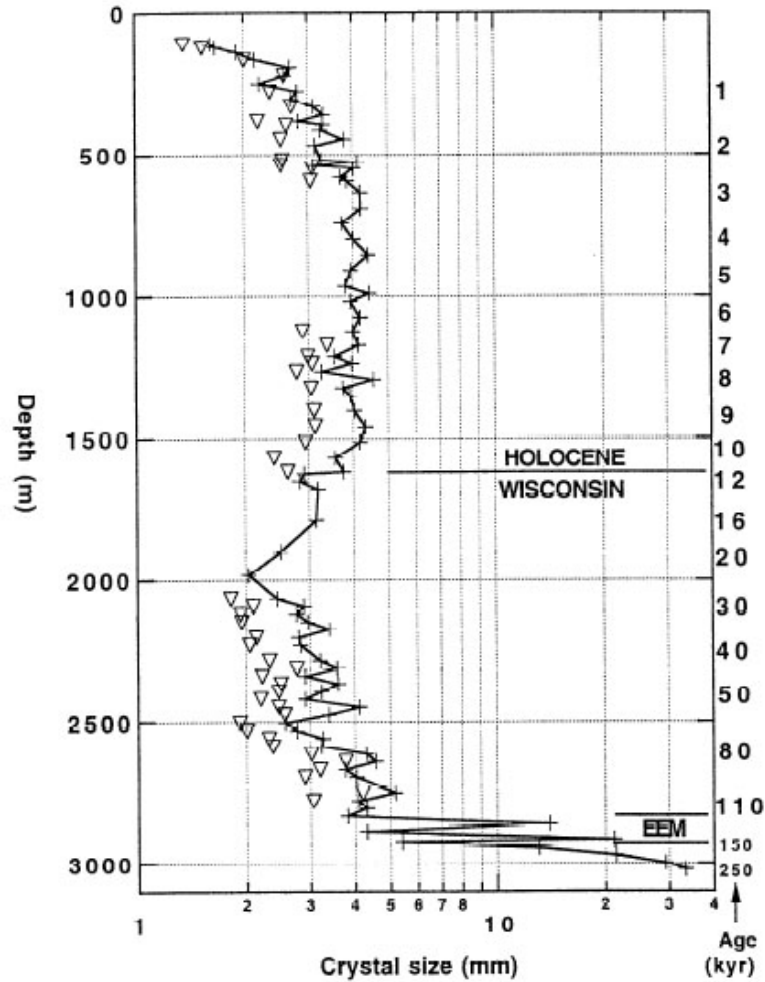


Figure 2.4 Average crystal (grain) size versus depth for the GRIP ice core (adapted from Thorsteinsson, 1997). Crosses denote horizontal diameters, triangle vertical ones. The general pattern of grain size vs. depth is observed in other cores as well. For most of the length of the core, values are relatively constant and vary between 2 and 4 mm, which is the range we use for our comparison of the different constitutive equations.

Figure 2.5 is a comparison of lateral shear stress computed using both flow laws for a given range of effective strain rate and grain size for ice with a temperature of -20°C . It is assumed for practical purposes that the shear strain rate is dominant and effectively equals the effective strain rate. In the figure, the red line shows the result when applying Glen's flow law. The value for the rate factor used in Glen's flow law is based upon a relation found by Hooke (1981) that best fitted available data. However, subsequent studies have found large fluctuations in this value that, according to Hooke, might be the result of, among others, grain size, density, impurity and fabric. We find here that the general shape of the two functions is similar, but calculated values can differ by as much as 35kPa depending both on the value of the effective shear stress and grain size. For common grain sizes in the order of 2-4 mm, Glen's flow law tends to underestimate the shear stress, which implies that basal drag is overestimated by the same amount using a force-budget approach. However, for any particular value of strain rate, this value can be minimized by selecting a slightly different value for the flow law exponent or the stiffness parameter used in the calculation of the rate factor B . The method can therefore be used to put error margins on the rate factor that we induce here to be in the order of $100 \text{ kPa a}^{1/3}$. The plot also shows that for grain sizes larger than about 2 mm the calculated shear stress is not significantly affected. It is important to note that, for a wide range of strain rates, where Glen's curve is practically parallel to the Goldsby-Kohlstedt curve, the actual calculated lateral drag is hardly affected when the ice thickness is assumed constant across flow. This is because, in order to calculate lateral drag, we are interested in the gradient of shear stress across flow rather than its absolute value. A systematic difference between the two curves therefore has hardly any effect.

In figure 2.6 the relation between effective strain rate and longitudinal stress is plotted for both flow laws for ice with a temperature of -20°C . It is assumed the longitudinal strain rate is of equal magnitude as the transverse strain rate, as is the case on a free floating ice shelf. The range of values chosen here are those found commonly on ice shelves. Again we find that Glen's flow law underestimates the stress, but more significantly, with differences of up to 75 kPa for the highest strain rates and largest grain size (4 mm). To illustrate how this difference translates into the calculation of the longitudinal resistance, consider an ice shelf 400 m thick that thins 100 m over a length of 50 km while the strain rate decreases from 0.003 a^{-1} to 0.001 a^{-1} . From Glen's flow law it follows that longitudinal resistance is about -0.8 kPa over this section. Using Goldsby-Kohlstedt, with a depth average grain size of 3 mm, we find a value of -1.05 kPa, which is about 30% higher. For a grain size of 1 mm this reduces to 20%.

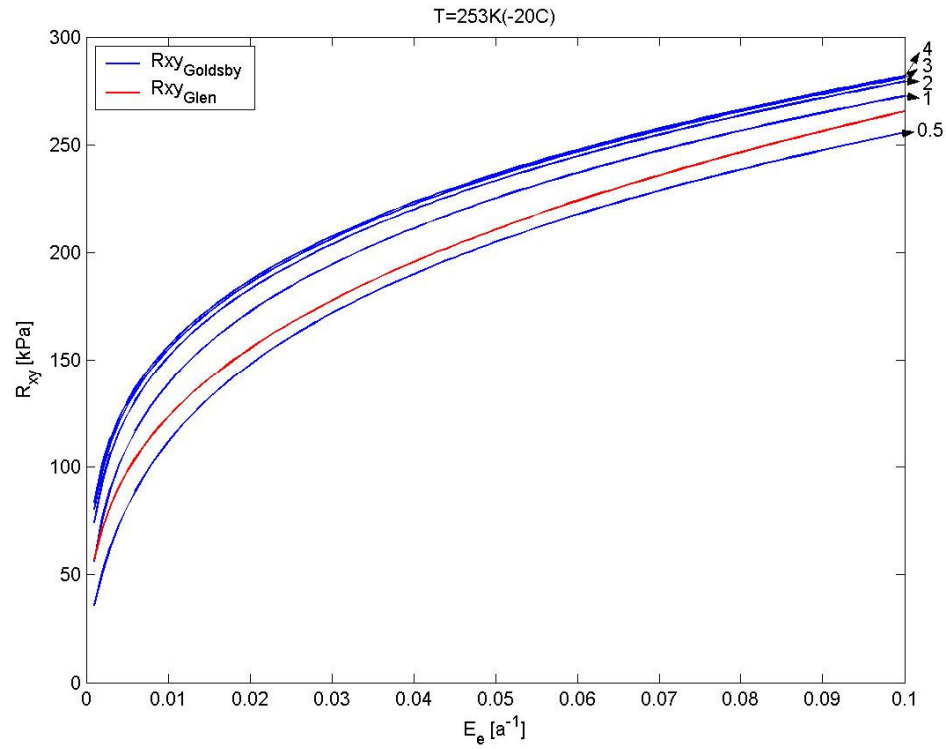


Figure 2.5 Comparison of the relation between effective strain rate and shear stress for ice at -20°C using both Glen's flow law (red) and the Goldsby-Kohlstedt constitutive equation (blue) for a range of grain sizes. The grain size is given in millimeters. For Glen's flow law we have here used a rate factor calculated from a relation found by Hooke (1981). There is a greater range of curves when taking into account for example fabric effects as done by some authors. Nevertheless the figure illustrates the importance of grain size.

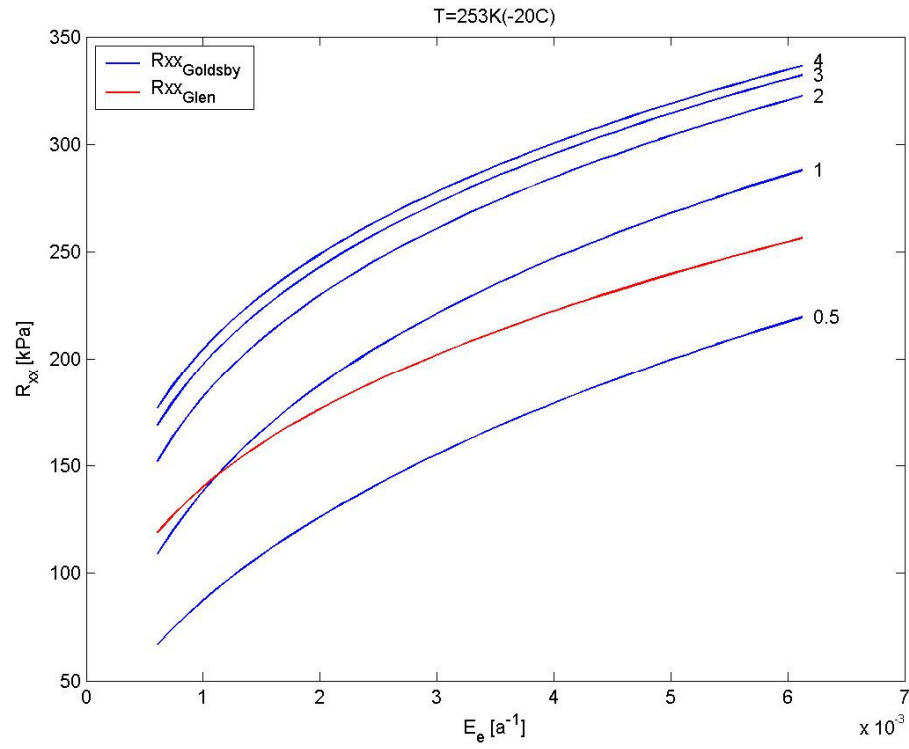


Figure 2.6 Comparison of the relation between effective strain rate and longitudinal stress for ice at -20°C using both Glen's flow law (red) and the Goldsby-Kohlstedt constitutive equation (blue) for a range of grain sizes. The grain size is given in millimeters.

2.8 Summary

This chapter outlined how resistive stresses can be estimated when surface velocity information and geometric data are available. Which datasets are available for this purpose and how we can derive glacier flow velocity from satellite imagery is discussed in Chapter 3. Using the force-budget technique we can estimate driving stress, longitudinal resistance and lateral drag. The assumption then is that basal drag is the remainder that is necessary to balance the balance equation. For floating ice bounded by

valley walls this term can be disregarded, while for completely free floating ice theoretically the lateral drag term falls away as well and driving stress should be balanced by longitudinal stress gradients.

An important step is to determine the uncertainty in the results that are based on various different datasets each with their own uncertainty. Here we showed how errors in the various parameters propagate into the calculation of resistive stresses and the balance equation.

The highly discontinuous motion, associated with tidal cycles, that is observed on several West Antarctic ice streams on sub-daily scales gives good reason for a reconsideration of how longer-term averaged strain rates, as derived from satellite images, are used to assess flow dynamics. However, to extrapolate these findings in order to study long term ice flow behavior requires velocity data averaged over longer time spans. As will be shown in subsequent chapters, this study finds that short term velocities (averaged over several weeks) are very similar to longer term averaged velocities for most of the study areas.

Most standard approaches for modeling ice sheet behavior use Glen's flow law in order to estimate stresses from velocity gradients. Here we have developed an approach on how to apply a recent constitutive relation by Goldsby and Kohlstedt (2001) in the force-budget technique and investigated its implications on the derivation of stresses. The formulation of this new flow law was brought about thanks to recently developed sample fabrication techniques which led to the discovery of a new creep regime dubbed superplastic flow. Subsequently there has been some debate on whether this regime is compatible with observations of fabric development and microstructures in the ice (Duval

and Montagnat, 2002). Nevertheless here we show that the application of Goldsby-Kohlstedt's constitutive relation can have a significant influence on the derivation of longitudinal and lateral shear stresses. They can be between 20-30% higher than those derived from Glen's flow law (using standard values for the rate factor and flow law exponent) for strain rates and grain sizes commonly found in ice sheets. We find that, because of the way it is calculated there is hardly any effect on inferred lateral drag. However, it does lead to higher calculated values for longitudinal resistance and therefore the implication for this on the calculation of basal drag is opposite. It is thus important to consider different flow laws when investigating glacier dynamics. This is done in subsequent chapters where we apply the force-budget technique to various glaciers.

CHAPTER 3

DATASETS AND METHODS

3.1 Introduction

The aim of this chapter is to describe, discuss and justify the different datasets and analysis methods used in this study. The primary datasets are 1997 and 2000 RADARSAT-1 synthetic aperture radar (SAR) imagery. We use these to derive ice flow velocity of several major Antarctic glaciers with a feature tracking algorithm called IMCORR. IMCORR has been widely used in the glaciological community to derive glacier velocity (e.g. Bindshadler and Scambos, 1991; Lucchita and others, 1993; Bindshadler and others, 1996; Berthier and others, 2003), but we have improved and expanded the procedure in several ways to optimize the velocity field derived from SAR imagery. First, we pre-process the imagery using an adaptive neighborhood filter. This reduces noise and results in more successful correlations and thus more velocity points. Second, we modified IMCORR, by incorporating a variable window size function, as to improve our results in areas where otherwise no valid matches are found. Third, we designed and apply a validation and filtering technique on the output data to eliminate invalid data points and fill small data gaps resulting in a more complete and consistent

velocity field. To complement our primary datasets we also use RADARSAT-1 derived InSAR velocity and velocity from earlier studies, available from the VELMAP database and literature. This allows for temporal comparisons and can be used to optimize the velocity field. Furthermore we use estimates of surface topography and ice thickness for our analyses. Here we use the OSU Digital Elevation Model (OSUDEM), ICESat laser elevation data and thickness data from the BEDMAP project. These datasets and their limitations are discussed. We conclude the chapter with a summary of the applied methods and data, and discuss what we have done to expand on this.

3.2 Flow velocity measurements

3.2.1 Introduction

Ice flow velocity is a fundamental parameter to characterize the behavior of an ice sheet. One approach to investigating the stress field of glaciers and changes therein is to use flow velocity gradients via the flow law. The flow velocity is also a key parameter to determine the mass balance of an ice sheet, that is whether it is losing or gaining mass or is in equilibrium. There are several methods available for measuring velocities. They can be divided into in situ methods and remote sensing based methods.

Most in situ methods currently rely on the use of either differential GPS surveys (DGPS) or optical surveys using a total station (e.g. Echelmeyer and Harrison, 1999; Bindshadler and others, 2003). In both approaches a network of stakes is set out on the glacier and repeatedly measured to estimate velocity. These methods work well for small mountain glaciers and over short periods of time. However, the sheer size of the Antarctic continent and the remoteness of the region make it very difficult, dangerous, impractical

and expensive to determine flow velocity with a conventional glaciological approach. Apart from that, to further complicate the matter, nearby (stationary) fiducial points, which are often not readily available in the interior of Antarctica, are necessary to set up a reference frame.

Fortunately we also have the means to determine flow velocity remotely using aerial photography and, more recently, satellite imagery and remote sensing techniques. More importantly, the remote sensing data record is now becoming sufficiently long to begin an investigation of natural flow variability and its link to climate. Where repeat SAR data is available, orbits fall close enough, and coherence is preserved, velocity can be determined using radar interferometry (InSAR). We can also determine velocity using feature tracking techniques on sequential SAR and optical imagery. Only this technique is capable of acquiring velocity data over short (days) as well as long time spans (years to decades) and of fast flowing regions. In this study, flow velocity is derived from sequential SAR imagery by means of feature tracking. We compare these velocities with InSAR derived velocity and data from previous studies to investigate changes and variability. Velocity gradients derived from the acquired data are then used to investigate flow dynamics.

3.2.2 Feature tracking

Flow velocities can be derived from sequential satellite imagery by means of feature tracking. In this approach, prominent surface features such as crevasses or rifts and edges (e.g. ice tongue edge) that move with approximately the same speed as the ice, and are identifiable on two co-registered images, are used to determine displacement and

hence velocity. Most studies that applied this or similar techniques made use of optical imagery, such as Landsat and Spot (*e.g.* Bindshadler and Scambos, 1991; Lucchita and others, 1993; Bindshadler and others, 1996). SAR imagery has several advantages including the ability to observe through cloud cover and during the polar night. Optical satellites depend on illumination from the sun and hence are limited to observations over only part of the year and, then only, under clear sky conditions. Another advantage is that penetration of radar waves into the upper snow layers reveals shallow sub-surface or snow-covered features that can be successfully tracked but are usually hidden in optical imagery. Furthermore there is a stronger contrast between different types of ice (*e.g.* sea ice and shelf ice) that are difficult to distinguish in optical imagery, allowing ice shelf edges to be tracked more easily. Feature tracking has been successfully applied before on glaciers in both Greenland and Antarctica using (ERS-1) SAR imagery (Fahnestock and others, 1993; Rosanova and others, 1998). A drawback of SAR imagery is the introduction of speckle noise which is inherent when using radar systems. This is best removed using a filtering technique of some kind to improve velocity extraction when using feature tracking.

Feature tracking on imagery can be done manually/visually or automatically. Manual feature tracking has the disadvantage of being very labor intensive. It requires relatively sharp features and is more subjective than an automated approach. With the use of automated feature tracking a dense velocity map can be created relatively fast, sub-pixel accuracy can be achieved and the method works well with small and sharp features but also with large diffuse features. A limitation of automated feature tracking is that to derive successful correlations the features should not change too much in appearance

between two acquisitions. Also, rotational movements can cause the cross-correlation algorithm to fail unless more sophisticated algorithms are used such as the RADARSAT Geophysical Processor System, which was especially designed for sea-ice applications (Kwok, 1998). In addition, automated feature tracking usually requires post-culling of the output in order to remove false matches and outliers, which introduces artifacts if not done correctly. In this study we apply an automated feature tracking algorithm, named IMCORR (see chapter 3.2.8) and developed by Scambos and others (1992) on RADARSAT-1 SAR imagery. Extracting velocity using feature tracking involves several steps and procedures illustrated in figure 3.1 and discussed in the next sections.

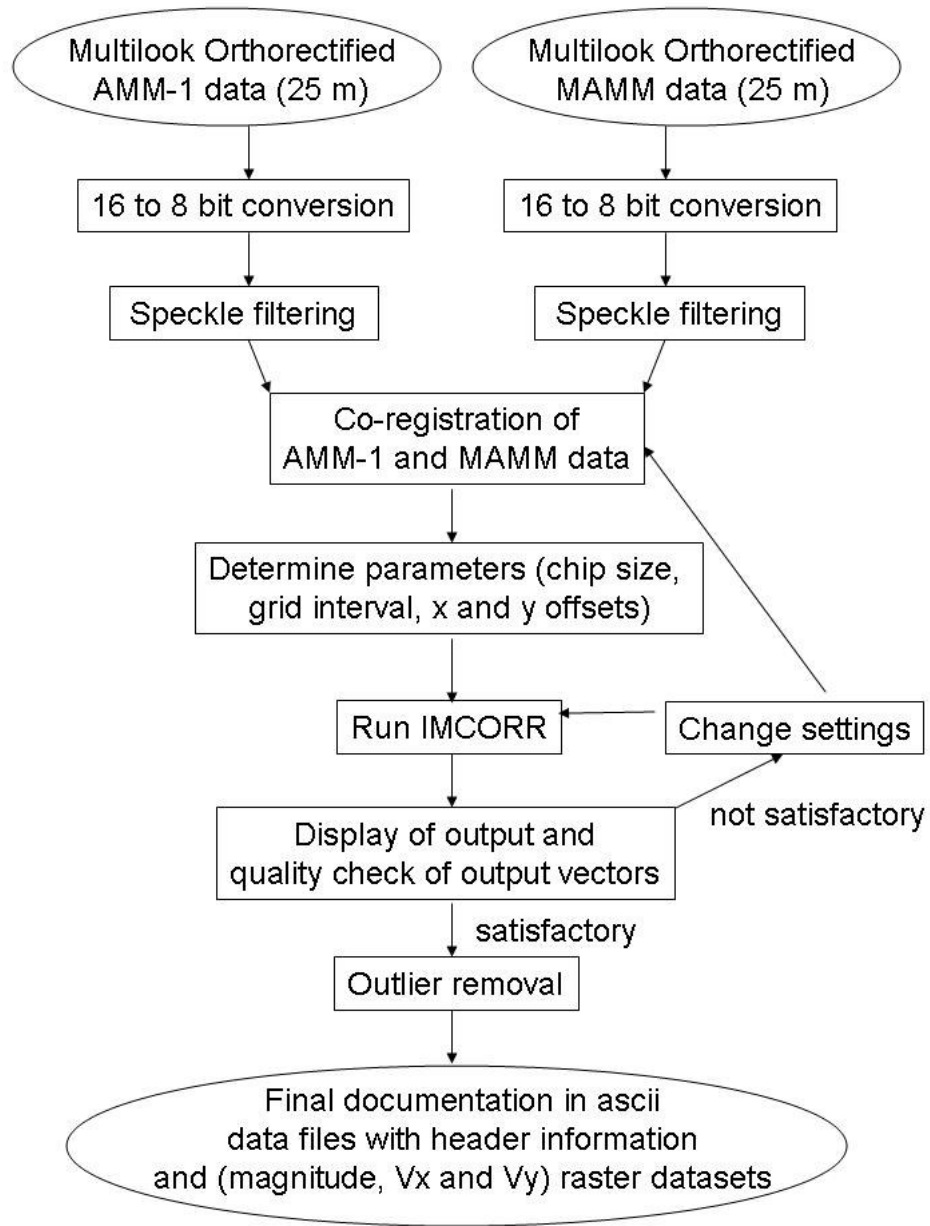


Figure 3.1 Flowchart detailing the various steps involved in velocity extraction from multi-look RADARSAT-1 SAR imagery using feature tracking.

3.2.3 RADARSAT missions AMM1 & MAMM data

Our primary data source for this study is multi-look RADARSAT-1 SAR imagery. The Canadian RADARSAT-1 satellite was launched by NASA in 1995 carrying on board a C-band (5.3 GHz) Synthetic Aperture Radar (SAR) with a variety of different beam modes. Because of its technical capabilities the satellite offered a unique chance for scientists to look at Antarctica. The RADARSAT-1 Antarctic Mapping Project (RAMP) completed two mapping missions, the Antarctic Mapping Mission 1 (AMM-1) in 1997 and the Modified Antarctic Mapping Mission (MAMM) in 2000. The AMM-1 mission provided the first high-resolution radar mosaic of the entire Antarctic continent (figure 3.2, left panel) (Jezek, 1998). This was made possible by rotating the satellite from the normal right-looking mode to a left-looking mode. The mission lasted 41 days and ran from September 9 till October 20, with nominal acquisition from September 26 until October 14. The mosaic is compiled from numerous radar swaths and has a 25 m resolution. It forms an important benchmark to gauge future changes. The MAMM mission in 2000 lasted from September 3 until November 17. The primary goals for the MAMM-mission were to produce image mosaics of the coastal areas of Antarctica (north of 80° S) for change detection and to measure surface velocity (figure 3.2, right panel) (Jezek, 2002). During this mission, due to technical reasons, the satellite was not rotated and the mosaic has therefore a black hole in the middle known as the polar gap.

After completion of the AMM-1 mosaic a number of studies have been done utilizing the data. Joughin and others (1999) used interferometric techniques on AMM-1 data to produce a surface velocity map of the West Antarctic Ice Streams. Their study highlighted the complexity of the drainage basins of the ice streams. Subsequently

Stearns and others (2005) used this velocity data for comparison with earlier velocity measurements and to correlate changes in velocity with features identifiable on the mosaic. Liu and Jezek (2004) used the mosaic to accurately extract the coastline of Antarctica through a sequence of automated image processing techniques.

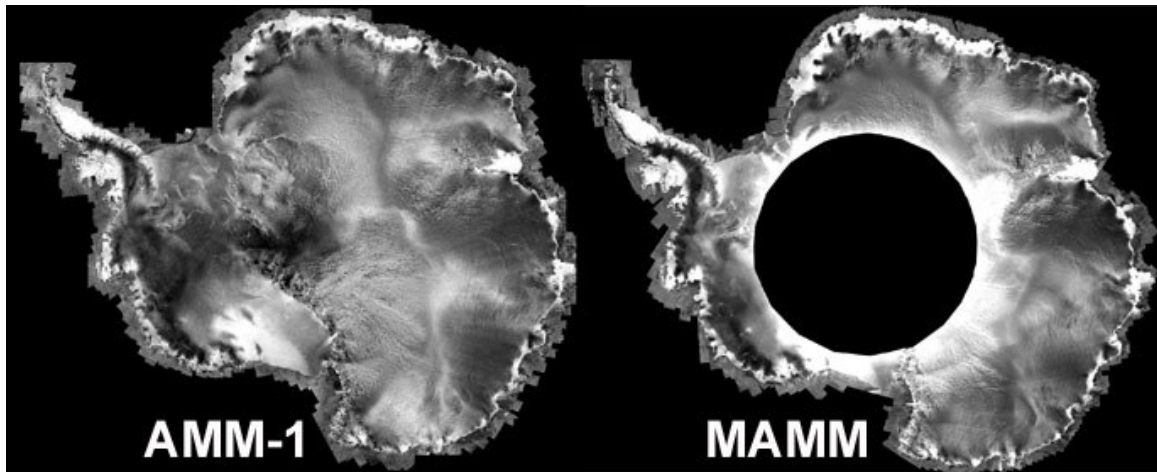


Figure 3.2 The AMM-1 mosaic (left) and MAMM mosaic (right) acquired as part of the RADARSAT-1 Antarctic Mapping Project (RAMP) during two mapping missions in 1997 and 2000 respectively. The radar imagery forms the primary data source for this study and is used to derive ice flow velocity. The black hole represents no data.

We use the RAMP imagery to obtain flow velocity using feature tracking techniques. Interferometric velocities were provided as part of the RAMP project. For feature tracking, we use both AMM-1 multi-look images, which have a nominal pixel size of 25m, and MAMM multi-look images. The MAMM mission yielded three successive datasets 24 days apart, which have a, processed, single-look, nominal pixel size of up to 10m. This higher resolution was made possible by using the Fine-1 beam

mode with a slant range resolution of 5.2 m and azimuth resolution of 8.4 m for a single-look image. In our study we use a polar stereographic projection referenced to the WGS 84 ellipsoid with latitude of true scale at 71°S.

Using the RAMP data, average velocities can be computed over different time scales (3 years, 24 and 48 days) to investigate variability in the velocity field. By using overlapping areas of two sub-repeat-cycle (MAMM-)swaths we can even measure velocity over sub-repeat cycles, for instance 21 and 27 days, with the feature tracking technique. Application of feature tracking on the shortest possible period (3 days) proved unsuccessful, likely due to the small absolute displacement over the time period.

3.2.4 Orthorectification

Orthorectification is the process whereby satellite images or aerial photographs are geometrically adjusted to correct for the terrain. Since these images are two dimensional a terrain distortion occurs when the surface model used is different from the actual surface. Therefore for accurate orthorectification a high resolution digital elevation model (DEM) is necessary that needs to be precisely registered to the imagery. The final result of the orthorectification process is a map-accurate image that can be compared with other datasets.

For the purpose of orthorectification, an accurate DEM, named the OSUDEM (see chapter 3.5), was developed for the Antarctic Mapping Missions, which incorporated several cartographic and remotely sensed datasets (Liu, 1999). A special software package, designed by Vexcel, is used for the orthorectification of the SAR data used in this study. This software handles both the geocoding and removal of terrain distortions.

Layover and radar shadow effects are predicted based upon the DEM and these areas are filled in with data from different radar beams or look directions (Liu and Jezek, 2004).

In order to refine the positional accuracy of the satellite ephemeris a database of ground control points was compiled, which also acted as a validation for the final map products. Apart from this a radar transporter deployed at South Pole was used in order to increase the positional accuracy of the final products. This accuracy is estimated to be better than 200 m (Jezek, 2003). The ground control points that were used to constrain the AMM-1 mosaic, together with tie points from the AMM-1 mosaic, are used to correct the MAMM image geometry.

3.2.5 Pre processing: 16 to 8 bits conversion and filtering

Because IMCORR was developed for 8 bits binary files, the RADARSAT-1 imagery, which is 16 bits, needs to be converted to 8 bits. This reduces processing time but at the expense of radiometric fidelity. Because the AMM-1 calibrated data and the MAMM data are scaled differently, a slightly different code is used for conversion of the respective datasets. DN values lower than 100 are assigned the value 0 after conversion. Values higher than 6000 (14800 for MAMM) are assigned the value 255. The remaining values are optimally distributed over the range 1-254 using a log function. For AMM-1 data we use:

$$DN' = 70 \log^{10}(DN^2) - 280 \quad (3.1)$$

and for MAMM data we use:

$$DN' = 59 \log^{10}(DN^2) - 237 \quad (3.2)$$

where DN and DN' stand for the original 16 bits value and the converted 8 bit value respectively.

To reduce speckle noise and enhance surface features on the SAR imagery we apply a filtering technique. Following Kim (2004) we used an adaptive neighborhood filter, based on a method described in Rangayyan and others (1998). The method is based on the Lee filter:

$$\hat{x} = \mu_y + \frac{\sigma_y^2 - \sigma_e^2}{\sigma_y^2} (y - \mu_y) \quad (3.3)$$

where \hat{x} is called the linear minimum mean-squares error (LMMSE), μ_y is the mean of seed pixel y and σ_y^2 is its variance.

Instead of using a fixed-sized neighborhood, the technique uses an adaptive neighborhood that identifies pixels belonging to a particular feature. In this way only pixels belonging to the same features are used to compute statistics of noise and signal. To indentify features the region growing technique uses a tolerance threshold T so that:

$$|y_{s'} - y_s| \leq T \quad (3.4)$$

where y_s is the seed pixel and $y_{s'}$ are its eight connected neighbors. The threshold T varies across the image based on local statistics of noise. Processed images have a higher visual quality and make the edges sharper (figure 3.3). The application of this filter greatly improved the retrieval of velocity information from the imagery.

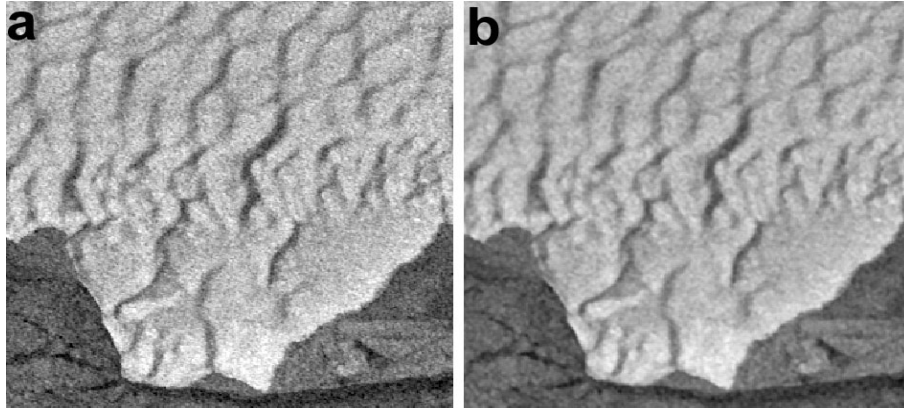


Figure 3.3 Two scenes illustrating the difference between an unfiltered image (a) and a filtered image (b). The filtering technique uses an adaptive neighborhood to calculate statistics of noise and signal.

3.2.6 Co-registration and tie points

An important step in feature tracking is co-registration of the image pairs. This must be done accurately because most of the velocity error is associated with co-registration errors. We use orthorectified image data with geolocation accuracies of 100-

200 m. Residual registration offsets are compensated with a linear transformation based on tie points and fixed features. This is done manually by matching pixels and features in ice-free fixed areas such as nunataks or islands or other fixed features (figure 3.4). By adjusting corner coordinates and using the flicker function in IMAGINE an optimal co-registration can be achieved. No rubber sheeting is involved in the process. Results show, however, that this method for co-registration is only accurate on relatively small scenes. For larger areas there is usually too much distortion caused by errors in the DEM used for orthorectification and these areas need to be subset for that reason or other more complicated scheme's need to be used.

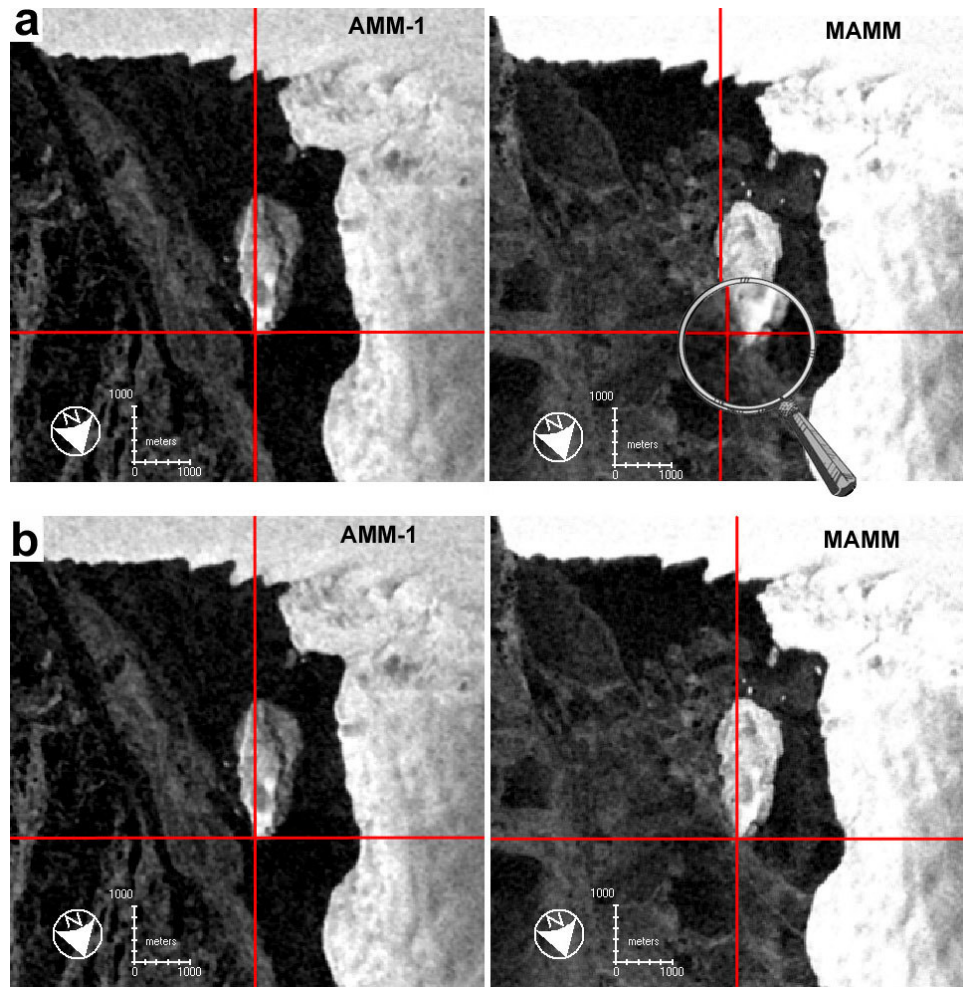


Figure 3.4 Illustration of the co-registration process. Shown are two linked scenes with the cross hair on the same position. On the left image (AMM-1) the cross hair is on the tip of the island. In (a), before co-registration, the cross hair in the MAMM image (right) points at a different location. After co-registration the cross hair falls on the same point (b).

3.2.7 Image cross-correlation: IMCORR

Feature tracking is done automatically using IMCORR image cross-correlation software described in Scambos and others (1992). Principally a ‘reference window’ from one image is extracted in a grid like pattern and compared with a larger ‘search window’ from another (co-registered) image (figure 3.5). A correlation index is calculated at every location where the reference window fits within the search window. The algorithm is based on the normalized cross-covariance method whereby the DN values of the two windows are normalized so they have a zero mean. This avoids problems associated with differences in illumination or brightness. The correlation index is calculated according to:

$$CI_{(L,S)} = \frac{\sum_{l,s} (r_{(l,s)} - \mu_r)(s_{(l,s)} - \mu_s)}{\left[\sum_{l,s} (r_{(l,s)} - \mu_r)^2 \right]^{1/2} \left[\sum_{l,s} (s_{(l,s)} - \mu_s)^2 \right]^{1/2}} \quad (3.5)$$

where $CI_{(L,S)}$ is the correlation index at the midpoint of the overlap between the reference and search windows, $r_{(l,s)}$ and $s_{(l,s)}$ are the DN values of the reference and search windows respectively at point (l,s) , μ_r and μ_s are the average DN values for the reference and search windows respectively. The values of the correlation index can vary between -1 and 1. For computational efficiency the cross-correlation is computed in the frequency domain rather than the spatial domain.

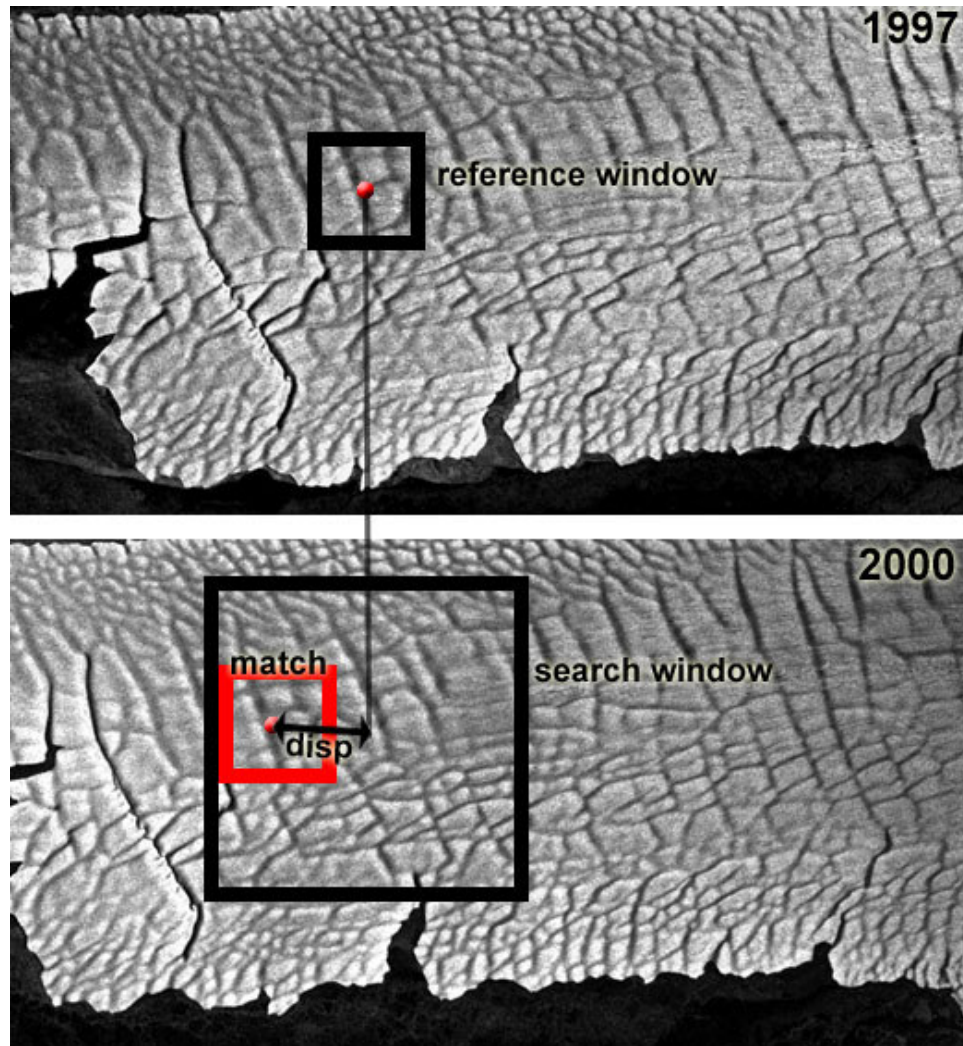


Figure 3.5 Two co-registered RADARSAT-1 scenes of Drygalski Ice Tongue illustrating IMCORR. A reference window from a 1997 scene is compared against a larger search window from a 2000 scene. A matching window, with maximum correlation, is found and the displacement of its midpoint (disp) from the original location is given. The displacement is given in number of pixels and should be multiplied by pixel size and divided by the time difference between the acquisitions of the two images to obtain the average velocity over period. We modified IMCORR by implementing a variable-sized window routine as to increase the number of valid matches and velocity data points (see chapter 3.2.10).

To obtain sub-pixel offsets a biquadratic function is fit through the correlation values creating a two-dimensional correlation surface (figure 3.6). The function of this surface (F) can be defined as (after Zhao, 2001):

$$F(x, y) = ax^2 + by^2 + cxy + dx + ey + f \quad (3.6)$$

where a-f are surface parameters that can be determined from the known correlation values of the central pixel and its 8 surrounding neighboring pixels. The maximum of this function is found by solving:

$$\begin{aligned} \frac{\partial F}{\partial x} &= 2ax + cy + d = 0 \\ \frac{\partial F}{\partial y} &= 2by + cx + e = 0 \end{aligned} \quad (3.7)$$

Combining these two equation yields the solution to the sub-pixel x- and y-offsets:

$$\begin{aligned} x &= \frac{2bd - ec}{c^2 - 4ab} \\ y &= \frac{2ae - dc}{c^2 - 4ab} \end{aligned} \quad (3.8)$$

The reported match is the location with the maximum correlation value. Subsequently several correlation statistics are calculated in order to assess the validity of the match.

These include the number of secondary peaks, the mean and variance of the correlation surface, peak-above-mean, peak-above-second-peak, and full width at half maximum for the primary peak (Scambos and others, 1992). When a valid match is found velocity is calculated from the time interval and the distance of displacement. Calculated velocity is considered to be the average surface velocity of the reference window over the time span concerned.

The shape of the correlation function is an important indicator of the measurement accuracy. The sharper the peak the more confidence can be placed in the reported match (figure 3.6). Differences can be caused by a different size or shape of features. Problems can arise if there are no obvious features in an extracted window, if the search and/or reference windows are too small, if features are one-dimensional, if features are repetitive in character, or if a feature has changed too much in appearance, for instance a closing, widening or rotating crevasse.

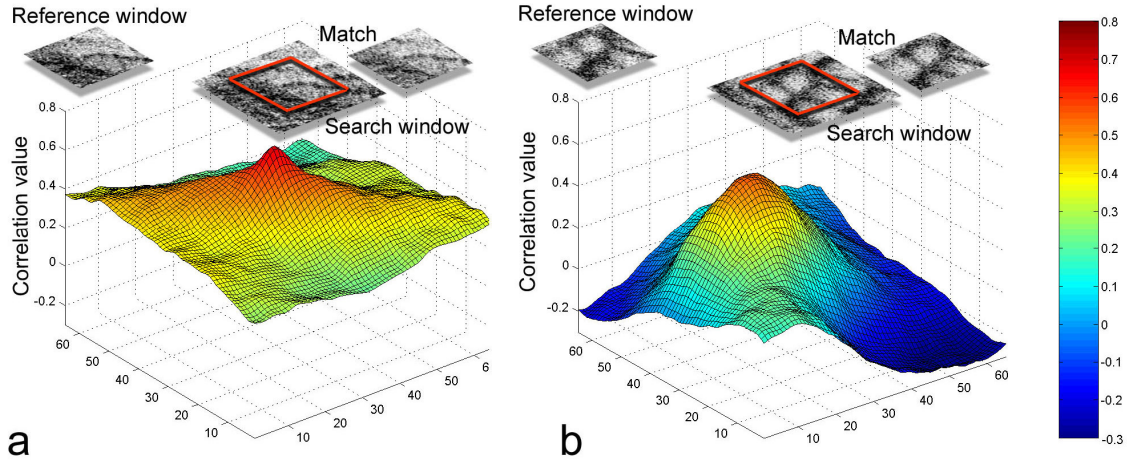


Figure 3.6 Two correlation plots derived from comparing a ‘reference window’ with a larger ‘search window’ extracted from two different scenes of the 2000 MAMM mission taken 24 days apart. The peak of the surface corresponds to the reported match. The shape of the correlation function is an important indicator of the measurement accuracy. Sharp pronounced peaks (a) have a higher accuracy than broader peaks (b)

3.2.8 IMCORR settings

When using IMCORR several settings must be specified that are important for successful retrieval of velocity. Among these are the search and reference window size, the grid spacing of window retrieval and (optional) x and y search offsets.

Window size: An important parameter for feature tracking is the reference and search window size. The size of the reference window determines the size of the features that are tracked. There is a trade off when setting the window size. If the window is too small there might not be enough information for successful correlations, especially if features are repetitive. If the window is too large the level of detail of the final velocity

map is reduced. We experimented with different window sizes and found the best result is achieved using a reference window size of 128 x 128 pixels (an area of 1280 m x 1280 m) for the 24 and 48 day velocities, derived from 10 m data, and 64 x 64 pixels (an area of 1600 m x 1600 m) for the 1997-2000 comparisons, that uses 25 m data.

The search window is the area against which the reference window is compared. It should be large enough to capture the full range of velocities within a particular scene. Its size strongly affects computational time and should therefore not be taken larger than necessary. By default the search window is centered on top of the reference window, but an offset can be given if velocities are too large (see below). Usually a search window of 192 x 192 pixels is sufficient. For scenes with a wide velocity range larger search windows are necessary. Often this is not practical and IMCORR is better run multiple times using different offsets after which the output files must be merged together (illustrated in figure 3.9).

Grid interval: The grid interval determines the spacing of extracted reference windows and thereby also the number of velocity vectors. By decreasing the grid interval the number of vectors increase, but if the interval is too small it can lead to over sampling because individual vectors are not entirely statistically independent. In this study we use a grid interval of 16 pixels for the 25 m data and 40 pixels for the 10 m data. This means that the individual reference windows overlap approximately 75 %. The setting determines the size of the final velocity pixel and leads to velocity pixels of 400 x 400 m for the presented velocity maps, which is the same as used for the InSAR velocity.

Offsets: Because by default the search window is centered on top of the reference window there is an upper limit on velocity that can be measured. The maximum

measurable displacement (D_{max}) depends on the size of both the reference and the search window as follows:

$$D_{max} = \frac{S}{2} - \frac{R}{2} \quad (3.9)$$

where S and R are the sizes (in pixels) of the search and reference window respectively. This means that for a reference window of 64 x 64 pixels and a search window of 192 x 192 pixels the maximum measurable displacement is 64 pixels. For 25 m data and a time interval of 3 years this means that velocities higher than 533 m a⁻¹ cannot be measured. Many glaciers in Antarctica move faster than that and it is therefore advantageous to either increase the search window size or give a preset offset for the search window in the main flow direction of the ice to capture the range of velocities. Enlarging the search window significantly lengthens computing time and the latter option is therefore often more desirable. However, where strong gradients in velocity exist the use of an offset can preclude successful correlations for slower moving areas.

3.2.9 IMCORR modifications

As mentioned the size of the reference window determines the size of features that can be tracked. Sometimes the eye can easily ‘track’ movement of features, but IMCORR does not give results. In that case the problem is likely a not optimal search or reference window size. The search window might be too small so that the actual corresponding match is not found or it can also be that the reference window is too small

and therefore does not contain enough features for successful correlations. We modified the original IMCORR code as to overcome this problem. In the modified version, if for a given reference and search chip size no valid match is found, both are expanded according to user specified settings. This greatly improved the number of successful matches because the correlation maximum becomes better distinguishable from the background correlation value (figure 3.7).

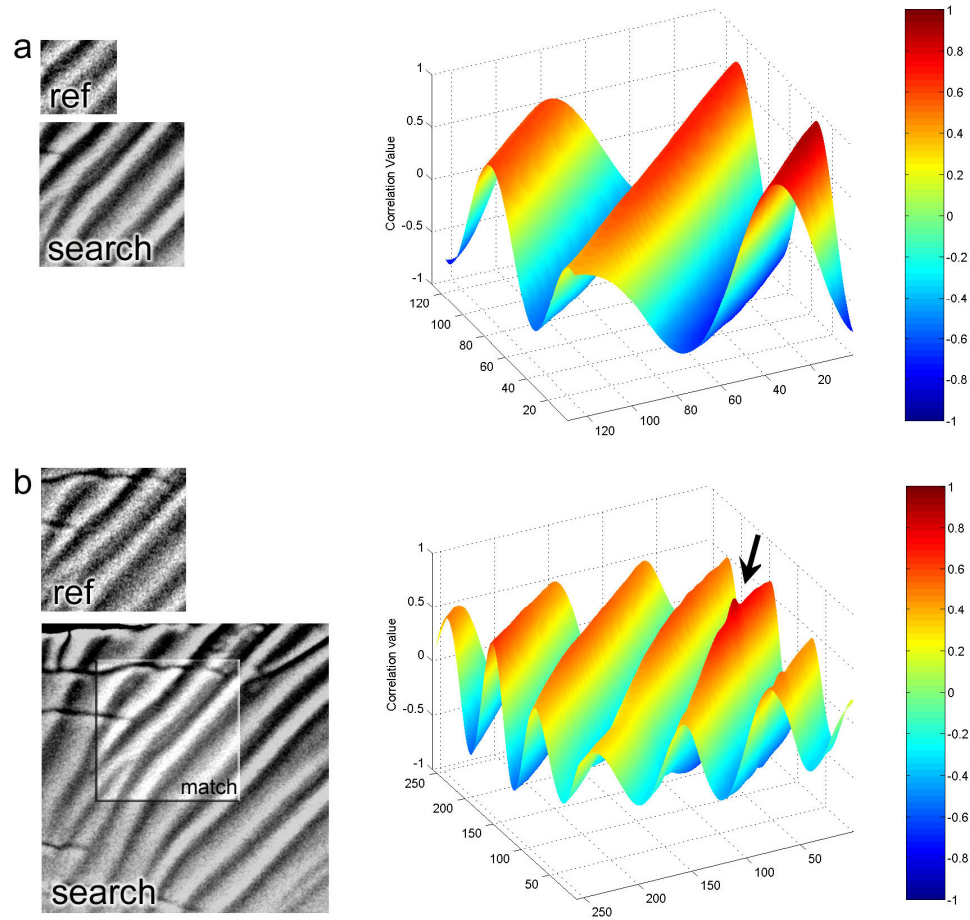


Figure 3.7 Two correlation plots derived from comparing a ‘reference window’ with a ‘search window’ for a test area and illustrating the effect of the modification of IMCORR developed in this study. In a) the reference and search windows are too small and because of the repetitive character of the features (crevasses) no valid match is found as the correlation plot consists of several ‘waves’ similar in strength with no distinguishable peak. In b) both the reference and search windows are enlarged and now there is a peak on one of the waves and a valid match is given. This is caused by the extra information in the extracted windows.

3.3 Validation and outlier removal

3.3.1 Visual check and vector validation

We test the validity of our results by visual inspection of the velocity field and by extracting several image windows manually and investigating the resulting correlation plot (figure 3.6). To identify any systematic effects we compare our velocity measurements, where possible, with field derived GPS measurements available through the online VELMAP database (see chapter 3.4).

Velocity has both magnitude and direction. Besides an investigation of the magnitude, it is important to visually verify output velocity vectors. We project the vectors on the original satellite image to check for consistency with other vectors and features in the image (figure 3.8).

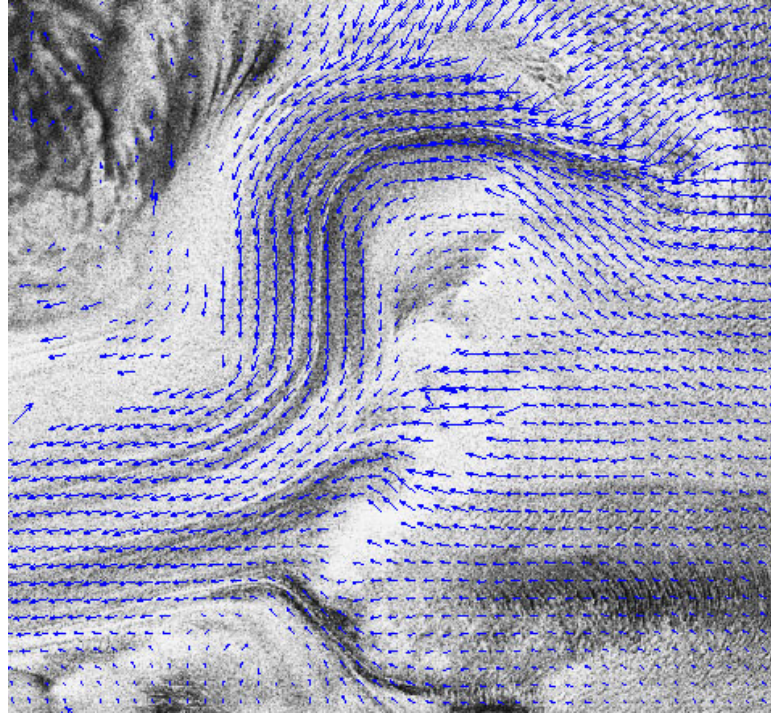


Figure 3.8 Velocity vectors projected on a RADARSAT-1 image of David Cauldron, an icefall on David Glacier. The vectors are well aligned with the flow lines indicating accurate co-registration.

3.3.2 Outlier removal

In some cases, for a number of reasons, IMCORR does not find a valid match and either gives an erroneous result or no result at all. This problem can arise, as mentioned earlier, if there are no obvious features in an extracted window, if the search and/or reference windows are too small, if the features are one dimensional, if the features are repetitive in character, or if a feature has changed too much in appearance. In the correlation function this translates into a correlation peak that is very low, multiple peaks similar in height, a peak that does not stand out against the background correlation value,

or a peak that falls too close to the edge of a search window. IMCORR has a built-in algorithm that deals with these situations and usually gives a result flag that indicates no valid match has been found and a displacement value 0 is assigned. However, often these invalid matches are mistakenly accepted resulting in incorrect displacements in the output file. These invalid matches are called outliers and are undesirable since they contaminate the velocity map, obscure valid flow features or can influence calculation of flow parameters such as strain rates.

There are different ways of dealing with these no-data gaps and outliers in an efficient way. In the case where IMCORR fails to find a valid match, but the eye can easily ‘track’ movement of features, the problem is often the size of the search and reference window (see chapter 3.2.8). To deal with remaining invalid matches and to fill up no-data gaps the threshold correlation value in IMCORR can be adjusted, but this likely also results in fewer valid matches being reported. Therefore using filtering and interpolation techniques on the output is often more desirable.

A first quality control is visual inspection of the output file by creating a velocity field (see chapter 3.3.1). Frequently the most extreme outliers are filtered out easily by setting limits on reasonable values of magnitude. Since magnitude is based on velocity in both x (V_x) and y-direction (V_y), it is necessary to plot and investigate these as well. If the approximate flow direction and magnitude in an area is known beforehand, based on visual inspection of satellite images, x or y velocity extremes are easily filtered out by setting limits on acceptable values. To deal with remaining outliers a different approach must be used, which we discuss next.

3.3.3 Mean and median filters

To deal with outliers there are various standard filtering techniques widely used in image processing, such as median and averaging filters. The standard approaches, however, often have drawbacks such as altering valid data points, introducing edge effects, or, in some cases, validating outliers. An average filter applies a moving window of preset size (usually 3x3 or 5x5 pixels) to the output file (in matrix form) and calculates the average value of the window which is then assigned to the central pixel. The problem with this is that outliers are used in the calculation of the average, so extreme outliers cause an undesirable result. A median filter does not have this drawback. It assigns the median value of a window to the central pixel lessening the influence of extreme outliers. At the boundary between a region with valid data and no data, however, an undesirable effect often occurs and valid data points are deleted or data is added. Apart from that the method is not suitable if there is a cluster of invalid data points.

3.3.4 Mask filter

The methods described above apply fixed windows to the data. A better approach is to apply a region growing technique that looks for regions with a similar velocity to calculate statistics of noise and signal and eliminate outliers. This is comparable to how the human eye would do it. Photoshop has a convenient tool which does just that. A pixel in a coherent region can be selected and then the 8 surrounding pixels are evaluated for similarity and rejected or accepted based on a user-specified tolerance. This type of algorithm loops around the selected pixels and the selected region ‘grows’ outward until no more valid points are found. Before doing this it is advantageous to first increase the

contrast of the magnitude image. Since the Photoshop formats do not have the actual velocity values of a pixel, we use the approach only to create a mask whereby the valid region is given a value of 1 and the rest 0. The mask is then imported in Matlab and applied to the original data. This method works exceptionally well to filter out most of the outliers and results in an improved velocity field (figure 3.9). The method however, does not fill in data gaps, which in some cases is favored rather than leaving gaps in the velocity map. Another drawback is that because it is manual work results are somewhat more subjective.

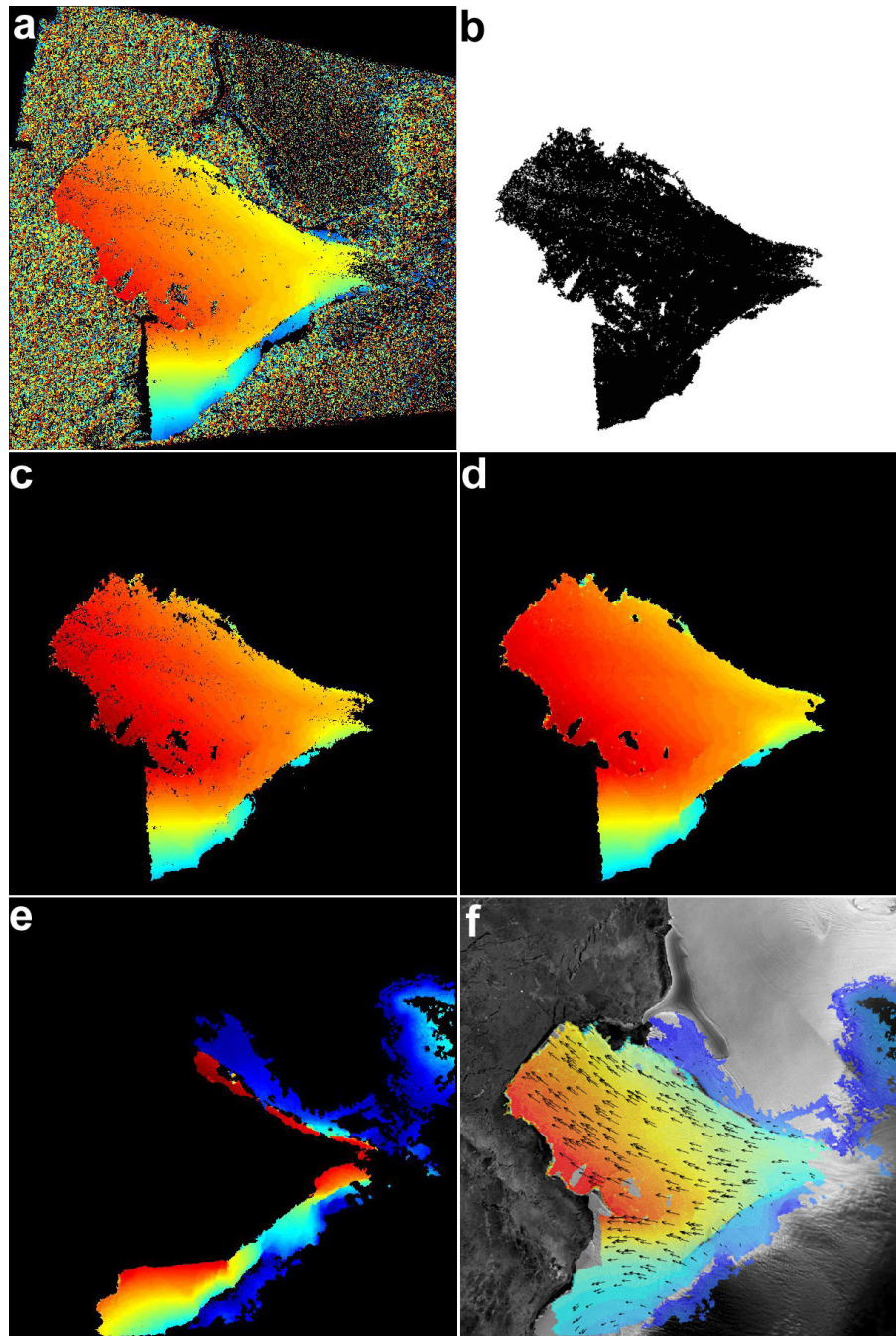


Figure 3.9 Ice flow velocity on Brunt Ice Shelf and Stancomb-Wills Ice Tongue, a) unfiltered IMCORR output of fast flow; b) mask created by a region growing technique; c) output after the mask filter is applied; d) same after leftover outliers are filtered out and small gaps are filled in using a standard deviation filter (see chapter 3.3.5); e) filtered output of slow flow; f) merged fast and slow flow projected on a RADARSAT-1 image with some vectors displayed.

3.3.5 Inverse distance weighted standard deviation filter

To eliminate leftover outliers and to fill in small data gaps we designed a modified averaging filter that is applied to both x and y velocity components. This filter extracts a window (5x5 or 7x7 pixels) and calculates the mean and standard deviation. It calculates a range of acceptable values by computing the mean plus the standard deviation and the mean minus the standard deviation and evaluates if the central pixel of the window falls within these limits. If so the original value is accepted and not altered (values are altered with a regular averaging filter). If the central pixel does not fall within the acceptable range its velocity value is predicted based upon velocity values of surrounding pixels. In our approach first the outliers of the window are excluded and then an inverse distance weighted average of the remaining surrounding values is calculated and assigned to the central pixel. In this way the averaging takes place after outliers are removed. The predicted result is therefore not contaminated or biased by outliers. We apply an inverse distance weighted interpolation algorithm based upon Liu (1999). The method predicts a value based on a linear weighted function of its (non outlying) neighbors within the window:

$$\hat{v}_q^* = \sum_{i=1}^s w_i v(p_i) \quad (3.10)$$

Where \hat{v}_q^* is the predicted velocity value for point q ; $v(p_i)$ is the value of neighboring (and non-outlying) point p_i ; s is the number of non-outlying neighbors, w_i is the weight of point p_i and is given by:

$$w_i = \frac{d_i^{-m}}{\sum_{j=1}^s d_j^{-m}} \quad (3.11)$$

where d_i is the distance between point q and neighboring point p_i and m is the distance friction factor, for which we use a value of 2. The idea of this approach is that points nearby will have a more similar velocity than points further away.

In the approach described above no-data points (meaning they have a value of 0) are included in the original calculation of acceptable range for a window. They cannot be thrown out upfront because otherwise if there are just a few pixels with either valid or erroneous data in a window with many no-data points they get validated right away and they will be used to determine the value of the central pixel. This is not desirable, if most pixels in a window are no-data points it is preferable to assign a zero to the central pixel rather than some value based on just a few data points. In the approach used here the central pixel will therefore become (or remain) a no-data point in this case, because the acceptable range will fall around zero and the few data points will be considered outliers. This, however, can result in rejection of valid points in rare cases. If there is enough actual data in a window zero values automatically fall outside of the acceptable range, but there is a conflict situation when a window has about as many zero values as data points. Therefore the algorithm checks how many no-data points are in a window and when about 50% of the values are no-data points it recalculates the acceptable range after they are removed. Again the central pixel is evaluated and its validity is determined. Its value is either accepted or replaced with a weighted average of the remaining values. After

applying the filter on both x and y velocity a final magnitude map can simply be calculated by:

$$v_{tot} = \sqrt{(v_x^2 + v_y^2)} \quad (3.12)$$

In our approach newly predicted values are taken into account for calculation of the statistics for the next extracted window. This might lead to slightly different results depending on in which corner the algorithm starts, but is preferable because it reduces the number of times the filter must be applied in order to fill up gaps. The whole process can be repeated several times to fill up more gaps without leading to noticeably more smoothing as values that are already accepted do not get not altered. The newly adapted method developed here greatly improves the consistency of the velocity data (figure 3.10).

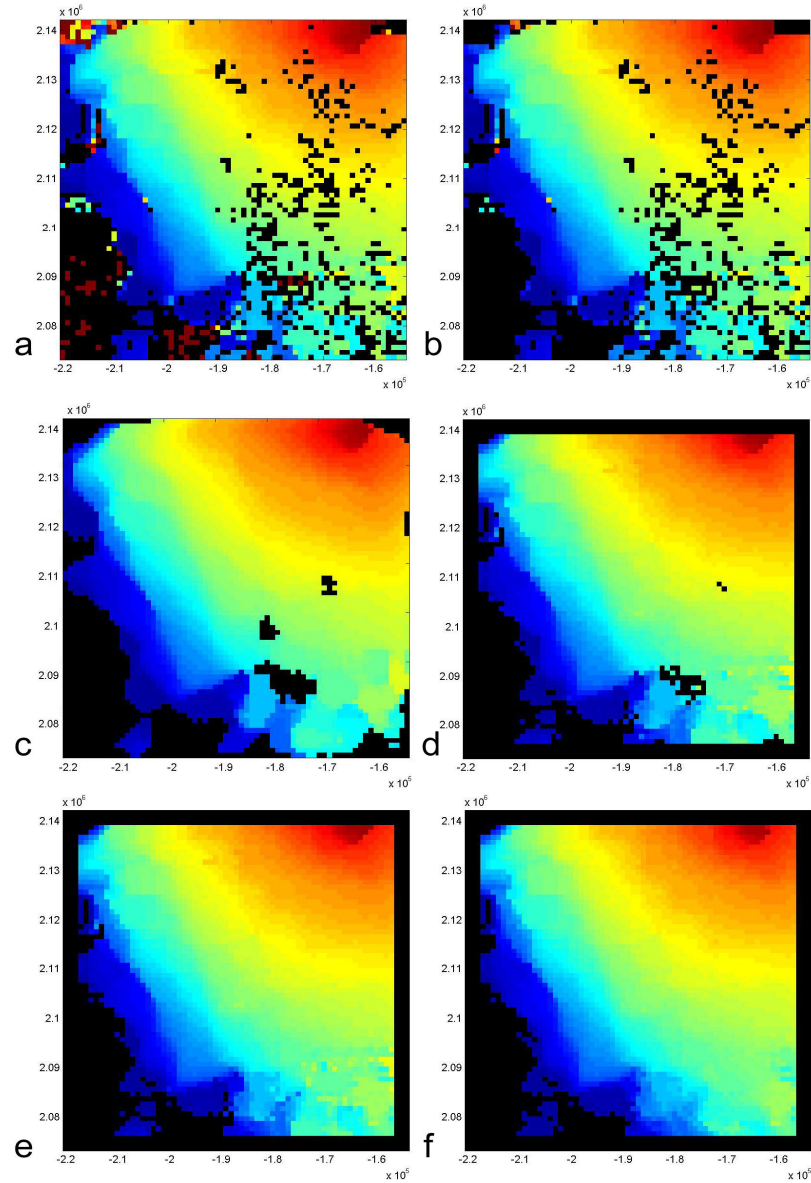


Figure 3.10 Various examples and stadia of the filtering and interpolation process for a region on Jelbart Ice Shelf, a) unfiltered IMCORR output; b) same after setting limits on extremes; c) normal median filter with window size 5 applied; d) inverse distance weighted standard deviation filter applied 1 time without including newly predicted values in the statistics; e) and f) inverse distance weighted standard deviation filter applied 1 and 5 times respectively, using a window size of 5 and with newly predicted values included.

3.4 Error estimates

The largest error source for feature tracking derived velocity is due to image geolocation and co-registration. These errors are assumed to be constant throughout the image and can therefore be considered systematic errors. Feature identification is more reliable over short intervals but systematic errors are more of a concern because of the much smaller absolute displacements. The percent error contribution relative to the velocity magnitude changes somewhat depending on the time interval between observations. We estimate that our 10 m repeat cycle images are accurately co-registered to within one pixel or 10 meter (for both the 24 and 48 day interval). We estimate an additional random error of about 0.5 pixel (or 5 m) associated with limitations of the algorithm used for feature tracking. The total error is the sum of these and translates into a velocity error of approximately 228 m a^{-1} for derived 24-day averaged velocities, and approximately 114 m a^{-1} for 48-day averaged velocities. For longer time intervals (3 years in our case) registration errors are offset to some degree by the increase in actual displacements and the longer time interval. On the other hand, we find that it can be more difficult to reliably locate similar features that may have changed appearance over that time period. Co-registration of AMM-1 25 m (1997) and MAMM 25 m data (2000) is believed to be accurate to within three or four pixels (75-100 m), a relatively small value compared to ice-feature displacements. This translates into an uncertainty of approximately 35 m a^{-1} for 3-year averaged velocity.

The error associated with the IMCORR algorithm partly arises from the ability to find the correlation peak. In order to investigate the peak finding ability we ran IMCORR using the same images, basically calculating the autocorrelation. This was done for

different reference and search window sizes and grid intervals. In all cases the reported values had a zero mean for both the x and y component of displacement (figure 3.11). The standard deviation is inversely related to reference window size. For the default reference window size (64) used primarily in this study the standard deviation is 0.030 pixels. Doubling the reference window size decreases the standard deviation by about 50%. Apart from this error there remains an error in locating the same feature in two different scenes and the geocoding issue discussed above.

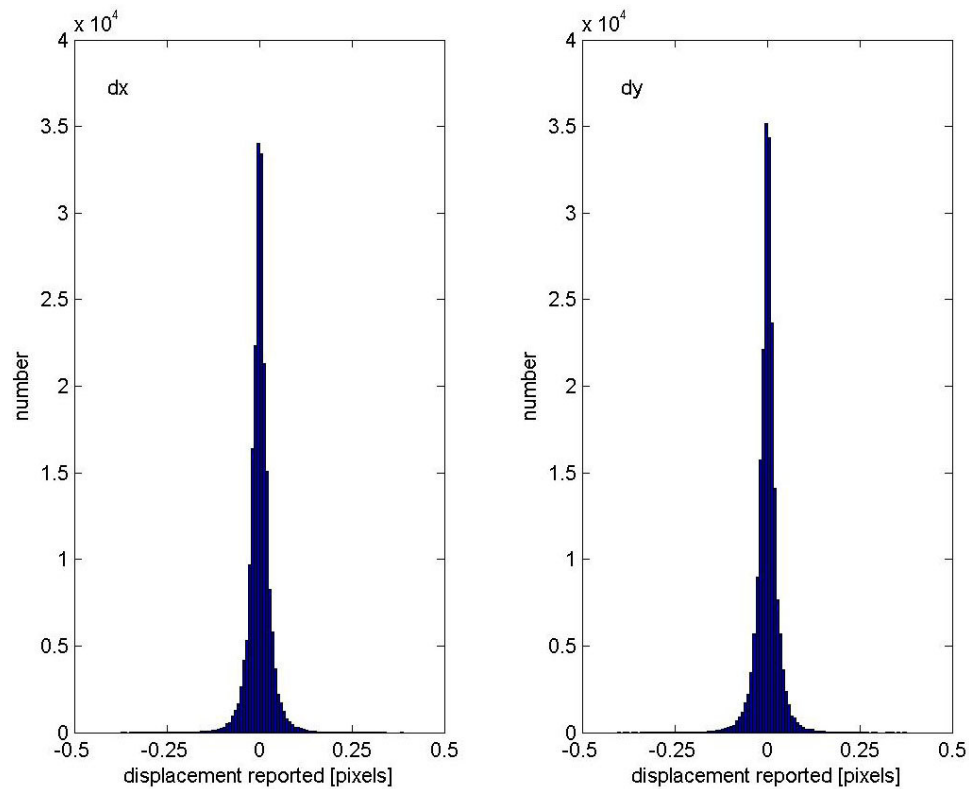


Figure 3.11 Two histograms showing the displacement in x (left) and y (right) direction given by IMCORR using the same image. The search and reference windows were set to 192 and 64 pixels respectively and the grid interval was set to 16 pixels. The histograms have a zero mean and a standard deviation of 0.030 pixels. Doubling the reference window size decreases the standard deviation by about 50%.

3.5 InSAR

3.5.1 Theory and applications

Synthetic aperture radar interferometry (InSAR) has been widely used to measure glacier surface velocity since the early 1990s, when Goldstein and others (1993) successfully retrieved velocity of the Rutford Ice Stream in Antarctica. It can be used to measure ice velocity as well as grounding line position to unprecedented detail. The technique is capable of producing high resolution and high precision uniform velocity fields, even when velocities are very small. It is usually combined with a different technique called speckle tracking, which uses displacements of correlated speckle patterns in pairs of SAR imagery, to derive ice motion.

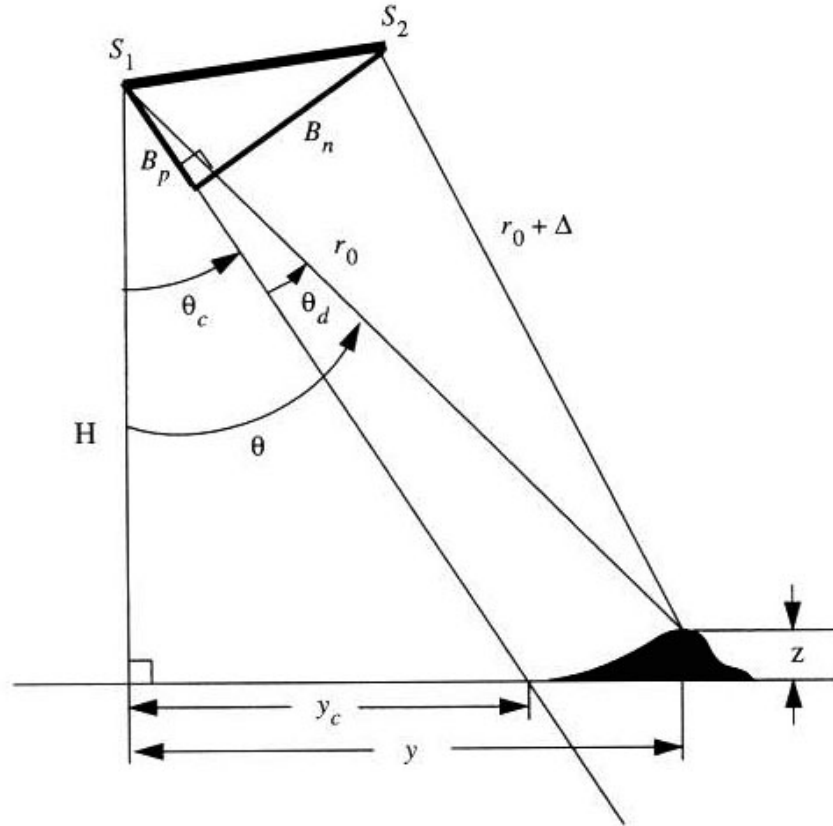


Figure 3.12 Geometry of an interferometric SAR (from Joughin and others, 1996).

In the InSAR technique the SAR is basically operated as an interferometer. The RAMP project utilizes so-called repeat-pass interferometry whereby the interferometer is operated from two nearly repeating orbits. Figure 3.12 shows the geometry of an interferometric SAR (adapted from Joughin and others, 1996). Two images are acquired from a slightly different position with the satellite located at S_1 and later at S_2 . During the first pass the satellite is at an altitude H . The range, r_0 , and look angle, θ , to a target point on the ground is determined by the ground range, y , and elevation, z . The difference in

range to the same target between the two passes is Δ . This range difference is determined by looking at the phase difference information (the difference in number of cycles). As part of the interferometric processing chain an interferogram is created with fringes representing phase difference. The phase difference must be unwrapped to remove the modulo- 2π ambiguity, this yields the unwrapped phase ϕ_{unwrap} . After that is done the range difference can be expressed as a function of a motion dependent term and a topography dependent term and can be determined using:

$$\Delta = \frac{\phi_{unwrap}}{2k} = \frac{\lambda}{4\pi} \phi_{unwrap} \quad (3.13)$$

where k is the wave number, λ is the radar wavelength and ϕ_{unwrap} is given by:

$$\phi_{unwrap} = \phi_{motion} + \phi_{topography} \quad (3.14)$$

Topography related fringes must thus be removed from the interferogram in order to retrieve the fringes related to ice motion, for this a high quality DEM is used. Once this is done the ice motion can be estimated to approximately one quarter of a radar-wave cycle, (a few centimeters in the case of RADARSAT-1; Jezek, 2003). The motion dependent term in equation 3.14 is related to changes in the y and z coordinates between the two passes, the wave number and the look angle as follows (Joughin and others, 1996):

$$\phi_{motion} = 2k[(y_2 - y_1)\sin\theta - (z_2 - z_1)\cos\theta] \quad (3.15)$$

Since interferometry only yields relative displacements absolute displacements must be derived by using control points with known motion. The InSAR data used in this study utilize ground control points from a variety of sources such as data from the VELMAP project (chapter 3.6).

3.5.2 InSAR method

In this study we use InSAR velocity data provided by the RAMP project, in particular we use the data acquired from the MAMM mission. This mission yielded three separate cycles 24 days apart from which coherent pairs were used to derive velocity, using a hierarchical approach. Images chips are cross correlated first using a complex correlation method. If this fails, an amplitude correlation method is applied. If this also fails then the chip size is increased and the amplitude correlation applied again as basically a feature tracking approach (Jezek and others, 2003). The several approaches are combined to provide the best correlation optimized on coherence. Range and azimuth speckle offsets measured using the amplitude and complex registration methods can be used to compute surface displacement between two acquisitions. Ascending and descending range displacements from interferograms provide the most accurate estimates. Velocity components are computed in these different ways and final velocity is computed based on a weighted average. Weights are determined based on estimated errors. In this study we use InSAR velocity maps gridded to 400 m, similar to our feature tracking velocity.

For InSAR velocity the accuracy using the speckle tracking is as good as 0.01 pixel size depending on the coherence. For RADARSAT-1 data this means about 0.05

meter, or 0.75 m a^{-1} for a 24 day acquisition interval and 0.38 m a^{-1} for a 48 day acquisition interval. The typical chip size is usually set to be 64 by 64, which corresponds to about 350 by 350 meters for the fine beam datasets. We note that the InSAR results are tidally corrected using a tidal model described in Robertson and others (1998).

3.5.3 InSAR versus feature tracking

Automatic feature tracking works well within areas of fast flow and with prominent surface features, while in slower more homogenous areas the method is not always satisfying. The differential InSAR technique on the other hand provides accurate results in slow moving homogeneous areas, while often failing in areas of rapid motion due to low coherence (also noted by Joughin and others, 1999). Feature tracking therefore represents a method whereby velocities can be determined even when interferometric coherence is low. In addition feature tracking is applicable on sub-repeats (orbits that partly overlap but with sub-cycle repeat time), yielding velocity data averaged over time spans not possible with interferometry and speckle tracking due to base line restrictions. IMCORR however, does only give the x- and y- components of velocity. The z- component cannot be determined from the method. In this study we use velocity derived from both methods to draw on the benefits of the two methods.

3.6. VELMAP velocity and literature

In addition to the velocity datasets derived from feature tracking and InSAR we use other sources for velocity comparisons. The National Snow and Ice Data Center (NSIDC) has compiled a dataset of Antarctic glacier velocities that is available online.

The velocity data is derived from various methods, including field derived GPS measurements and feature tracking methods using LANDSAT imagery of various different times.

The data is in ASCII format and includes latitude, longitude, speed, bearing and error range. The dataset was used as absolute control for the InSAR velocities used in this study. We use the data for comparison with derived velocities and quality control purposes. Furthermore we use data reported in literature.

3.7 Additional datasets

3.7.1 Surface topography

For the stress analysis in this study we need detailed information of glacier geometry, in particular the ice thickness and surface gradient. We use two sources for surface topography: the OSU Antarctic Digital Elevation Model (OSUDEM) and ICESat data.

The OSUDEM is a very detailed and accurate representation of Antarctic elevation (figure 3.13). It was developed in order to correct for terrain distortion in the RADARSAT-1 mosaics. A variety of cartographic and remotely sensed data have been integrated to form the elevation model (Liu, 1999). The reported accuracy is about 100 to 130 m over rugged terrain, about 35 m for the steeper ice sheet margins, better than 15 m for the interior and better than 2 m for ice shelves. Several DEM's at continental scale were produced at different grid intervals; in this study we use the version with a grid resolution of 200 m for the ice dynamics calculations.

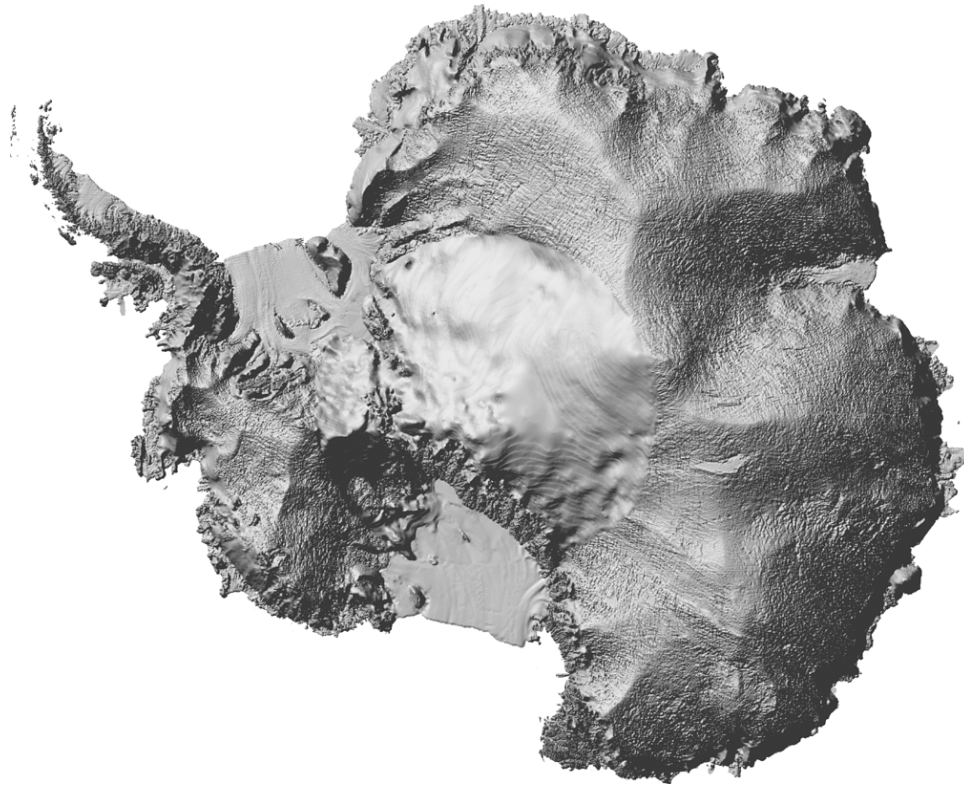


Figure 3.13 Hill shaded relief map of the OSUDEM (*adapted from Liu, 1999*). The DEM is a compilation of different datasets, with different resolution, and looks therefore smoother in the center.

We also use surface topography data derived from the Ice, Cloud and land Elevation Satellite (ICESat) launched by NASA in 2003. On board, this satellite has the Geoscience Laser Altimeter System (GLAS), which is the first laser-ranging (lidar) instrument for continuous global observation (Schutz and others, 2005). It is especially designed to measure ice-sheet topography and cloud and atmospheric properties. The laser-ranging device transmits pulses of infra-red and green light at 40 Hz and records the time it takes for the pulse to reflect from the earth's surface and back to the satellite.

Laser footprints are about 70 m in diameter and are spaced at 170 m intervals. We use the level 2 altimeter product (GLA12) which has data from all available missions incorporated. The data is originally referenced to the OSU91A geopotential model (Rapp et al., 1991). To obtain heights relative to the WGS-84 ellipsoid we add the geoidal undulation. For floating ice, surface elevation can be used to estimate ice thickness by assuming hydrostatic equilibrium and estimating an ice density. We use ICESat derived ice thickness where the quality of the BEDMAP thickness (see chapter 3.7.2) is poor. The error associated with this approach is believed to be in the order of 50-100 m, which includes errors associated with the laser elevation, density and geopotential model.

3.7.2 BEDMAP ice thickness

In this study we use ice thickness estimates from BEDMAP. This is a database, compiled by the British Antarctic Survey, which is available online and consists of a compilation of ice thickness estimates from numerous surveys taken over the past 50 years (Lythe and Vaughan, 2000). The goal of the BEDMAP project was to integrate all available ice thickness estimates and form a model of the bedrock topography underneath the Antarctic ice sheet, which in some locations is buried beneath more than 4000 m of solid ice. We use a digital thickness model with a nominal spatial resolution of 5 km (figure 3.14). This model is, like the SAR imagery, in Polar Stereographic projection with latitude of true scale at -71° . The most important sources of error in the ice thickness data are associated with inaccuracies in navigational systems and the precision to which the actual ice thickness observations are determined (Lythe and Vaughan, 2000). The precision of the ice thickness data is highly variable and, depending on location, ranges

from 10m to 180 m (figure 3.15, adapted from Wu and Jezek, 2004). For floating ice we use thickness estimates derived from ICESat data (see chapter 3.7.1) to complement the BEDMAP data.

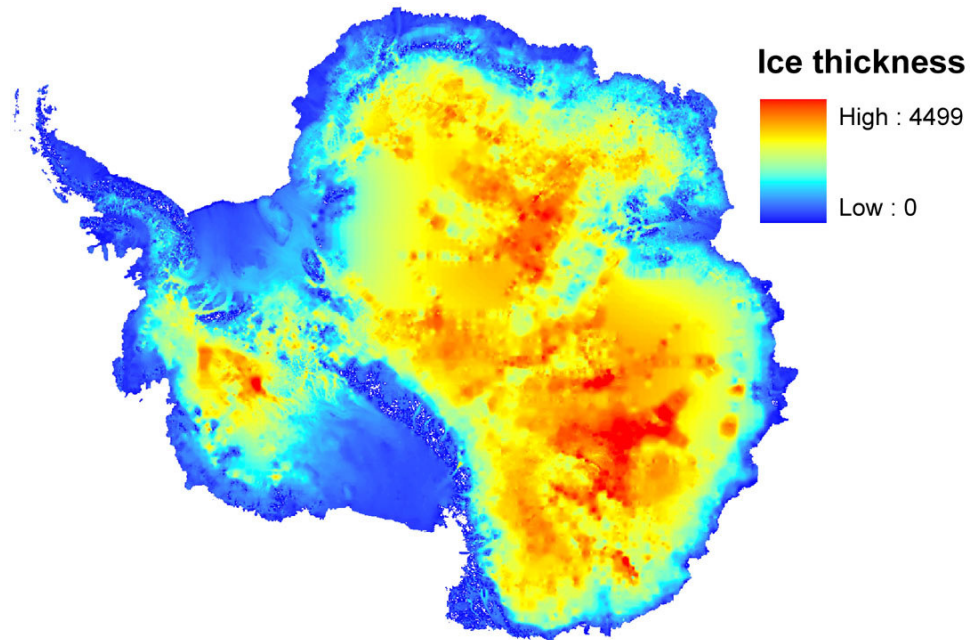


Figure 3.14 BEDMAP digital ice thickness model of Antarctica. Ice thickness is given in meters.

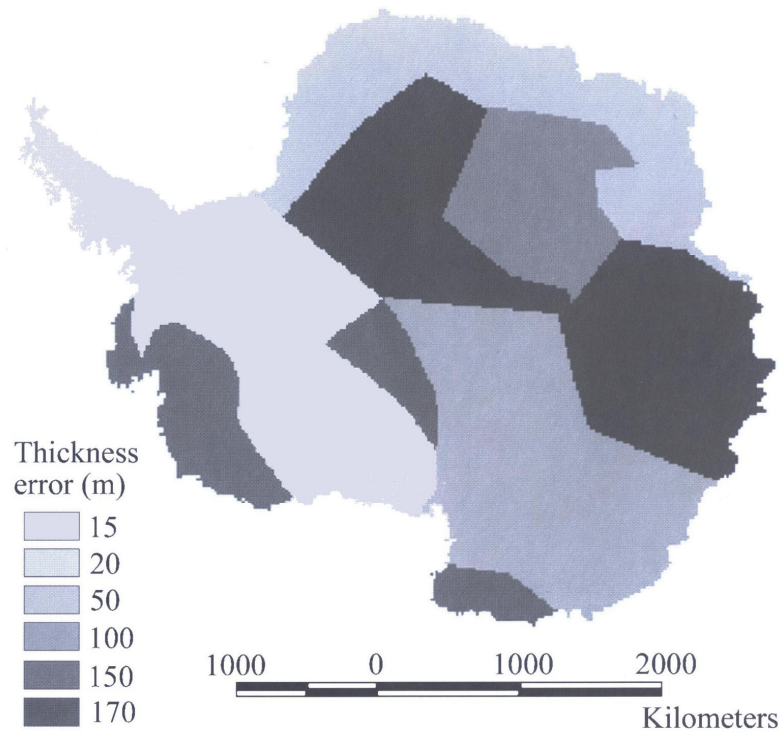


Figure 3.15 Bedmap thickness error (adapted from Wu and Jezek, 2004)

3.8 Summary

In this chapter we have discussed and laid out the various datasets and methods that we use to gather data utilized in this study. We gather and combine a number of remotely sensed datasets that form the starting point for the stress analysis described in chapter 2. Although the concept of the feature tracking technique is straight forward, the actual implementation of the procedure on the SAR data requires a number of modifications that are developed and highlighted in this chapter. These include the application of a speckle filter on the RADARSAT-1 images, the modification of the feature tracking algorithm by including a variable sized window function and the development of a filtering technique to get rid of outliers and fill gaps. All these

procedures led to a great improvement in the quality of the derived velocity field, which is necessary for a detailed assessment of glacier dynamics. The use of various other sources of velocity data complements the data gathered in this study and allows for a detailed investigation of temporal and spatial variability.

Apart from velocity data we also need to include the use of a number of other datasets in order to do the stress analysis. These include extensive datasets of surface topography and ice thickness. The datasets that we use and describe here are the best available datasets at the time for the purpose of this study and highlights the importance of these previous studies. Although each dataset and method has its drawbacks and limitations, the application and integration of the various datasets allow for a more detailed investigation of glacier dynamics on a wider scale than previously possible and adds to the value of the RAMP project.

CHAPTER 4

THE FLOW REGIME OF DAVID GLACIER AND DRYGALSKI ICE TONGUE

4.1 Introduction

In this chapter we analyze spatial and temporal variability of the surface velocity field of David Glacier and Drygalski Ice Tongue in northern Victoria Land, Antarctica. First we summarize the geographic setting and results from previous studies. Then we present velocity maps. We compare InSAR with feature tracking results and also, where available, with VELMAP velocities. We find the velocity to be very constant over the time intervals of observation and good agreement with earlier studies extends this time. We determine basal melting along the entire ice tongue and the calving behavior. Finally we investigate the stress partitioning along the glacier and its tributaries using the velocity data and derive an equilibrium profile for the ice tongue. Our stress calculations show that upstream glacier flow is largely controlled by basal drag, as opposed to, for instance, the dynamic West Antarctic ice streams.

In the fjord, glacier flow is controlled largely by basal drag but its role decreases once the fjord gets wider. Along the ice tongue the driving stress is balanced by longitudinal stress gradients to within our limits of detection.

4.2 David Glacier- Drygalski Ice Tongue

David Glacier is the largest outlet glacier in northern Victoria Land (figure 4.1). It drains approximately 212,000 km² of the interior ice sheet into the Ross Sea, and its annual flux is estimated to be about 15.4 ± 2 km³ a⁻¹ (Rignot, 2002). Frezzotti and others (2000) estimated the grounding line position of the main (southern) flow to be located near the mouth of David Cauldron. Subsequently, Rignot (2002) estimated the grounding line position using InSAR fringes and found it to be several kilometers upstream of the original estimate.

The glacier is funneled through a narrow gap in the Transantarctic Mountains where it starts to float and forms a floating ice tongue, extending more than 140 km beyond the grounding line and varying in width from 13 km at the upstream end to more than 25 km after leaving the confining valley walls.

The ice tongue forms an effective barrier that traps southerly fast ice and keeps the Terra Nova Bay Polynya free from northward drifting pack ice (Bromwich and Kurtz, 1984). A significant amount of surface area was lost during several calving events in 2005 associated with the drifting iceberg B-15. The fact that the David Glacier drains a largely marine-based sector of the East Antarctic Ice Sheet (BEDMAP bottom topography data) suggests that the region has the potential for rapid change.

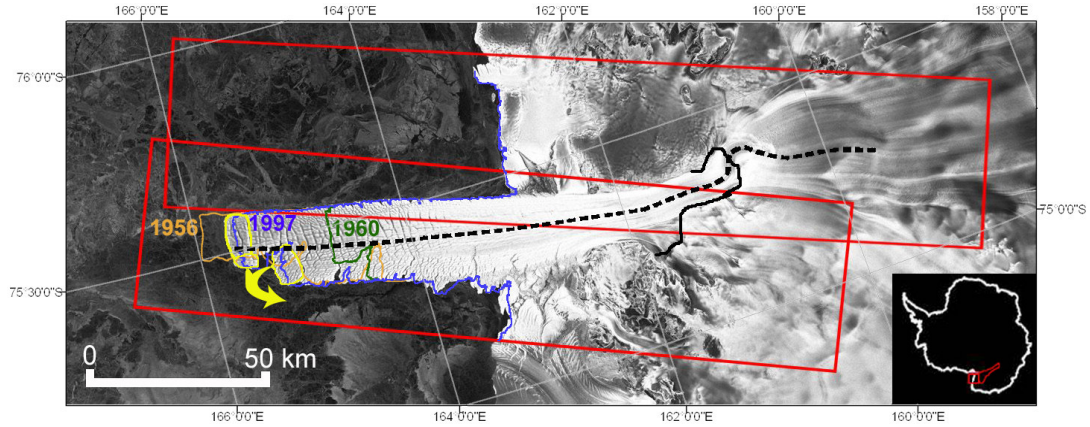


Figure 4.1 RADARSAT-1 mosaic of David Glacier and Drygalski Ice Tongue in Victoria Land, acquired during the MAMM mission in September 2000. The inset shows the location of the David Glacier drainage basin. Depicted are in red: the outline of swaths used for feature tracking and their overlapping area; in blue: coastline of 1997 derived from the AMM-1 mosaic; in green: 1960 outline (from USGS map), after approximately 40 km calved off in 1957; in orange: 1956 outline (Frezzotti and Mabin, 1994); solid black: approximate position of the grounding line (Rignot, 2002); dashed black: velocity profile shown in figure 4.6; in yellow: sections that calved off in early 2005 (totaling approximately 150 km²).

4.3 Previous studies

Investigators have measured surface velocity on the glacier since the mid-1980's. Holdsworth (1985) made velocity estimates by measuring the displacement of a notch in the ice tongue 50 km from the coast. Swithinbank (1988) compared identifiable features in Landsat multispectral scanner (MSS) images to estimate average velocity at the landward end of the ice tongue over a 14 month time span. Lucchitta and others (1993) also used Landsat-image pairs to derive displacement over the period between 1973 and 1988. Frezzotti has used both sequential satellite imagery and GPS field surveys to determine velocity for different time intervals (e.g. Frezzotti, 1993, 1998, and 2000).

Rignot (2002) used InSAR and speckle tracking on ERS-1/2 data to derive velocity in the grounding area. The measurements derived in these studies will be used in this chapter for comparison.

4.4 Velocity

We present 2000 velocity measurements of David Glacier and Drygalski Ice Tongue derived using feature tracking and interferometry on sequential RADARSAT-1 synthetic aperture radar imagery. We compare 24-day and 48-day averaged velocities, 3-year averaged velocities, and velocities from earlier studies to investigate variability in the velocity field. We go on to use the velocities to compute mass balance and basal melting along the ice tongue and to examine the calving process from the tip of the ice tongue. Finally we use the derived velocities to investigate the dynamics of the glacier system in an effort to determine the glaciological significance of the ice tongue.

To obtain short term velocity fields we use two radar swaths, per MAMM-cycle, covering our study area (figure 4.1). For each cycle these two adjacent swaths are acquired 3 days apart. The time interval of repeat pass swaths is exactly 24 days (table 4.1). We applied feature tracking on these corresponding swaths. For each time frame under consideration the resulting files are then merged to create 24 and 48 day velocity maps of the whole area. By using overlapping areas of two sub-repeat-cycle swaths we can also measure velocity over other time spans, for instance 21 and 27 days. We could not successfully apply feature tracking techniques to the 3 day sub-repeat cycle, likely due to the small amount of absolute displacement.

Data	Orbit pair	Dates	Time span	Resolution
MAMM cycle 1 - cycle 2	25509-25852	9/23/00 10/17/00	24 days	10 m
MAMM cycle 1 - cycle 2	25552-25895	9/26/00 10/20/00	24 days	10 m
MAMM cycle 1 - cycle 2	25509-25895	9/23/00 10/20/00	27 days	10 m
MAMM cycle 1 - cycle 2	25552-25852	9/26/00 10/17/00	21 days	10 m
MAMM cycle 1 - cycle 3	25509-26195	9/23/00 11/10/00	48 days	10 m
MAMM cycle 1 - cycle 3	25552-26238	9/26/00 11/13/00	48 days	10 m
MAMM cycle 2 - cycle 3	25852-26195	10/17/00 11/10/00	24 days	10 m
MAMM cycle 2 - cycle 3	25895-26238	10/20/00 11/13/00	24 days	10 m
AMM-1 1997 MAMM 2000	AMM-1/MAMM mosaic	Oct 1997 Oct 2000	3 years	25 m

Table 4.1 RADARSAT-1 data used in this study. The different time spans allows for an investigation of variability.

The RADARSAT images reveal that the ice tongue has a distinct crevasse pattern that can be tracked automatically over 3 years (figure 4.2 a). There is a gradual increase in velocity on the floating section from around 550 m a^{-1} reaching a maximum of 750 m a^{-1} at the ice front. Upstream on David Glacier, measured velocities are sparse due to a lack of traceable features over this 3-year time span. There, we measure velocities that range from about 150 m a^{-1} to 300 m a^{-1} .

Figures 4.2 b-f show feature tracking and InSAR velocity derived using the MAMM mission acquisitions. For this shorter time span we get good results, even above

the grounding line. We measure the fastest velocity on a section called the David Cauldron, an ice fall caused by a sub-glacial ridge (Swithinbank, 1988). Velocities increase sharply from the grounded inland ice towards the ice fall, reaching values of up to 1039 m a^{-1} , and then decrease again. Velocity increases yet again towards the ice front. The velocity plots also reveal large patches of trackable multi-year sea ice south of the ice tongue. This fast ice is generally moving in the same direction and at the same speed close to the glacier, and gradually slower away from it. This suggests a coupling between the two.

We subtracted displacements from the second 24 day period with those from the first 24 days and plotted the resulting difference and histogram (figure 4.3). The spatial patterns visible in the plot are likely the result of limitations of the feature tracking algorithm. The histogram seems to be slightly skewed, but we do not measure any significant changes.

The difference between 48-day averaged velocity, derived by feature tracking between cycle 1 and 3 in 2000, and 3-year averaged velocity, derived by feature tracking between imagery from 1997 and 2000, is plotted in figure 4.4. Differences are small and fall within the error limits and the associated histogram reveals an approximate zero mean in differences. This implies that ice flow has been at most slowly changing over the past 3 years and more likely has been nearly constant.

Figure 4.2 Ice flow velocity on Drygalski Ice Tongue and David Glacier, in meters per year, derived using:

a) feature tracking (1997 and 2000),

b) feature tracking (cycle 1-2),

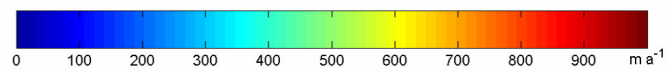
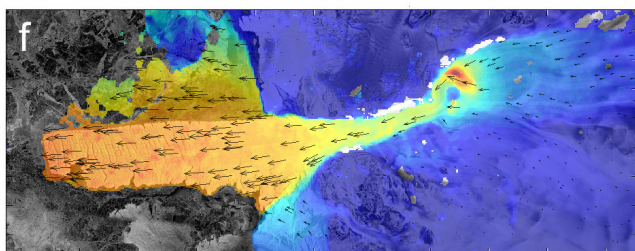
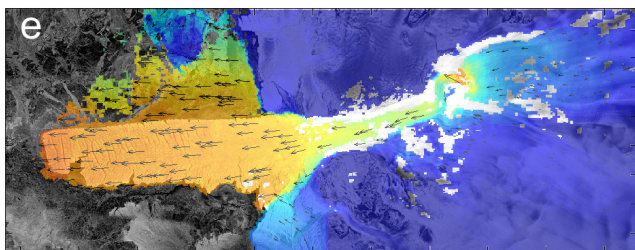
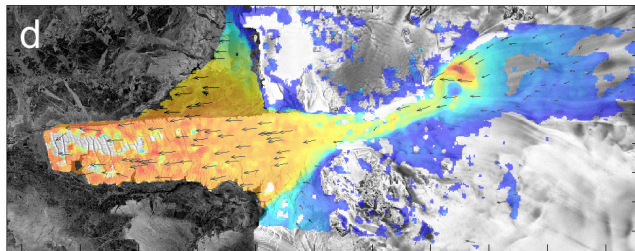
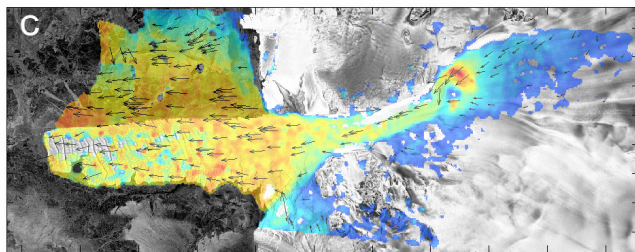
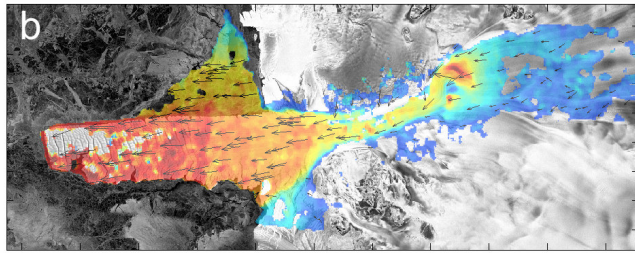
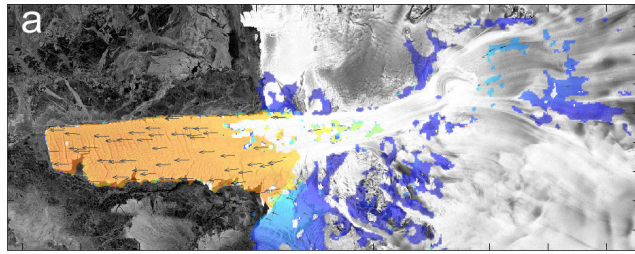
c) feature tracking (cycle 2-3),

d) feature tracking (cycle 1-3),

e) InSAR

f) InSAR and feature tracking combined.

Velocity rapidly increases from just a few meters per year in the inland to approximately 1000 m a^{-1} in the David Cauldron ice fall after which they drop to 500 m a^{-1} and gradually rise towards 750 m a^{-1} at the calving front. Visible in b-f are large patches of multi-year sea ice attached to the glacier. Vectors show direction of flow and their length is proportional to magnitude; the vector density has been decimated for display purposes. Coordinates are polar stereographic, velocity pixels are $400 \times 400 \text{ m}$.



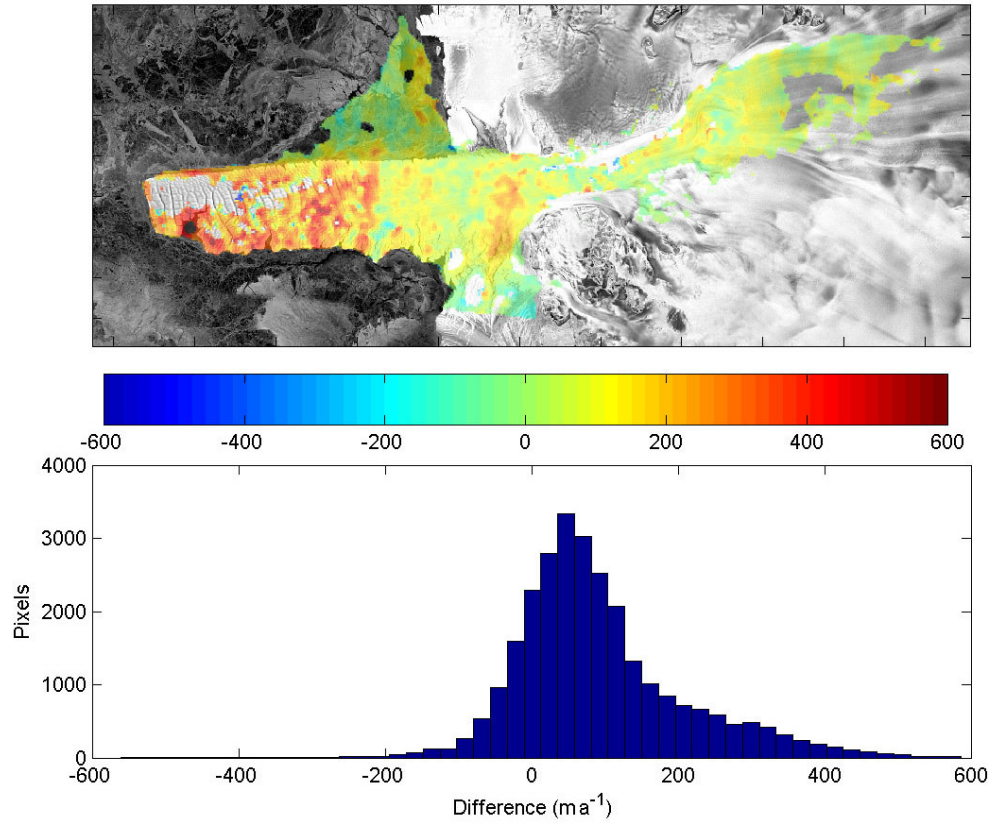


Figure 4.3 Displacements between cycle 2 and cycle 3 subtracted from displacements between cycle 1 and 2 and associated histogram. Both timeframes are 24-day periods. We do not measure any significant change. The spatial patterns are likely the result of limitations of the feature tracking algorithm.

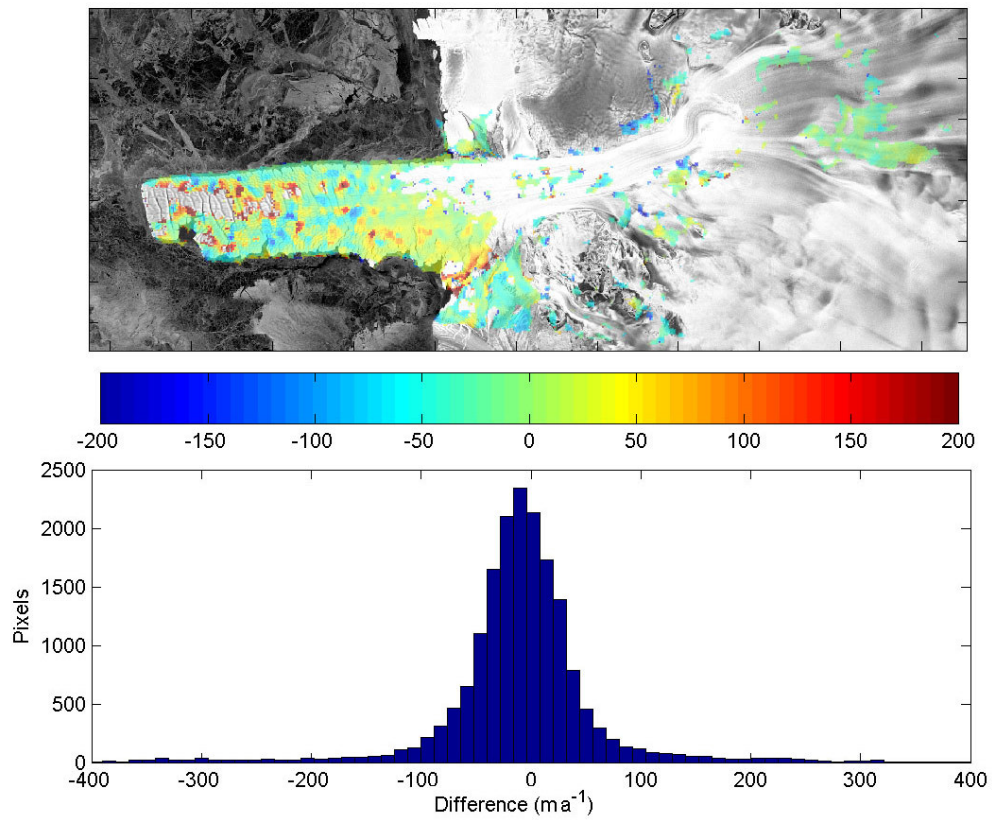


Figure 4.4 Displacements between cycle 1 and cycle 3 (48-day averaged velocity) subtracted from displacements between 1997 and 2000 (3-year averaged velocity) and associated histogram. Differences are very small and have an approximate zero mean indicating little change between these time intervals.

To identify any systematic effects we compare our velocity measurements, where possible, with field derived GPS measurements, made by Frezzotti and others (1998) in the period 1991-94 and available through the online VELMAP database (figure 4.5). A comparison of derived feature tracking and InSAR velocities with velocities derived by Frezzotti and others (1998), from the Velmap database, using Landsat imagery from 1990-1992 (black dots) and in situ GPS data obtained in the period 1991-1994 (triangles) extends the apparent steady behavior even further back in time (figure 4.5). We plotted the velocity differences but could not detect a spatial pattern in their distribution, implying that the apparent steady flow holds true for our whole study area.

Figure 4.6 shows three velocity profiles of about 180 km taken along a flow line in the center of the ice tongue. One is derived from averaged MAMM feature tracking data (24 and 48 days), one from 3-year averaged feature tracking and one from InSAR. All show that the velocity varies nearly linearly with distance from the point at which the ice tongue escapes the confining rock walls. Jezek and others (2003) estimated the strain rate to be about $1.2 \times 10^{-3} \text{ a}^{-1}$ by fitting a line through the velocity data. Assuming the ice tongue is freely floating and assuming that lateral strain rates on the seaward portion of the tongue are small, then based on the nearly constant strain rate, we expect nearly constant ice thickness based on Weertman's (1957) analysis of ice shelf flow. This seems to be consistent with ice thickness measurements (see next section). We ascribe the higher variation of the blue curve and the slight bias between the black curve and the other two to a combination of errors discussed earlier and tidal influences.

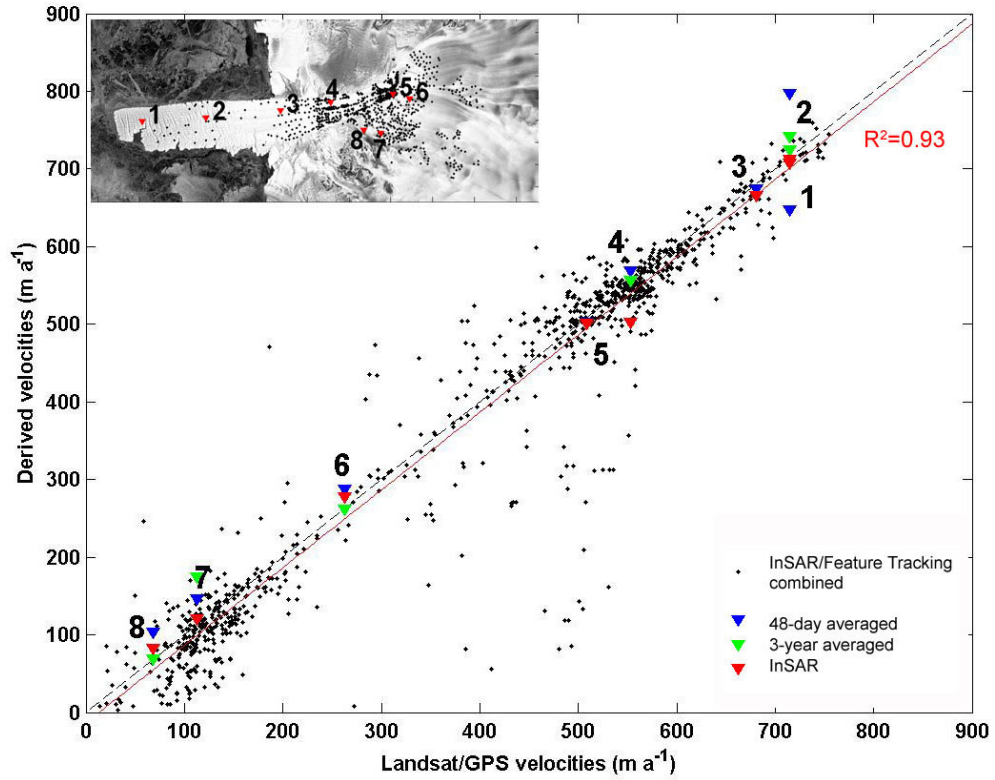


Figure 4.5 Comparison of derived feature tracking and InSAR velocities with velocities from the Velmap database (derived by Frezzotti and others (1998) using Landsat imagery from 1990-1992 (black dots) and in situ GPS data obtained in the period 1991-1994 (triangles)). Locations are shown on the inset. We took the value of our closest velocity pixel for the GPS point comparison. Error bars are left out for clarity.

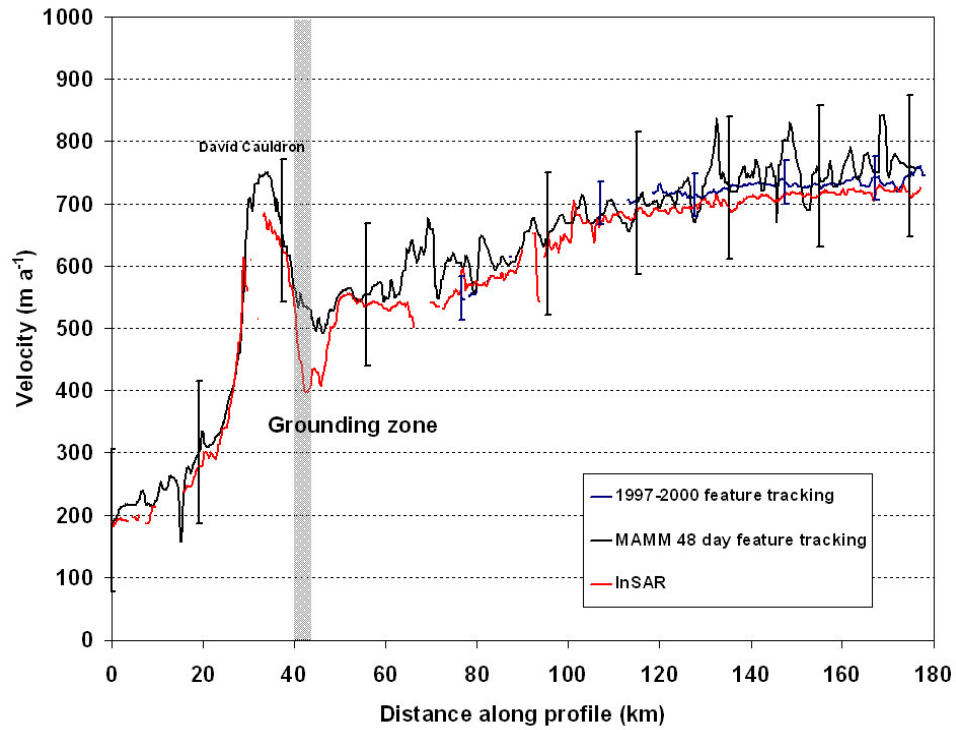


Figure 4.6 Velocity profiles taken along a flow line derived from feature tracking over different time intervals and InSAR (see figure 4.1 for location). Velocity rapidly increases and then decreases at the David Cauldron ice fall. On the floating section there is a gradual increase again. Only a few error bars are plotted for clarity, error bars for InSAR results are not included because they are very small.

4.5 Basal Melting

We use a fluxgate approach to estimate basal melting on the floating section of the glacier. Ice thickness (H) is derived using ICESat laser elevation data (h) (Zwally and others, 2005) in combination with the OSU 91 geoid model and assuming hydrostatic equilibrium:

$$H = h / (1 - \rho_i / \rho_w) \quad (4.1)$$

where ρ_i and ρ_w are the column-averaged densities of ice and sea water, taken to be constant here at 900 kg m^{-3} and 1028 kg m^{-3} respectively. The equation is not valid just downstream of the grounding line, where ice can still be partly supported by bedrock. For that reason we put our first gate several kilometers downstream from the grounding line as determined by Rignot (2002). To investigate the accuracy of the elevation data and the OSU 91 geoid model we plotted the difference between geoidal height and mean ICESat elevations for the sea ice region around the ice tongue (figure 4.7). Mean ICESat values are calculated based on a neighborhood size of $1000 \times 1000 \text{ m}$. The plot shows that the corrected ICESat elevations give values close to 0 for the whole area, giving confidence in the geoidal model used.

Because of the relatively sparse ICESat coverage over our study area, we use kriging to generate an elevation model. To reduce errors associated with the kriging method we place our fluxgates nearly collinear to the satellite ground tracks. Since the use of a constant ice density is an oversimplification, we compare our thickness estimates with radar sounding thickness by Frezzotti and others (2000) (figure 4.8). We find a good

fit for most of our fluxgates, except where the ice leaves the fjord. The column-averaged density could be less there due to large crevasses and perhaps snow accumulation leading to an overestimation of ice thickness. The hydrostatic approach is used here because near the grounding line, where most basal melting occurs, the radar sounding did not prove to be successful (M. Frezzotti *in* Rignot, 2002). Moreover, along the length of the ice tongue a good number of tracks are available perpendicular to flow enabling a better spatial picture of the melt rate not attainable with previous topographic models that are much coarser.

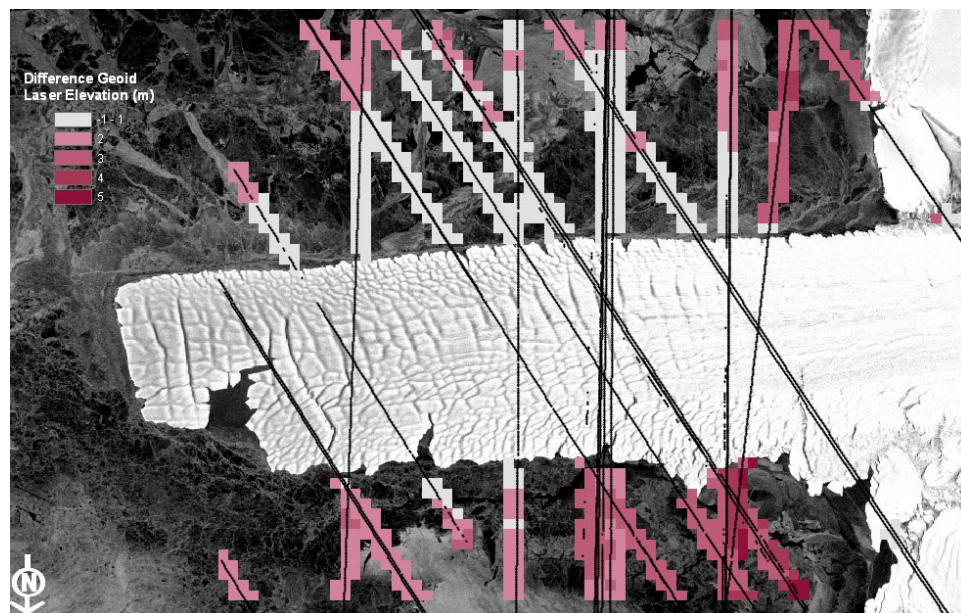


Figure 4.7 Difference between geoidal height and mean ICESat elevations given for the sea ice region around Drygalski Ice Tongue. Mean ICESat values are calculated based on a neighborhood size of 1000 x 1000 m. The plot shows that the corrected ICESat elevations give values close to 0 for the whole area, giving confidence in the geoidal model used.

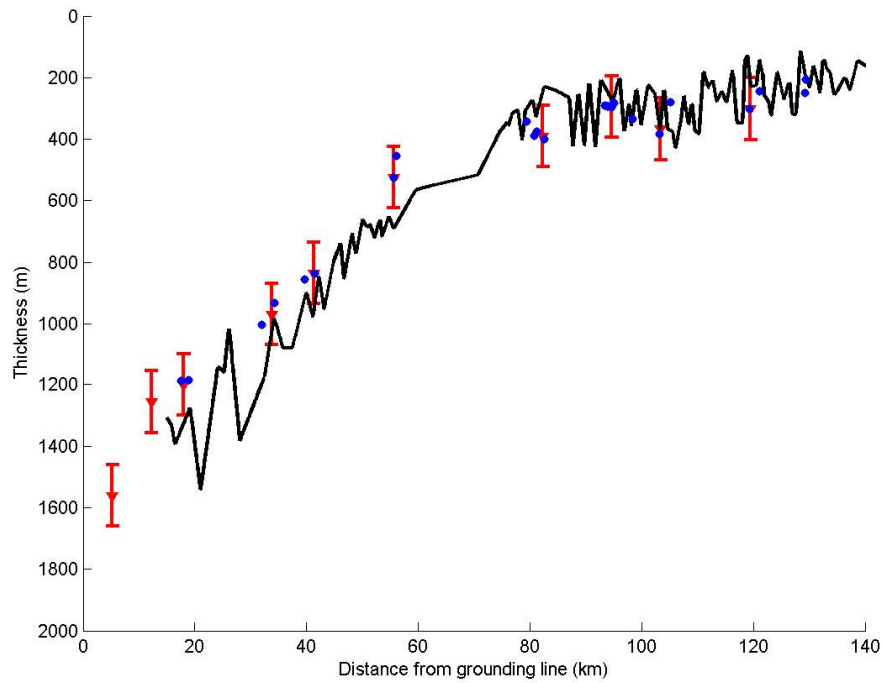


Figure 4.8 Comparison of ice thickness estimates along Drygalski Ice Tongue. Black line represents radar sounding thickness (digitized from Frezzotti and others 2000). Red triangles represent ice thickness at gates used for fluxgate calculations (see figure 4.9) where they intersect the radar profile. Thickness is based upon ICESat laser elevations (referenced to sea level using OSU 91 geoidal model) assuming hydrostatic equilibrium with a density of 900 kg m^{-3} for ice and 1028 kg m^{-3} for sea water; blue dots give ice thickness where ICESat ground tracks intersect the radar profile.

Basal melt rate \dot{B} is calculated by:

$$\dot{B} = \frac{\Phi_i - \Phi_{i+1}}{S} + \dot{A} \quad (4.2)$$

where S is the surface area between the gates, \dot{A} is the accumulation rate (Frezzotti, 2000) and Φ is the mass flux through a fluxgate computed from:

$$\Phi = \sum_i v_{\perp i} H_i \delta W_i \quad (4.3)$$

The gates are taken perpendicular to local velocity vectors and their width W is determined by two flow lines, one of them the southern margin of the ice tongue, the other one a very distinct line close to the northern margin. Thickness is estimated at each location across the fluxgate where we calculate velocity and representing a width δW (400 m). We use a combination of feature tracking and InSAR derived velocity for the calculation. For two small sections of gate 2 and 3 where no reliable velocity was available we use nearby velocity points from the same flow band derived by Frezzotti and others (1998) and projected these on the gates. We believe we can do this as our velocity measurements show no significant along-flow variation in this area (i.e. longitudinal strain rates are small). We assume no vertical variation in velocity which is a reasonable assumption for floating ice. The uncertainty using this approach is a function of several factors, including errors in velocity, elevation, geoidal height, ice density, accumulation, surface area and width. Following Rignot (2002) and Berthier and others (2003) we

ignore errors in surface area and width and assume a total constant error in ice thickness of ± 100 m. We calculate basal melt rates using 10 gates encompassing most of the floating area (figure 4.9, table 4.2). We confirm earlier studies (Frezzotti and others, 2000; Rignot, 2002) that found the highest melt rates close to the grounding line. Our estimate of 20.9 ± 9.6 m ice a^{-1} is about 70 % of Rignot's estimate of 29 ± 6 m ice a^{-1} . Basal melt rates quickly decrease downstream and we find an area of slight basal freeze on (0.95 m ice a^{-1}). After the ice leaves the fjord basal melting is small and fairly constant averaging between 0.03 ± 2.0 m and 1.60 ± 1.7 m ice a^{-1} . These values agree well with Frezzotti and others (2000) (who estimate 1.0 ± 0.5 m ice a^{-1}). Differences between other areas are likely the result of different and wider fluxgates used here that encompass the complete southern flow, a different ice thickness model and higher velocity point density.

We find that the pattern of basal melting at great depth, followed by freeze-on is consistent with the 'ice pump' mechanism proposed by Lewis and Perkins (1986), and confirm an earlier study by Frezzotti (1993) who suggested this mechanism for the area (figure 4.10). This circulation mechanism causes cold and fresh (less dense) Ice Shelf Water (ISW), formed by the extensive melt near the grounding line, to rise. Because of the pressure dependence of the freezing point, which increases with decreasing pressure, basal melting becomes smaller and, when a critical depth is reached, the ISW becomes supercooled with respect to the local freezing point. Subsequently marine ice is accreted at the bottom of the ice tongue. Our observations suggest that this occurs at approximately 900 m depth at the point where the valley walls widen and the thickness rapidly declines because the glacier can spread more easily. Once this effect is overcome only moderate melting occurs.

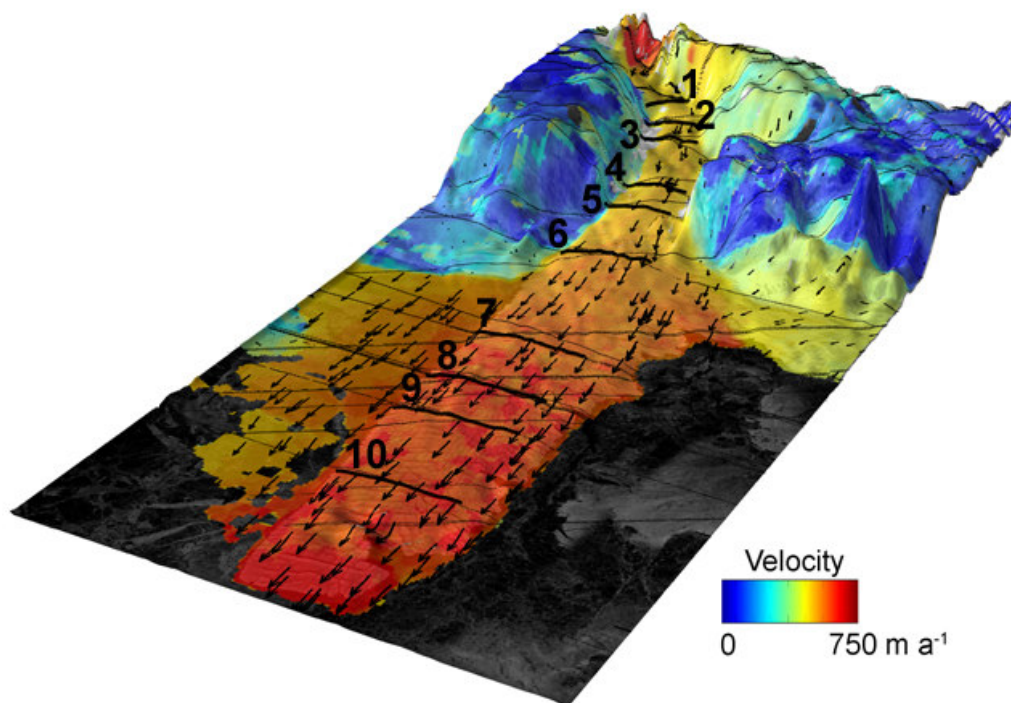


Figure 4.9 3-dimensional model of the study area showing the location of fluxgates (numbered thick black lines) used to calculate basal melt rates (see table 4.2). Velocity is derived from a combination of InSAR, speckle tracking and feature tracking and elevation is derived from ICESat data using ordinary kriging. The fluxgates encompass the main southern flow and are chosen nearly collinear to the ICESat ground tracks (thin black lines) to reduce errors associated with kriging.

Gate	Width h (km)	Flux (km ³ yr ⁻¹)	δ Flux (km ³ yr ⁻¹)	Area (km ²)	A (mm yr ⁻¹)	w.eq. B (m ice yr ⁻¹)
1	7.84	4.98±0.32				
			-0.87±0.56	41.58	50.00	20.91±9.6
2	6.77	4.12±0.24				
2	8.73	5.34±0.27				
			-0.64±0.53	50.57	50.00	12.65±7.4
3	8.45	4.71±0.25				
			-0.95±0.46	135.71	185.00	7.21±2.4
4	9.19	3.76±0.20				
			0.08±0.40	69.62	185.00	-0.95±4.1
5	9.51	3.84±0.20				
			-0.22±0.38	154.65	185.00	1.60±1.7
6	12.49	3.62±0.19				
			-0.42±0.38	385.52	-80.00	1.01±0.7
7	15.18	3.20±0.19				
			-0.12±0.39	191.29	130.00	0.77±1.5
8	16.16	3.08±0.20				
			0.02±0.40	143.72	130.00	0.03±2.0
9	16.39	3.10±0.20				
			-0.16±0.40	263.96	130.00	0.76±1.1
10	15.91	2.93±0.20				

Table 4.2 Values used to calculate basal melt rates in this study. For the area between gate 1 and 2 a slightly different flow line was chosen as margin. Thickness and velocity are estimated at many points across the fluxgate. Accumulation data is from Frezzotti and others (2000). The melt rate is highest near the grounding line (20.91±9.6 m ice a⁻¹) and decreases downstream. Some freeze on occurs between gates 4 and 5, after that there is only moderate basal melt. The pattern is consistent with the ‘ice pump’ mechanism (figure 4.10).

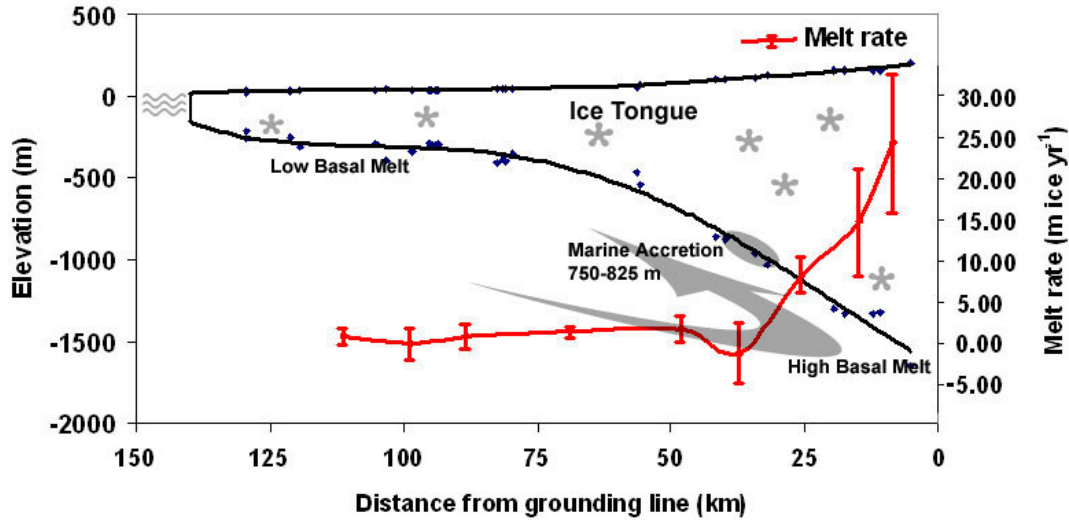


Figure 4.10 Cross section of Drygalski Ice Tongue showing surface elevation from ICESat and derived bottom elevation (blue dots). The red line gives basal melt rates plotted against distance from the grounding line. We find that the pattern of basal melting at great depth, followed by freeze-on is consistent with the ‘ice pump’ mechanism proposed by Lewis and Perkins (1986). Arrow denotes circulation pattern.

4.6 Ice margin and calving

Tracing the ice margin along the tongue, we find that the area of the ice tongue increased by almost 45 km² between 1997 and 2000 or about 14.8 km² a⁻¹. This is a similar value as Frezzotti’s (1993) estimate for 1973 to 1990 (15 km² a⁻¹). Comparing the ice front position depicted on the USGS map (based on aerial photographs from October 1960) with the MAMM image from 2000 (roughly 40 years) we observe an advance of about 29.4 km which corresponds to an advance rate of 734 m a⁻¹, assuming no calving took place (figure 4.1). Comparison between the AMM-1 and MAMM images shows that the front of the Drygalski Ice Tongue advanced approximately 2200 meter over the 3-year time interval between September 1997 and September 2000. The corresponding

advance rate is 733 m a^{-1} which is surprisingly similar to the long term average suggesting steady state flow over this period. Holdsworth (1985) reports a similar advance rate of 730 m a^{-1} between 1960-1973 and Frezzotti and Mabin (1994) report an average advance rate between $730\text{-}830 \text{ m a}^{-1}$ for the period 1909-1956 and an average ice front velocity of approximately 800 m a^{-1} for the period 1960-1993, which appears to be slightly higher.

We note that the forward motion of the ice tongue is almost equal to the ice surface velocity near the edge (our estimates are averaged around 740 m a^{-1}) implying that small calving events are not a primary mechanism for discharging ice from the tongue. Instead, it seems that large sections of the ice tongue break off during more dramatic episodes. Frezzotti and Mabin (1994) suggest that no major calving event took place since sometime between December 1956 and December 1957, when approximately 40 km broke off, after that only a smaller detachment occurred in 1960. In 2000 the floating tongue margin was within 6.5 km from its maximum position of 1956. Captured by a series of Envisat images in early 2005 (ESA, 2005), the giant iceberg B15-a was on a collision course with the ice tongue and eventually collided. Before the collision the iceberg caused a break-up of sea-ice south of Drygalski. This was followed by two sections of the ice tongue calving off on the north side with a total surface area of about 87.5 km^2 (figure 4.1). The timing of this event, perhaps the first of any significance since 1960, strongly suggests a relation with B-15a's presence, the sudden break-up of the sea-ice and the calving. Perhaps an alteration of along shore sea-currents and/or wind patterns caused by the iceberg may have led to the event. The actual collision that followed several weeks later caused another section of about 64.5 km^2 to break off from the front.

4.7 Resistive stresses

We calculate resistive stresses along David Glacier and Drygalski Ice Tongue using strain rates derived from an optimized velocity dataset. This is done by combining the best available velocity datasets, which is justified by the apparent steady behavior of the glacier in recent years. Driving stress and resistive stresses are calculated along two tributaries of David Glacier and along the floating ice tongue. We divide the area above the grounding line in five sub-areas for each of which we calculate the driving stress and resistive stresses separately. The areas' boundaries are based on similarity in velocity and slope. Figure 4.11 shows the optimized velocity dataset and the five sub-areas above the grounding line. The dynamics of the floating part are discussed in chapter 4.8.

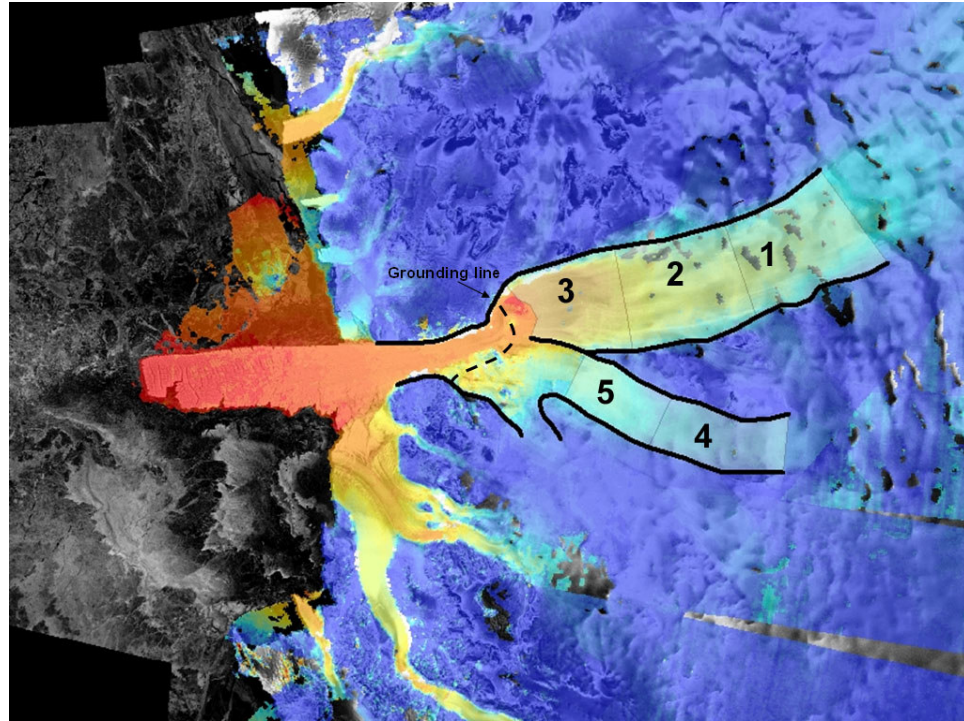


Figure 4.11 Optimized velocity field showing the 5 areas above the grounding line that are discussed in chapter 4.7. The section downstream from the grounding line is discussed in chapter 4.8.

4.7.1 Driving Stress

To estimate the driving stress we calculate the average surface slope of each particular area and the average ice thickness. The average surface slope is derived from 5 elevation profiles along flow lines, spread evenly along the width of the ice stream, using the OSUDEM and RADARSAT imagery. These profiles are about 30 to 50 km long. A trend line is fitted through each profile and the mean of the slopes of the trendlines is assumed to be the average surface slope for the respective area (figure 4.12). For all areas we use an ice density $\rho_i = 900 \text{ kg m}^{-3}$ and $g = 9.81 \text{ m s}^{-2}$. The ice thickness is derived from

the BEDMAP dataset. For each area we calculate the mean ice thickness (H) using ARCGIS. Table 4.3 shows values used to calculate the driving stress. We find the driving stress for most of the areas to be relatively large. These large driving stresses are largely maintained by a steep surface gradient, especially near the ice fall just above the grounding line.

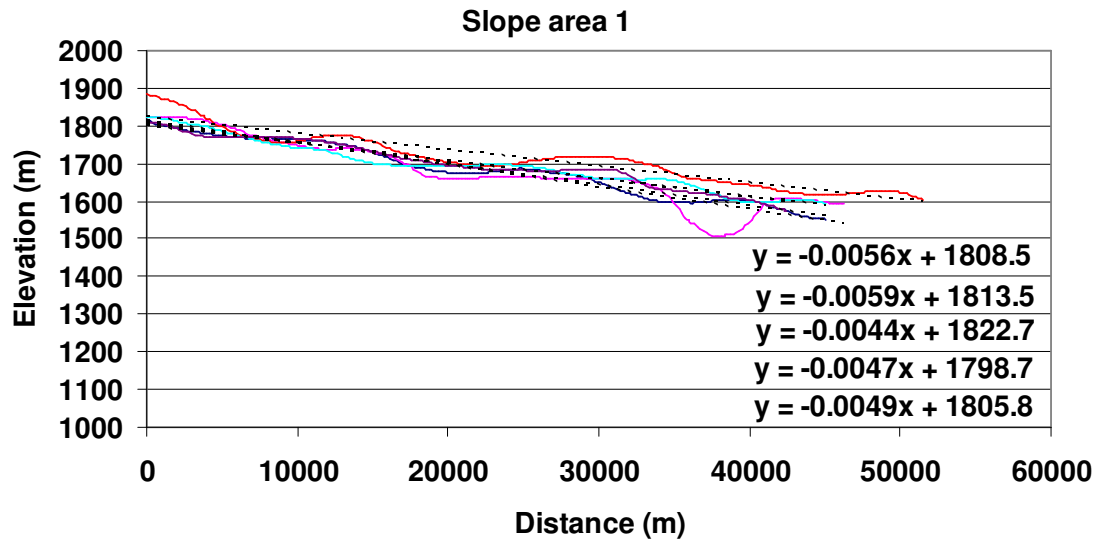


Figure 4.12 Five surface elevation profiles taken along flow lines in area 1. The slope for each is derived by fitting a linear line through the profiles (dashed lines). The function of these lines is given in the figure. The mean of the slopes is used as average surface slope for each respective area.

Area	H [m]	dh/dx	τ_{dx} [kPa]
1	1778 (50)	-0.005 (5×10^{-4})	78.5 (8.2)
2	1285 (50)	-0.006 (5×10^{-4})	68.1 (6.3)
3	1041 (50)	-0.012 (5×10^{-4})	110.3 (7.0)
4	1556 (50)	-0.003 (5×10^{-4})	41.2 (7.0)
5	1038 (50)	-0.009 (5×10^{-4})	82.4 (6.1)

Table 4.3 Values for average ice thickness (H) and surface slope (dh/dx) used to calculate the driving stress τ_{dx} for the five sub-areas. Errors are given in parentheses.

4.7.2 Longitudinal stress gradients

As with the driving stress we calculate resistive stresses for each area separately. Longitudinal stress gradients are calculated using velocity gradients and ice thickness information along a profile in the center of the ice stream. The across flow gradient in the y-component of velocity is calculated based on several transects. To minimize local small scale effects a line is fit through the profile to derive the gradient in velocity U and ice thickness H that are necessary to calculate the longitudinal resistance (figure 4.13). The slopes of the lines are used to calculate the strain rates according to:

$$\frac{\partial u}{\partial x \left(n + \frac{1}{2} \right)} \approx \frac{U_{x(n+1)} - U_{x(n)}}{x_{(n+1)} - x_{(n)}} \quad (4.4)$$

and

$$\frac{\partial H}{\partial x \left(n + \frac{1}{2} \right)} \approx \frac{H_{(n+1)} - H_{(n)}}{x_{(n+1)} - x_{(n)}} \quad (4.5)$$

The longitudinal resistive stress R_{xx} is then calculated from equation 2.28 using a rate factor $B=575 \text{ kPa yr}^{1/3}$ (for ice of -20°C). Finally we estimate the longitudinal stress gradients. The derived values for the longitudinal stress gradients are given in table 4.4. We find the relative role of longitudinal resistance in opposing the driving stress to be small ($<5\%$), but its magnitude can be up to 30% of the lateral drag. The largest uncertainty is associated with the rate factor. We assume that the uncertainty in the rate factor is large $\sim 100 \text{ kPa yr}^{1/3}$. This can influence the calculated value of the resistive stress by as much as 20%.

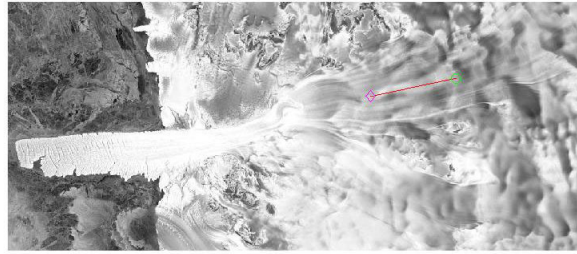
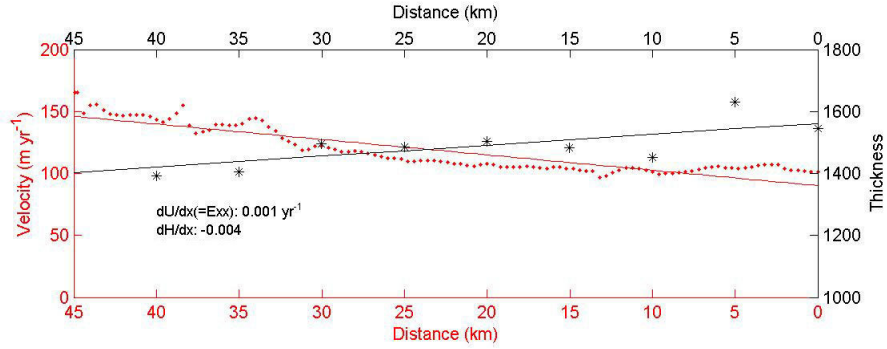


Figure 4.13 Velocity profile (red dots) and ice thickness profile (black asterisks) along the center of the main tributary of David Glacier in area 2. The solid lines show a best linear fit and their slopes are used to calculate gradients in velocity and thickness.

4.7.3 Lateral drag

Resistance from lateral drag is calculated by taking up to 20 across flow velocity profiles for each of the areas under consideration (figure 4.14). The number of profiles is used to filter out the effect of small scale variations in lateral drag. A polynomial is fitted through the values and used to calculate the velocity gradient in the across flow direction and subsequently $\dot{\epsilon}_{xy}$ and R_{xy} . The assumption is made that lateral shear is the dominant strain rate so that:

$$\dot{\epsilon}_{xy} = \dot{\epsilon}_e = \frac{1}{2} \left(\frac{\partial u}{\partial y} \right) \quad (4.6)$$

where u is the discharge velocity and y the transverse distance. The lateral shear stress R_{xy} is then estimated according to:

$$R_{xy} = B \left[\frac{1}{2} \left(\frac{\partial u}{\partial y} \right) \right]^{1/3} \quad (4.7)$$

whereby the rate factor B is taken constant ($575 \text{ kPa yr}^{1/3}$) and the velocity gradient is calculated similarly as in equation 4.4. The average lateral resistance F_s on the section of the glacier is then calculated from:

$$F_s = \frac{H_w \times \max(R_{xy}) - H_{-w} \times \min(R_{xy})}{2W} \quad (4.8)$$

In this equation H_w and H_{-w} is the ice thickness at the respective margins and W is the half width of the glacier. The calculated values for lateral drag are given in table 4.4. Lateral drag accounts for roughly 10% of the driving stress for most of the areas. Its relative role in area 4 is higher (~30%) possibly associated with the presence of a subglacial valleywall, which is revealed by BEDMAP topography.

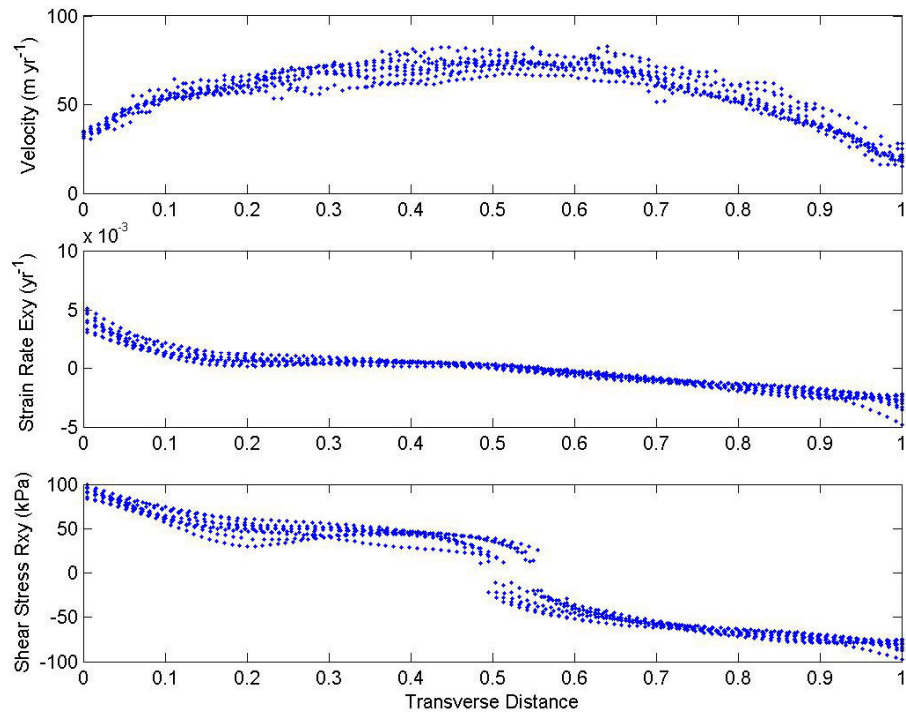


Figure 4.14 Several across flow profiles of velocity, strain rate and shear stress used to calculate lateral drag in area 1. The top figure shows the location of the profiles.

4.7.4 Basal Drag

Basal drag cannot be estimated directly and must be inferred from knowledge of the driving stress, longitudinal resistance and lateral drag. It is here assumed that the driving stress is balanced by all resistive stresses and therefore basal drag is the residual necessary to balance the force balance equation. Table 4.4 gives the calculated values for basal drag for each of the sub areas. We find that basal drag is the most important factor in opposing the driving stress for all areas under consideration. The large relative contribution of basal drag clearly distinguishes the tributaries of David Glacier from the ice streams in West Antarctica, where resistance to flow mostly stems from lateral drag and basal drag is believed to be very small (Whillans and Van der Veen, 1997).

Area	Driving Stress [kPa]	Long. Stress Gradients [kPa]	Lateral Drag [kPa]	Basal Drag [kPa]
1	78.5 (8.2)	1.7 (0.8)	7.9 (0.7)	68.9 (8.3) ~88%
2	68.1 (6.3)	0.5 (0.7)	5.8 (0.6)	61.8 (6.4) ~91%
3	110.3 (7.0)	3.1 (0.9)	7.4 (1.2)	99.8 (7.2) ~90%
4	41.2 (7.0)	1.7 (1.2)	12.9 (1.2)	26.6 (7.2) ~65%
5	82.4 (6.1)	0.7 (0.6)	9.8 (1.4)	71.9 (6.3) ~87%

Table 4.4 Calculated values for driving stress, longitudinal stress gradients, lateral drag and basal drag (errors are given in parentheses). The relative contribution of basal drag in opposing the driving stress is also given.

Reported errors in table 4.4 (given in parentheses) are calculated based on the error analysis described in chapter 2. For example the error in the driving stress of area 1 is calculated from equation 2.3 and 2.4:

$$\sigma_{\alpha} = \sqrt{2} \left(\frac{\sigma_h}{\delta x} \right) = \sqrt{2} \left(\frac{15 \text{ m}}{40 \text{ km}} \right) \approx 0.0005 \quad (4.9)$$

$$\begin{aligned} \sigma_{\tau_{dx}} &= \left[(-\rho g \alpha \sigma_H)^2 + (-\rho g H \sigma_{\alpha})^2 \right]^{\frac{1}{2}} = \\ &= \left[(-\rho g \times -0.005 \times 50 \text{ m})^2 + (-\rho g \times 1778 \text{ m} \times 0.0005)^2 \right]^{\frac{1}{2}} \approx 8.2 \text{ kPa} \end{aligned} \quad (4.10)$$

Here, 40 km is the length over which the surface slope is calculated, 15 m is the error in surface elevation (discussed in chapter 3.7.1) and 50 m is the error in ice thickness (see figure 3.15). The error in longitudinal stress is calculated from equation 2.51:

$$\sigma_{R_{xx}} = \left[\left(\frac{\partial R_{xx}}{\partial \dot{\epsilon}_{xx}} \sigma_{\dot{\epsilon}_{xx}} \right)^2 + \left(\frac{\partial R_{xx}}{\partial \dot{\epsilon}_{yy}} \sigma_{\dot{\epsilon}_{yy}} \right)^2 + \left(\frac{\partial R_{xx}}{\partial B} \sigma_B \right)^2 \right]^{\frac{1}{2}} \quad (4.11)$$

Using equation 2.50 and 2.52 the first term of this equation becomes:

$$\begin{aligned}
\frac{\partial R_{xx}}{\partial \dot{\epsilon}_{xx}} \sigma_{\dot{\epsilon}_{xx}} &= \left[2B\dot{\epsilon}_e^{-2/3} - \frac{4}{3} B\dot{\epsilon}_{xx}\dot{\epsilon}_e^{-1/3} \left(\frac{\partial \dot{\epsilon}_e}{\partial \dot{\epsilon}_{xx}} \right) - \frac{2}{3} B\dot{\epsilon}_{yy}\dot{\epsilon}_e^{-1/3} \left(\frac{\partial \dot{\epsilon}_e}{\partial \dot{\epsilon}_{xx}} \right) \right] \times \sigma_{\dot{\epsilon}_{xx}} \\
&= [2 \times 575 \text{ kPa a}^{1/3} \times (0.001 \text{ a}^{-1})^{-2/3} - \frac{4}{3} \times 575 \text{ kPa a}^{1/3} \times \\
&\quad 0.0008 \text{ a}^{-1} \times (0.001 \text{ a}^{-1})^{-1/3} \times 0.945 - \frac{2}{3} \times 575 \text{ kPa a}^{1/3} \times \\
&\quad 0.0004 \text{ a}^{-1} \times (0.001 \text{ a}^{-1})^{-1/3} \times 0.945] \times 0.0001 \text{ a}^{-1} \approx 11.1 \text{ kPa}
\end{aligned} \tag{4.12}$$

Using equation 2.50 and 2.53 the second term of equation 4.11 becomes ~5.5 kPa and using equation 2.54 the third term in equation 4.11 becomes:

$$\begin{aligned}
\frac{\partial R_{xx}}{\partial B} \sigma_B &= \dot{\epsilon}_e^{-2/3} (2\dot{\epsilon}_{xx} + \dot{\epsilon}_{yy}) \sigma_B = (0.0011 \text{ a}^{-1})^{-2/3} \times \\
&\quad (2 \times 0.0008 \text{ a}^{-1} + 0.0004 \text{ a}^{-1}) \times 100 \text{ kPa a}^{1/3} \approx 19.3 \text{ kPa}
\end{aligned} \tag{4.13}$$

From these values the standard error in longitudinal stress becomes ~22.9 kPa. This value is then used in equation 2.56 to calculate the error in the longitudinal stress gradient (~0.8 kPa). The error in lateral shear stress is calculated using equation 2.49:

$$\begin{aligned}
\sigma_{R_{xy}} &= \left[\left(\frac{1}{3} B\dot{\epsilon}_{xy}^{-2/3} \sigma_{\dot{\epsilon}_{xy}} \right)^2 + \left(\dot{\epsilon}_{xy}^{1/3} \sigma_B \right)^2 \right]^{1/2} = \\
&\quad \left[\left(\frac{1}{3} \times 575 \text{ kPa a}^{1/3} \times (0.003 \text{ a}^{-1})^{-2/3} \times 0.0005 \text{ a}^{-1} \right)^2 + \left((0.003 \text{ a}^{-1})^{1/3} \times 100 \text{ kPa a}^{1/3} \right)^2 \right]^{1/2} \approx 15 \text{ kPa}
\end{aligned} \tag{4.14}$$

This is used to calculate the error in lateral drag according to:

$$\sigma_{F_s} = \left[\left(\frac{R_{xy}}{2W} \sigma_H \right)^2 + \left(\frac{H_w}{2W} \sigma_{R_{xy}} \right)^2 \right]^{\frac{1}{2}} =$$

$$\left[\left(\frac{110 \text{ kPa}}{37 \text{ km}} \times 50 \text{ m} \right)^2 + \left(\frac{1778 \text{ m}}{37 \text{ km}} \times 15 \text{ kPa} \right)^2 \right]^{\frac{1}{2}} \approx 0.7 \text{ kPa} \quad (4.15)$$

Finally the error in basal drag is calculated from the error estimates above, according to:

$$\sigma_{\tau_{bx}} = \left[(\sigma_{\tau_{dx}})^2 + (\sigma_{R_L})^2 + (\sigma_{F_s})^2 \right]^{\frac{1}{2}} =$$

$$\left[(8.2 \text{ kPa})^2 + (0.8 \text{ kPa})^2 + (0.7 \text{ kPa})^2 \right]^{\frac{1}{2}} \approx 8.3 \text{ kPa} \quad (4.16)$$

4.8 Floating part

Downstream of David Cauldron, David Glacier starts to float and becomes an ice tongue. This ice tongue is bordered by valley walls along the first 50 km. Figure 4.15 shows a plot with locations of some of the gates used for flux calculations (see chapter 4.5) and referred to in this section. Also shown in the figure are ICESat ground tracks that we use to estimate ice thickness along this section.

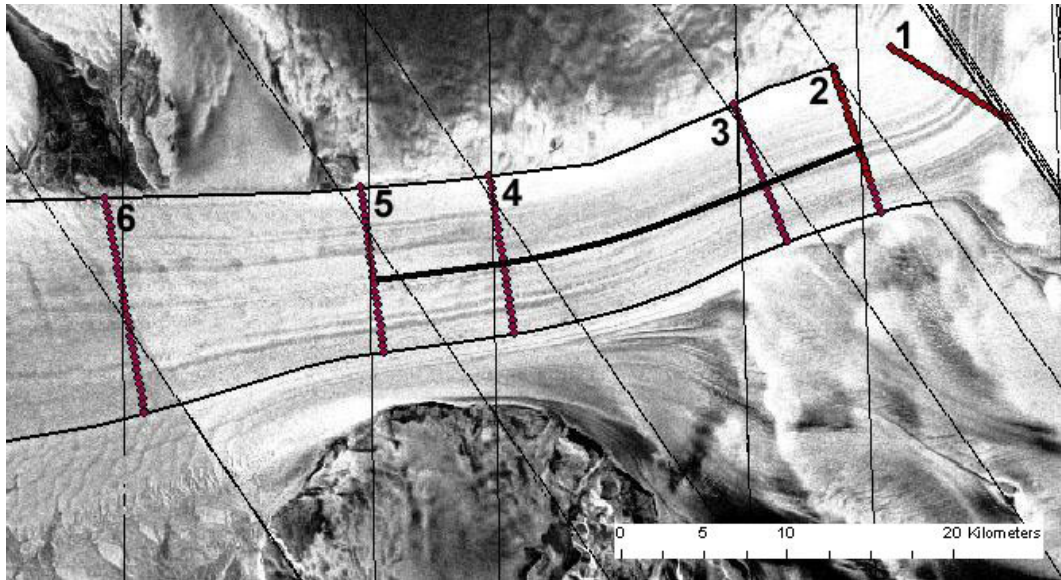
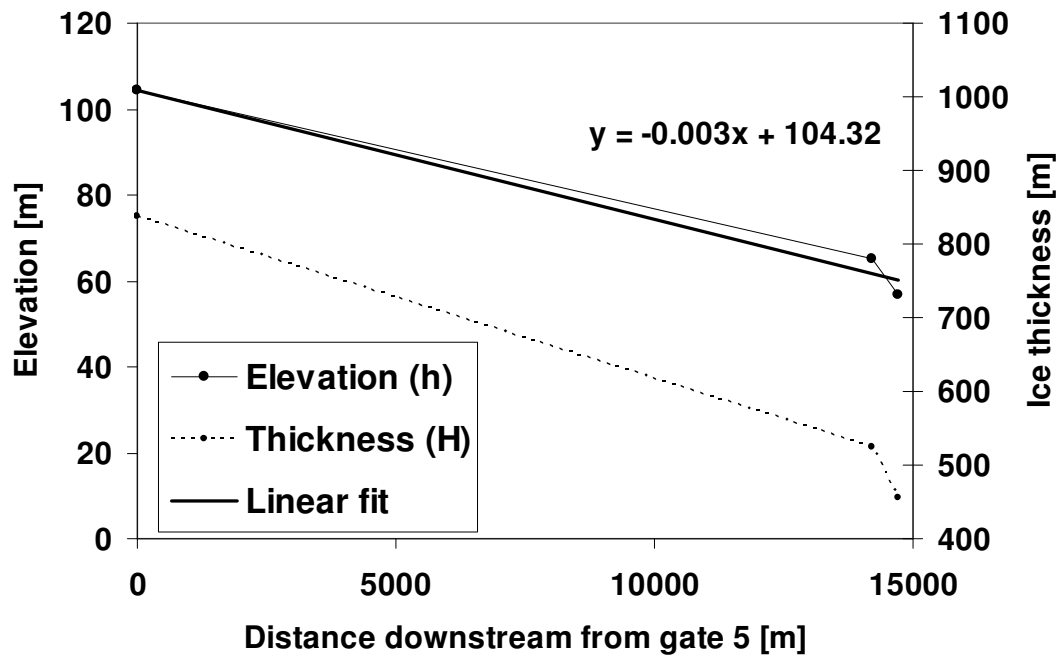
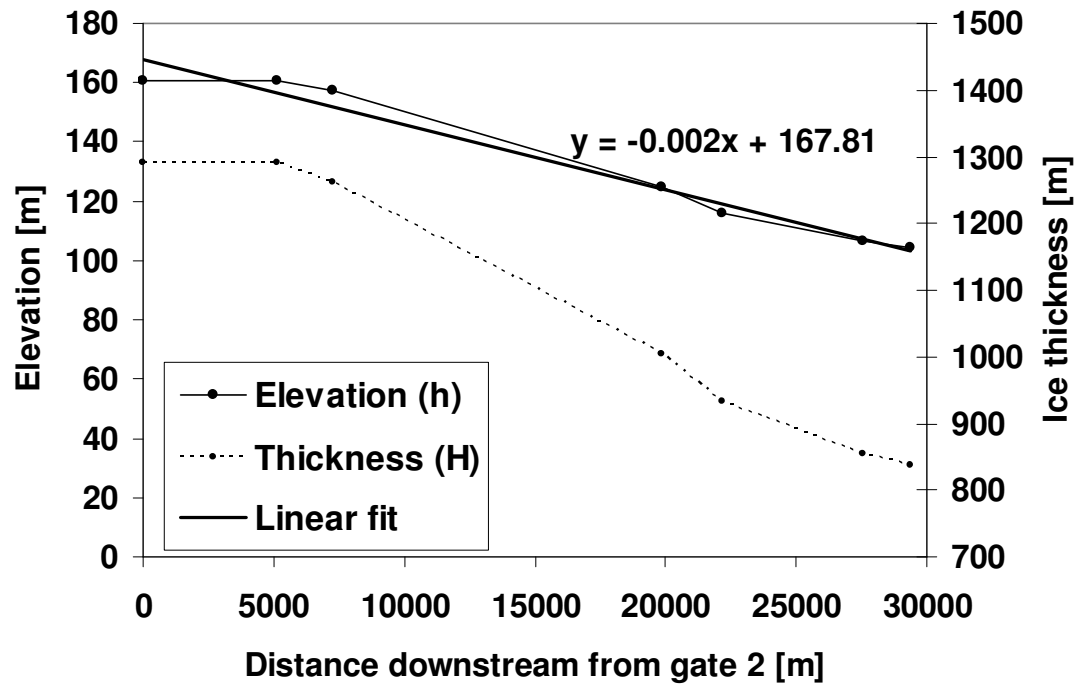


Figure 4.15 Location plot with fluxgates (red), ICESat ground tracks (thin dotted lines) and profile (thick line) used for calculations, the margins of the stream used for fluxgate calculations (see chapter 4.5) are also clarified (thin lines). This part of the glacier is floating and bounded by a fjord. Therefore a combination of both lateral drag and longitudinal stress gradients is expected between gate 2 and gate 6, and no basal drag.

4.8.1 Driving stress

To estimate the driving stress we need to find the surface slope and ice thickness. The surface slope for this section of the glacier is calculated based upon a linear fit through ICESat elevation data, along the same flow line that we use for calculating the velocity gradient. For a floating glacier the ice thickness H is related to the surface elevation h through the floatation criterion (see equation 4.1). Figure 4.16 shows the elevation data used to calculate the surface gradient (linear fit) and ice thickness (see figure 4.15 for location). The surface slope for the area between gate 2 and 5 is approximately -2.0×10^{-3} . Between gate 5 and 6 the surface slope is slightly higher at about -3.0×10^{-3} indicating that the ice becomes quickly thinner there where it leaves the fjord. We use an ice density $\rho_i = 900 \text{ kg m}^{-3}$ and $g = 9.81 \text{ m s}^{-2}$. We find that the driving stress decreases from about $23 \pm 4 \text{ kPa}$ to about $15 \pm 4 \text{ kPa}$ between gates 2 and 5 as ice thickness decreases downstream (figure 4.17). As the surface slope becomes steeper between gates 5 and 6 we actually find the driving stress to go up slightly before decreasing again.

Figure 4.16 Elevation data (h) between gate 2 and 5 (a) and between gate 5 and 6 (b) (see figure 4.15 for location) which is used to derive ice thickness (H) and surface slope as a function of distance. The dots represent points where IceSAT data crosses the profile (see figure 4.15). The equation of a line fitted through the elevation data and used to estimate the average surface slope is given in the figure.



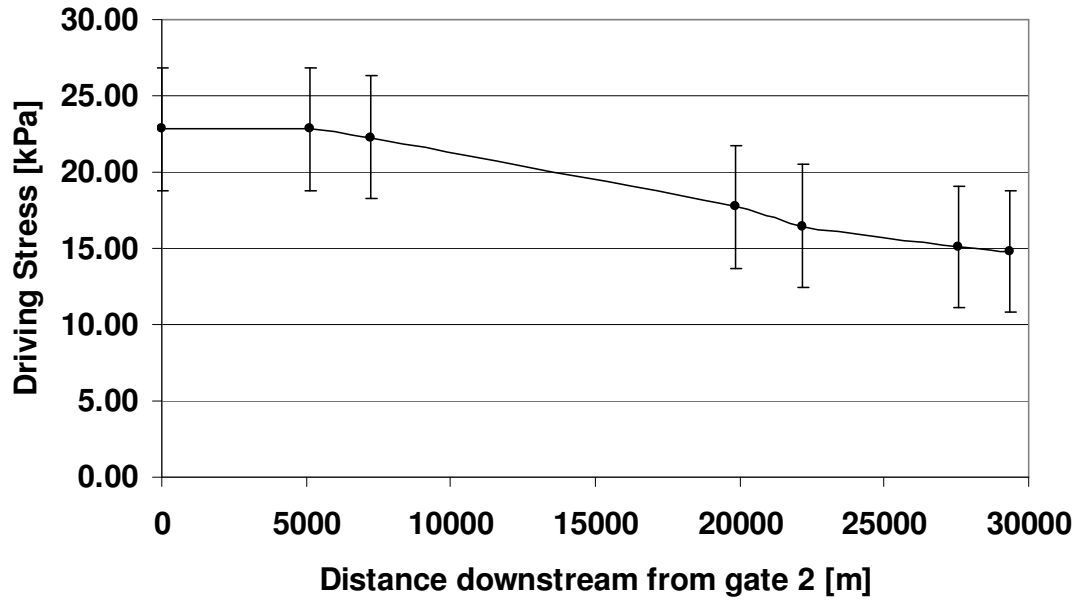


Figure 4.17 Driving stress between gates 2 and 5 calculated from elevation and derived ice thickness given in figure 4.16.

4.8.2 Longitudinal stress gradients

To calculate the longitudinal stress gradient we need estimates for $\dot{\epsilon}_{xx}$ and $\dot{\epsilon}_{yy}$, which can be derived from the velocity field. The strain rate in the x direction is estimated by fitting a line through a velocity profile along a flow line and measuring the gradient (see figure 4.18). Between gates 2 and 5 we find a reasonable constant strain rate, although small-scale variations exist:

$$\dot{\epsilon}_{xx} = \frac{\partial u}{\partial x} \approx 0.002 \quad (4.17)$$

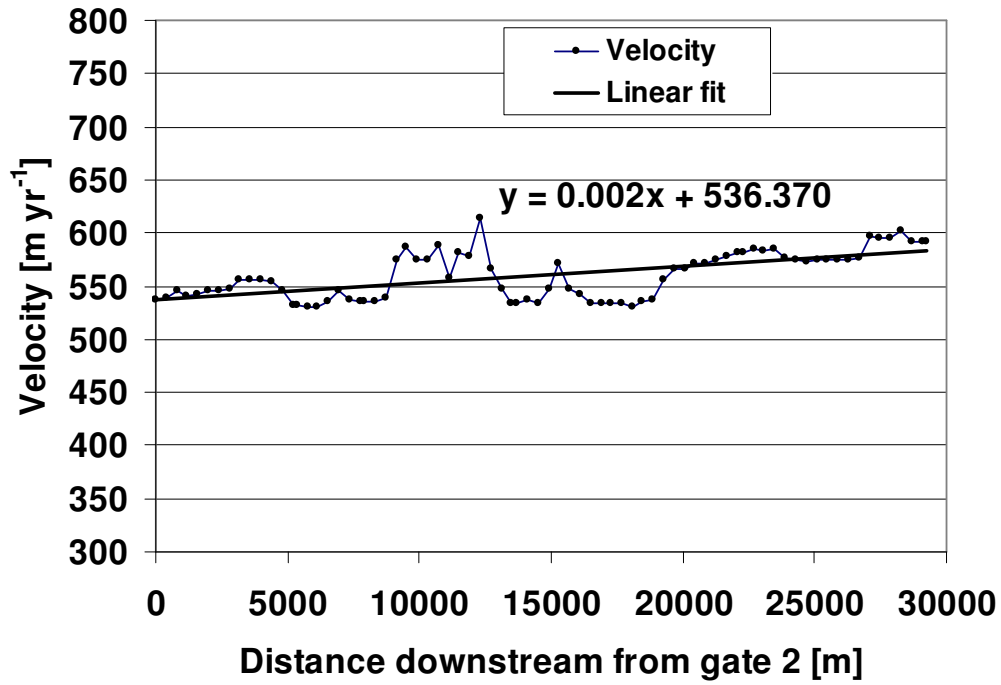


Figure 4.18 Velocity along a flow line between gate 2 and 5 as a function of distance (see figure 4.15 for location). The linear fit is used to estimate $\dot{\epsilon}_{xx}$ in the direction of flow.

We estimate $\dot{\epsilon}_{yy}$ from the gradient in the y component of velocity in the across flow direction. Figure 4.19 shows a profile of the y-component of velocity in the across flow direction taken between gates 3 and 4. By fitting a line through the profile we find:

$$\dot{\epsilon}_{yy} = \frac{\partial v}{\partial y} \approx 0.003 \quad (4.18)$$

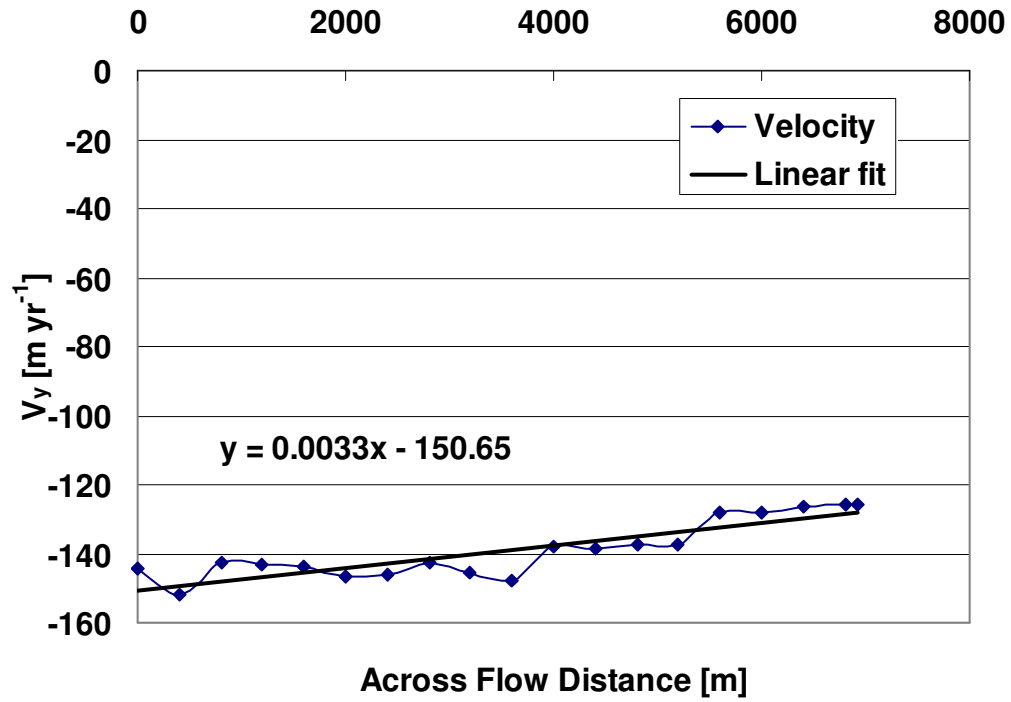


Figure 4.19 Y-component of velocity as a function of across flow distance. The linear fit is used to estimate the strain rate $\dot{\epsilon}_{yy}$.

As outlined in chapter 2 we can also estimate the rate of lateral spreading based upon geometry of the valley walls. We find that the rate of spreading fairly constant between gates 2 and 5:

$$\dot{\epsilon}_{yy} = \frac{u}{W} \frac{\partial W}{\partial x} \approx \frac{0.550}{8.730} \times \frac{0.780}{29.000} \approx 0.002 \quad (4.19)$$

This value is close to the value calculated from the velocity gradient. The longitudinal resistance along the center line R_{xx} is estimated from equation 2.32.

$$R_{xx} = B \left[\left\{ \left(\frac{\partial u}{\partial x} \right)^2 + \left(\frac{\partial v}{\partial y} \right)^2 + \left(\frac{\partial u}{\partial x} \frac{\partial v}{\partial y} \right) \right\}^{1/2} \right]^{-2/3} \left(2 \frac{\partial u}{\partial x} + \frac{\partial v}{\partial y} \right) \quad (4.20)$$

Using a value of $500 \text{ kPa yr}^{1/3}$ for B , which is the value for ice with a temperature of -17°C we find $R_{xx} = 131.0 \pm 27 \text{ kPa}$. The value for the chosen rate factor is based upon the temperature at 10 m depth of a bore hole drilled in the tip of Drygalski Ice Tongue (Caprioli and others, 1998). The measured temperature was about -20°C , therefore the depth averaged value should be somewhat less since the temperature at the base of the ice tongue is near zero. We assume the value for B is accurate to within $100 \text{ kPa yr}^{1/3}$.

Applying a similar approach to the region between gate 5 and gate 6 we find the strain rate in both x and y direction increasing. As the valley becomes wider the ice can spread more freely leading to a 7 fold increase in $\dot{\epsilon}_{yy}$ when calculated based on the geometry of the valley walls:

$$\dot{\epsilon}_{yy} = \frac{u}{W} \frac{\partial W}{\partial x} \approx \frac{0.625}{9.51} \times \frac{2.98}{14.350} \approx 0.014 \quad (4.21)$$

Estimating $\dot{\epsilon}_{yy}$ from the gradient in the y-component of velocity in the across flow direction we find a similar value (figure 4.20). By taking the slope of a line fitted through the profile we find:

$$\dot{\epsilon}_{yy} = \frac{\partial v}{\partial y} \approx 0.015 \quad (4.22)$$

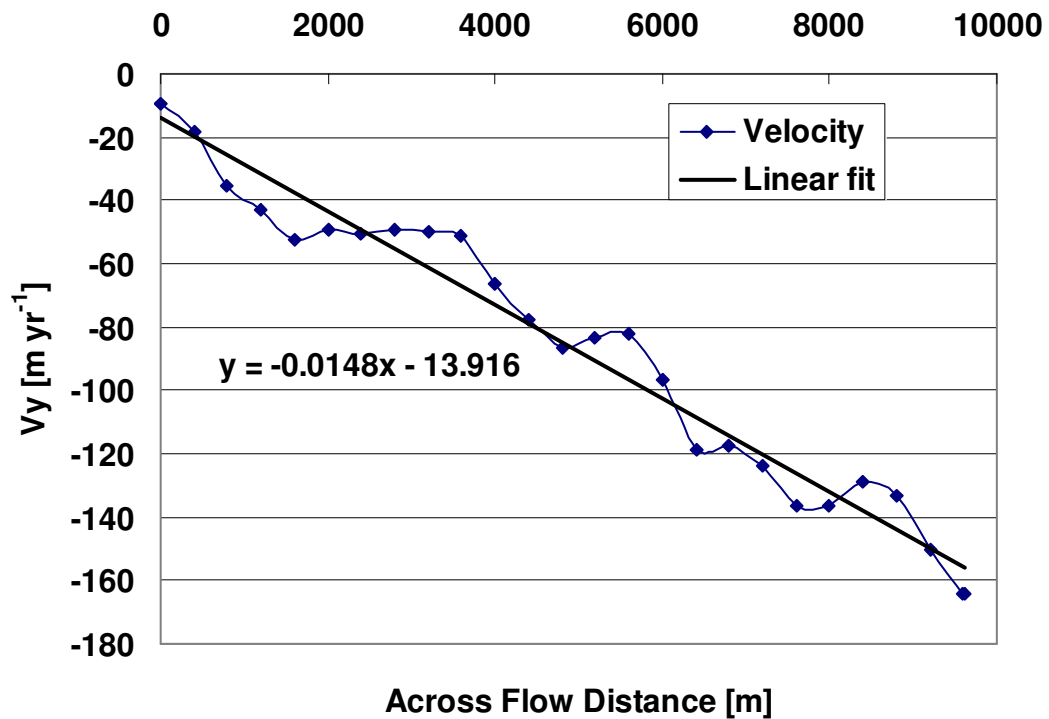


Figure 4.20 Profile of V_y taken across flow between gate 5 and 6 as a function of across flow distance. The linear fit is used to estimate $\dot{\epsilon}_{yy}$.

Based upon the gradient of a line fitted through a velocity profile (figure 4.21) we find more than a doubling of the longitudinal strain rate between gates 5 and 6.

$$\dot{\epsilon}_{xx} = \frac{\partial u}{\partial x} \approx 0.005 \quad (4.23)$$

We find the rate of transverse spreading in this section to be about 3 times higher than in the x direction. Calculating the longitudinal resistance between gates 5 and 6 we find $R_{xx} = 181.4 \pm 36 \text{ kPa}$. Based on the calculated longitudinal stress gradients, we find the longitudinal resistance between gates 2 and 5 to be approximately $2.1 \pm 0.8 \text{ kPa}$ or roughly 10% of the driving stress and between gates 5 and 6 this doubles to about $4.4 \pm 1.1 \text{ kPa}$ or about 30% of the driving stress.

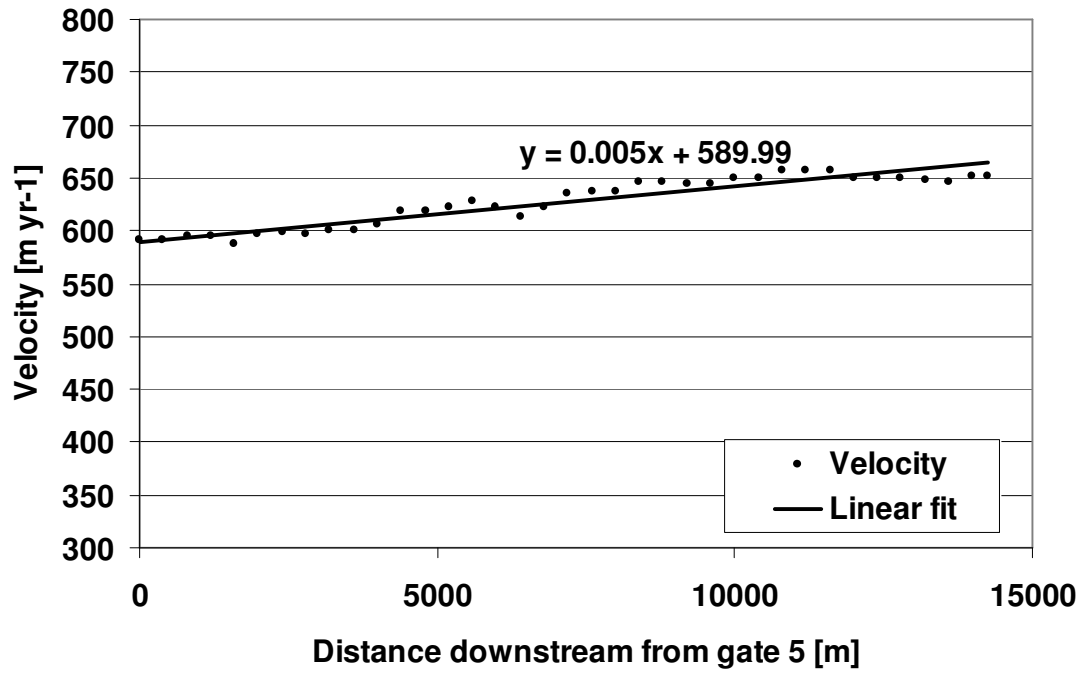


Figure 4.21 Velocity along a flowline between gate 5 and 6 (see figure 4.15) as a function of distance. The linear fit is used to estimate the longitudinal strain rate ($\dot{\epsilon}_{xx}$).

4.8.3 Lateral Drag

As in the previous section we calculate lateral drag by taking several across flow velocity profiles (figure 4.22). These profiles are used to calculate $\dot{\epsilon}_{xy}$, R_{xy} and lateral drag averaged over the width of the ice stream. Based on the profile in figure 4.22 we find lateral drag averaged over the width of the ice stream near gate 4 to be:

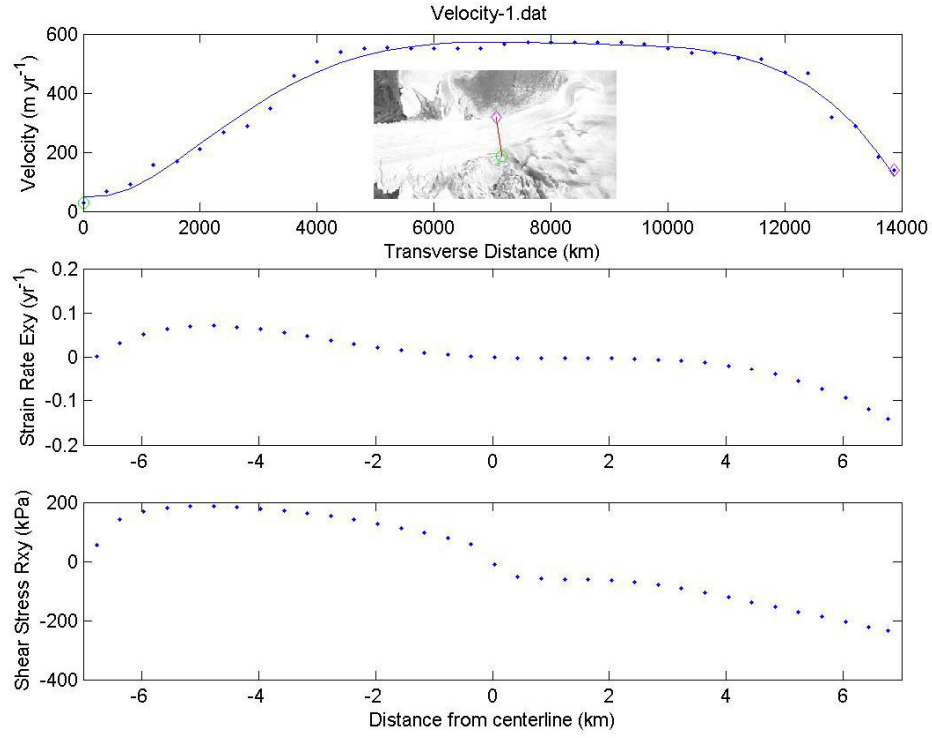


Figure 4.22 Across flow velocity profile (top; blue line gives best fit) used to calculate shear strain rate (middle) and shear stress (bottom) along a section of Drygalski Ice Tongue bounded by valley walls. Inset shows location of profile.

$$F_s = \frac{H_w \times \max(R_{xy}) - H_{-w} \times \min(R_{xy})}{2W} \approx 20.3 \pm 3 \text{ kPa} \quad (4.24)$$

This calculated value is somewhat larger than the estimated driving stress, which is 17.7 ± 4 kPa, but falls within our uncertainty levels. Despite the uncertainties in lateral drag the calculation shows that resistance to flow mostly stems from lateral drag along the fjord walls.

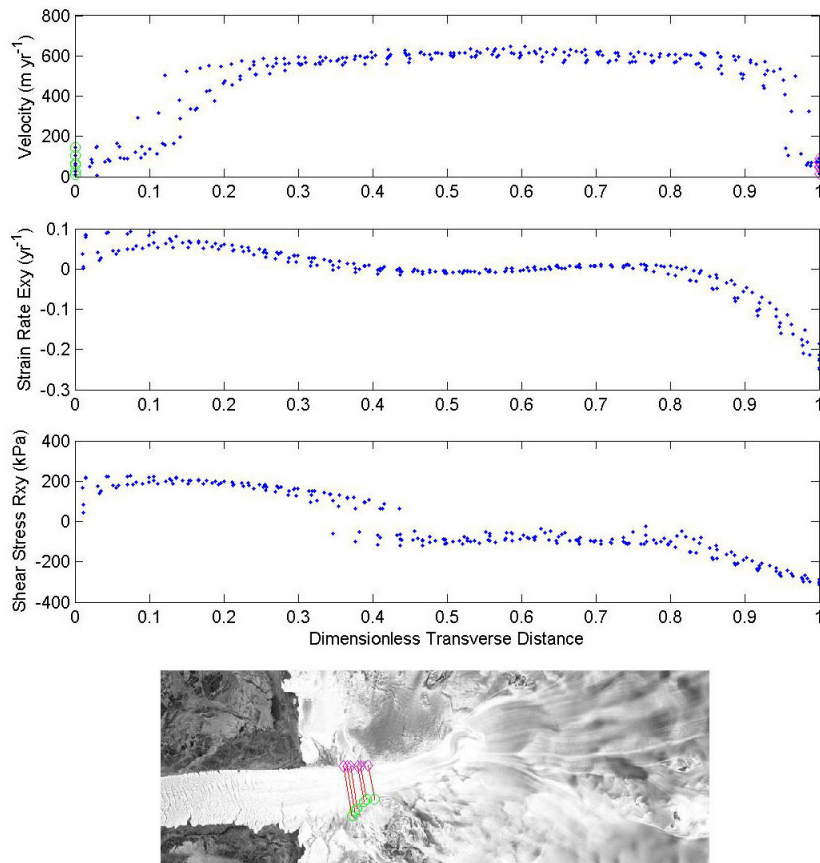


Figure 4.23 Measured velocity, strain rate and shear stress across several profiles between gates 5 and 6.

Figure 4.23 shows a number of profiles taken between gates 5 and 6. We find high shear strain rates varying between 0.084 yr^{-1} and -0.245 yr^{-1} . Using these values R_{xy} varies roughly between 225 kPa and -315 kPa for $B=500$. We find a value of about 25 kPa for the width averaged lateral drag at gate 5, about 98% of the driving stress.

We find a value of about 11.4 kPa for the width averaged lateral drag at gate 6, which is about 80% of the driving stress. When using $B=450 \text{ kPa yr}^{1/3}$ (for ice of -15°C) this reduces to about 63%.

Using a different approach (see chapter 2) we can also estimate the fraction of the driving stress that is supported by lateral drag (ψ) by assuming that the driving stress is balanced by longitudinal stress gradients and lateral drag, using only estimates of the first two and the thickness gradient.

$$\psi = 1 + \frac{R_{xx}}{\tau_{dx}} \frac{\partial H}{\partial x} \quad (4.25)$$

The ice thickness gradient is related to the surface slope according to:

$$\frac{\partial H}{\partial x} = \frac{\frac{\partial h}{\partial x}}{\left(1 - \frac{\rho_i}{\rho_w}\right)} \quad (4.26)$$

We find a value of -0.016 for the thickness gradient between gates 2 and 5 and -0.024 between gates 5 and 6. Values of ψ versus distance along the profile are given in figure 4.24. The high values of ψ show that lateral drag is very important; however, it declines from about 0.89 to 0.83 over a distance of approximately 30 km between gates 2 and 5, indicating a decreasing role of lateral drag in opposing driving stress. Between gates 5

and 6 we find ψ going down quickly reaching a value of 0.59 at gate 6. These values roughly agree with those derived from strain rates using $B=450 \text{ kPa yr}^{1/3}$. We find that as the glacier nears the head of the widening fjord lateral drag becomes less important.

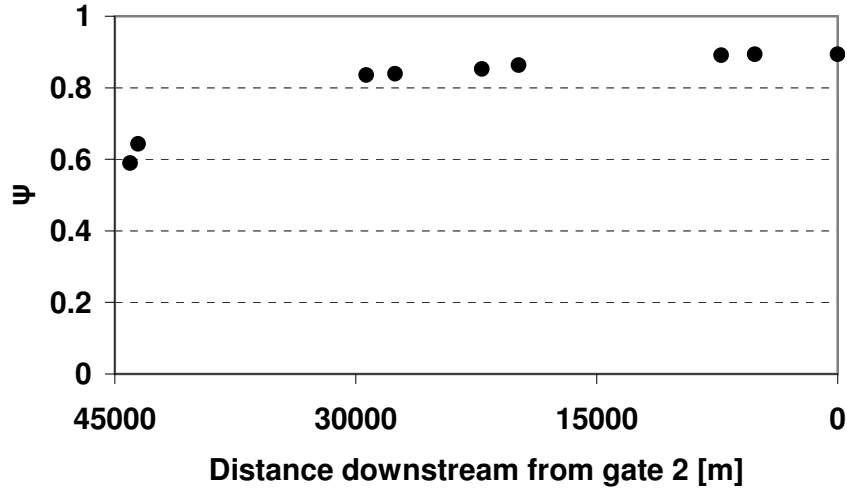


Figure 4.24 Values of ψ as a function of distance between gate 2 and 6. The declining relative role of shear stress in opposing the driving stress is clear from this graph.

4.9 Free floating section

Where the ice leaves the fjord ice thickness decreases significantly. Figure 4.25 shows velocity, surface elevation, thickness and surface gradient along the part of Drygalski Ice Tongue sticking out in the sea. The surface elevation, thickness and surface gradient are derived from ICESat data using a constant ice density of 900 kg m^{-3} . Since the ICESat data does not cover the entire region evenly we fit a polynomial through the

available data points on the profile. We calculate strain rates and longitudinal resistance and driving stress (figure 4.26). We assume that the ice can spread freely and that the strain rate in the x and y direction have a similar magnitude along the entire length of the profile. The driving stress is calculated according to:

$$\tau_{dx} = -\rho g H \frac{\partial h}{\partial x} \quad (4.27)$$

From force balance in the absence of lateral drag it follows that:

$$-\rho g H \frac{\partial h}{\partial x} = \frac{\partial}{\partial x}(H R_{xx}) + \Delta \quad (4.28)$$

where Δ is an error term associated with an incorrect ice thickness, surface gradient or rate factor or a force imbalance not accounted for in the model. Both sides of the equation can be calculated from the available data.

The lower panel in figure 4.26 shows the driving stress calculated according both ways. We find that the two do not match along the first section of the profile but after the ice leaves the fjord differences fall within the error limit.

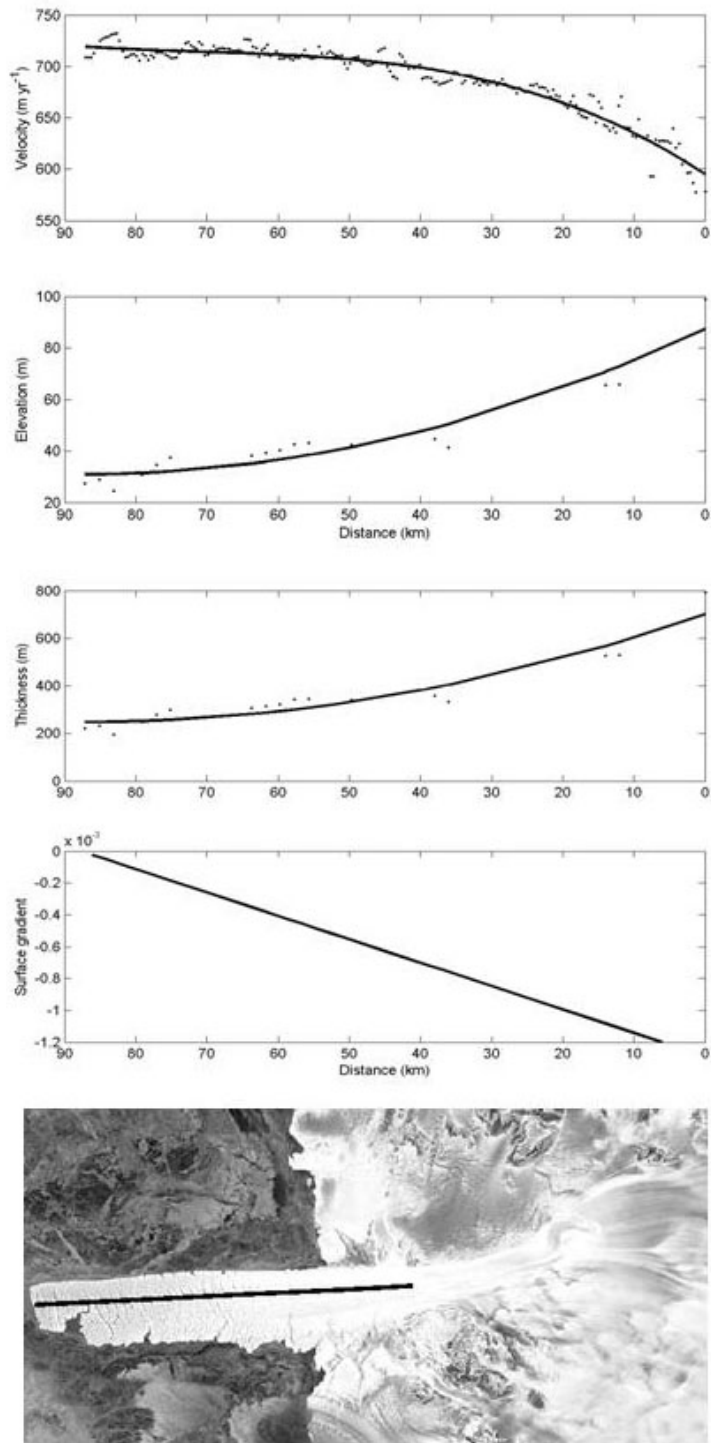


Figure 4.25 Velocity, elevation, ice thickness and surface gradient along a profile on Drygalski Ice Tongue. The dots represent data points; the lines are fitted and used in the calculations to avoid small scale variations.

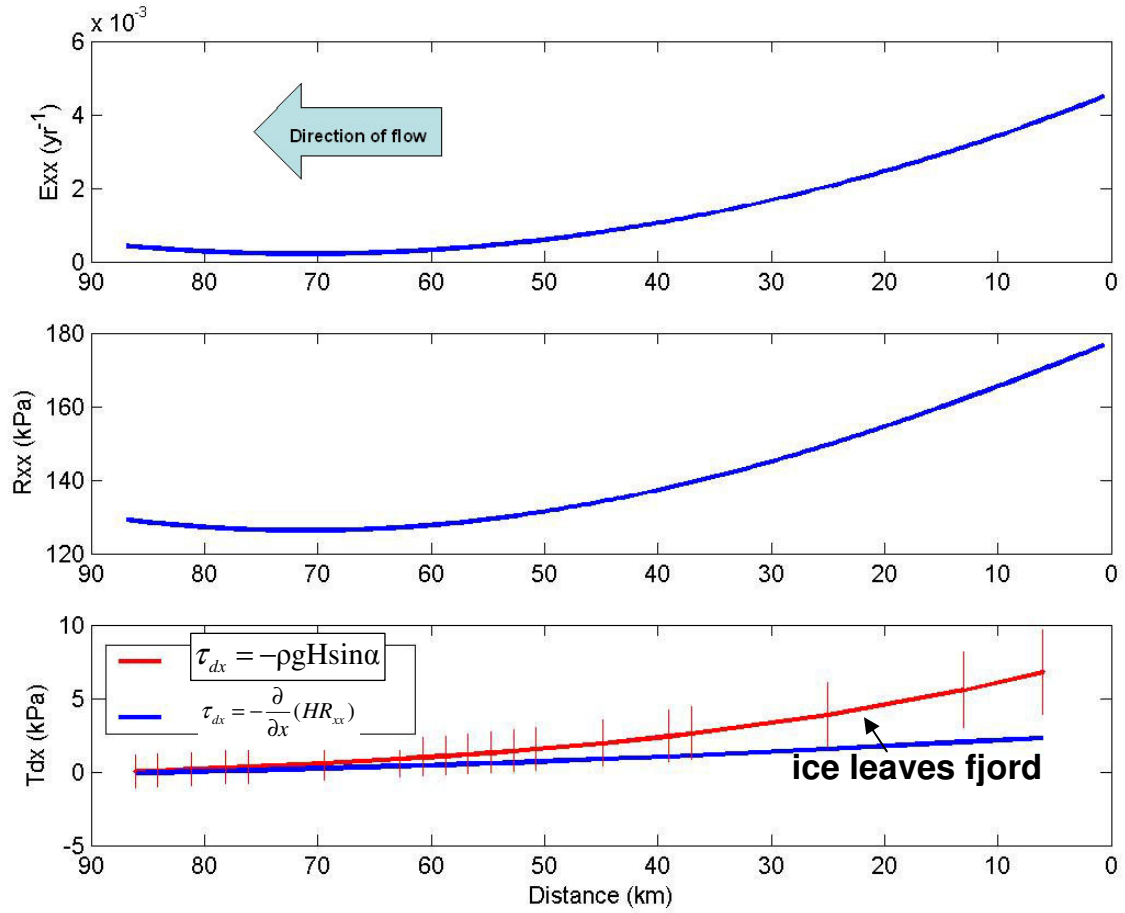


Figure 4.26 Values of longitudinal strain rate (top), longitudinal stress (middle) and driving stress (bottom) versus distance along the free floating section of Drygalski Ice Tongue. The driving stress is calculated based on geometry (red) and from strain rates (blue) by assuming longitudinal stress gradients provide the sole resistance to flow. The difference along the first section could indicate additional lateral drag from sub-surface valley walls or the adjacent Nansen Ice Shelf.

4.10 Equilibrium profile

The previous analysis justifies the use of two different models when calculating the equilibrium profile of the ice tongue. One section controlled by lateral drag and one section controlled by longitudinal resistive forces. For the free-floating steady state

profile we use the following equation (the derivation of these functions is discussed in Van der Veen, 1999, pp. 162-170):

$$H = \left(\frac{U_0^{(n+1)} \left(1 - \frac{C}{M} H_0^{(n+1)} \right)}{(H_0 U_0 + Mx)^{(n+1)}} + \frac{C}{M} \right)^{-1/(n+1)} \quad (4.29)$$

For the steady state profile of a glacier controlled by side drag we use:

$$\left(\frac{H}{H_0} \right)^{(1+1/n)} = 1 - \frac{U_0^{(1+1/n)}}{MA_0^{(1/n)}} \left(\left(\frac{Mx}{H_0 U_0} + 1 \right)^{(1+1/n)} - 1 \right) \quad (4.30)$$

In these equations H_0 and U_0 are the thickness and velocity at the start of the profile. M is the net accumulation. To calculate the basal melt rates we used a fluxgate approach along the entire ice tongue (described in chapter 4.5). C is a constant given by:

$$C = \left(\frac{\rho_i g}{4B} \left(1 - \frac{\rho_i}{\rho_w} \right) \right)^3 \quad (4.31)$$

and A_0 is given by:

$$A_0 = \frac{2}{n+2} \frac{W^{n+1}}{B^n} (\rho_i g)^n \quad (4.32)$$

Where W is the width of the ice stream, B is the rate factor and ρ_i and ρ_w the density of ice and water. Figure 4.27 shows the derived profiles for the two cases as well as the thickness profile of the ice tongue from ICESat elevation measurements. The modeled profile fits the measured profile very well.

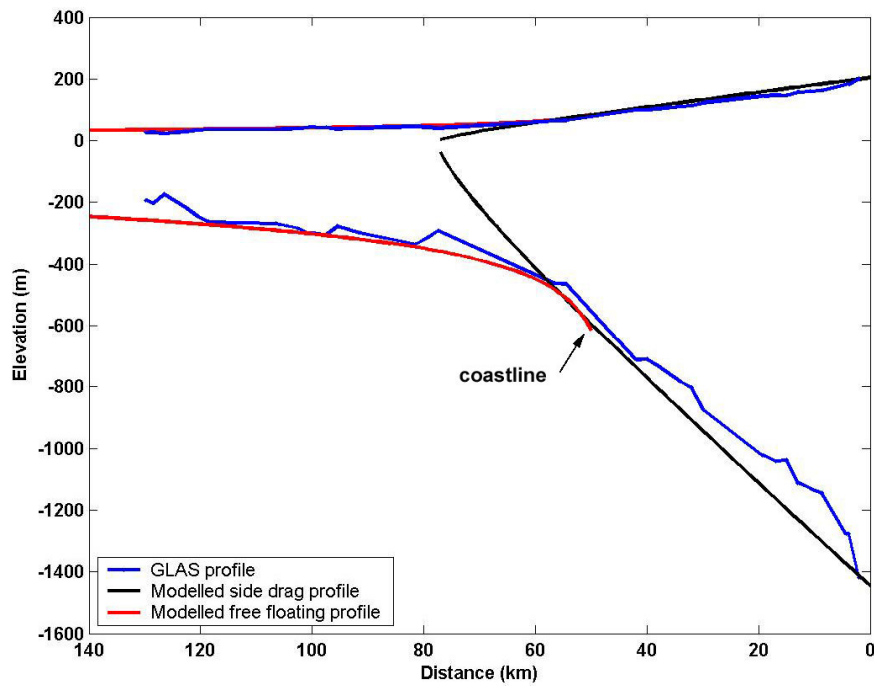


Figure 4.27 Comparison between modeled profiles and profile derived from ICESat data (blue). The black line is the profile of an ice shelf controlled by side drag. The red line is a profile if the ice shelf were to float freely. Drygalski Ice Tongue behaves like the first when still in the fjord and like the latter after leaving it. The good agreement indicates steady flow.

4.11 Summary and conclusions

We measured surface velocity over large portions of the Drygalski Ice Tongue and David Glacier from combinations of feature tracking, interferometric speckle tracking and phase interferometry using RADARSAT images acquired during the AMM-1 and MAMM missions. In this way, average velocities are computable over periods of years to tens of days (potentially as short as 3 days using orbit sub-cycle overlaps). We compared short term velocity derived from feature tracking and interferometry with 3-year averaged velocity and literature. Unlike for example the West Antarctic Ice Streams (Stearns, 2005), Thwaites Glacier Ice Tongue (Rosanova and others, 1998) and Jakobshavn Isbræ (Thomas and others, 2003), our data suggests that the David Glacier velocity field has remained relatively constant from about 1991 – 2000 and, based on earlier front positions and measurements, likely much longer.

We find that derived velocities, in combination with the use of derived ice thickness data from ICESat and accumulation data, are suitable to examine the distribution of bottom melt rates. Based upon our fluxgate calculations we find the pattern of calculated melt rates to be consistent with the so-called ‘ice pump’ mechanism.

Drygalski Ice Tongue advanced seaward about 2.2 km over the period of RAMP observations, and might currently approach its critical length. By comparing the velocity at the ice front with the advance rate of the front margin we have shown that small calving events are of minor importance for ice discharge. This is surprising considering the severely segmented surface of the glacier. Instead, we propose that larger calving events control the length of the tongue, possibly precipitated by the occasional collision of large icebergs with the ice tongue as occurred when iceberg B15 recently approached

the tongue. We suspect that the likelihood of a larger event and the opportunity for collision with other icebergs will increase as the ice tongue lengthens seaward towards its previous maximum position.

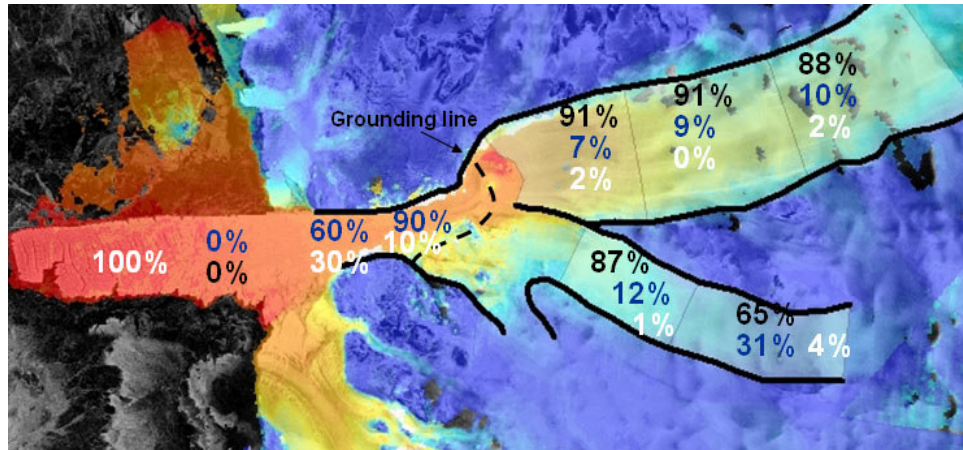


Figure 4.28 Relative contribution of basal drag (black), lateral drag (blue) and longitudinal stress gradients (white) in opposing the driving stress for the David Glacier-Drygalski Ice Tongue System. Based on data shown in table 4.4.

Figure 4.28 is a summary figure of the stress partitioning along the David Glacier-Drygalski Ice Tongue drainage basin. By utilizing several datasets and force-budget theory we find that above the grounding line David Glacier has two main tributaries that are largely controlled by basal drag, whereas lateral drag balances roughly 10% of the driving stress. The relative role of longitudinal resistance in opposing the driving stress is small ($<5\%$), but can be up to 30% of the lateral drag. Past the grounding line in the fjord lateral drag becomes an important factor. The widening fjord allows ice to spread

increasingly, first at a rate similar to spreading in the flow direction, while more downstream this increases to about 3 times the rate of longitudinal spreading. The spreading calculated from strain rates is similar to that calculated from the geometry of the valleys. Finally we find a favorable comparison between a modeled equilibrium profile of the glacier with the actual profile as derived from ICESat elevation data. This seems to be consistent with the apparent constant velocity.

CHAPTER 5

THE FLOW REGIME OF STANCOMB-WILLS ICE TONGUE

5.1 Introduction

This chapter describes the velocity field and flow regime of the Brunt Ice Shelf System, with emphasis on Stancomb-Wills Ice Tongue. First a brief overview will be given on the geographic setting and previous velocity studies. Then a 3-year averaged velocity map is presented and discussed and a comparison is made with ‘instantaneous’ InSAR velocity. Based on the velocity measurements we estimate ice-shelf spreading, longitudinal stress gradients and the role of lateral drag and compare this with the driving stress that we calculate from ICESat freeboard-derived ice thicknesses. Furthermore we analyze the pattern of relict flow stripes along the Stancomb-Wills Ice Tongue and find this to deviate from present day flow lines. We find a correlation between the flow stripe bending and local mass balance. We use the derived velocity field to extrapolate the configuration of the stripes in the past, and discuss how and why the relict flow stripes differ from present day flow lines. We believe the flow line deviation indicates a change in dynamics perhaps due to thinning and an associated shift in the grounding line position.

5.2 Area description and previous studies

The Brunt Ice Shelf System is situated on the Caird coast on the western shore of the Weddell Sea. It is part of an almost continuous fringing ice shelf along the coast of Coats Land and Queen Maud Land in East Antarctica. The Brunt Ice Shelf System consists of Brunt Ice Shelf (BIS) and adjacent Stancomb-Wills Ice Tongue (SWIT). SWIT is a fast moving ice tongue that is fed by Stancomb-Wills Glacier and extending more than 225 km beyond its grounding line. The width at the ice front is approximately 70 km. SWIT is bordered on the eastside by the Riiser-Larsen Ice Shelf and Lyddan Island, separated by a large rift system in places filled with sea ice. Rignot (2002) used InSAR to investigate velocity and mass budget of the glacier. He found a flow velocity of 700 m a^{-1} , near the grounding line, accelerating to more than 1200 m a^{-1} at the calving front. The estimated mass flux of $16.6 \pm 2 \text{ km}^3 \text{ ice a}^{-1}$ gives the glacier a slightly positive mass balance of about $0.9 \text{ km}^3 \text{ ice a}^{-1}$.

SWIT is separated from the slower moving BIS by a large shear zone consisting of a mélange of large ice rafts and sea ice covered with snow. Hulbe and others (2005) estimated that between 20 % and 30 % of the ice shelf is marine ice. They tracked several large rafts over a time interval of about 2.5 years and found their relative position rather constant implying that the icebergs and the marine ice in which they are embedded move as one mechanically connected unit.

BIS is west of SWIT and is bounded on the seaward side by an area known as the McDonald Ice Rumples, a zone of ice grounded on a number of pinning points. This ice shelf has received more scientific attention than SWIT since it houses the British Halley V station. Several studies have been done to measure movement of the current station and

its predecessors. Older studies were complicated due to the absence of fixed points in a wide radius around the station. Survey techniques included astro-fixes, repeated magnetic surveys, and mapping using grounded icebergs as control points (Thomas, 1973). The studies showed velocities ranging from 349 to 431 m a⁻¹ for the period up to 1972 (Ardus, 1965; Thomas, 1973; Simmons and Rouse, 1984). Simmons and Rouse (1984) report a pronounced acceleration of the ice shelf starting in 1972, velocity of the station nearly doubled to 740 m a⁻¹. This velocity remained relatively constant until 1999, after which it has reportedly been decelerating at an average rate of about 40 m a⁻¹ (BAS, 2005).

5.3 Velocity

We derived 3-year averaged velocities for BIS and SWIT for the time interval between 1997 and 2000 using feature tracking methods described in chapter 3. Figure 5.1 shows 3-year averaged feature tracking velocity and vectors on the ice shelf. Successful velocity estimates are mainly restricted to the area below the grounding line where clear features (crevasses and rifts) are plentiful. Upstream of the grounding line velocity mapping is not possible over this time span due to a lack of trackable features. Nevertheless, the velocity map encompasses more than 200,000 velocity data points, with a 400 m pixel size, and gives a very detailed view of the velocity field in the area.

Velocity increases significantly downstream of the grounding line, but the velocity structure on the ice tongue is asymmetric. We find velocities up to 1350 m a⁻¹ on the northwest corner of the ice shelf, while the northeast corner shows maximum values of up to 1200 m a⁻¹. We do not believe that this is an artifact. Because of the difference the ice tongue is effectively making a rotational movement. The measured velocity field

gives some clues as to what might cause this behavior. First, near the grounding line on the left margin of SWIT several distinct velocity jumps can be observed. These jumps are associated with large rifts that are opening up and filled with thick sea ice, clearly visible in the RADARSAT imagery. This is at the point where the main ice shelf breaks off from the inland ice and could perhaps indicate tidal effects on the flow. A profile across the rifts can be used to determine their opening rate. Figure 5.2a shows a velocity profile across the main rift. The velocity across the rift jumps abruptly from about 450 m a^{-1} to 1100 m a^{-1} and is therefore opening at a rate of roughly 650 m a^{-1} . So it appears that the ice on the west side of the ice tongue is not as mechanically connected to the inland ice as the east where Stancomb-Wills Glacier enters the ice tongue.

Second, we see a strong velocity jump across the entire right lateral margin of SWIT. This is where the fast moving ice stream is separated from the nearly stagnant ice of the Riiser-Larsen ice shelf and the ice in the Lyddan Island embayment. This jump hints at some shearing on this side of the ice tongue. Figure 5.2b shows a velocity profile across the boundary. The jump between Riiser-Larsen Ice Shelf and the fast flowing ice tongue indicates most of the shearing occurs in marine ice in the rift. Nevertheless, we find shear strain rates in the order of 0.005 yr^{-1} on the ice tongue close to the margin. A third possibility is that the glacier is grazing the bed along the right margin and flow is retarded. This possibility was suggested by Holdsworth (1974) to explain the curvature of the Erebus Glacier Tongue. However, this effect is likely small because we do not find any evidence of compressive flow. But the comparison between two profiles in figure 5.3, taken approximately 7.5 km apart, clearly shows a difference in longitudinal strain rates along the margin and mid-flow for the first 20 km or so.

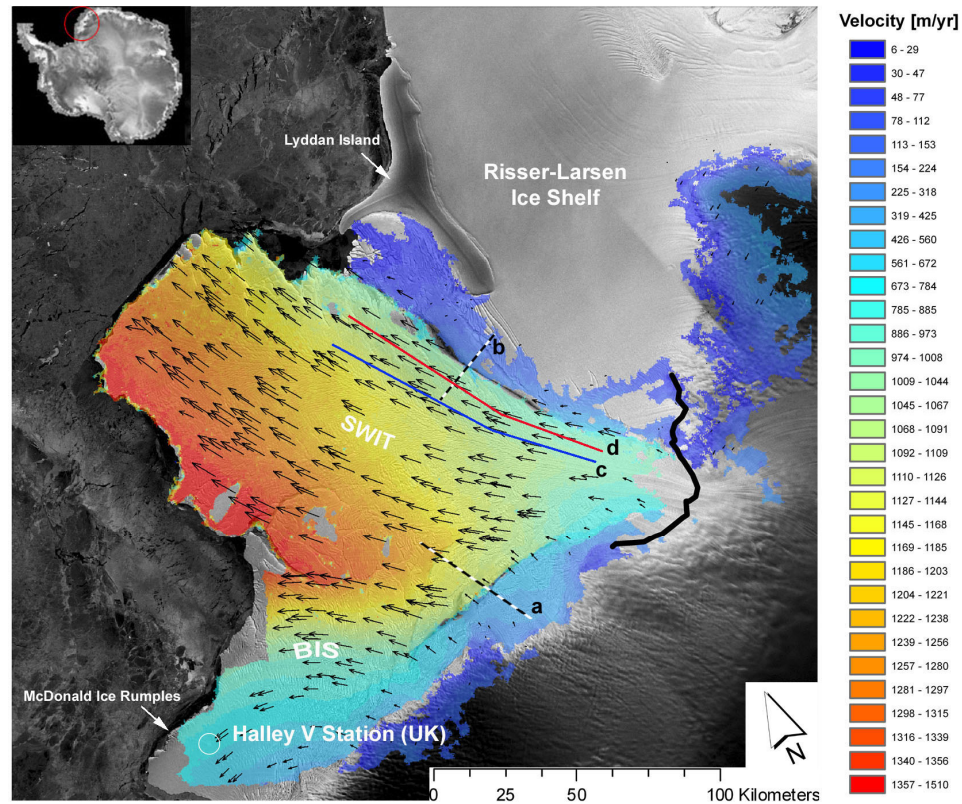


Figure 5.1 Ice flow velocity on Brunt Ice Shelf (BIS) and Stancomb-Wills Ice Tongue (SWIT) on the Caird Coast in East Antarctica (see inset). The velocity field is derived using feature tracking techniques on RADARSAT-1 images of 1997 and 2000 and represents a 3-year average. The map is compiled of more than 200,000 velocity data points with a pixel size of 400 m. Vectors show the direction of flow. Vector density has been decimated for display purposes. The solid black line gives the approximate position of the grounding line (adapted from Rignot, 2002). Dashed lines a and b show velocity profiles across two large rifts given in figure 5.2. Blue and red lines c and d show strain rate profiles in figure 5.3.

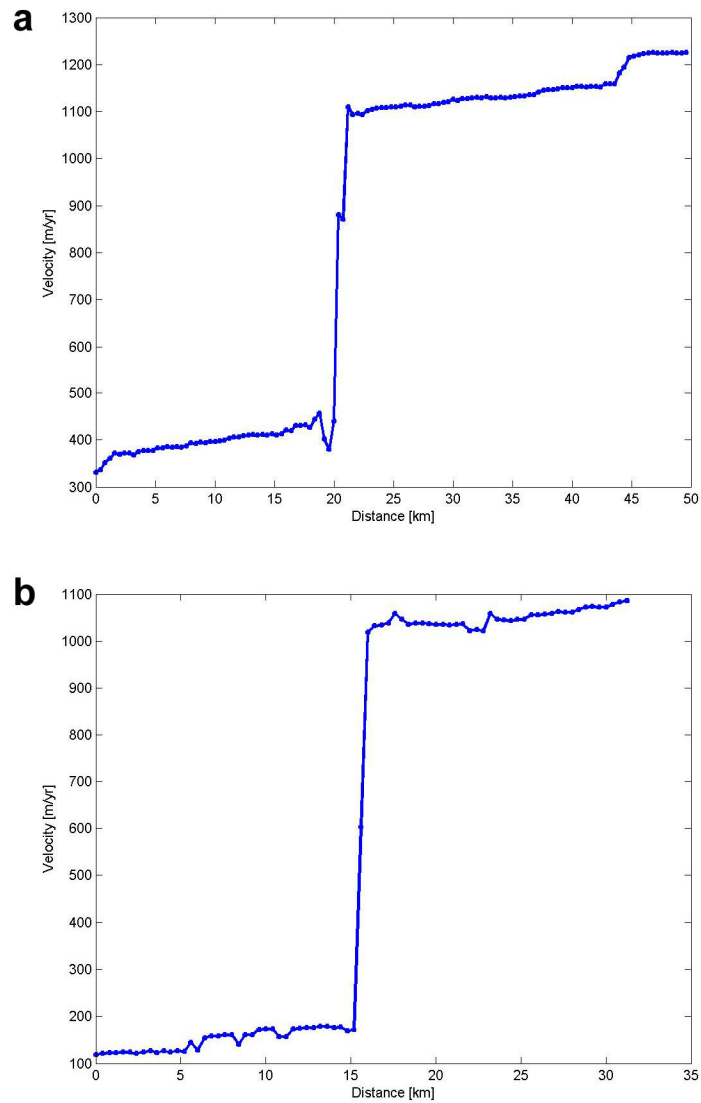


Figure 5.2 Two velocity profiles taken from the velocity field shown in figure 5.1 (letter location marks start of profile). a) Profile across a large rift separating the ice shelf from the mainland. The velocity jump indicates that the rift is opening at a rate of about 650 m a^{-1} . A smaller jump is visible signifying another, smaller, rift. b) Profile across the right lateral margin of SWIT showing the jump between the nearly stagnant ice of the Riiser-Larsen Ice Shelf and the fast flowing ice tongue. Dots represent actual data points.

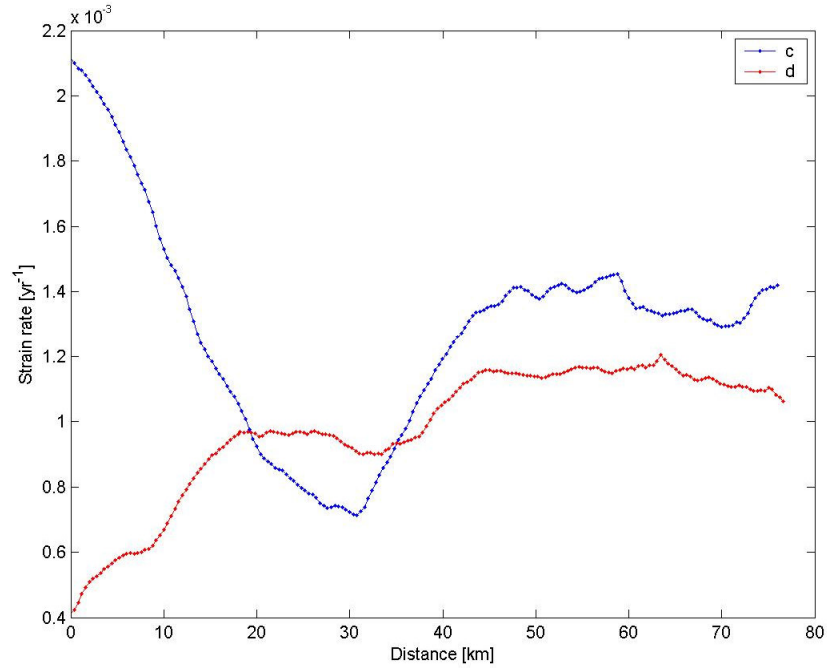


Figure 5.3 Longitudinal strain rates determined along two profiles indicated in figure 5.1. The red line shows a profile along the right margin of SWIT. The blue one is further to the center of the stream. As can be seen along the first 20 km the two differ significantly. Although there is no compressive flow the longitudinal strain rate along the margin is much lower suggesting grazing along the bottom.

5.4 Velocity comparison

Figure 5.4 shows the difference between 3-year averaged feature tracking velocity (1997-2000) and ‘instantaneous’ 2000 InSAR velocity. The associated histogram is given in figure 5.5. As can be seen differences are very small and have an approximate zero mean. Higher values are mostly associated with ambiguities in the different techniques or the movement of the large rift system discussed in the previous section. The similarity between the InSAR and feature tracking velocities indicates little change in flow over the time interval of observation.

We find a velocity of $720 \pm 35 \text{ m a}^{-1}$ for Halley V station which agrees well with a reported value of approximately 750 m a^{-1} for that period (BAS, 2005). We find velocities between 850 m a^{-1} and 950 m a^{-1} on SWIT about 10 km downstream of the grounding line which agrees with values reported in Rignot (2002) and Hulbe and others (2005).

We do not find any evidence of deceleration on Brunt Ice Shelf, this is not surprising because it reportedly started after 1999 (BAS, 2005). Instead our data seems to confirm the apparent constant velocity observed between 1972 and 1999.

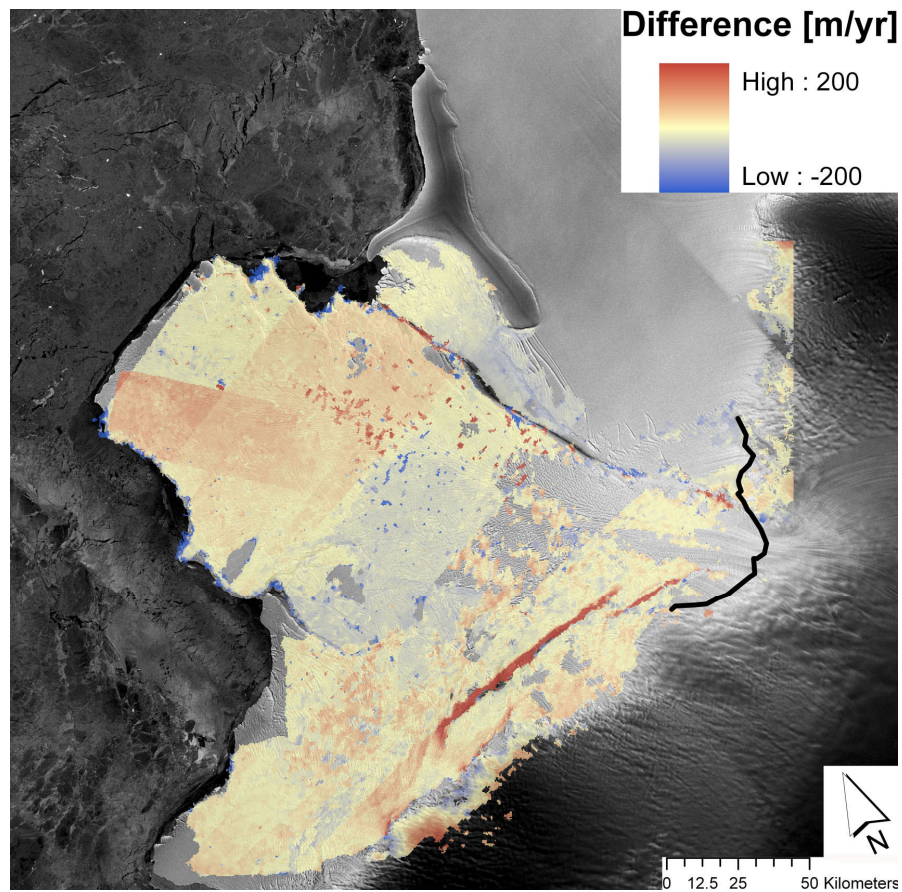


Figure 5.4 Velocity difference between 3-year averaged feature tracking velocity (1997-2000) and 2000 InSAR velocity. Differences between the two are small and do not show significant change. The largest values are associated with the movement of the rift separating the main ice shelf from the land.

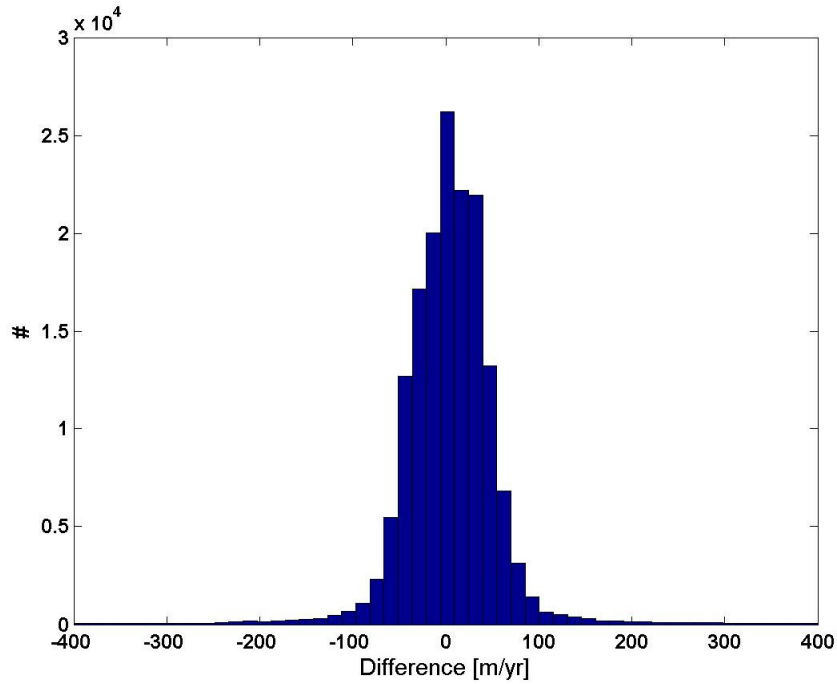


Figure 5.5 Histogram of differences between 3-year averaged feature tracking and InSAR velocities as depicted in figure 5-3.

5.5 Ice shelf spreading and basal melting

Using a combination of both InSAR and feature tracking velocity we can determine strain rates from the grounding line all the way to the ice front. In order to do this we define the x-axis along the main flow direction and the y-axis across the main flow direction. Since the flow direction is not parallel to the boundaries of the satellite image, used in IMCORR to derive flow velocity, a rotation must be applied. This can be done by the following matrix multiplication:

$$\begin{bmatrix} Vx' \\ Vy' \end{bmatrix} = \begin{bmatrix} \cos \phi & -\sin \phi \\ \sin \phi & \cos \phi \end{bmatrix} \begin{bmatrix} Vx \\ Vy \end{bmatrix} \quad (5.1)$$

where Vx and Vy are the old components of velocity, Vx' and Vy' the new components and ϕ is the angle between the old axis and new axis, approximately -25° in this case.

After applying the rotation, strain rates in x and y direction along the ice tongue are readily calculated. Figure 5.6 shows strain rates derived from the rotated velocity field along SWIT in units of 10^{-3} yr^{-1} . The strain rates for the along flow direction are 30 km average values for sections in between the blue circles. For the across flow direction the strain rates are averages for the across flow profiles (dotted black lines). As observed on Mertz Glacier Tongue the across flow spreading rate along the first part of the floating ice tongue are about double the along flow spreading rate.

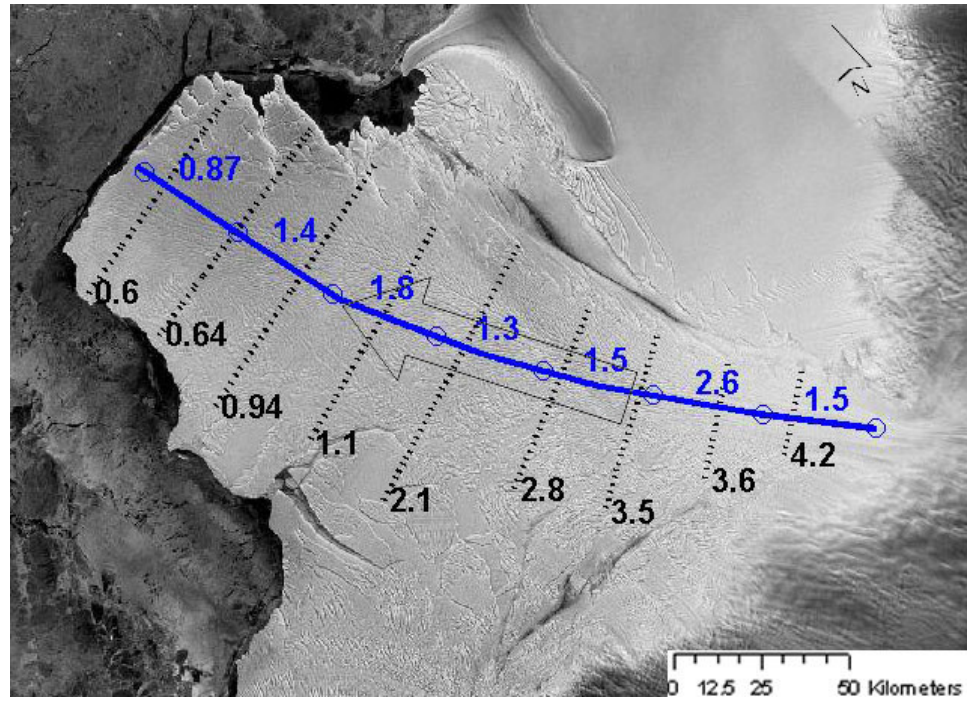


Figure 5.6 Strain rates in the along and across flow direction determined from derived velocity. Strain rates are given in 10^{-3} yr^{-1} and are calculated based on a linear fit through the dotted transects for across flow direction or the sections between the circles for along flow direction (flow direction indicated by arrow).

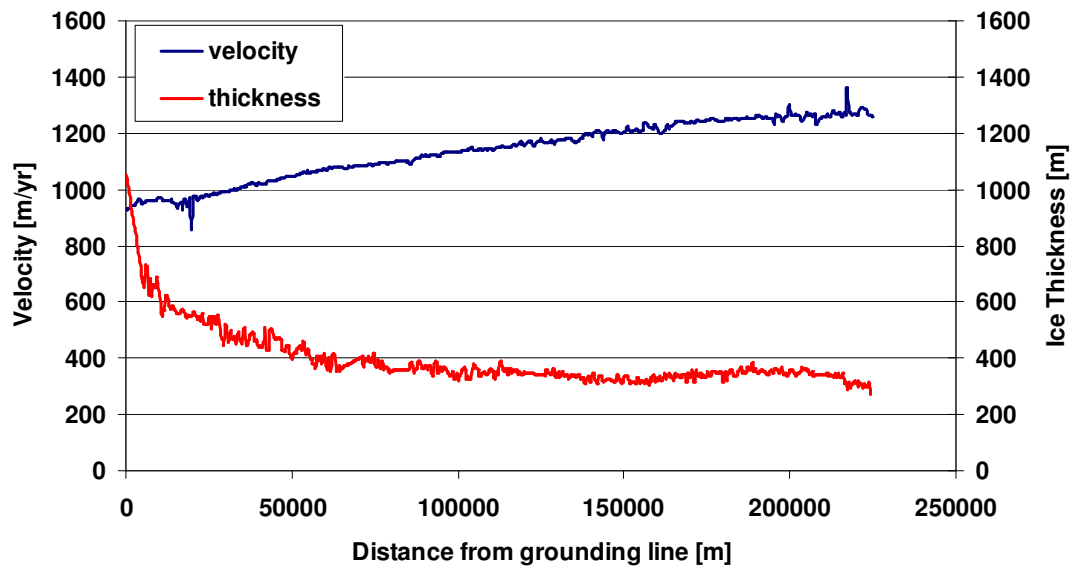


Figure 5.7 Velocity profile (blue) and thickness profile (red) taken along the center of the Stancomb-Wills Ice Tongue. The velocity profile is taken from a combination of InSAR and feature tracking velocity. The two peaks are most likely malicious data points. The thickness profile is derived from gridded ICESat elevation data (200 m) assuming hydrostatic equilibrium. It shows an almost constant ice thickness along most of the ice tongue.

To estimate basal melting we use strain rates from the velocity profile given in figure 5.7. We also use gridded ICESat elevation data (h) and convert this to ice thickness (H) assuming hydrostatic equilibrium:

$$H = h / (1 - \rho_i / \rho_w) \quad (5.2)$$

with $\rho_i = 900 \text{ kg m}^{-3}$ and $\rho_w = 1028 \text{ kg m}^{-3}$. The resulting profile is given in the same figure and shows that ice thickness is nearly constant along most of the ice tongue except near the grounding line. For a glacier the continuity equation for steady state along a flow line is given by:

$$\frac{\partial H}{\partial t} = -H[\dot{\epsilon}_{xx} + \dot{\epsilon}_{yy}] - u_x \frac{\partial H}{\partial x} + M = 0 \quad (5.3)$$

where H is the ice thickness and M the net accumulation. The basal melt rate \dot{B} (along a flow line) can then be calculated from:

$$\dot{B} = \dot{A} - M \quad (5.4)$$

Where \dot{A} is the accumulation rate in m ice a^{-1} . An accumulation map by Vaughan and others (1999) shows a reasonably constant accumulation rate of about $0.23 \text{ m w.e. a}^{-1}$, which translates into $0.26 \text{ m ice a}^{-1}$. Using this value and our calculated strain rates in combination with the derived thickness and velocity profile we calculate basal melt rates

along the center of the glacier (figure 5.8). The computation shows that basal melting occurs near the grounding line, about $6.6 \pm 2.0 \text{ m ice a}^{-1}$, but along most of the rest of the glacier there is a negative melt rate, i.e. freeze on, of 1 or 2 meters per year. This is confirmed by Rignot (2002) who estimated basal melt rates near the grounding line in the order of $4 \pm 8 \text{ m a}^{-1}$ and further downstream basal freezing of a few meters per year based on fluxgate calculations. We find a maximum basal freeze on rate of $2.4 \pm 2.5 \text{ m ice a}^{-1}$ at about 170 km from the grounding line.

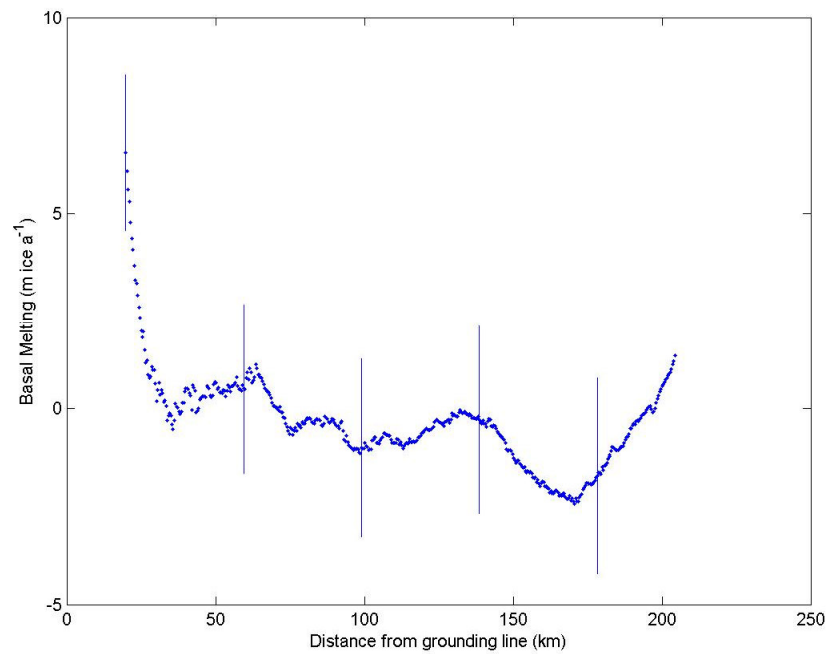


Figure 5.8 Basal melting calculated along a profile in the center of SWIT using equation 5.3 and 5.4. Negative melt rate implies freeze on. We find slight freeze on along most of the glacier. Basal melting occurs near the grounding line.

5.6 Flow dynamics

5.6.1 Driving stress and longitudinal stress gradients

Using the velocity and ice thickness data shown in figure 5.7 we calculate longitudinal stress gradients along the center line of SWIT. Figure 5.9 shows longitudinal stress gradients computed using both Glen's flow law and Goldsby-Kohlstedt. We use a rate factor for ice of -16°C , a depth averaged temperature we adopt from Thomas (1971) who determined the temperature for Brunt Ice Shelf. For Goldsby-Kohlstedt we use a grain size of 3 mm and a temperature of -16°C . A comparison with the driving stress, given in the same figure and calculated from ICESat derived surface gradients and thickness shows a discrepancy along the first 70 km. This implies that lateral drag plays a significant role along that part and that the tongue is thus not floating freely there. We calculate lateral drag in chapter 5.6.2. Furthermore we note that the driving stress shows a slightly negative value at approximately 170 km from the grounding line, but looking more closely at the thickness data we observe that along that section the ice seems to become thicker, but it falls outside our detection limits. If real, it could be an effect of basal freeze on, calculated in chapter 5.5. However, if the net accumulation is assumed zero it might also indicate that the ice is thinning over time (see chapter 5.9).

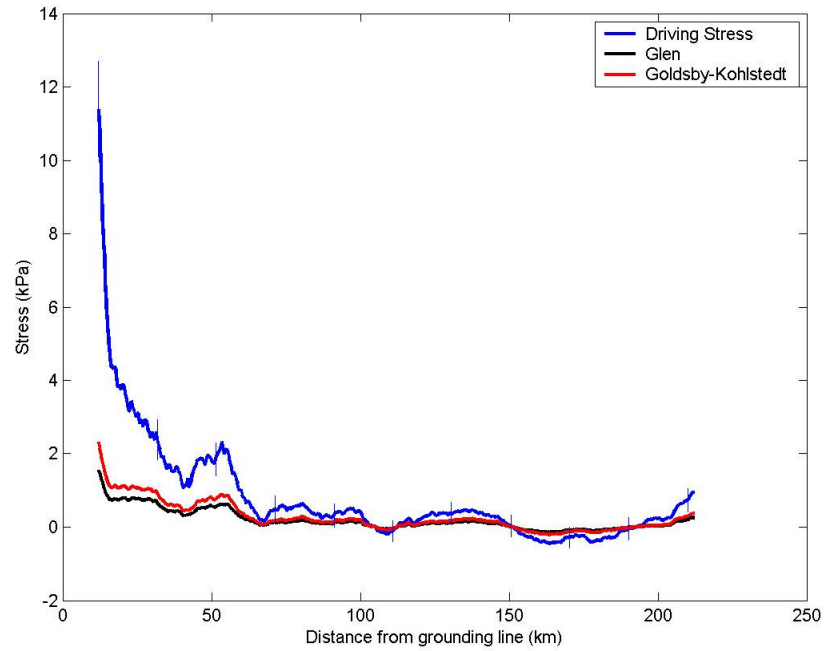


Figure 5.9 Driving stress (blue) calculated along a profile shown in figure 5.5. The red line shows the longitudinal stress gradient from force balance in the absence of lateral drag using the Goldsby-Kohlstedt constitutive relation. The black line shows the same for Glen's flow law.

5.6.2 Lateral drag

Our calculations in chapter 5.6.1 indicate that along the first 60-70 km beyond the grounding line of SWIT the driving stress is not balanced by longitudinal stress gradients alone. To estimate what the contribution of lateral drag is we use derived strain rates from across flow profiles (figure 5.10) in combination with thickness estimates. Based on this we find lateral drag close to the grounding line to be in the order of 8.5 ± 0.9 kPa or about 74% of the driving stress using Glen's flow law. For Goldsby-Kohlstedt lateral drag is higher at 10.8 kPa (94%). In combination with longitudinal stress gradients lateral drag

balances the driving stress along the first section of the glacier. Further downstream near Lyddan Island the ice tongue is only bounded on one side. We measure shear strain rates in the order of 0.005 a^{-1} close to the margins, but the width averaged lateral drag is tiny accounting for less than 5% of the driving stress.

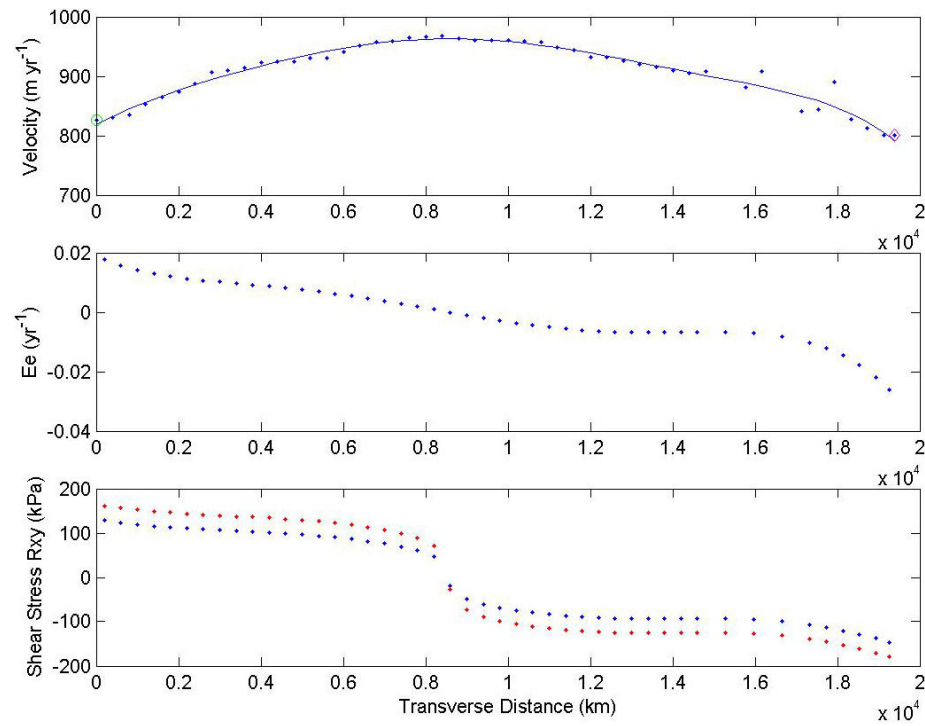


Figure 5.10 Across flow profile of velocity (upper panel), used to calculate shear strain rate (middle panel) and shear stress (lower panel) along the profile indicated at the bottom. The red dots shows shear stress calculated from Goldsby-Kohlstedt, The blue dots are for Glen's flow law, which gives somewhat lower values. The approximate position of the grounding line is indicated by the heavy black line on the satellite image.

5.7 Relict flow stripes

The RADARSAT images of BIS and SWIT reveal marked curvilinear stripes and crevasse bands, some of which are more than 200 km long. Similar features have been found and studied on Ross Ice Shelf (Casassa and others, 1991; Fahnestock and others, 2000) and Ronne-Filchner Ice Shelf (Crabtree and Doake, 1980; Swithinbank and others, 1988). The features are not actual flow lines, which are imaginary lines tangent to the local velocity vector. The exact mechanism that produces the stripes is unclear, but it is commonly thought that they represent relict flow lines and are associated with subtle topography (Casassa and others, 1991). They can be thought of as the line that a fixed marker of some sort, placed on a point on the ice, would leave on the moving ice, and analysis of these relict flow features can reveal past ice-stream fluctuations when compared to present-day flow lines (MacAyeal and others, 1988; Casassa and others, 1991). In a steady state system the flow features would eventually line up with contemporary flow lines (Fahnestock and others, 2000). Analysis of relict flow stripes can thus reveal glacial events in the past and place present day fluctuations in a context.

In an effort to study the history of the ice shelf we traced several relict flow stripes on BIS and SWIT. The yellow lines in figure 5.11a mark the stripes and show feature tracking (red) and InSAR (black) velocity vectors on a 1997 RADARSAT image. The grey lines show the current flow lines and are derived from the velocity vectors. Closer investigation of the current velocity field reveals a pronounced deviation of the relict flow stripes with contemporary flow lines near the front of SWIT (figure 5.11b). This disparity can indicate a change in the past. Furthermore on BIS, near Halley V station, we observe that the relict flow stripes make a very sharp bend to the west.

However, the stripes run nearly parallel to modern day flow lines. The pronounced curving of the stripes is likely caused by shallow seabed topography around the McDonald Ice Rumples. Small deviations do exist, perhaps indicating the variable flow of recent decades, but they are not nearly as distinct as on SWIT.

On SWIT the alignment between the current flow lines and the relict flow stripes is reasonably good from the point where the stripes become visible, close to the grounding line, and along the first part of the ice tongue. This suggests that, during the time represented by this distance, flow has been more or less constant. We therefore assume here that the present day velocity field can be used to estimate the timing of the perturbation. This assumption is also based on a paper by MacAyeal and Barcilon (1988) who showed that when an ice stream fluctuation occurs two trajectories can be distinguished. One in which a perturbation in the grounding line velocity is transmitted instantaneous to all points downstream. This is in contrast to thickness changes at the grounding line that propagate much slower downstream. The calculation of the timing of the perturbation is done by integrating the product of distance and inverse velocity along a flow line. Since velocity V can be defined as:

$$V = \frac{dx}{dt} \quad (5.5)$$

we can estimate the time passed since the perturbation through:

$$T = \int_0^z \frac{dx}{v(i)} \quad (5.6)$$

Here T is the time it takes for a particle to travel from the grounding line to the point where the relict flow stripes deviate from the present flow line (χ). These points are marked with a star in figure 5.11a. The way we implement this is by taking a velocity profile along a flow stripe from the star located at the grounding line to the star marking the deviation between flow vectors and relict flow stripes (figure 5.12). We then plot distance x against V^{-1} and calculate the area under the curve from:

$$T = \sum \left[\frac{v_i^{-1} + v_{(i-1)}^{-1}}{2} (x_i - x_{(i-1)}) \right] \quad (5.7)$$

Using this approach we find a value of about 137 yr for T . This value would be less if the grounding line position retreated over time.

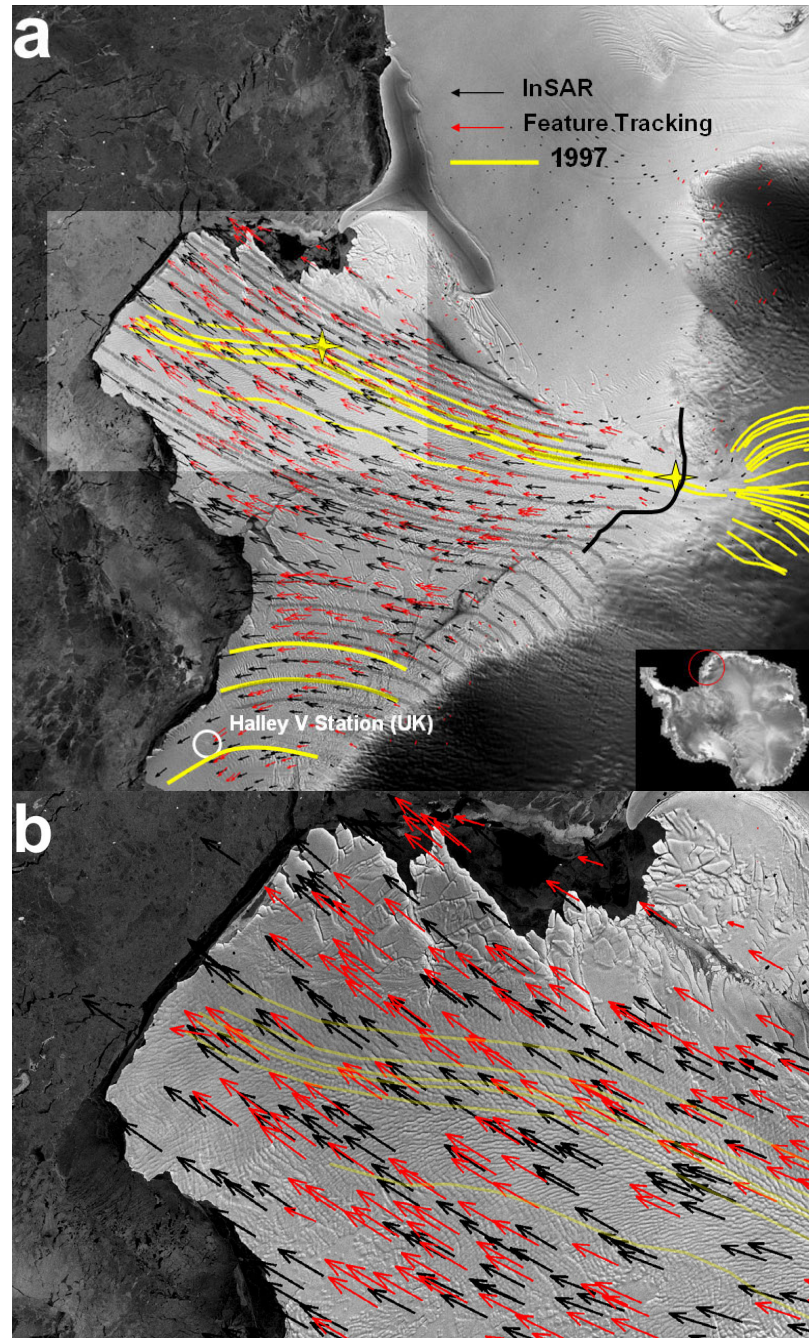


Figure 5.11 a) RADARSAT image of BIS and SWIT showing flow lines inferred from the velocity field (grey), traced flow stripes (yellow), feature tracking (red) and InSAR (black) velocity vectors. The solid black line indicates the approximate location of the grounding line (adapted from Rignot, 2002). Stars mark beginning and end of velocity profile shown in figure 5.12 that is used to estimate the timing of the perturbation. Highlighted square shows area of enlargement in b. b) Close up of the front of SWIT showing clearly the deviation between relict flow stripes and current velocity vectors.

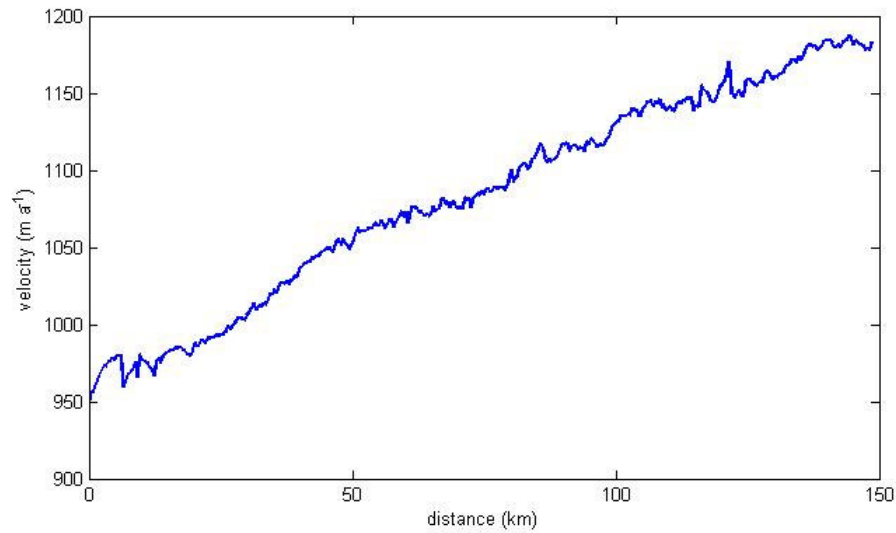


Figure 5.12 Velocity profile along a flow line used to calculate the elapsed time since the perturbation. By integrating the product of distance with the inverse velocity the time of perturbation is estimated to be approximately 137 yr.

5.8 Flow stripe extrapolation

To find out what kind of glacial event is recorded by the bending of the stripes we investigate flow stripe migration over time by tracing two relict flow stripes identifiable on both 1997 and 2000 RADARSAT images and also on a co-registered Landsat image of 1986. We estimate the configuration of the 1997 flow lines in 2000 and 1986 by extrapolating the position of each point along the line using the derived velocity field.

Figure 5.13 shows a comparison between the extrapolated flow stripes and the actual position of the stripes visible in the image. Based on MacAyeal and Barcilon (1988) theory we believe that the good agreement indicates relative constant flow since 1986 and justifies further extrapolation to find the configuration during the time of

perturbation. Using the same flow stripes and assuming steady flow we can estimate their approximate configuration during the timing of the perturbation calculated in chapter 5.7 (figure 5.14). The figure shows that during that time the flow stripes were bent sharply towards the west. Over time the creep of the ice shelf has stretched the markings and concealed their original configuration.

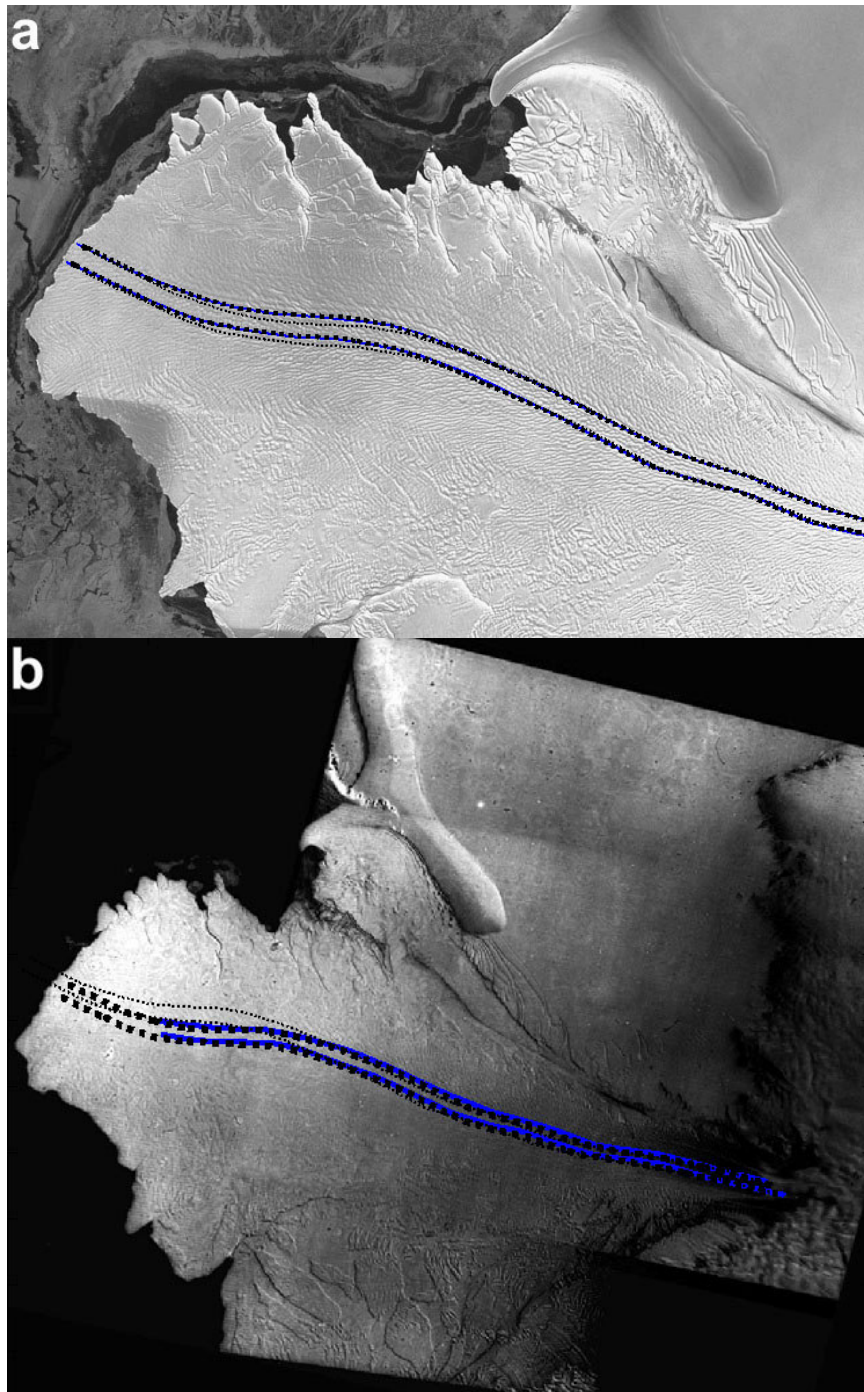


Figure 5.13 Comparison between extrapolated relict flow stripes (thick dotted line) and actual position of the same flow lines (blue) on a 2000 RADARSAT image (a) and a 1986 Landsat image (b). The thin dotted line gives the 1997 position of the same flow stripes. The good agreement indicates that flow has been relatively constant since 1986.



Figure 5.14 Extrapolated configuration of two relict flow stripes during time of perturbation (solid lines) and position of the stripes on a 1997 image. The extrapolation makes use of the present velocity field to predict the location in the past. Time of perturbation is estimated to be 137 years earlier (see discussion in text). The figure shows that the bending of the flow stripes was more extreme in the past and has stretched out over time due to velocity gradients in the ice tongue.

5.9 Discussion

There are several scenarios to account for the behavior of the flow stripes. First, it could indicate a more westerly flow of SWIT in the past. Perhaps ice from the western part of the Risser-Larsen Ice Shelf found an outlet west of Lyddan Island blocking SWIT. A subsequent surge of SWIT could have blocked this outlet.

Alternatively, assuming the flow lines have remained virtually unchanged with time, the initiation point of the stripes might have shifted over time. This could indicate a change in dynamics perhaps due to thinning and an associated shift in the grounding line position. A similar model is described in Jezek (1984) to explain a series of debris tracks from Crary Ice Rise crossing present day flow lines on Ross Ice Shelf.

Earlier observations by Shackleton's expedition seem to support the latter hypothesis. When Shackleton was there in 1914-1915 he made a map of the ice front of Stancomb-Wills Ice Tongue. At the time there was an enormous promontory sticking out into the Weddell Sea that has since calved off (Thomas, 1973). Perhaps there was less fast ice to cement the tongue around the flanks. It would be plausible to assume that the ice tongue was probably thicker as well around that time and the grounding line more advanced. The Lyddan Island ice rise would, as it does today, limit SWIT's eastern flank and force a more westerly flow. A subsequent thinning could have led to decoupling from the bed and a simpler more easterly flow. The thinning hypothesis is supported by the local mass balance. The flow stripe bending occurs at approximately the same location as our peak inferred basal melt rates assuming no thickness change over time. Were we to assume that basal melting equals surface accumulation the basal melting (i.e.

net accumulation is zero), then the continuity equation along a flow line (equation 5.3) reduces to:

$$\frac{\partial H}{\partial t} = -H[\dot{\epsilon}_{xx} + \dot{\epsilon}_{yy}] - u_x \frac{\partial H}{\partial x} \quad (5.8)$$

And we find a peak thinning rate in the order of 2.2 ± 2.5 m ice a^{-1} . To explore this idea even further we looked at the sea floor topography using the BEDMAP dataset (figure 5.15). The bottom topography west of Lyddan Island is reasonably flat and indeed very shallow (between 250 and 350 m). Using ICESat derived ice thickness estimates we find that even today most of the ice on the east flank of SWIT is nearly grounded (<100 m). Figure 5.16 shows several profiles of sea floor topography. The profiles show very shallow bed topography close to Lyddan Island and something that looks like a trough more to the west. A slightly thicker ice tongue would have run aground close to the island and favor a more easterly flow following the trough. This trough is aligned with the direction of the extrapolated flow stripes.

The hypothesis is further supported by the difference between the crevasse pattern of the ice in the northeast front of the ice tongue and the rest of the ice tongue (visible in figure 5.13b). This area lacks the fine structure found elsewhere and seems to consist of larger rafts glued together by marine ice. This could indicate a different source for this part of the ice tongue. In appearance it looks more like the ice currently attached in the Lyddan Island embayment to the south of it. Perhaps this section was grounded and blocked flow in the past and has recently become ungrounded and detached.

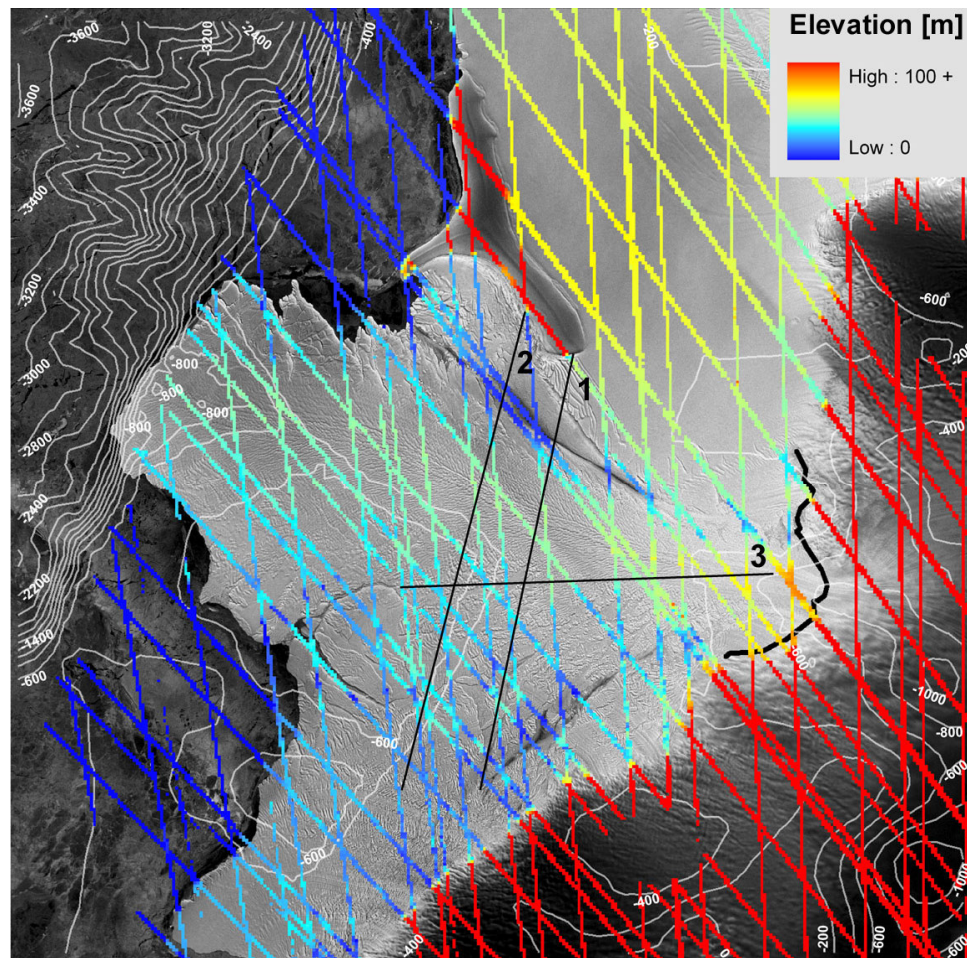


Figure 5.15 1997 RADARSAT image of BIS and SWIT showing bed topography (white contours -contour interval 200 m) and ICESat elevation along satellite tracks. Black lines give location of profiles in figure 5.16.

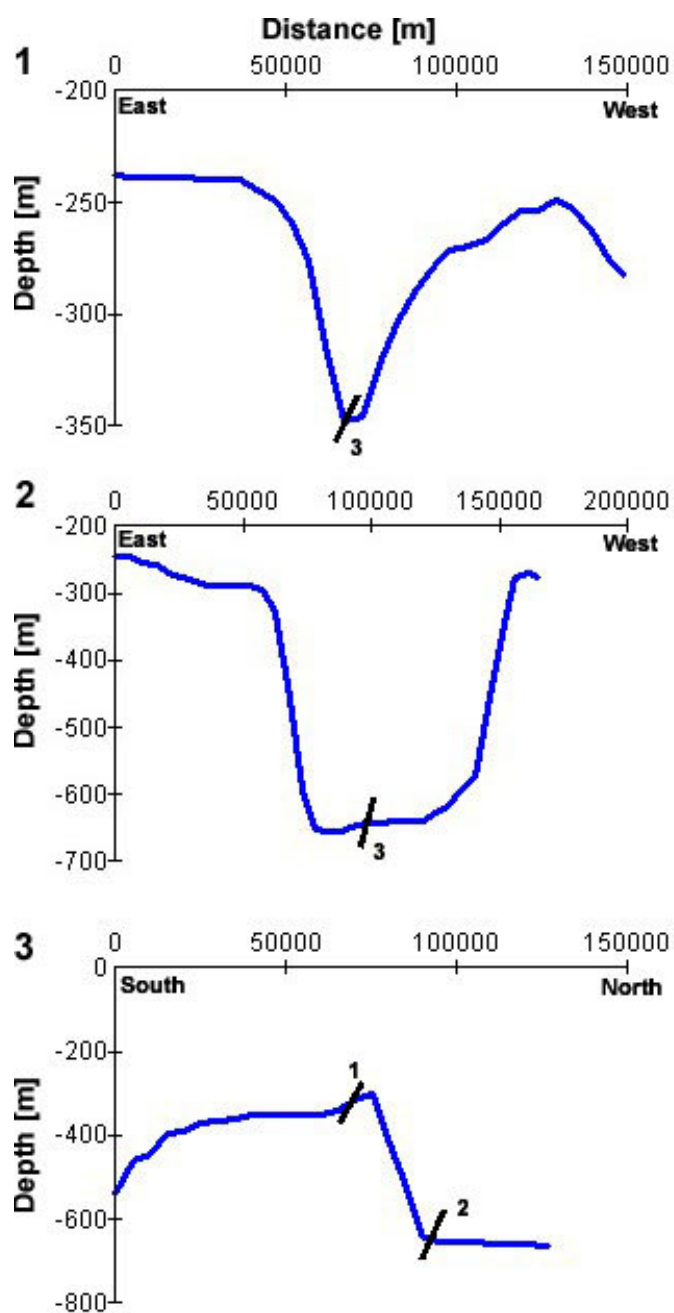


Figure 5.16 Three profiles of bed topography underneath SWIT from BEDMAP data (for location see figure 5.15). The black lines give location of cross-over points. Profiles 1 and 2 are across flow profiles and they show the shallow bed topography close to Lyddan Island (left) and a deep pronounced trough. Profile 3 runs parallel to flow across the deepest part of the trough visible in profile 1 and 2.

5.10 Conclusions

We presented 3-year averaged feature tracking velocities of Brunt Ice Shelf and Stancomb-Wills Ice Tongue. The ice tongue has an asymmetric velocity field that we find is likely caused by detachment of the ice along a large rift on one margin and shearing on the other. We find little significant change between derived 3-year averaged velocities and 2000 InSAR data implying little change over this time interval. From the velocity field in combination with ICESat derived thicknesses we find that along most of the ice tongue longitudinal stress gradients balance the driving stress, except along the first 60 km beyond the grounding line where lateral drag accounts for most of the driving stress. The ice shelf is thus not floating freely along its entire length. We find a deviation between relict flow stripes and current flow lines. The good agreement between the extrapolated 1997 flow lines and their actual position on the 1986 Landsat image show that the stripes are in fact old relict flow lines. A comparison between present day flow lines, derived from the velocity field, and the relict flow stripes on the ice tongue show that a regime change occurred on the ice tongue less than 140 years ago. The pattern of relict flow stripes suggests recent ungrounding associated with grounding line retreat of the Stancomb-Wills Ice Tongue and subsequent ice thinning, which seems to be supported by local mass balance and bottom topography.

CHAPTER 6

THE FLOW REGIME OF MERTZ GLACIER TONGUE

6.1 Introduction

There is a striking similarity between Mertz Glacier Tongue (MGT) in East Antarctica and Drygalski Ice Tongue (figure 6.1 and figure 4.1). Both glaciers form in a fjord and terminate as long, narrow ice tongues extending far into the sea. In doing so they form a barrier for moving sea ice and are therefore critical for the formation of polynya that are found at both locations. Williams and Bindoff (2003) stress that the break off of MGT may result in a reduced polynya with associated consequences for formation of Antarctic Bottom Water and ocean circulation. In this chapter we combine a number of remotely sensed datasets which allow us to investigate the surface velocity field, flow dynamics and glaciological importance of MGT. We apply automatic feature tracking on RADARSAT-1 imagery acquired in 1997 and 2000 to generate an accurate velocity field that is averaged over a 3 year time span. Using the same technique on 2000 MAMM repeat cycle data another velocity field is derived that is averaged over 48 days. We find this to give much better results on the ice tongue than velocity derived from

InSAR, but use the InSAR data to complement our (short term) feature tracking results. The datasets thus derived allow for a comparison between short term averaged velocity, longer term averaged velocity and data from a previous study, available through VELMAP, that applied feature tracking on Landsat imagery over two different time spans. The comparisons suggest that no appreciable changes in velocity have occurred between 1989 and 2000. We use derived velocity, in combination with RADARSAT-1 imagery, ICESat derived elevation and thickness from ice penetrating radar, to investigate calving and stress partitioning along the glacier in an effort to investigate the significance of the ice tongue on glacier flow. We find a calving rate on the order of 150 m a^{-1} on the western margin that appears to be constant along the entire ice tongue. Along the eastern margin calving is much more episodic, which we ascribe to the presence of thick multi-year sea ice on that side, visible in the RADARSAT imagery, and that glues the glacial ice.

We observe an asymmetry in both magnitude and direction of the velocity field near the front of the ice tongue with velocities up to 70 m a^{-1} higher on the east side. The absence of this asymmetry at the point where the ice leaves the valley rules out an upstream effect. Instead it seems the ice tongue is slowly rotating and breaking off at a point about 20 km out in the ocean where a large rift is opening up. The direction of movement suggests that the westward moving along-shore current plays a role in this. We calculate that the current, in addition to the tensile stress, might exert enough force to reinitiate and propagate the rifting. The longer the ice tongue becomes, the more influence this current is likely to have, until the ice tongue eventually breaks off.

Strain rates derived from our velocity field show that after leaving the fjord the ice has the tendency to spread out laterally more strongly rather than longitudinally. Only after about 60 km do we find similar values for spreading in both x and y direction, which implies that the glacier needs time to adjust to freely floating conditions. We find this to be in the order of 50 years. Nevertheless we show that a doubling in the lateral spreading rate does not significantly affect the magnitude of calculated longitudinal stress and that the driving stress is nearly balanced by longitudinal stress gradients, assuming the ice tongue is free floating, to within our error limits.

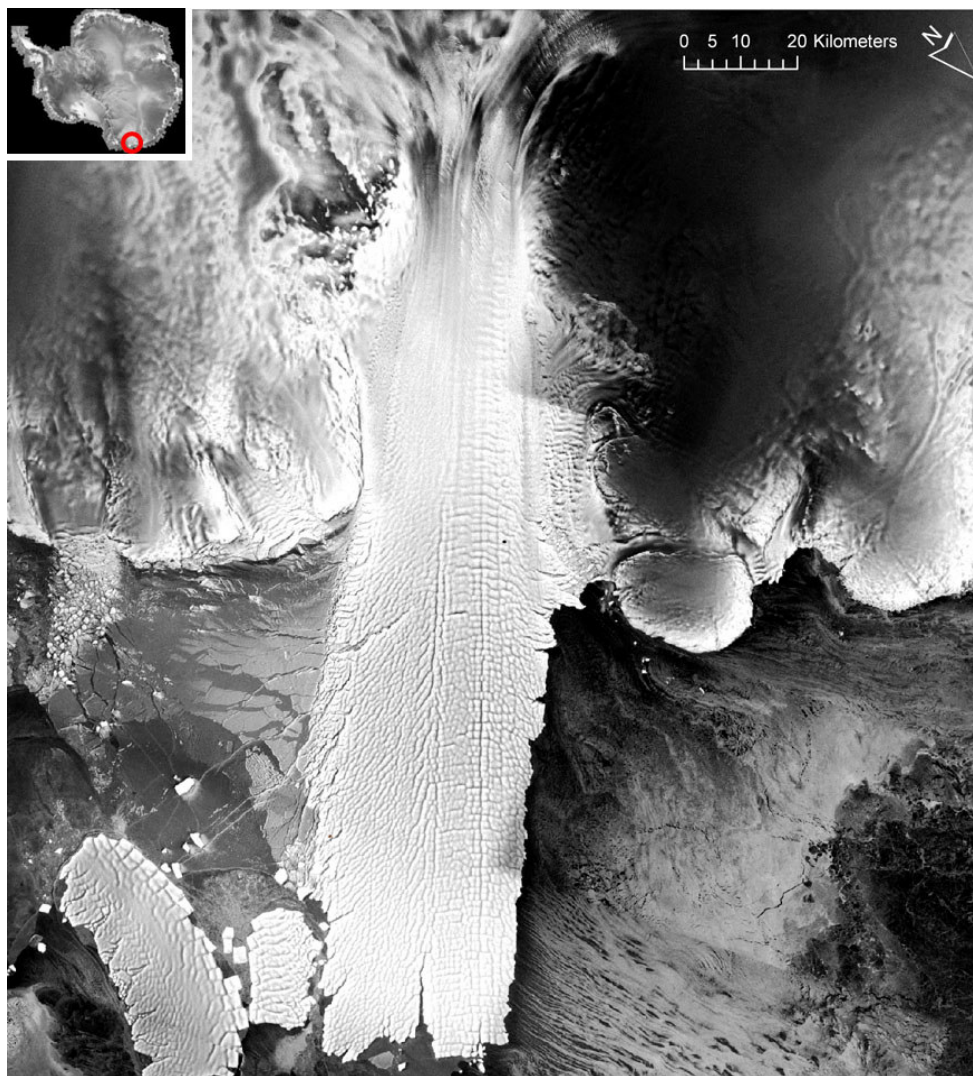


Figure 6.1 RADARSAT-1 image of Mertz Glacier Tongue acquired during the MAMM mission in 2000. Inset shows location in Antarctica.

6.2 Mertz Glacier Tongue

Mertz Glacier Tongue (MGT) is located in King George V Land in East Antarctica and, as its name implies, forms a large ice tongue that extends more than 90 km into the ocean, varying in width between 15 and 35 km. MGT drains an area of more than 80,000 km² from the flanks of Dome C (Rignot, 2002). Since Mawson's team first explored the area, between 1911 and 1914, the ice tongue increased both in width and length and has more than doubled in size (Wendler and others, 1996). Between 1962 and 1993 the average advance rate was about 900 m a⁻¹; between 1993 and 1994 this appeared to be higher at 1200 m a⁻¹ (Wendler and others, 1996). Pötzsch and others (2000) determined the position of the grounding line from SAR interferometry and found it to be about 60 km inland of the coast line (figure 6.2). Using a combination of InSAR velocity, a DEM and accumulation data Rignot (2002) estimated the mass flux across the grounding line to be $19.8 \pm 2 \text{ km}^3 \text{ a}^{-1}$ and, comparing this with mass accumulation, proposed a slightly positive mass balance of $+1.5 \pm 3 \text{ km}^3 \text{ ice a}^{-1}$ for Mertz Glacier. Based on mass continuity he estimated basal melt at the grounding line to be about $18 \pm 6 \text{ m ice a}^{-1}$. Berthier and others (2003) used automated feature tracking on two Landsat images acquired in January 2000 and December 2001 to generate a velocity field of, primarily, the grounding line area. They compared this with 11-year mean velocity, derived using another Landsat image acquired in January 1989, but could not detect significant change between the two periods. Their acquired velocities are available through the VELMAP database and used here for comparison with derived velocity in this study. Legrésy and others (2004) used a number of remotely sensed datasets to investigate the influence of tides and currents on the flow of Mertz Glacier. They found a tide induced flexure of 2 m

per day. More interestingly they found tide induced daily fluctuations in flow speed between 1.9 m d^{-1} (694 m a^{-1}) and 6.8 m d^{-1} (2482 m a^{-1}). The fluctuations seemed to be associated with the current moving the glacier tongue laterally. The faster flow occurs when the glacier is pushed towards its eastern ‘soft dead ice’ boundary. The slower flow is believed to be caused by increased lateral drag when the glacier is pushed toward its western ‘valley wall’ boundary.

6.3 Velocity

We applied feature tracking on 1997 AMM-1 and 2000 MAMM 25 m RADARSAT-1 images of MGT, yielding 3 yr averaged velocities. In addition, we applied feature tracking on two images from the MAMM mission, one from cycle 1 and one from cycle 3, that were taken 48 days apart. The short term InSAR results did not produce a complete velocity field for this area and are used here to supplement short term feature tracking results, primarily for the slower moving sections. The velocity maps presented encompass the grounded tributaries of Mertz Glacier as well as the floating MGT (figure 6.2). The pixel spacing on both maps is 400 m. The 3-year averaged velocity map is compiled of more than 66,000 displacement vectors, the 48 day averaged velocity yielded almost double as many. At the grounding line we find a velocity of about 850 m a^{-1} . Velocities on MGT gradually increase to more than 1200 m a^{-1} at the ice front. The velocity maps clearly show a main tributary coming from the west. In addition a smaller tributary can be distinguished coming from the south. The velocity map also shows the softer west margin (composed of ice instead of rocky valley walls), mentioned earlier, near the head of the fjord where ice moves slower (approximately 300 m a^{-1}).

Furthermore we note that the velocity on the tongue is somewhat asymmetric with higher velocities along the eastern margin. We believe that this is related to the formation of a large rift across the glacier (see chapter 6.6).

Comparing the ice front on the 1997 and 2000 images we find an advance rate of approximately 1200 m a^{-1} . This is in excellent agreement with the value found by Wendler and others (1996) who found the same value for the time frame 1993-1994. The average velocity at the front is of a similar magnitude implying small calving rates at the front. Instead it seems that lateral calving is more important as the ice tongue seems to taper along flow despite lateral spreading. We calculate lateral calving in chapter 6.6.

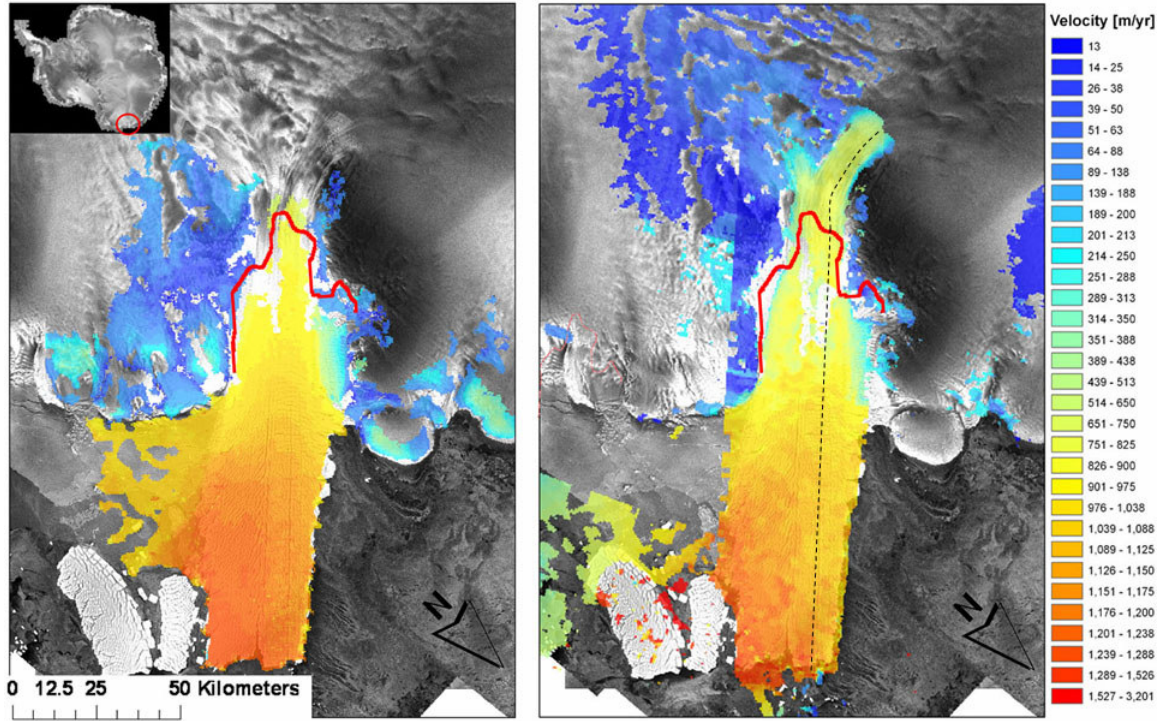


Figure 6.2 3-year averaged velocity (left panel) and 48 day averaged velocity (right panel) depicted on a 1997 RADARSAT-1 scene of Mertz Glacier Tongue in East Antarctica (see inset). The red line depicts the approximate position of the grounding line determined from SAR interferometry (adapted from Pötzsch and others, 2000). Dashed line is velocity/thickness profile shown in figure 6.8.

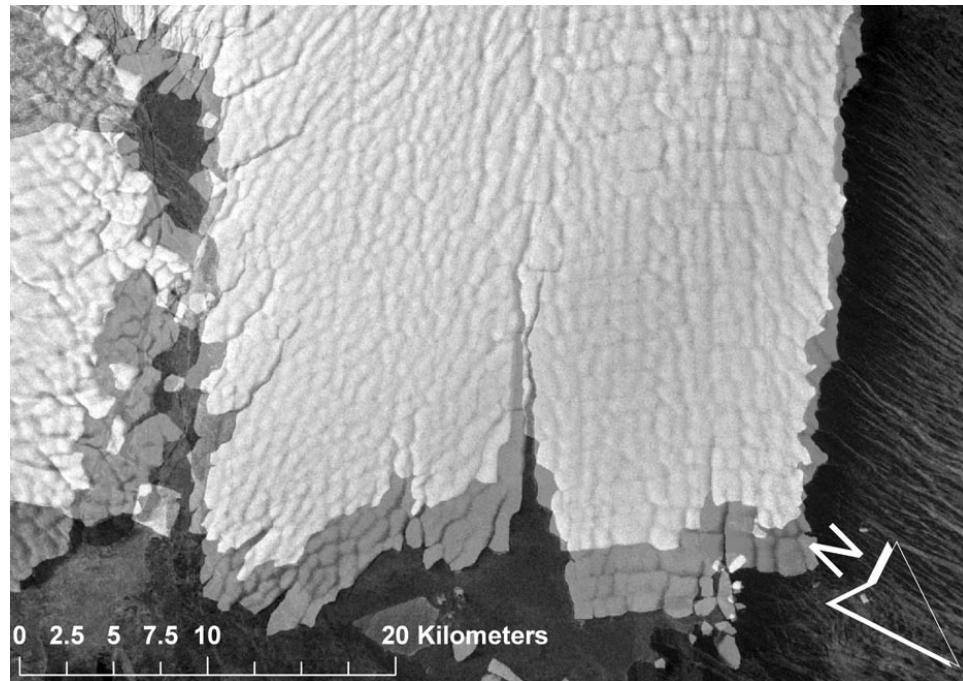


Figure 6.3 Close up of the front of Mertz Glacier Tongue illustrating the advance between September 1997 and September 2000. The front advanced approximately 3600 m over the 3 year period translating into an advance rate of 1200 m a^{-1} .

6.4 Velocity comparison

We compare 3 year averaged velocity with 48 day averaged velocity to investigate if any significant changes have occurred. This is done by subtracting the 3 year averaged velocity from the short term velocity field and investigating the plot and histogram (figure 6.4). The histogram has a mean of -52 m a^{-1} ; however, given the errors in the velocity field (approximately 100 m a^{-1} for the short term velocity) we cannot conclude that a significant change has occurred over this time interval.

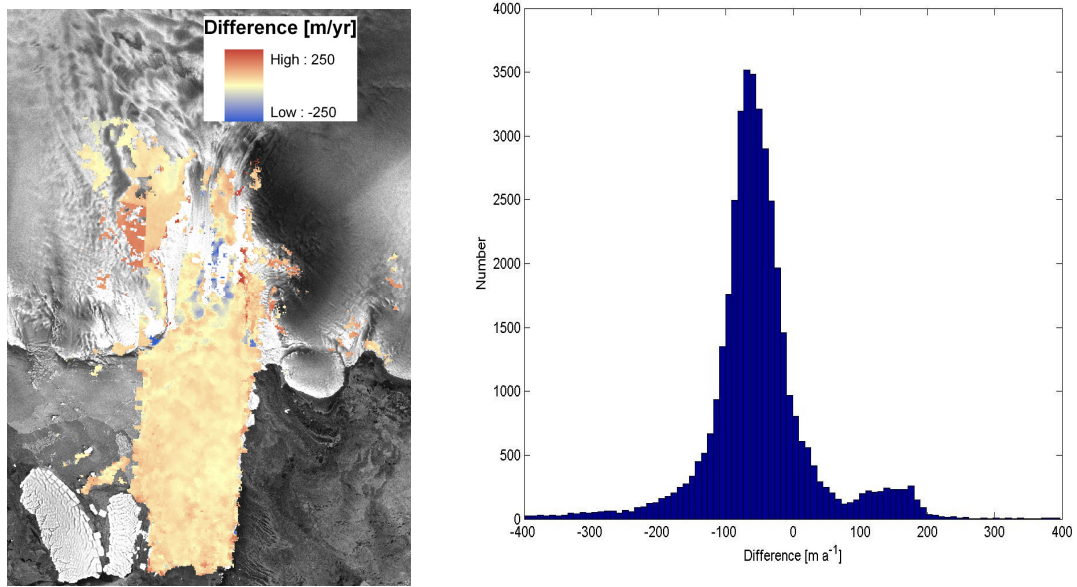


Figure 6.4 Difference map calculated by subtracting 3-year averaged velocity (1997-2000) from 48-day averaged velocity (2000) (left panel) and associated histogram (right panel). The histogram has a mean of -52 m a^{-1} which is below our sensitivity limit.

We also compare our velocity estimates with those from Berthier and others (2003). They used automated feature tracking on three Landsat images acquired in January 1989, January 2000 and December 2001 to generate a 1-year and an 11-year averaged velocity field. Their 1-year averaged velocity data comprised 16,700 displacement vectors. The 11-year averaged results proved to be more problematic and yielded only 433 vectors. Figure 6.5 shows locations of the data points that are used in this comparison. For the comparison we only use those points that fall within the limits of our velocity pixels. The result of the comparison is illustrated in figures 6.6 and 6.7 in the form of scatter plots and difference histograms. Across the whole range of velocities, from slow to fast, we find a good agreement between the datasets. We therefore conclude here that no significant velocity change occurred between 1989 and 2000 based on these data.

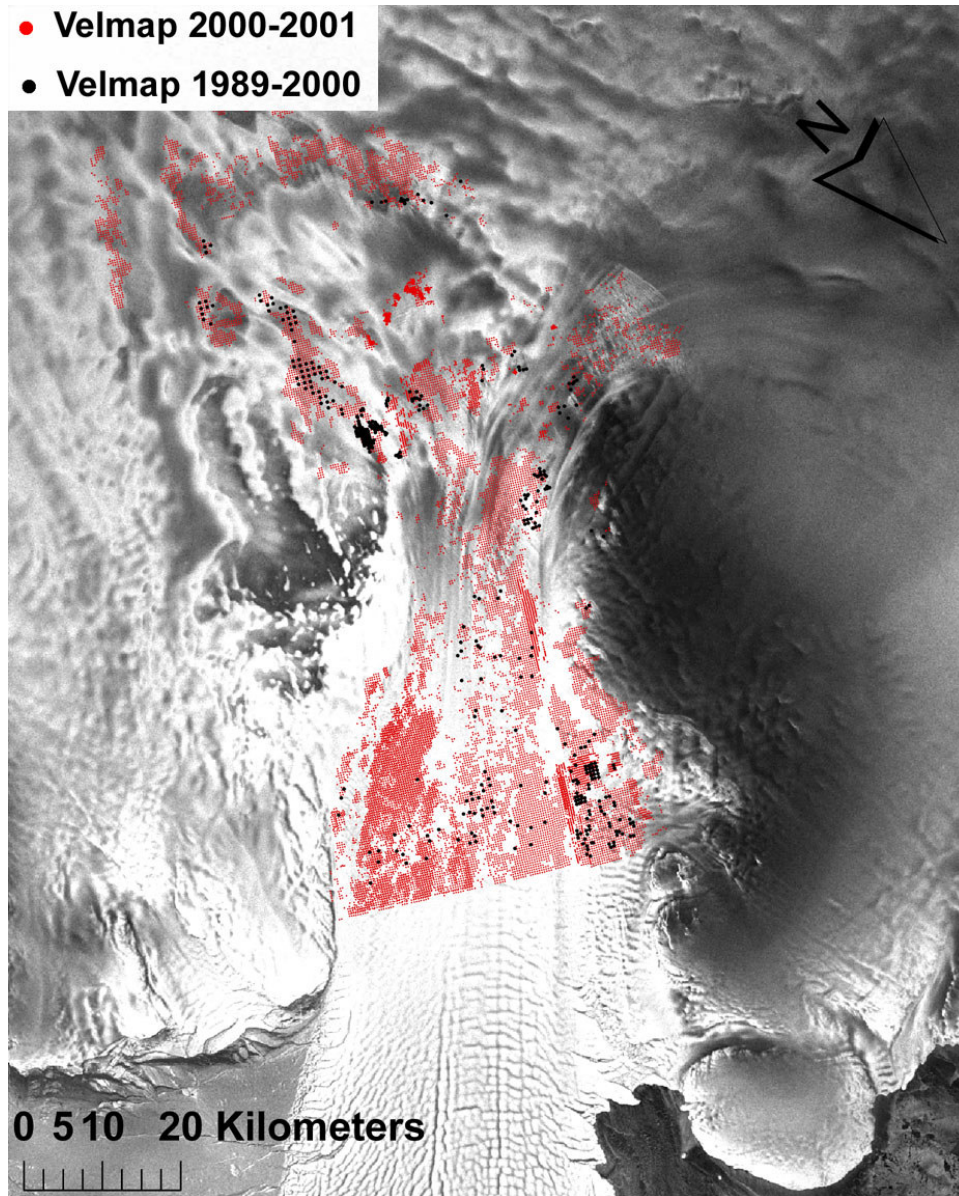


Figure 6.5 Locations of displacement vectors, derived by Berthier and others (2003), that are used for comparison with velocity derived in this study. Red dots represent 1 year averaged velocity data points, black dots represent 11-year averaged velocity data points.

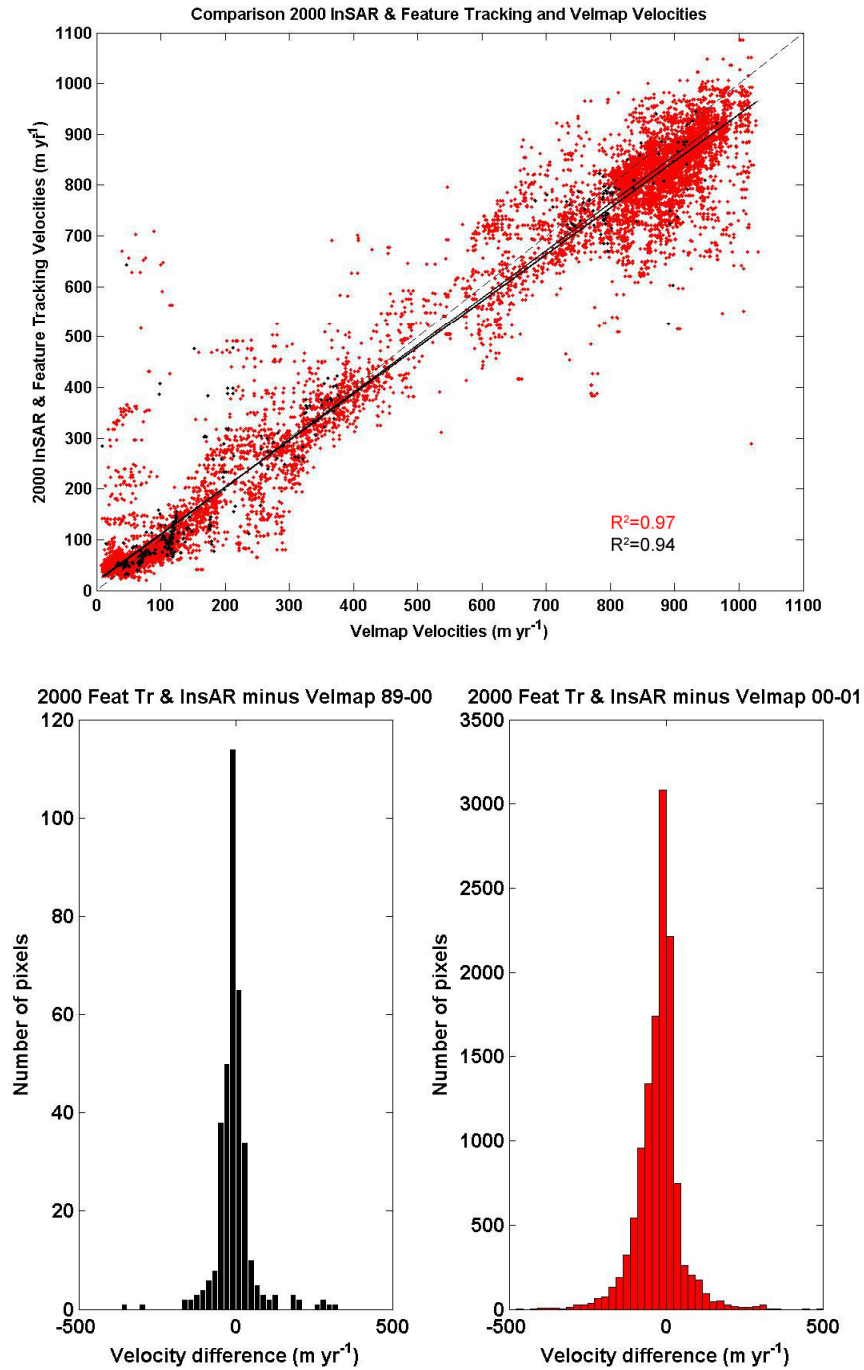


Figure 6.6 Scatter plot showing a comparison between velocities from Berthier and others (2003) and 48-day averaged velocities derived in this study (top panel) and associated histograms of velocity differences (bottom). The red color represents the 1-year averaged data ($n=12,475$), the black color represents the 11-year averaged velocity ($n=362$). Both histograms have an approximate zero mean.

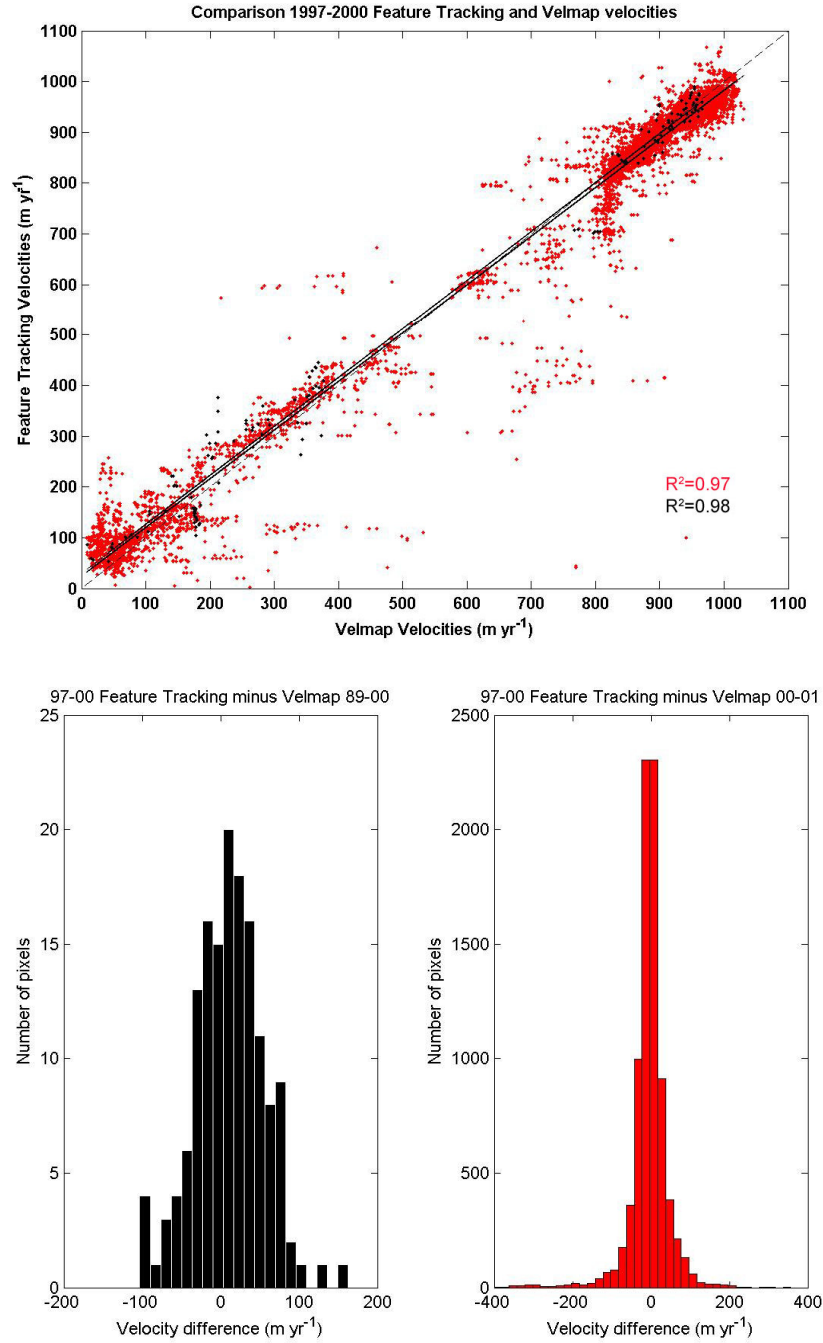


Figure 6.7 Scatter plot showing a comparison between velocities from Berthier and others (2003) and 3-year averaged velocities derived in this study (top panel) and associated histograms of velocity differences (bottom). The red color represents the 1-year averaged data ($n=8245$), the black color represents the 11-year averaged velocity ($n=149$). Again both histograms have an approximate zero mean.

6.5 Ice shelf spreading

Figure 6.8 shows a velocity profile taken along the length of the glacier starting from about 45 km upstream of the grounding line. The location of this profile is depicted in figure 6.2. Using this profile we can determine longitudinal strain rates all the way to the ice front by fitting a trend line through the velocity data. Based on this profile we distinguish three distinct regimes in longitudinal stretching. From the start of the profile 45 km above the grounding line we see a sharp increase in velocity from 350 m a^{-1} to 750 m a^{-1} over a short distance of about 10 km resulting in very high longitudinal strain rates of about 0.038 a^{-1} . Then there is a 120 km long section characterized by a constant longitudinal strain rate about a tenth of that (0.004 a^{-1}). We note that we do not see a significant jump in velocity at the grounding line, which might be expected from the sudden decrease in basal drag. Neither do we see an appreciable change at the point where the glacier leaves the valley. Finally along the last 55 km of the glacier tongue we find a low strain rate regime of 0.001 a^{-1} . This transition starts about 35 km beyond the coast line.

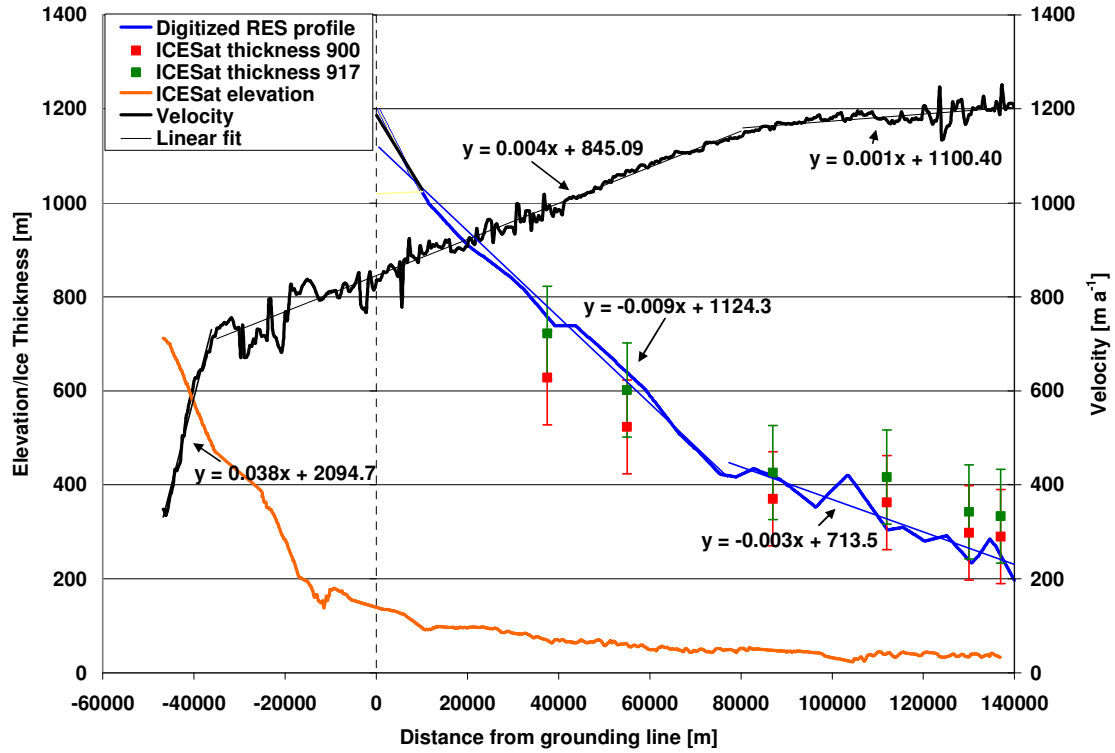


Figure 6.8 Transect of velocity (black line), elevation (orange) and ice thickness (blue) along the Mertz Glacier (location of profile indicated by the dotted line in figure 6.2). The straight lines show a linear fit through the data of which the equations are shown in the graph. The slopes of these are an approximation of the longitudinal spreading rate. Three distinct regimes can be identified. The RES thickness profile is digitized from Legrésy and others (2004). The green and red squares show ice thickness derived from ICESat freeboard using a density of $\rho_i = 917 \text{ kg m}^{-3}$ and $\rho_i = 900 \text{ kg m}^{-3}$ respectively. The location of the slope breaks are indicated in figure 6.9.

By taking a series of transects of the across flow component of velocity we can determine lateral spreading rates (figure 6.9). As can be seen lateral spreading varies along the ice tongue. We find the highest values ($\sim 0.01 \text{ a}^{-1}$) where the glacier leaves the fjord. At this point the lateral spreading rate is more than twice the longitudinal spreading rate. Along the floating part it gradually declines to a value of about 0.002 a^{-1} at the front. By measuring the rate of change in width of a flow band we can make an independent estimate of lateral spreading (black lines in figure 6.9). Using equation 2.42 we find a value of 0.004 a^{-1} , which is about the average value measured from the velocity field.

The observation that the lateral spreading rate along the first part of the ice tongue is much larger than the longitudinal spreading rate is an interesting one. It implies that this section of the glacier does not spread uniformly in all directions as discussed in a model by Thomas (1973). Based on the above analysis we find that for MGT this point occurs only about 60 km after leaving the fjord. The distance of this point is likely a function of, among others, ice thickness, ice temperature and velocity. From our velocity field we determine that, for MGT, it takes roughly 50 years for the ice to transform into a truly free floating ice shelf.

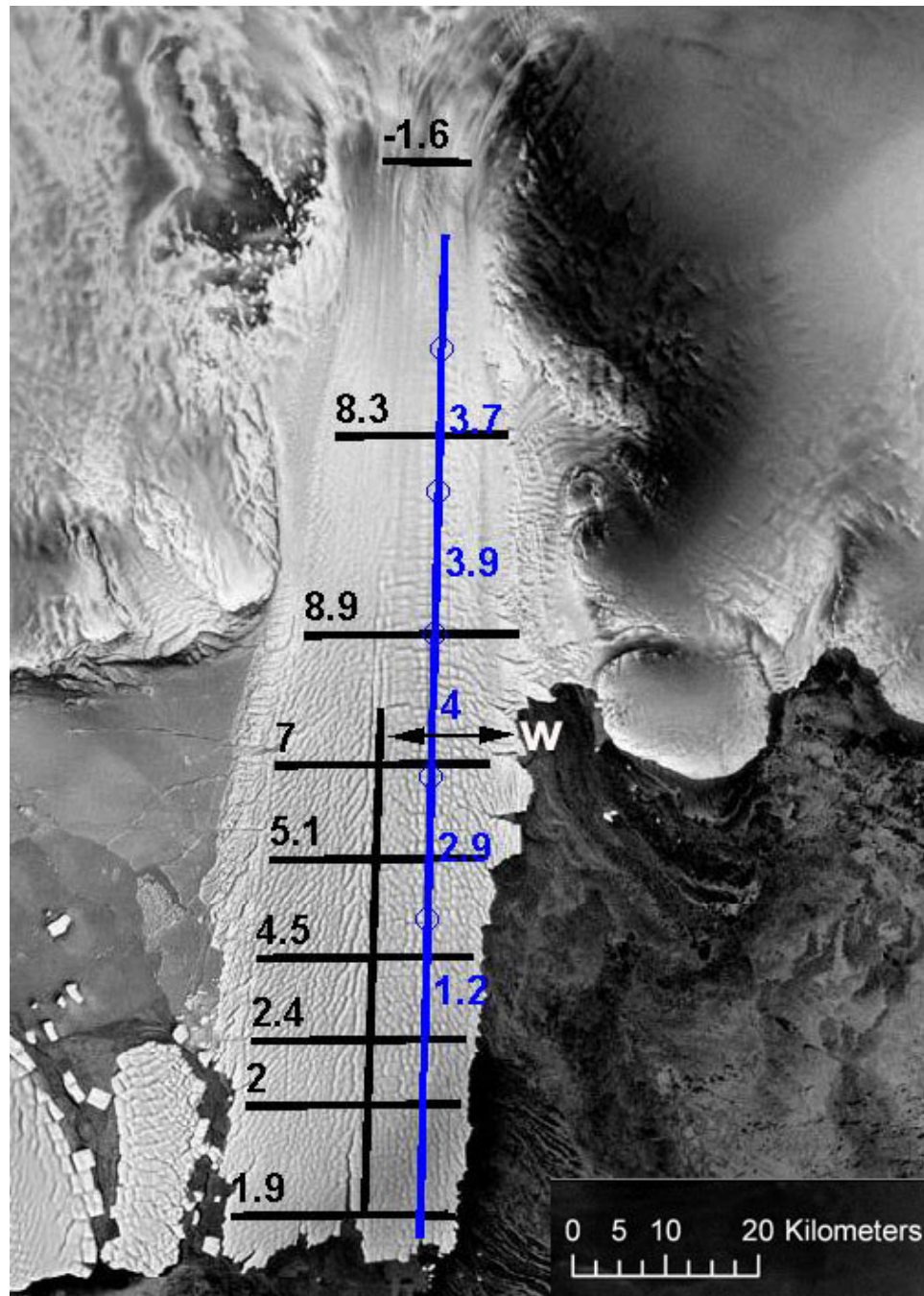


Figure 6.9 Values of ϵ_{yy} and ϵ_{xx} along the Mertz Glacier Tongue calculated from derived velocities along several profiles. The vertical lines indicate the margin of the flow band used to calculate ϵ_{yy} independently. W marks the distance between a flow line and the margin used to calculate the lateral calving rate (chapter 6.6).

6.6 Calving

As mentioned earlier the average velocity at the front (\bar{v}_f) is of a similar magnitude as the advance rate (\dot{a}) implying small calving rates (\dot{c}) at the front, since:

$$\dot{c} = \bar{v}_f - \dot{a} \quad (6.1)$$

Instead it seems that lateral calving is more important. Having an estimate for the lateral spreading we can estimate the calving rate at the side. This is done by measuring the rate of change of distance perpendicular to flow between the margin of the ice tongue and a flow line and adding a component associated with lateral spreading:

$$\dot{c} = \frac{\Delta W}{t} + W\dot{\epsilon}_{yy} \quad (6.2)$$

here W is the distance between the flow line and the margin at the first point (see figure 6.9), ΔW is the difference in distance between the flow line and the margin between the two chosen points, $\dot{\epsilon}_{yy}$ is the lateral spreading rate and t the time which can be estimated by integrating the product of distance and inverse velocity along a flow line (equation 5.4 and 5.5). Based on this we find we find an average calving rate of about 150 m a^{-1} for the west margin of the ice tongue. The calving on this side appears to be of a similar magnitude along the entire length. However, the calving on the east margin is more episodic and seems to be dictated by the presence of thick sea ice. This sea ice appears to be firmly attached to the ice tongue and we are able to track it over the 3-year time span,

indicating that it is very persistent. Only where the thick pack ice stops do we see calving on the east side. From these observations two scenarios are suggested; one in which sea ice on the east side is merely gluing the glacier ice and thus limiting calving and one in which the ice is actually influencing the ice flow by limiting the spreading rate on that side. However, the high spreading rates that we measure make the second an unlikely scenario. It thus appears that the glacier ice at the east side does become mechanically weak but is glued to the tongue. This is supported by the fact that at the point where the thick pack ice stops, a large amount of calving suddenly occurs.

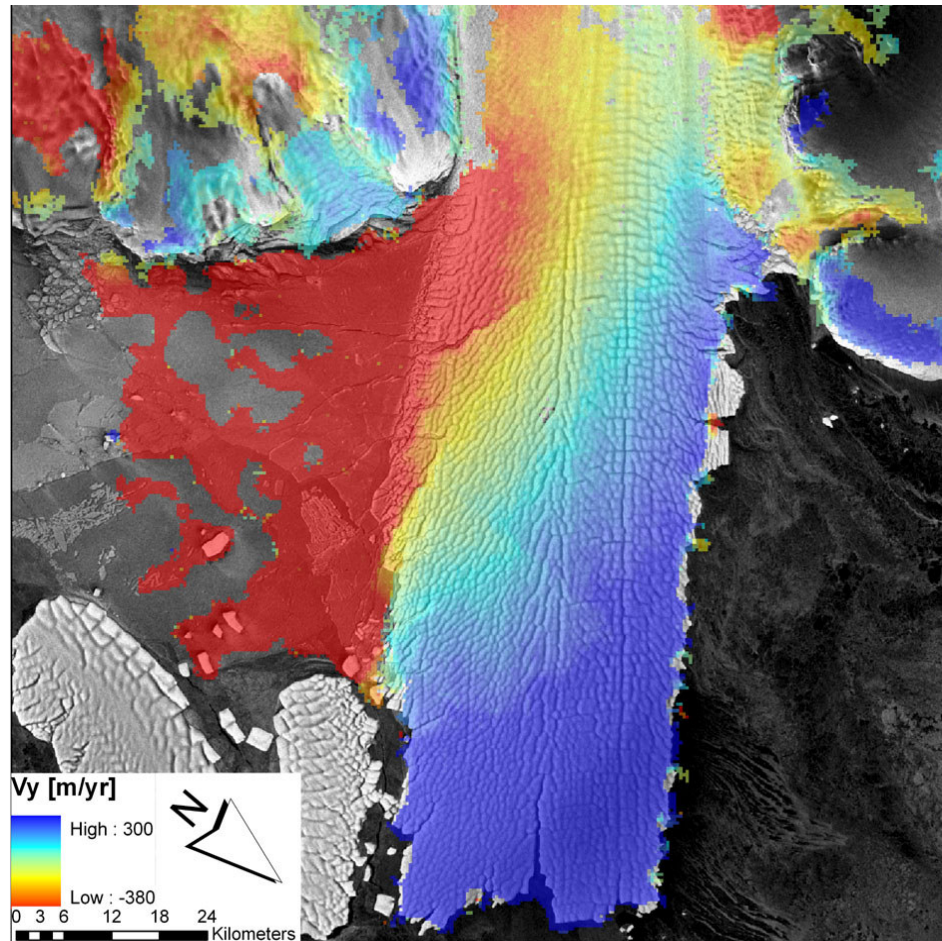


Figure 6.10 The y-component of velocity on MGT. Note the distinct step along the eastern margin that is associated with a large rift clearly visible in the image. The rift is opening up at a speed of roughly 100 m a^{-1} and decouples the remainder of MGT.

Closer investigation of the velocity field reveals a distinct step in velocity along the eastern boundary of MGT. Velocity across this step suddenly increases from 1050 m a⁻¹ to 1150 m a⁻¹. This step appears to be associated with a large rift that is opening up at a rate of approximately 100 m a⁻¹ in the direction of flow. The sudden velocity jump is especially pronounced in the y-component of velocity (figure 6.10). From the RADARSAT images we measure that the propagation speed of the rift (between 1997 and 2000) is in the order of 1500 m a⁻¹, which, if assumed constant, would lead to the break off of MGT somewhere around 2015. In reality it is far more likely that rift propagation varies through time, as observed on Pine Island Glacier (Bindshadler, 2002) and Amery Ice Shelf (Bassis and others, 2005). The opening of the rift is in synchrony with a westward rotation of MGT and a decoupling from the rest of the glacier hence the asymmetry in the velocity field. This rotation is also evident in the pattern of crevasses on the glacier. We believe that the original fracture might have been initiated at the point where MGT leaves the valley, because of shear along its margin, but that the fracture now acts as a weak point along which the built up of stresses, possibly associated with the westward moving sea current, are released. We compute the bending moment following a simple model by Thomas (1973) on the effects of sea currents on floating ice tongues. We adopt this elastic model rather than Holdsworth and Glynn's plastic analysis (1981) since the latter would be more appropriate for a curved tongue such as Erebus Glacier Tongue. For a vertical element of unit width the force acting in the y-direction is given by the moment lost per second by the sea given by (after Holdsworth, 1973):

$$F = V_w^2 \rho_i H \quad (6.3)$$

where V_w is the speed of the current, H the ice thickness and ρ_i the density of ice. The total moment on the vertical axis is then given by:

$$M = FL^2 / 2 \quad (6.4)$$

where L is the length of the glacier tongue. From bending theory the tensile stress at the origin (where the glacier leaves the fjord) is given by:

$$\sigma_x = 6MD_n^{-2}H^{-1} \quad (6.5)$$

Combining equation 6.3, 6.4 and 6.5 we find that:

$$\sigma_x = 3\rho_i(V_w R)^2 \quad (6.6)$$

Where R is the length to width ratio of the ice tongue, which is approximately 3 for MGT. Taking $\rho_i = 900 \text{ kg m}^{-3}$ and $V_w = 1.0 \text{ m s}^{-1}$ (a value we adopt from Legrésy and others, 2004) we find that the bending stress thus induced is in the order of 25 kPa which is about a sixth of the tensile stress at that point as calculated from strain rates with Glen's flow law. This is probably too small to instigate rift formation. However, once a crack has developed it would become larger, since the crack effectively increases the length to width ratio by decreasing the width at that point. In addition, tensile strength is likely reduced along previously developed crevasses. So in combination with tensile stress and current drag along the bottom the proposed mechanism might be enough to

reinitiate and propagate a rift. We thus conclude that the along shore current is a very likely contributor for the rift formation, propagation and eventual calving of MGT and the only feasible explanation, at least that we can think of, of the apparent rotation of the tongue. Over time the sea current would exert more pressure on the ice tongue as it gets longer. It seems intuitive that the current thus influences the critical length and that rift propagation is initiated whenever this length is reached. For MGT this critical length appears to be in the order of 80 to 90 km.

6.7 Flow dynamics

6.7.1 Driving Stress

Upstream from the grounding line velocities rapidly increase, figure 6.8 shows that this coincides with a very steep surface gradient of up to 0.016. Ice thickness measurements in this area are rather sparse and BEDMAP gives values ranging between 400 m and 700 m, which seem somewhat questionable considering the ice thickness of 1200 m at the grounding line estimated by radio echo sounding (Legrésy and others 2004). Even so this translates into values of up to 100 kPa for the driving stress.

To calculate the driving stress along the floating part of the Mertz Glacier Tongue we use the thickness profile as determined by radio echo sounding (RES) along the profile given in figures 6.2 and 6.8. Figure 6.8 also shows several thickness estimates derived from ICESat free board using ice densities of 900 kg m^{-3} and 917 kg m^{-3} . As can be seen in the figure along the first part of the floating glacier there is a better fit using a high density, while along the last part there is a better fit using the lower density. This can be explained by differences in snow accumulation since in the area very high wind

speeds are observed that are among the strongest in the world close to sea level (Wendler and others, 1994). The high wind speeds might prevent accumulation of snow along the first section. However, due to uncertainties in the depth averaged density we calculate the surface gradient of MGT from gridded ICESat elevation data (figure 6.8) and use the RES profile for ice thickness. Figure 6.11 shows the driving stress along the floating part of Mertz Glacier Tongue calculated using this data. The driving stress quickly declines from a value of about 21.4 ± 5.4 kPa at the grounding line to about 3.0 ± 2.4 kPa downstream where the glacier leaves the valley ($x \approx 55$ km). It then gradually declines to a value of about 0.2 ± 0.9 kPa at the calving front.

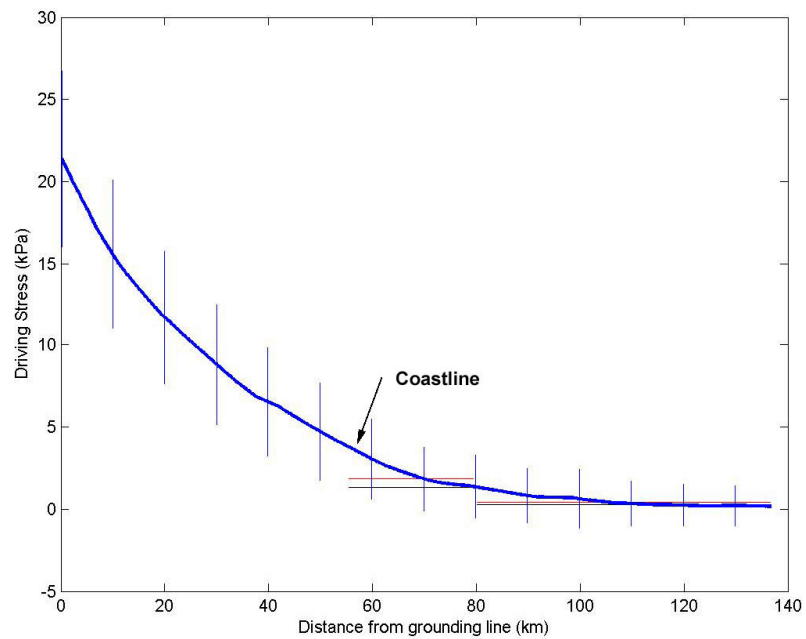


Figure 6.11 Driving stress of Mertz Glacier Tongue as a function of distance from the grounding line. The glacier leaves its valley about 55 km downstream from the grounding line. Error bars are shown in the figure. Horizontal lines show calculated values for longitudinal resistance for the ice tongue, assuming it is freely floating, according to Glen's flow law (black) and the Goldsby-Kohlstedt constitutive relation (red) (see chapter 6.7.3)

6.7.2 Lateral Drag

The relative importance of lateral drag in opposing the driving stress can be estimated where across flow velocity profiles and estimates of surface slope are available. This can be done even though ice thickness might be uncertain by assuming the ice thickness does not vary much across the width of the ice stream. Since the width averaged lateral resistance can be calculated by (equation 4.8):

$$F_s = \frac{H_w \times \max(R_{xy}) - H_{-w} \times \min(R_{xy})}{2W} \quad (6.7)$$

the relative contribution F_r in controlling glacier flow can be estimated by:

$$F_r = \frac{F_s}{\tau_{dx}} = \frac{\max(R_{xy}) - \min(R_{xy})}{2W(-\rho g \alpha)} \times 100\% \quad (6.8)$$

R_{xy} is calculated from across flow velocity profiles from Glen's flow law (and a rate factor corresponding to that of ice at -20°C) in a similar way as explained in chapter 4.7.3. Using this approach we find increasing values from about 20% to 32% for the very steep part above the grounding line. Using the Goldsby–Kohlstedt constitutive relation following the approach outlined in chapter 2.7, we find for a grain size of 3 mm values in the same range. This is as expected because this is a strain rate regime where both flow laws have parallel curves, so the gradient in shear stress is (almost) equal despite the different absolute value (figure 2.5).

At the grounding line we find lateral drag to be 21.2 ± 1.5 kPa for Glen's flow law (using a rate factor for ice at -16°C) and 24.3 kPa for Goldsby-Kohlstedt (for ice at -16°C and with a grain size of 3 mm). The driving stress is 21.5 ± 5.4 kPa which makes the relative contribution of lateral drag 98% for Glen's flow law and 100+% for Goldsby-Kohlstedt. Approximately 20 km downstream from the grounding line where Mertz Glacier flows through a fjord we find a lateral drag in the order of 11.4 ± 1.1 kPa for Glen's flow law. At this point the driving stress is 11.7 ± 3 kPa, signifying that lateral drag accounts for 97% of flow resistance. At the point where the glacier leaves the valley

velocity in the center of the stream is about 1050 m a^{-1} , while at the sides we measure velocities close to 900 m a^{-1} . A profile of the velocity taken at that point is given in figure 6.12. Associated lateral shear strain rates at the location vary between -0.007 a^{-1} and 0.007 a^{-1} . Since this is in the same order of magnitude as the longitudinal and transverse strain rates we choose here not to ignore these in the calculation of lateral drag and consider them constant across flow. To calculate shear stress we use:

$$R_{xy} = B \left[\left\{ \left(\frac{\partial u}{\partial x} \right)^2 + \left(\frac{\partial v}{\partial y} \right)^2 + \left(\frac{\partial u}{\partial x} \frac{\partial v}{\partial y} \right) + \left(\frac{1}{2} \left(\frac{\partial u}{\partial y} \right) \right)^2 \right\}^{1/2} \right]^{-2/3} \frac{1}{2} \left(\frac{\partial u}{\partial y} \right) \quad (6.9)$$

Using this we find the effective strain rate to be about 0.12 a^{-1} . We calculate a resistive stress of about 60 kPa and an averaged lateral resistance of $2.2 \pm 0.4 \text{ kPa}$ (using a rate factor for ice at -16°C) which is about 60% of the driving stress at that location ($3.7 \pm 2.6 \text{ kPa}$). Because here shear strain rates fall in a range where the slopes of the Glen and Goldsby-Kohlstedt curve are not parallel we find different values for the latter. Using Goldsby-Kohlstedt (for ice at -16°C and with a grain size of 3 mm) we find a resistive stress of about 78 kPa and an averaged lateral resistance of 2.9 kPa , which is 78% of the driving stress. Both approaches show that lateral drag controls flow here, although according to the Goldsby-Kohlstedt approach to a higher degree. The two approaches yield similar results if we use a grain size of 0.5 mm or a value for B that is about $100 \text{ kPa a}^{1/3}$ higher.

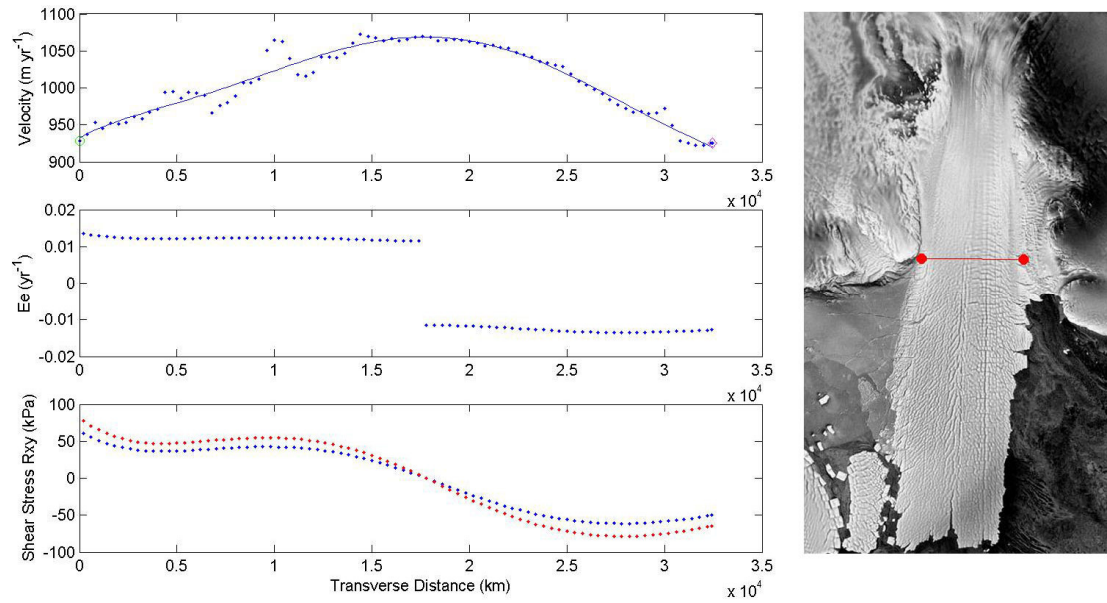


Figure 6.12 Velocity, effective strain rate and calculated shear stress (left panel) along a transect at the point where MGT leaves the fjord (right panel). In the upper panel the dots represent data points, the line is a best fit through the data and its slope is used, in combination with determined values for longitudinal and transverse strain rate, to calculate the strain rates (middle panel). In the lower panel the blue dots represent shear stress calculated from Glen's flow law (using a rate factor for ice at -16°C); the red dots represent shear stress calculated from the Goldsby-Kohlstedt constitutive relation (for ice at -16°C and with a grain size of 3 mm).

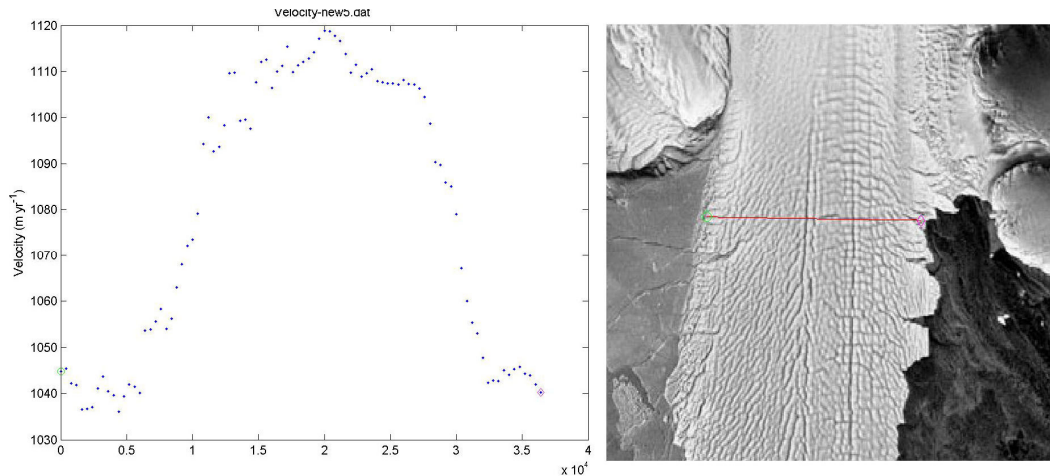


Figure 6.13 Across flow profile of velocity taken 10 km after MGT leaves the valley walls. A likely explanation for the gradient in velocity is an effect of sub-surface valley walls.

Another across flow profile, taken approximately 10 km after MGT leaves the valley walls shows it is nearly flat along its sides signifying that no lateral shearing occurs there (figure 6.13). However, we do measure a gradient in across flow velocity roughly between 5 and 15 km from the sides. A manual check of crevasse intersection displacements, along the margin and the center, confirms the difference in velocity is not an artifact (figure 6.14). This is approximately 0.004 a^{-1} or about half of that measured 10 km upstream. This could indicate that lateral drag from sub-surface valley walls still plays a role. We find the percentage of driving stress resisted in this way to be in the order of 50% (or 60% for Goldsby-Kohlstedt). Another 5 km further this effect is not seen. If the ice tongue would break off at the coast line, the reduced backpressure could potentially lead to an increase in along flow creep.

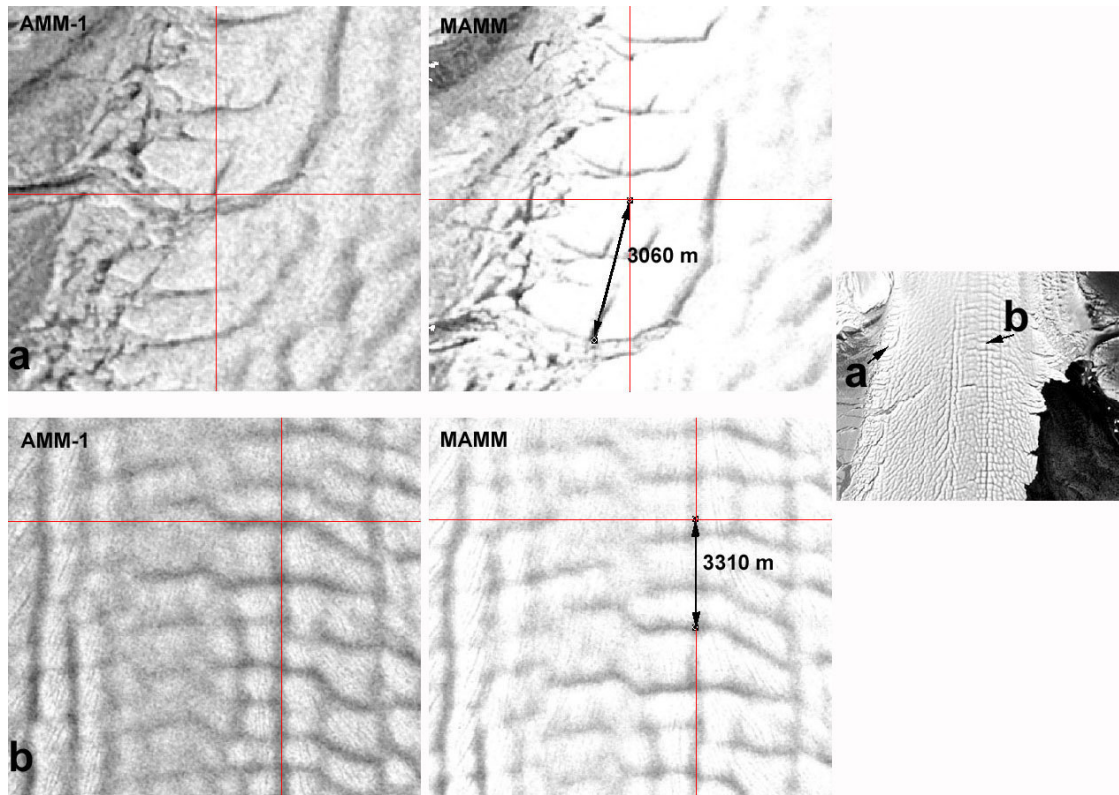


Figure 6.14 Manual check of displacements of two crevasse intersection points. The left two figures are AMM-1 images with the cross hair located on an intersection. The right two images show the cross hair in the same geographic location and the distance to the reference features is shown. Corresponding velocities are approximately 1020 m a^{-1} for the top images taken at the ice margin and 1103 m a^{-1} for the images at the bottom taken in the center of the glacier (see inset).

6.7.3 Longitudinal Stress Gradients

With the calculated values for the longitudinal and lateral spreading and the thickness profile (figure 6.8 and 6.9) we estimate the longitudinal stress gradients along the center of the floating part of the ice tongue. By fitting a line through the thickness profile we find a thickness gradient of approximately -0.009 along the first 80 km and -0.003 along the last part, with some small scale local variations that are ignored in this

analysis. Applying equation 2.32 we find an average longitudinal stress gradient of about 1.3 kPa which should be considered as an average value for the fjord and seems, taken together with lateral drag, to roughly balance the driving stress.

Along the ice tongue the thickness gradient is -0.009 along the first 30 km and -0.003 along the last 60 km. The change in slope of the thickness gradient falls at roughly the same point as the change in slope of the longitudinal strain rate as can be seen in figure 6.8. Thus, for a constant rate factor and when assuming the entire tongue is freely floating and spreading equally in both directions, we find two values for the longitudinal resistance. Along the first 30 km we find a value of about 1.3 ± 2.0 kPa and along the last section we find a value of about 0.3 ± 0.7 kPa. If we apply the Goldsby-Kohlstedt constitutive relation for a grain size of 3 mm this becomes 1.8 kPa and 0.4 kPa respectively. These values should then theoretically balance the driving stress. We find that within their error limits they do, although residuals are largest along the first part of the tongue and the assumption that horizontal spreading rates are equal in both directions does not apply there (figure 6.11). This apparent paradox is explained by the following analysis. First consider a free floating glacier where:

$$\begin{aligned}\dot{\epsilon}_{xx} &= \dot{\epsilon}_{yy} \\ \dot{\epsilon}_{zz} &= -2\dot{\epsilon}_{xx}\end{aligned}\tag{6.10}$$

In the absence of side drag we calculate the longitudinal stress from:

$$R_{xx} = B \left[\left\{ \frac{\dot{\epsilon}_{xx}^2}{2} + \frac{\dot{\epsilon}_{yy}^2}{2} + \frac{\dot{\epsilon}_{zz}^2}{2} \right\}^{1/2} \right]^{-2/3} (2\dot{\epsilon}_{xx} + \dot{\epsilon}_{zz}) \quad (6.11)$$

Combining equations 6.10 and 6.11 gives longitudinal stress as a function of longitudinal strain rate:

$$R_{xx} = \frac{3B\dot{\epsilon}_{xx}}{(3\dot{\epsilon}_{xx}^2)^{1/3}} \quad (6.12)$$

Next consider that the lateral spreading rate is twice the longitudinal spreading rate, then:

$$\begin{aligned} 2\dot{\epsilon}_{xx} &= \dot{\epsilon}_{yy} \\ \dot{\epsilon}_{zz} &= -3\dot{\epsilon}_{xx} \end{aligned} \quad (6.13)$$

Using this in equation 6.11 gives:

$$R'_{xx} = \frac{4B\dot{\epsilon}_{xx}}{(7\dot{\epsilon}_{xx}^2)^{1/3}} \quad (6.14)$$

The ratio of longitudinal stress between the two cases becomes:

$$\frac{R_{xx}}{R'_{xx}} = \frac{\frac{3B\dot{\epsilon}_{xx}}{(3\dot{\epsilon}_{xx}^2)^{1/3}}}{\frac{4B\dot{\epsilon}_{xx}}{(7\dot{\epsilon}_{xx}^2)^{1/3}}} = \frac{3}{4} \left(\frac{7}{3} \right)^{1/3} \approx 0.995 \quad (6.15)$$

Equation 6.15 shows that a doubling in the lateral spreading rate has thus hardly any effect on the magnitude of the longitudinal stress and its gradient along flow. The relative role of resistive stresses along the glacier is shown in figure 6.15.

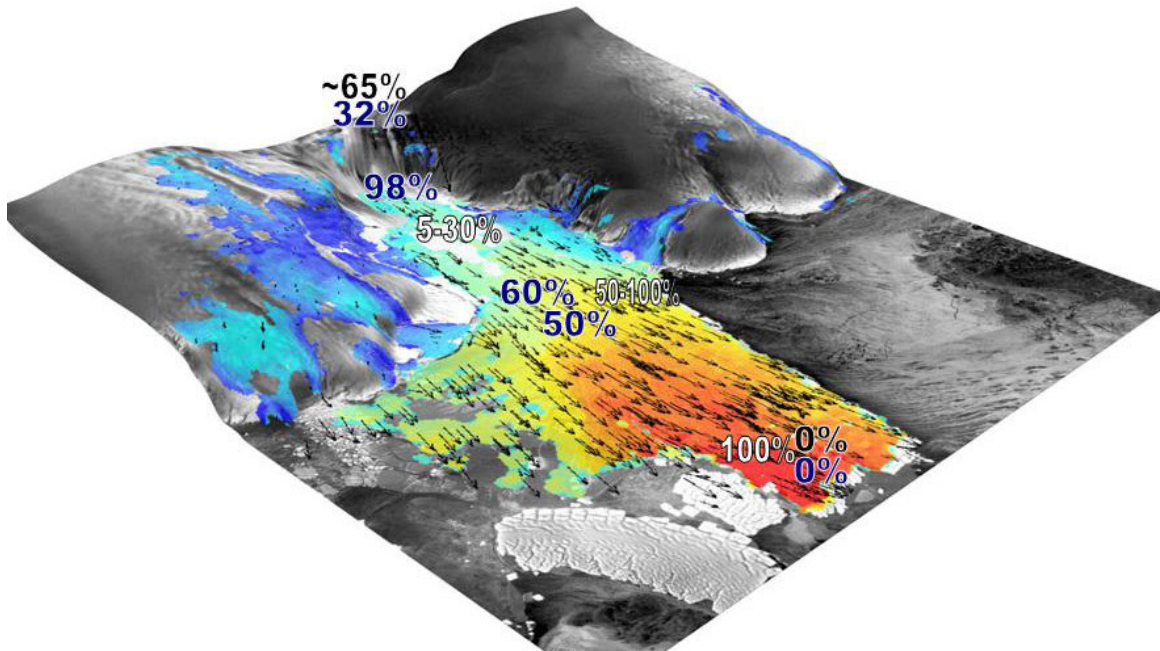


Figure 6.15 Relative contribution of basal drag (black), lateral drag (blue) and longitudinal stress gradients (white) in opposing the driving stress for the Mertz Glacier.

6.8 Summary and Conclusions

In this chapter we have produced two detailed velocity fields of Mertz Glacier Tongue derived from repeat RADARSAT imagery through feature tracking techniques over different time spans. A comparison with velocity estimates from an earlier study suggests no appreciable changes have occurred between 1998 and 2000.

We investigated calving along the ice tongue and found that calving occurs predominantly along its margins. Along the western margin the calving rate is constant with a rate of about 150 m a^{-1} , but on the eastern margin the glacier is welded by thick pack ice and calving occurs episodically. We observed a large rift along the eastern margin of MGT that seems to be opening at a rate of 100 m a^{-1} and propagating across the ice tongue at a rate of 1500 m a^{-1} . The opening of the rift is likely enhanced by a westward moving sea current that causes the remainder of the tongue to slightly rotate westward leading to a slightly asymmetric velocity field with higher measured velocities on the north east margin.

The stress analysis suggests that driving stress along the ice tongue is balanced by longitudinal stress gradients to within our error limits but indicate that along the first section of the ice tongue after it leaves the fjord the glacier is not a perfectly free floating glacier. Using the velocity data we calculated strain rates in the entire area and showed that MGT has the tendency to spread out laterally, rather than longitudinally, when it leaves the confining valley walls. Only after about 60 km (or about 50 years) do we find similar values for spreading in both x and y direction, implying that the glacier needs time to adjust to truly freely floating conditions. We have shown, however, that larger lateral spreading does not significantly affect the longitudinal stress gradient. Along the first 15 km after the glacier leaves the coast we still find some lateral drag, which implies that were the ice tongue to break off at the coastline this could lead to an increase in creep.

CHAPTER 7

THE SIGNIFICANCE OF ICE TONGUES

7.1 Introduction

The aim of this chapter is to discuss the significance of the ice tongues in our study areas on glacier flow and compare the results of our studies of David Glacier-Drygalski Ice Tongue, Brunt Ice Shelf-Stancomb-Wills Ice Tongue and Mertz Glacier Tongue presented in chapters 4-6. We also provide answers to our research questions discussed in chapter 1. These were: (1) Have velocities and stress fields changed over time? (2) What are the dominant forces for different glaciers in Antarctica and how do they vary within and between catchments? (3) Do present day ‘instantaneous’ velocities differ significantly from longer-term (3-year) averages? (4) Are selected areas behaving differently and if they do what are the responsible mechanisms and how do they affect mass balance?

7.2 Significance of ice tongues

7.2.1 Glaciological significance of ice tongues

In order to discuss the glaciological significance of a floating ice tongue on flow upstream it is necessary to define the term *backstress*. Van der Veen (1997, p. 178) defines the term as “the backstress at any point on an ice shelf represents the fraction of

the total driving force acting on the section of shelf extending from that point to the calving front, that is supported by lateral drag and/or basal drag acting on that section”.

As mentioned in chapter 2 the driving force of a glacier is opposed by the three flow-resistive forces: lateral drag, acting on the sides, basal drag from shearing along the bottom, and longitudinal stress gradients. Thus the net effect of the total backstress on a section of a glacier is the reduction of the longitudinal stress gradients on that section, in other words the additional backstress reduces the along flow creep rate from what it would be if this backstress was absent. For a floating glacier this backstress can stem from lateral drag from valley walls, rocky embayment's or any other source of lateral drag, and basal drag from pinning points at the bottom that lead to temporary re-grounding of the ice. If for any reason the ice shelf or ice tongue were to break off, the reduced backstress could lead to an increase in velocity. The sudden acceleration and thinning of several glaciers in the Antarctic Peninsula after the break up of Larsen A and Larsen B ice shelves has been ascribed to both melt water percolation (and associated reduction of basal drag) as well as to the reduced back stress effect (Scambos and others, 2004). Also the substantial thinning and acceleration of Jakobshavn Isbræ in Greenland is partly ascribed to reduction of back stress due to weakening of drag at grounded areas along the floating tongue initiated by thinning from enhanced basal melt (Thomas and others, 2003). For a free floating glacier, spreading in one direction and experiencing no backstress, the creep rate is related to the ice thickness according to a relation first derived by Weertman (1957):

$$\dot{\epsilon}_{xx} = \frac{1}{9} \left(\frac{\rho g}{2B} \left(1 - \frac{\rho_i}{\rho_w} \right) \right)^3 H^3 = \frac{1}{9} \left(\frac{\rho g h}{2B} \right)^3 \quad (7.1)$$

where B is the flow rate factor, H the ice thickness and h the surface elevation. In our study areas we found no evidence for any significant re-grounding once the glaciers leave their valley wall. In chapter 6 we showed that Mertz Glacier Tongue experiences some influence of lateral drag along the first 15 km after leaving its valley walls. Beyond that we find no evidence of any significant lateral shearing or re-grounding. As mentioned earlier, this implies that if the glacier breaks off after that point, no upstream effect is expected. This is supported by the good fit between calculated driving stress and longitudinal stress gradients along most of the ice tongue (figure 6.11). We find similar good fits on Drygalski Ice Tongue (figure 4.26) and Stancomb-Wills Ice Tongue (figure 5.9). However, if an ice tongue were to break off at the coast line the reduced backpressure could potentially lead to an increase in along flow creep. To estimate the magnitude of this effect we include additional lateral drag in the model for an ice shelf described in chapter 2. The longitudinal resistive stress then becomes a combination of equation 2.47 plus a component associated with the down-glacial integrated resistance associated with lateral drag (after Van der Veen, 1997):

$$R_{xx}(x) = \frac{1}{2} \rho_i g \left(1 - \frac{\rho_i}{\rho_w} \right) H - \sigma_b(x) \quad (7.2)$$

where $\sigma_b(x)$ is the backstress at x defined as:

$$\sigma_b(x) = \frac{1}{H} \int_x^L \frac{H\tau_s}{W} d\bar{x} \quad (7.3)$$

In this equation L is the length over which the additional drag occurs. For Mertz Glacier Tongue we find a width-averaged lateral drag of 2.2 ± 0.4 kPa at the point where the glacier leaves the fjord, whereas 15 km farther this is practically absent. If we assume that the drag effect declines linearly then we find $\sigma_b(\text{coastline}) \approx 27.5$ kPa. In comparison with the calculated longitudinal stress at the coast line (approximately 160 kPa.) this is about 17%. If the ice tongue were to break off at the coast line, the measured longitudinal stress would theoretically increase by this amount (at least temporarily). To estimate what the effect on the creep rate would be, we first need to invert the constitutive relation:

$$\dot{\epsilon}_{xx} = \Theta \left(\frac{R_{xx}}{B} \right)^3 \quad (7.4)$$

In this equation $\dot{\epsilon}_{xx}$ is the measured strain rate before the calving event ($\sim 4.0 \times 10^{-3} \text{ a}^{-1}$) and Θ is given by (after Thomas, 1973b):

$$\Theta = \frac{(1 + \alpha + \alpha^2)}{(2 + \alpha)^n} \quad (7.5)$$

where α is the ratio between $\dot{\epsilon}_{yy}$ and $\dot{\epsilon}_{xx}$. We showed that $\alpha = 2$ so Θ becomes 7/64.

After break off of the ice tongue the new creep rate ($\dot{\epsilon}'_{xx}$) is calculated from:

$$\dot{\epsilon}'_{xx} = \Theta \left(\frac{R_{xx} + \sigma_b}{B} \right)^3 \quad (7.6)$$

Here R_{xx} is the calculated value of longitudinal stress. From this we find that the creep rate becomes $\sim 6.0 \times 10^{-3} \text{ a}^{-1}$, which is about a 50% increase of the creep rate before break off. This shows that there potentially could be a significant change in flow rate, caused by the sudden reduction of the lateral drag exerted on the ice tongue. Also a possible thinning of the glacier could lead to reduced lateral drag, by reducing the contact area between sub-surface valley walls and the ice tongue.

Also on Drygalski Ice Tongue, based on the gradient in across flow velocity, there appears to be some lateral drag after the glacier leaves the valley walls (figure 7.1). This could perhaps stem from sub-surface valley walls or the adjacent Nansen Ice Shelf. The calculated magnitude of lateral drag is about $5.3 \pm 0.4 \text{ kPa}$, which is about 80% of the driving stress. A profile taken about 6 km from the coast line indicates that lateral drag quickly reduces to zero. This is much faster than observed on Mertz Glacier Tongue, likely because of a different configuration of (sub-surface) valley walls.

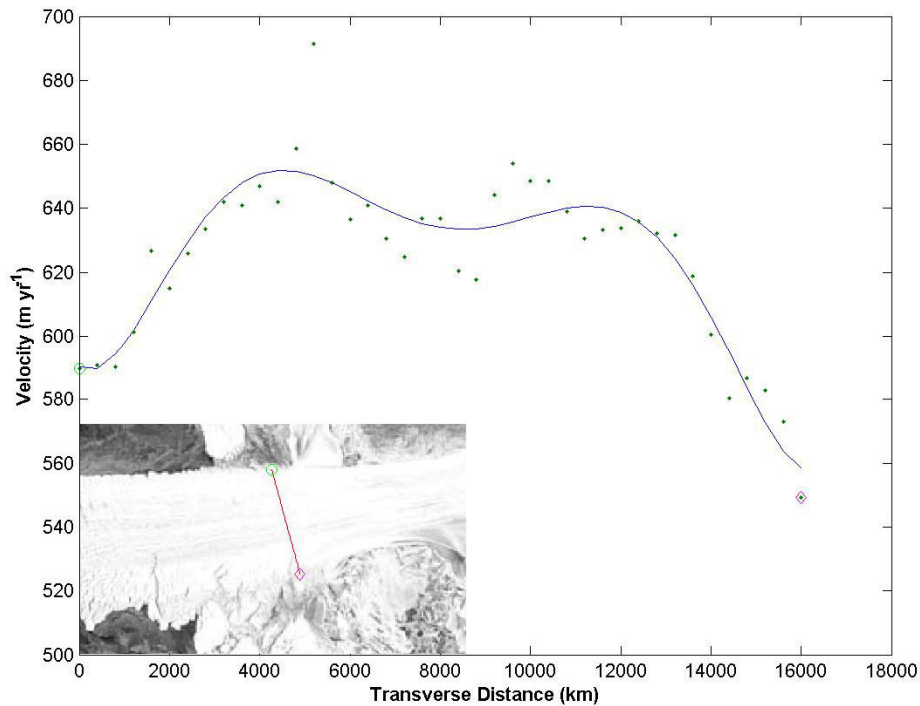


Figure 7.1 Across-flow profile of velocity on Drygalski Ice, just after the ice leaves the fjord walls. The location of the profile is indicated on the inset. The slight gradient in velocity could possibly stem from sub-surface valley walls or the adjacent Nansen Ice Shelf.

It is worth noting that these ice tongues do not behave as the theoretical free floating ice shelf, at least not along their entire length. We showed that the spreading rate in the across flow direction is at least twice the spreading rate in the along flow direction along the first section. For Mertz Glacier the two become more or less equal only after approximately 60 km from the coast line; we estimated the time associated with this to be about 50 years. More interestingly, even in the fjords of both Drygalski Ice Tongue and Mertz Glacier Tongue we found that lateral spreading rates at least equaled the longitudinal creep rate, signifying that these fjords do not prevent lateral spreading and

are not the hypothetically parallel valley walls that they at first sight appear to be and that are used in many models. Nonetheless, the fluctuations in lateral spreading do not affect the longitudinal resistance in a significant way (see chapter 6.7.3).

For the areas we investigated, we showed what the dominant forces along their drainage areas were. The relative role of lateral drag in their fjords declines from 100% to 60%. The relative high spreading rates that we measure in the fjords ensures that the ice will remain in contact with the valley walls and that release of back pressure is unlikely to occur for a given ice thickness. However, if the ice were to thin due to external causes, such as enhanced basal melting or reduced accumulation, the reduced thickness at the valley walls could lead to a change in lateral drag. Because both basal melt and lateral drag is found to be most important near the grounding line, this effect will be the strongest there. Stancomb-Wills Ice Tongue experiences some shear on its entire east margin, but almost none on the west side where it is bounded by a faster moving part of the Brunt Ice Shelf that appears to have calved. Although there is not a defined fjord near the grounding line, lateral shearing still accounts for 75% of the driving stress; further along the ice tongue it is less than 5%. Figure 7.2 shows a comparison of cross sections and longitudinal velocity in our study areas. The effect of the fjord walls on the profiles of Drygalski Ice Tongue and Mertz Glacier Tongue is clearly visible in the figure. These glaciers do not thin nearly as fast as Stancomb-Wills Ice Tongue.

Our stress analysis further shows that the large relative contribution of basal drag clearly distinguishes the tributaries of David Glacier and Mertz Glacier from the ice streams in West Antarctica, where resistance to flow mostly stems from lateral drag and basal drag is believed to be very small (Whillans and Van der Veen, 1997).

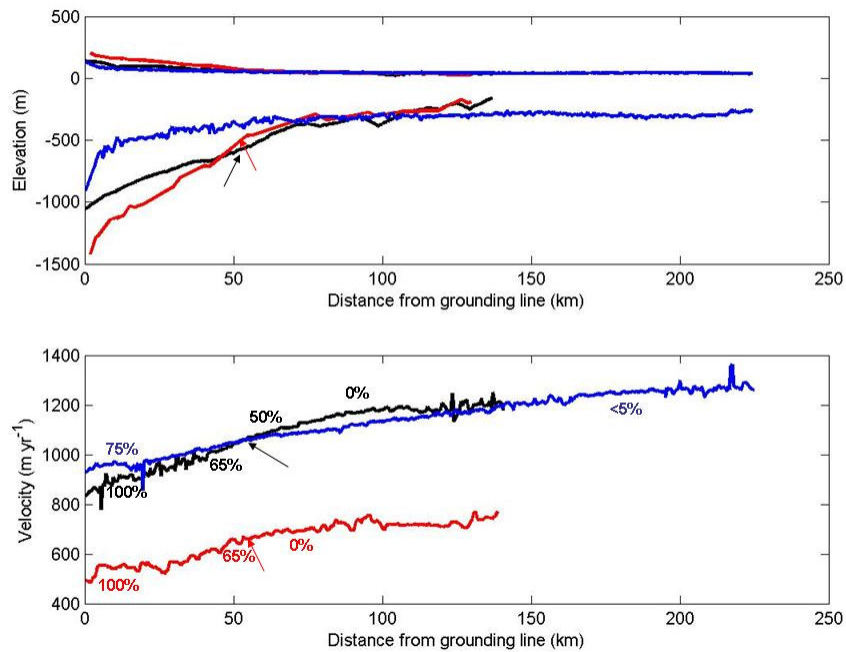


Figure 7.2 Comparison of cross sections and longitudinal velocity in our study areas: Drygalski Ice Tongue (red), Mertz Glacier Tongue (black) and Stancomb-Wills Ice Tongue (blue). Arrows denote the position where the glacier leaves the fjord, Relative contribution of side drag along flow is given in the figure.

7.2.2 Oceanographic significance of ice tongues

Near or adjacent to all of our study areas we find polynyas. These are large areas of open ocean water that do not freeze, but are surrounded by sea ice. Polynyas are important sea ice production sites. For example Kurtz and Bromwich (1985) suggest that as much as 10% of the annual sea ice production in the Ross Sea occurs in the Terra Nova Bay polynya. The sea ice formation leads to the production of high-salinity shelf water (HSSW). This cold high density water sinks to the bottom and polynyas are therefore thought to be important production sites of Antarctic Bottom Water (AABW). AABW is an important component in the global thermohaline circulation and supplies

nutrients to the deep oceans (Williams and Bindorff, 2003). Although strong katabatic winds are necessary to maintain a polynya, both Drygalski Ice Tongue and Mertz Glacier Tongue play a significant role in the existence of their adjacent polynyas, because they prevent sea ice build up by blocking along-shore currents (Bromwich and Kurtz, 1984; Massom and others, 2001). The Mertz Glacier polynya is the second largest polynya in East Antarctica (Cavalieri and Martin, 1985). Bromwich and Kurtz (1984) suggest the absence of this blocking effect as an important reason why polynyas are not found along other coasts with similar wind regimes.

The sea ice on the east side of Mertz Glacier, and south side of Drygalski Ice Tongue, moves with approximately the same speed and direction as the ice tongue close to it, but slower away from it, suggesting that the glacier and sea ice are coupled, with shearing occurring in the sea ice. The sea ice flow on Mertz Glacier Tongue seems to be coupled to the glacier even over prolonged time spans (3 year). Thus ice tongues play a role in the blocking and diverging of sea ice and currents, but are also partly responsible for the formation of them.

On the other hand the sea ice and currents also have an effect on an ice tongue. We showed that the presence of thick pack ice can reduce calving rate along parts of a glacier significantly by cementing the ice (chapter 6.6). The formation of HSSW activates an ocean circulation pattern that creates an ‘ice pump’ mechanism (Lewis and Perkins, 1986). This causes basal melting near the grounding line, which in turn creates fresh (less dense) rising Ice Shelf Water (ISW) that subsequently refreezes when it becomes super-cooled with respect to the local freezing point leading to basal freeze on. We showed that, on Drygalski Ice Tongue, the pattern of basal melting and freeze on is consistent with this

mechanism, with high melt rates near the grounding line and basal freeze on occurring where the valley walls widen and thickness rapidly declines (chapter 4.5). In addition, sea currents can have an effect on an ice tongue by reinitiating rifts in pre-existing crevasses, which could potentially lead to the calving of an ice tongue as demonstrated by our calculations for Mertz Glacier Tongue (chapter 6.6). Worth noting in this respect is that large icebergs brought along with currents can collide with an ice tongue and lead to large calving events, as observed on Drygalski Ice Tongue recently (chapter 4.6).

What exactly the consequences are for a glacier if changes in basal melt occur depends heavily on the configuration of the bed at the grounding line: sloping away from the ice front or towards the ice front. On a bed sloping away from the calving front, retreat would have a less dramatic impact as were the bed to slope towards the ice front. From the apparent stable configuration of the grounding line position of Mertz Glacier (determined from InSAR), despite very different tide levels, Legrésy and others (2004) conclude that the bed slope must be steep at the grounding line, sloping away from the ice front. Based on this, a sudden change in basal melt would not have a very dramatic impact. Due to the lack of accurate bed data near the grounding line of David Glacier and Stancomb-Wills Ice Tongue it is hard to make any predictions for these areas.

7.3 Temporal changes on ice tongues

We compared derived velocity on Drygalski Ice Tongue-David Glacier and Mertz Glacier-Mertz Glacier Tongue with data from VELMAP. Our velocity comparisons suggest longer term steady behavior as shown in chapters 4 and 6. For Stancomb-Wills Ice Tongue, the good agreement that was found from our flow stripe extrapolation using

RADARSAT images from 1997 and 2000 and a Landsat image from 1986 advocate that no dramatic changes have occurred. Thus for these areas we do not find the dramatic changes found in Greenland or the Antarctic Peninsula (e.g. Zwally and others, 2002; Thomas and others, 2003; Thomas and others, 2004; Rignot and Kanagaratnam, 2006; Luckman and others, 2006).

We also compared 3-year averaged feature tracking velocities with short term averaged (48-day) InSAR and feature tracking velocity and found these to agree as well to within their error limits. Table 7.1 shows a comparison of average velocity values in our study areas measured near the ice front and near the grounding line. The table shows values of 3-year averaged feature tracking results and 48-day averaged InSAR and feature tracking results.

Glacier	1997-2000		2000	
Drygalski Ice Tongue (~140 km)	736±35	560±35	744±114	530±114
Mertz Glacier Tongue (~150 km)	1225±35	846±35	1175±114	843±114
Stancomb-Wills Ice Tongue (~235 km)	1252±35	1000±35	1259±114	998±114

Table 7.1 Averaged velocity values in m a^{-1} near the ice front (black) and grounding line (red) in our study areas (approximate length of floating part is given between parentheses). In the case of Stancomb-Wills and Drygalski Ice Tongue, where little data at the grounding line was acquired over the 3-year time span, we measured velocity about 20 km downstream.

The constant velocities that we measure over these time spans imply that the short term velocities are representative for longer time spans and can be used to study longer term glacio-dynamic processes. We believe that the lack of any significant change in velocity also implies that the stress field for these areas did not change either. This, thus, permits the combination of various datasets, derived from both InSAR and feature tracking over different time spans, to optimize the velocity field in order to investigate the stress field. The lack of major changes in our study areas, however, does not indicate that no changes have occurred in other parts of East Antarctica. The combination of various datasets is therefore not per se applicable elsewhere in East Antarctica

7.3.1 Pine Island Glacier: a changing glacier

Not all ice tongues in Antarctica proper are in a steady state. In figure 7.3 we present feature tracking velocity of Pine Island Glacier in the Amundsen Bay region in West Antarctica, an area known to be undergoing rapid thinning (Rignot and others, 2002). We measure an average velocity of 2800 m a^{-1} near the calving front, making it one of the fastest moving glaciers in Antarctica. The feature tracking results did not provide enough coverage to warrant a detailed stress analysis, but do provide enough velocity data points for comparison with VELMAP velocity data from earlier studies (figure 7.4). Figure 7.4a shows a scatter plot that compares data derived in this study (1997-2000) with VELMAP data, derived using feature tracking techniques on Landsat images from 1973-1975 (data by Rosanova and Lucchitta) and 1986-1988 (data by Scambos and Bohlander). The locations of data points are shown in figure 7.3. For the comparison we only use those data points that fall within our velocity pixels; this

includes 29 data points for '73-'75 and 456 for '86-88. The figure clearly shows that velocity increased significantly over this ~25 yr time span. The amount of increase is represented by the two difference histograms shown in figure 7.4b. We measure an increase in velocity of, on average, 210 m a^{-1} between the 1986-1988 period and 1997-2000, which is roughly a 12 year period. The average increase in velocity between the 1973-1975 period and 1997-2000 is about 460 m a^{-1} . This increase occurred in a time span of about 24 years. This suggests that the velocity increase over time is nearly constant ($\sim 19 \text{ m a}^{-2}$) and not significantly increasing or decreasing.

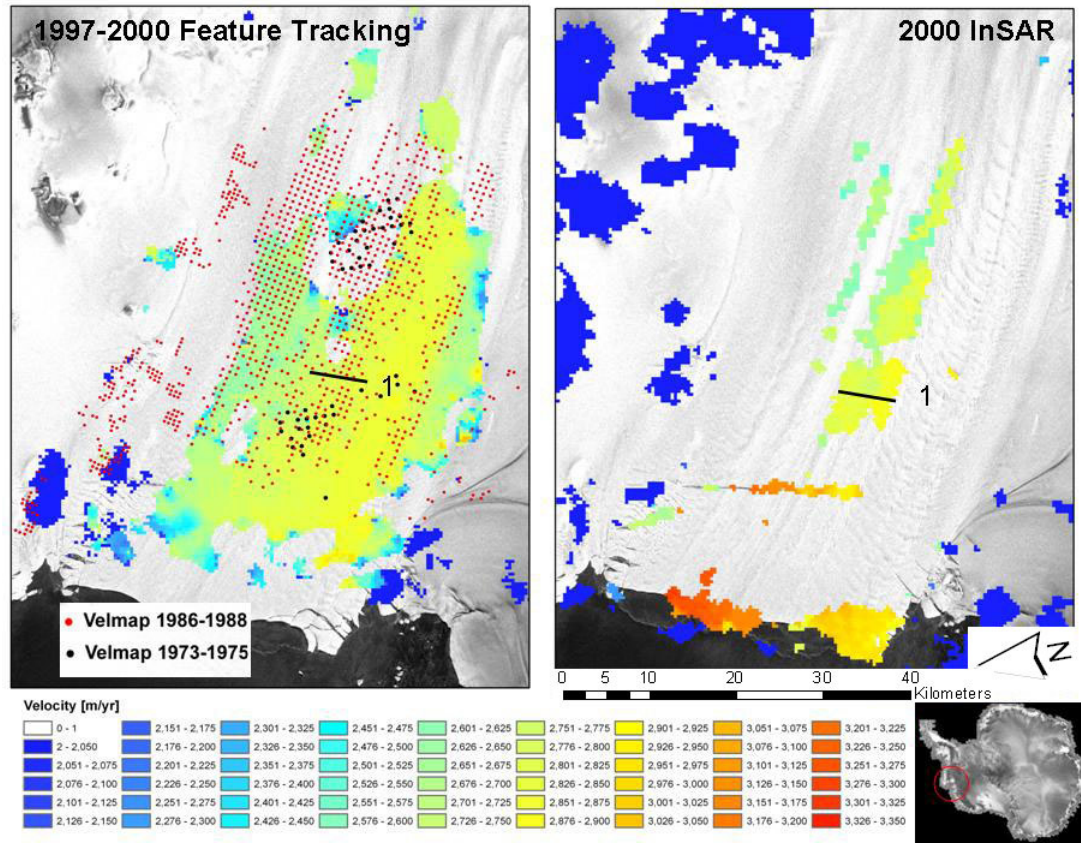


Figure 7.3 3-year averaged feature tracking velocity (left panel) and 2000 InSAR velocity (right panel) near the calving front of Pine Island Glacier in the Amundsen Bay region in West Antarctica (inset). Dots in left panel are VELMAP velocity data points derived from feature tracking on Landsat images between 1986-1988 (red) and 1973-1975 (black). A comparison between VELMAP data and feature tracking data is shown in figure 7.4. The line marked 1 is the location of a profile used for comparison between InSAR and feature tracking velocity (figure 7.5).

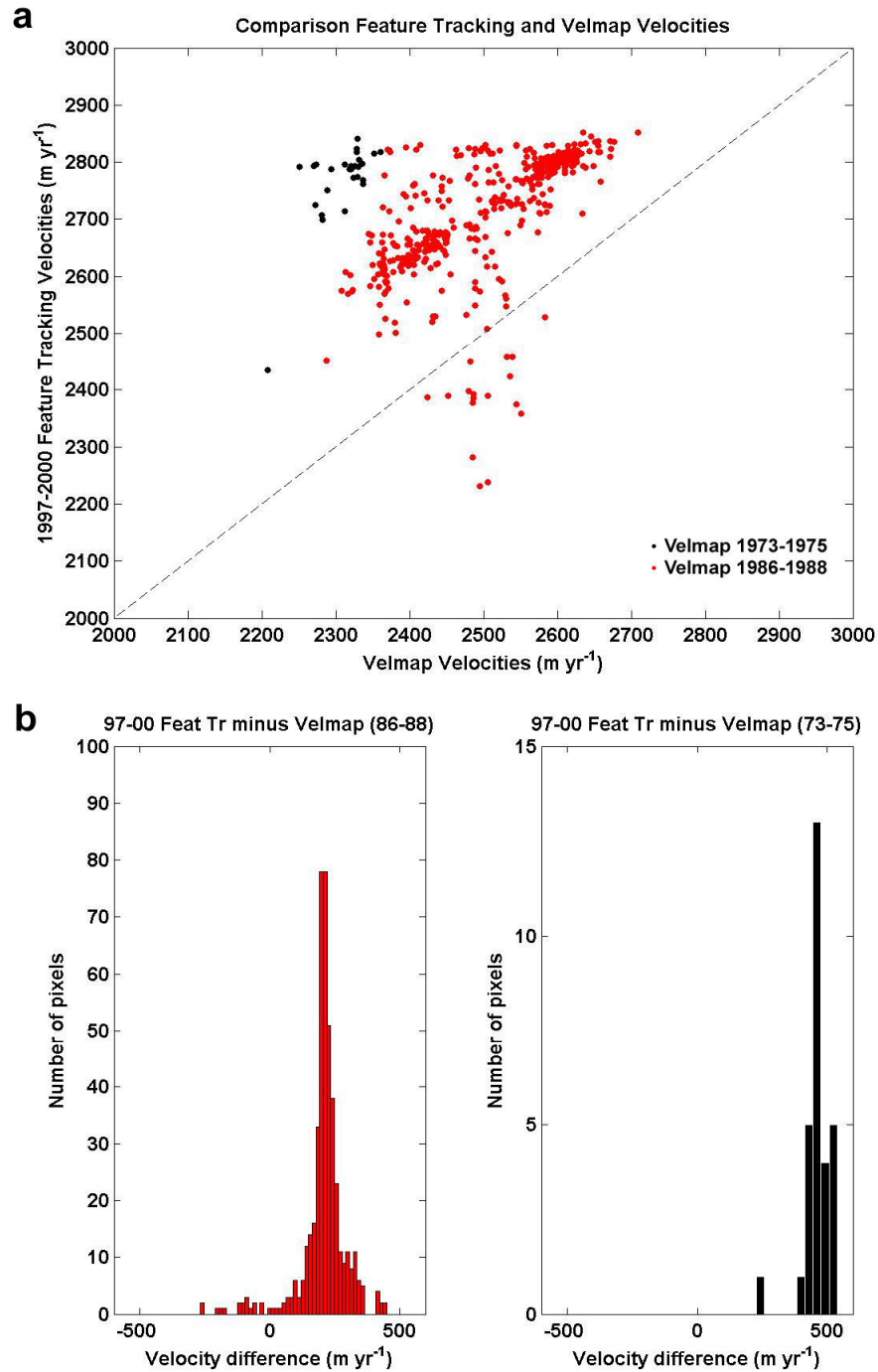


Figure 7.4 Comparison of velocity data derived in this study with earlier measurements available through VELMAP. a) Scatter plot of 1997-2000 velocity data points plotted against 1986-1988 (red) and 1973-1975 (black). b) Histogram of differences (same color coding) showing that there is a doubling in velocity change between '86-'88 and '97-'00 compared to '73-'75 and '97-'00.

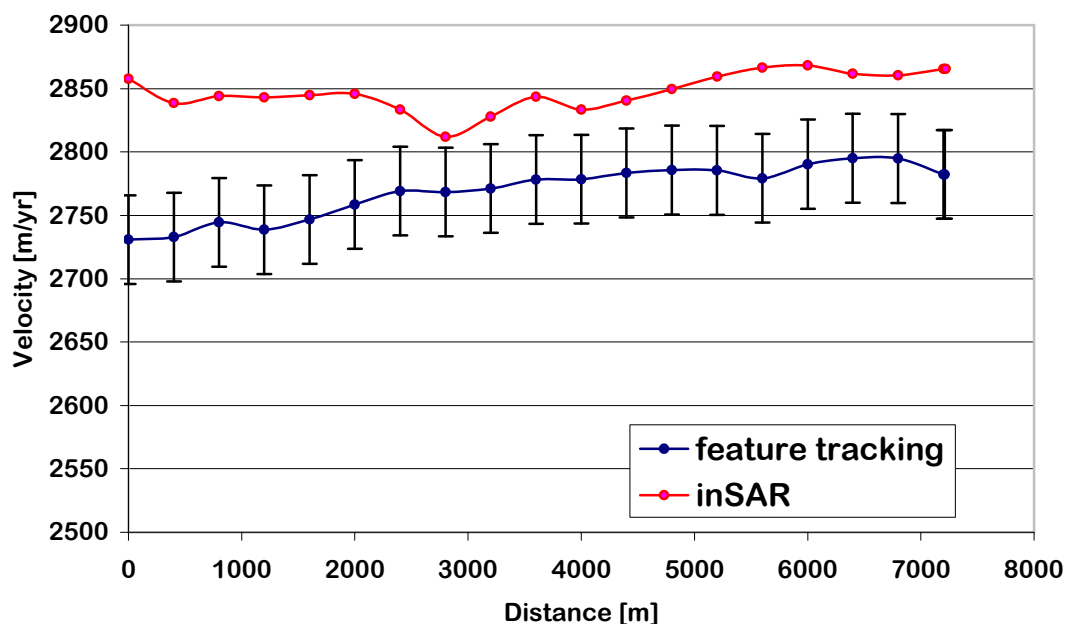


Figure 7.5 Comparison between a profile derived from 1997-2000 feature tracking velocity (blue) and 2000 InSAR velocity (red).

InSAR results in this area were especially poor, likely due to the fast velocity and associated de-correlation between acquisitions. Nevertheless we are able to compare feature tracking velocity with InSAR velocity along a profile close to the calving front of the glacier (figure 7.5). The profile shows a significant increase in velocity along its entire length and shows that our methods are capable of detecting changes. We did not observe a similar increase in velocity in any of our other study areas, indicating that the behavior of Pine Island Glacier is rather exceptional.

7.4 Ice tongues can provide clues to past ice sheet behavior

Our flow stripe analysis on Stancomb-Wills Ice Tongue (chapter 5.7 and 5.8) revealed another important value of ice tongues. Floating glacier tongues can be relevant in studying ice sheet behavior by providing indicators of past ice flow behavior and fluctuations.

While flow stripe deviations have been observed on Ross Ice Shelf and linked to changes in dynamics (Jezek, 1984), to our knowledge, the flow line pattern on SWIT, and the analysis we have done, provides the first glaciological evidence of this type that surge-type events can also occur and have occurred in East Antarctica. The abruptness of the relict flow stripe deviations suggests that these events can happen on short time scales. The configuration of the valley walls of Drygalski Ice Tongue and Mertz Glacier Tongue likely prevents similar extreme flow stripe-flow line deviations at those locations.

7.5 summary and conclusions

In this chapter we discussed the significance of floating ice tongues and provided answers to our research questions. For David Glacier-Drygalski Ice Tongue, Brunt Ice Shelf-Stancomb-Wills Ice Tongue and Mertz Glacier Tongue, we do not find the kind of velocity changes that are found in other more dynamic parts of Antarctica and Greenland. Instead this study presents evidence that the research areas seem to be rather stable over longer (decadal) time scales. Based on this we infer that the stress field has likely not changed significantly either. Additionally we showed that for our research areas, discussed in chapter 4-6, short term InSAR velocities are very similar as longer term (3

year) feature tracking results. This suggests that, on InSAR timescales (24-48 days), no serious fluctuations occur. It should be said, though, that we do not assert that no significant changes could have occurred elsewhere in East Antarctica.

In chapters 4, 5 and 6 we have investigated what the dominant forces for our study areas are and how they vary within their catchments. We showed that none of these glaciers behaves exactly like a theoretical free floating ice shelf for at least part of their flow. We find lateral strain rates to be higher than longitudinal strain rates along a significant length of their flow. And we find that once a glacier leaves a valley, there is still some lateral drag likely associated with sub-surface valley walls. Only farther on the ice tongues do lateral strain rates equal longitudinal strain rates. It emerged that both Drygalski Ice Tongue and Mertz Glacier Tongue show very similar behavior, as might be expected from the peculiar similarities in configuration of their flow paths. The relative role of lateral drag decreases from about 100% to 60% along their fjords. Stancomb-Wills glacier is much wider and longer but also experiences lateral drag near its grounding line but not any from the adjacent Brunt Ice Shelf.

We show that the reduction of lateral drag could potentially lead to an increase in along-flow creep if an ice tongue were to break off. We further conclude that floating ice tongues are important, apart from their oceanographic role, because they can provide clues to past ice sheet behavior and fluctuations.

CHAPTER 8

CONCLUSIONS

8.1 Summary

Recent observations show that some outlet glaciers in Greenland and Antarctica undergo rapid changes in flow velocity and ice thickness. At least part of these changes has been ascribed to changes in their dynamics. Measuring ice flow velocity of glaciers and gradients in velocity are first steps in studying their dynamics and possible response to climatic changes. With the launch of the Canadian RADARSAT-1 satellite in 1995 and the RADARSAT-1 Antarctic Mapping Project (RAMP) a great opportunity arose to derive ice flow velocity of Antarctica's glaciers remotely and averaged over various time spans. This allowed for a detailed study of spatial and temporal fluctuations in their velocity and stress fields.

One of the foremost contributions of this study are the high-resolution surface velocity maps, derived from the RAMP data, of several major Antarctic outlet glaciers up to the calving front. For some of these earlier data was, to say the least, scarce. We have improved, optimized and streamlined the feature tracking procedure in order to extract as

much reliable velocity data as possible from the wealth of data provided by the satellite images. This included several steps: image pre-processing, inclusion of a variable sized window extraction routine and noise removal.

We have used derived velocity maps to investigate velocity variability and the dynamics of several outlet glaciers in great detail. To do this we extracted velocity gradients and used this by means of ice flow models in combination with various other datasets, including BEDMAP, VELMAP, OSUDEM, ICESat and InSAR-derived velocity, to infer stresses acting on the glacier. A second contribution is the implementation and investigation of implications of a different flow law, which has recently been developed, in the existing force-budget model. We find that, depending on the regime, derived stresses can be affected, but caution that in order to get a true grip on the differences, detailed information on both depth-averaged grain size and temperature are required. This is information that is often not readily available and forms one of the major limitations of this study.

A third contribution of this study is the detailed analysis of the flow regimes of David Glacier-Drygalski Ice Tongue, Mertz Glacier-Mertz Glacier Tongue and Brunt Ice Shelf-Stancomb-Wills Ice Tongue, with special emphasis on their floating termini. We investigated whether or not our selected study areas in East Antarctica undergo the same rapid changes, or are susceptible to them, as some changing glaciers found elsewhere. The investigations revealed several interesting things about these glaciers. First of all we presented velocity comparisons that suggest their flow has been rather constant over decadal timescales confirming that they do not undergo rapid changes currently, in sharp contrast with some glaciers found elsewhere, such as Pine Island Glacier. Based on the

apparent constant velocity we infer that their stress field has likely not changed significantly either, thus permitting the combination of various data sets (averaged over different time spans) to optimize the velocity field in order to study their dynamics in greater detail than previously possible. Secondly, we show that the flow stripes found on Stancomb-Wills Ice Tongue are in fact relict flow lines and likely represent evidence of a glacial surge, followed by thinning and a grounding line retreat that occurred on Stancomb-Wills glacier more than 100 years ago. This, to our knowledge, is the first glaciological evidence of such type that surge type events can occur and have occurred in East Antarctica. Thirdly, we discovered a large rift on Mertz Glacier Tongue that seems to propagate under the influence of along-shore currents and might ultimately be the point of calving in the near future. Fourth, we show that the relative contribution of side drag declines along the fjords in our study areas, but demonstrate that the glaciers are not immediately true free floating ice shelves once they leave the valley walls. We find lateral spreading rates to be at least double the longitudinal spreading rates. We also find some lateral drag, likely from sub-surface valley walls, which could potentially lead to an increase in along flow creep if an ice tongue were to break off or thin. Finally, we conclude that floating ice tongues are important, because they can provide clues to past ice sheet behavior and fluctuations.

8.2 Recommendations for future research

Projects such as the ICESat missions and GRACE make it possible to establish whether changes in glacier mass and ice thickness occur. It is of importance to investigate how changes in thickness over time affect the velocity and stress field of real outlet glaciers.

The timeframe of the study did not allow for detailed analysis of many other interesting areas. We investigated several major outlet glaciers in East Antarctica, but many smaller and larger ones deserve more attention as well. One question that remains, for instance, is why did Ninnis Glacier retreat, while the adjacent Mertz Glacier Tongue advanced. It is likely that they are in a different stage of their lifespan but a detailed dynamic investigation is needed.

Finally this study uses a variety of remotely sensed datasets. New technologies will arise that likely lead to more accurate datasets and allow for more detailed analyses. As the satellite era gets longer, temporal variability can be studied in greater detail and with more confidence, making it easier to establish links with climatic changes. This study forms an important benchmark for such a future study.

REFERENCES

- Alley, R.B., Clark, P.U., Huybrechts, P. and Joughin, I. 2005. Ice-sheet and sea-level changes. *Science*, 310, 456-460.
- Ardus, D.A. 1965. Surface Deformation, Absolute Movement and Mass Balance of the Brunt Ice Shelf near Halley Bay, 1961. *BAS Bulletin*, 6, April 1965. 21-41.
- BAS. 2005. Proposed Construction and Operation of Halley VI Research Station, Brunt Ice Shelf, Antarctica. Draft Comprehensive Environmental Evaluation (CEE). *British Antarctic Survey Report*, February 2005. 79pp
- Bassis, J. N., R. Coleman, H. A. Fricker, and J. B. Minster. 2005. Episodic propagation of a rift on the Amery Ice Shelf, East Antarctica, *Geophys. Res. Lett.*, 32, L06502, doi:10.1029/2004GL022048.
- Benn, D.I. and Evans, D.J.A. 1998. *Glaciers and glaciation*. London, Edward Arnold.
- Berthier, E., B. Raup and T. Scambos. 2003. New velocity map and mass-balance estimate of Mertz Glacier, East Antarctica, derived from Landsat sequential imagery. *J. Glaciol.*, 49 (167), 503-511.
- Bindschadler, R. A. 2002. History of lower Pine Island Glacier, West Antarctica, from Landsat imagery. *J. Glaciol.*, 48 (163), 536-44.
- Bindschadler, R.A., M. King, R.A. Alley, S. Anandakrishnan and L. Padman. 2003. Tidally Controlled Stick-Slip Discharge of a West Antarctic Ice Stream, *Science*, 301, 1087-1089
- Bindschadler, R.A., P. Vornberger, D. Blankenship, T.A. Scambos and R. Jacobel. 1996. Surface velocity and mass balance of ice streams D and E, West Antarctica, *J. Glaciol.* 42 (142), 461-475.
- Bindschadler, R. A. and T. A. Scambos. 1991. Satellite-image-derived velocity field of an Antarctic ice stream. *Science*, 252 (5003), 242-246.

- Bromwich, D. H. and D. D. Kurtz. 1984. Katabatic wind forcing of the Terra Nova Bay Polynya. *J. Geophys. Res.*, 89(C3), 3561-3572.
- Caprioli R., A.M. Della Vedova, R. Gragnani, P. Grigioni, V. Maggi, F. Serra, B. Stenni and S. Torcini. 1998. Stratigraphic, isotopic and chemical profiles of a firn core from Drygalski Ice Tongue and of a snow pit from Aviator Glacier (Northern Victoria Land, Antarctica). *Terra Antarctica Rep.*, 1, 1997, 71-76.
- Casassa, G., K. C. Jezek, J. Turner, and I. M. Whillans. 1991. Relict flow stripes on the Ross Ice Shelf, *Ann. Glaciol.*, 15, 132-138.
- Cavalieri, D. J., and S. Martin. 1985. A passive microwave study of polynyas along the Antarctic Wilkes Land Coast, in *Oceanology of the Antarctic Continental Shelf, Antarct. Res. Ser.*, **43**, pp. 227- 252, edited by S. Jacobs, AGU, Washington, D.C.
- Crabtree, R.D. and C.S.M. Doake. 1980. Flow lines on Antarctic ice shelves. *Polar Rec.*, 20(124), 31-37.
- Dansgaard, W., H.B. Clausen, N. Gundestrup, C.U. Hammer, S.J. Johnsen, P. Krinstindottir and N. Reeh. 1982. A new Greenland deep ice core. *Science*, 218, 1273-1277.
- Dansgaard, W., J.W. White and S.J. Johnsen. 1989. The abrupt termination of the Younger Dryas climate event. *Nature*, 339, 532-534.
- De Angelis, H, and P. Skvarca. 2003. Glacier surge after ice shelf collapse. *Science*, 299, 1560-1562.
- Duval, P., Montagnat, M. 2002. Comment on “Superplastic deformation of ice: Experimental observations” by D.L. Goldsby and D.L. Kohlstedt. *J. Geophys. Res.* 107, 2082, 10.1029/2001JB000946.
- Echelmeyer, K.A. and W.D. Harrison. 1999. Ongoing migration of Ice Stream B, Antarctica. *J. Glaciol.* 45(150), 361-369.
- ESA. 2005. Envisat: Antarctica B-15A iceberg monitoring in Ross Sea. http://earth.esa.int/ew/special_events/iceberg-b15_antartic (accessed on March 9, 2006).
- Frezzotti, M. 1993. Glaciological study in Terra Nova Bay, Antarctica, inferred from remote sensing analysis. *Ann. Glaciol.*, 17, 63-71.

- Frezzotti, M., I. E. Tabacco and A. Zirizzotti. 2000. Ice discharge of eastern Dome C drainage area, Antarctica, determined from airborne radar survey and satellite image analysis. *J. Glaciol.*, 46 (153), 253-264.
- Frezzotti, M., A. Capra and L. Vittuari. 1998. Comparison between glacier ice velocities inferred from GPS and sequential satellite images. *Ann. Glaciol.*, 27, 54-60.
- Frezzotti, M. and M. C. G. Mabin. 1994. 20th Century behavior of Drygalski Ice Tongue, Ross Sea, Antarctica. *Ann. Glaciol.*, 20, 397-400.
- Goldsby, D.L., 2006. Superplastic flow of ice relevant to glacier and ice-sheet mechanics. In: P. Knight, ed. 2006. *Glacier science and environmental change*. CITY Blackwell Publishing. 544 pp.
- Goldsby, D.L., Kohlstedt, D.L. 2001. Superplastic deformation of ice: experimental observations. *J. Geophys. Res.* 106, 11017–11030.
- Goldstein, R. M., H. Engelhardt, B. Kamb, and R. M. Frolich. 1993. Satellite radar interferometry for monitoring ice-sheet motion: application to an Antarctic ice stream, *Science*, 262, 1525-1530.
- Gow, A.J. 1970. Preliminary results of studies of ice cores from the 2164 m deep drill hole, Byrd Station, Antarctica. *IASH*, 86, 78– 90.
- Gow, A. J., D. A. Meese, R. B. Alley, J. J. Fitzpatrick, S. Anandakrishnan, G. A. Woods, B. C. Elder. 1997. Physical and structural properties of the Greenland Ice Sheet Project 2 ice core: A review. *J. Geophys. Res.*, 102(C12), 26,559–26,576.
- Hayes, K. 2004. Brunt Ice Shelf: Lifetime of Halley. Unpublished report. BAS, Cambridge.
- Holdsworth, G. 1985. Some effects of ocean currents and wave motion on the dynamics of floating glacier tongues. *Antarctic Res. Ser.*, 43, 253-271.
- Hooke, R. 1981. Flow law for polycrystalline ice in glaciers: comparison of theoretical predictions, laboratory data, and field measurements, *Rev. Geophys. Space Phys.* 19,664-672.
- Hughes, T. 2003. Geometrical force balance in glaciology, *J. Geophys. Res.*, 108(B11), 2526, doi:10.1029/2003JB002557.
- Hulbe, C.L., R. Johnston, I. Joughin, T. Scambos. 2005. Marine ice modification of fringing ice shelf flow. *Arctic, Antarctic, and Alpine Research*, 37 (3), 323-330.

- IPCC. 2001. Climate Change 2001: The Scientific Basis, Contribution of working group I to the third assessment report of the Intergovernmental Panel on Climate Change, IPCC Rep.
- IPCC. 2001. Summary for policymakers, a report of working group I of the Intergovernmental Panel on Climate Change, IPCC Rep.
- Jacobs, S.S., C.F. Giulivi, and P.A. Mele. 2002. Freshening of the Ross Sea during the late 20th century, *Science*, 297, 386-389.
- Jezek, K. C. 2003. Observing the Antarctic Ice Sheet Using the RADARSAT-1 Synthetic Aperture Radar. *Polar Geography*, 27 (3), 197-209.
- Jezek, K. C. 2002. RADARSAT-1 Antarctic Mapping Project: change detection and surface velocity campaign. *Ann. Glaciol.*, 34, 263-268.
- Jezek, K. C. 1998. RADARSAT Antarctic Mapping Project, proceedings of the Post Antarctic Imaging Campaign-1 working group meeting. *Tech. Rep.*, 17, Byrd Polar Res. Cent., The Ohio State University, Columbus, OH.
- Jezek, K. C. 1984. Recent changes in the dynamic condition of the Ross Ice Shelf, Antarctica, *J. Geophys. Res.*, 89, 409-416.
- Jezek, K. C., R. Carande, N. Labelle-Hamer, K. Farness and X. Wu. 2003. RADARSAT-1 synthetic aperture radar observations of Antarctica: Modified Antarctic Mapping Mission, 2000. *Radio Science*, 38(4), 8067. (10.1029/2002RS002643.)
- Joughin, I., W. Abdalati and M. Fahnestock. 2004. Large fluctuations in speed on Greenland's Jakobshavn Isbræ glacier. *Nature*, 432, 608-610.
- Joughin, I., and S. Tulaczyk. 2002. Positive mass balance of the Ross Ice Streams, West Antarctica, *Science*, 295, 476-480.
- Joughin, I., L. Gray, R. Bindshadler, S. Price, D. Morse, C. Hulbe, K. Mattar, C. Werner. 1999. Tributaries of West Antarctic ice streams revealed by RADARSAT interferometry. *Science*, 286(5438), 283-286.
- Joughin I., D. Winebrenner, M. Fahnestock, R. Kwok, and, W. Krabill. 1996. Measurement of ice-sheet topography using satellite radar interferometry, *J. Glaciol.*, 42 (140), 10-22.
- Kim, K-T. 2004. Satellite mapping and automatic feature extraction: geographic information system-based change detection on the Antarctic coast. Ph.D. Dissertation, The Ohio State University.

- Kwok, R. 1998. Chapter 11: The RADARSAT Geophysical Processor System. In: *Analysis of SAR Data of the Polar Oceans*. C. Tsatsoulis and R.Kwok, Eds., Springer-Verlag, 235–257.
- Lambeck, K., T. M. Esat and E-K. Potter. 2002. Links between climate and sea levels for the past three million years. *Nature*, 419, 199-206 (12 September 2002) | doi: 10.1038/nature01089
- Legrésy, B., A. Wendt, I. Tabacco, F. Remy and R. Dietrich. 2004. Influence of tides and tidal current on Mertz Glacier, Antarctica. *J. Glaciol.*, 50 (170), 427-435.
- Lewis, E. L. and R. G. Perkin. 1986. Ice pumps and their rates. *J. Geophys. Res.*, 91(C10), 11756-11762.
- Liu, H. 2000. Development of An Antarctic Digital Elevation Model, *BPRC report*, No.19, ISSN: 0896-2472, Byrd Polar Research Center, Ohio State University, Columbus, Ohio, 157pp.
- Liu, H. and K.C. Jezek. 2004. A complete high-resolution coastline of Antarctica extracted from orthorectified RADARSAT SAR imagery. *Photogrammetric Engineering and Remote Sensing*, 70(5), 605-616.
- Lucchitta, B.K., C.E. Rosanova, and K.F. Mullins. 1995. Velocities of Pine Island Glacier, West Antarctica, from ERS-1 SAR Images. *Ann. Glaciol.* 21:277-283.
- Lucchitta, B. K., K. F. Mullins, A. L. Allison and J. G. Ferringo. 1993. Antarctic glacier tongue velocities from Landsat images: first results. *Ann. Glaciol.*, 17, 356-366.
- Luckman, A., T. Murray, R. de Lange, and E. Hanna. 2006. Rapid and synchronous ice-dynamic changes in East Greenland, *Geophys. Res. Lett.*, 33, L03503, doi:10.1029/2005GL025428.
- Lythe, M.B., Vaughan, D.G. and the BEDMAP Consortium. 2000. BEDMAP - bed topography of the Antarctic. 1:10,000,000 scale map. BAS (Misc) 9. Cambridge, British Antarctic Survey. (<http://www.antarctica.ac.uk/aedc/bedmap/>)
- MacAyeal, D. R. and V. Barillon. 1988. Ice-shelf response to ice-stream discharge fluctuation: I. Unconfined ice tongues. *J. Glaciol.*, 34(116), 121-127.)
- MacAyeal, D.R., R.A. Bindshadler, K.C Jezek, and S. Shabtaie, 1988. Can relict crevasse plumes on Antarctic ice shelves reveal a history of ice-stream fluctuation? *Ann. Glaciol.*, 11, 77-82.

- Massom, R.A., Hill, K.L., Lytle, V.I., Worby, A.P., Paget, M., Allison, I. 2001. Effects of regional fast-ice and iceberg distributions on the behaviour of the Mertz Glacier polynya, East Antarctica. *Ann. Glaciol.*, 33, 391–398.
- Mercer, J.H. (1978). West Antarctic Ice Sheet and CO₂ greenhouse effect: a threat of disaster. *Nature*, 271:321-325.
- Monaghan, A.J., D.H. Bromwich, R.L. Fogt, S-H. Wang, P.A. Mayewski, D.A. Dixon, A.A. Ekaykin, M. Frezzotti, I.D. Goodwin, E. Isaksson, S.D. Kaspari, V.I. Morgan, H. Oerter, T.D. van Ommen, C.J. van der Veen, and J. Wen. 2006. Insignificant change in Antarctic snowfall since the International Geophysical Year, *Science*, 313, 827-831.
- Noltimier, K., K. Jezek, H. Sohn, B. Li, H. Liu, F. Baumgartner, V. Kaupp, J. Curlander, B. Wilson, and R. Onstott. 1999. RADARSAT Antarctic mapping project – Mosaic construction. Proceedings of the International Geoscience and Remote Sensing Symposium IGARSS'99, Hamburg, Germany, 28 June – 2 1999, IEEE, Piscataway, NJ, USA, 5, 2349–2351.
- NSIDC. 2000. VELMAP: Antarctic ice velocity data. <http://nsidc.org/data/velmap/>
- Nye, J.F. 1957. The distribution of stress and velocity in glaciers and ice sheets. *Proceedings of the Royal Society of London*, Series A, 239, 113-133.
- Nye, J. F. 1953. The flow law of ice from measurements in glacier tunnels, laboratory experiments and the Jungfraufirn borehole experiment. *Proceedings of the Royal Society of London*, Series A, 219 (1139), 477-489.
- Oeschger, H., J. Beer, U. Siegenthaler, B. Stauffer, W. Dansgaard and C.C. Langway. 1984. Late glacial climate history from ice cores. In: *Climate processes and climate sensitivity*, J.E. Hansen and T. Takahashi (eds.), American Geophysical Union, Washington. 299-306
- Pötzsch, A., B. Legresy, W. Korth and R. Dietrich. 2000. Glaciological Investigation of Mertz Glacier, East Antarctica, using SAR Interferometry and field observations. *Proceedings of ERS - ENVISAT Symposium*, Gothenburg, 16 - 20 October 2000. (ESA Publication SP-461).
- Rack, W. 1995. *Strueverhalten und morphologie der antarktischen Shneedecke aus Scattero-Messungen von ERS-1*. Diploma Thesis, Science Faculty, University of Innsbruck.
- Rapp, Y. M. Wang, and N. K. Pavlis. 1991. Geopotential and Sea Surface Harmonic Coefficient Models, 410, Dept. of Geodetic Sci. and Surv., Ohio State Univ.

- Rangayyan, R. M., M. Ciuc and F. Faghih. 1998. Adaptive-neighborhood filtering of images corrupted by signal-dependent noise. *Applied Optics*, **37**(20), 4477-4487.
- Rignot, E. 2002. Mass balance of East Antarctic glaciers and ice shelves from satellite data. *Ann. Glaciol.*, **34**, 217-227.
- Rignot, E. and P. Kanagaratnam. 2006. Changes in the velocity structure of the Greenland Ice Sheet, *Science*, **311**, 986-990
- Rignot, E., G. Casassa, P. Gogineni, W. Krabill, A. Rivera, and R. Thomas. 2004. Accelerated ice discharge from the Antarctic Peninsula following the collapse of Larsen B ice shelf. *Geophys. Res. Lett.*, **31**, L18401, doi:10.1029/2004GL020697.
- Rignot, E., D. G. Vaughan, M. Schmeltz, T. Dupont and D. MacAyeal. 2002. Acceleration of Pine Island and Thwaites Glaciers, West Antarctica. *Ann. Glaciol.*, **34**, 189-195.
- Rignot, E., and R.H. Thomas, 2002. Mass balance of polar ice sheets, *Science*, **297**, 1502-1506.
- Robertson, R.A., L. Padman, and G. D. Egbert. 1998. Tides in the Weddell Sea. In: Ocean, Ice, and Atmosphere: Interactions at the Antarctic Continental Margin, edited by S. S. Jacobs and R. F. Weiss, *Antarctic Research Series*, **75**, 341-369.
- Rosanova, C. E., B. K. Lucchitta and J. G. Ferrigno. 1998. Velocities of Thwaites Glacier and smaller glaciers along the Marie Byrd Land coast, West Antarctica. *Ann. Glaciol.*, **27**, 47-53.
- Rosanova C. and B. Lucchitta. Velmap data: Velocity data for Pine Island Glacier 1973-1975, West Antarctica. http://nsidc.org/data/velmap/pine_getz/pine73_75/pine73_75.html
- Rott, H. 1984. The analysis of backscattering properties from SAR data of mountain regions. *IEEE Journal of Oceanic Engineering*, **9**(5), 347-355.
- Rott, H., W. Rack, P. Skvarca and H. de Angelis. 2002. Northern Larsen Ice Shelf, Antarctica: further retreat after collapse. *Ann. Glaciol.*, **34**, 277-282.
- Scambos, T. A., J. A. Bohlander, C. A. Shuman, and P. Skvarca. 2004. Glacier acceleration and thinning after ice shelf collapse in the Larsen B embayment, Antarctica, *Geophys. Res. Lett.*, **31**, L18402, doi:10.1029/2004GL020670.

- Scambos, T. A., M. J. Dutkiewics, J. C. Wilson and R. A. Bindshadler. 1992. Application of image cross-correlation to the measurement of glacier velocity using satellite image data. *Remote Sensing Environ.*, 42(3), 177-186.
- Scambos, T.A. and J.A. Bohlander. Velmap data: Velocity Data for Pine Island Glacier 1986-1988, http://nsidc.org/data/velmap/pine_getz/pine86_88/pine86_88.html
- Schutz, B. E., H. J. Zwally, C. A. Shuman, D. Hancock, and J. P. DiMarzio. 2005. Overview of the ICESat Mission, *Geophys. Res. Lett.*, 32, L21S01, doi:10.1029/2005GL024009.
- Simmonds, A. and J.R. Rouse. 1984. Accelerating flow of the Brunt Ice Shelf, Antarctica. *J. Glaciol.*, 30,377-380.
- Stearns, L., 2002. The dynamics of Whillans Ice Stream, West Antarctica, MS thesis, The Ohio State University, Columbus, Ohio.
- Stearns, L. A., K. C. Jezek and C. J. van der Veen. 2005. Decadal scale variations in ice flow along Whillans Ice Stream and its tributaries, West Antarctica. *J. Glaciol.*, 51 (172), 147-157.
- Swithinbank, C. 1988. Antarctica. In: Williams, R. S. Jr. and J. G. Ferringo, eds. *Satellite Image Atlas of Glaciers of the world*. U.S. Geological Survey Professional Paper 1386-B, U.S. Government Printing Office, Washington, D.C. 145pp.
- Swithinbank, C., K. Brunk and J. Sievers. 1988. A glaciological map of Filchner-Ronne Ice Shelf. *Ann. Glaciol.*, 11, 150-155.
- Thomas, R. A. 1973. The dynamics of the Brunt Ice Shelf, Coats Land, Antarctica. *Scientific Reports British Antarctic Survey*, 79, 45pp.
- Thomas, R. H. 1973. The creep of ice shelves: theory, and interpretation of observed behavior. *J. of Glaciol.*, 12 (64), 45-53, and 55-70.
- Thomas, R.H. 1971. Flow law for Antarctic ice shelves. *Nature Physical Science*, 322 (30), 85-87.
- Thomas, R. H., E. Rignot, G. Casassa, P. Kanagaratnam, C. Acuña, T. Akins, H. Brecher, E. Frederick, P. Gogineni, W. B. Krabill, S. Manizade, H. Ramamoorthy, A. Rivera, R. Russell, J. Sonntag, R. Swift, J. Yungel and J. Zwally. 2004. Accelerated sea-level rise from West Antarctica. *Science*, 306, 255-258.
- Thomas, R. H., W. Abdalati, E. Frederick, W. B. Krabill, S. Manizade and K. Steffen. 2003. Investigation of surface melting and dynamic thinning on Jakobshavn Isbræ, Greenland. *J. Glaciol.*, 49(165), 231-239.

- Thorsteinsson, T., J. Kipfstuhl, and H. Miller. 1997. Textures and fabrics in the GRIP ice core, *J. Geophys. Res.*, 102(C12), 26,583–26,600.
- Van der Veen, C.J. 1999. Fundamentals of glacier dynamics. A.A. Balkema, Rotterdam.
- Van der Veen, C.J. 1997. Backstress: what it is and how it affects glacier flow. In: *Calving Glaciers: Report of a Workshop, February 28 - March 2, 1997* (ed. C.J. van der Veen). BPRC Report No. 15, Byrd Polar Research Center, The Ohio State University, Columbus, Ohio, 173-180.
- Vaughan DG, Bamber JL, Giovinetto M, Russell J, Cooper. 1999. Reassessment of Net Surface Mass Balance in Antarctica. *Journal of Climate*, 12 (4), 933–946.
- Weertman, J. 1957. Deformation of floating ice shelves. *J. Glaciol.* 3(21), 38-42.
- Wendler, G., C. Stearns, G. Weidner, G. Dargau and T. Parish. 1997. On the extraordinary katabatic winds of Adélie Land. *J. Geophys. Res.*, 102(D4), 4463-4474, 10.1029/96JD03438
- Wendler, G., K. Ahlnas, and C.S. Lingle. 1996: On Mertz and Ninnis Glaciers, East Antarctica, *J. Glaciol.*, 42, 447-453.
- Whillans, I. M., and C.J. van der Veen. 1997. The role of lateral drag in the dynamics of Ice Stream B, Antarctica. *J. Glaciol.*, 43, 231-237.
- Williams, G.D. and Bindoff, N.L. 2003. Wintertime oceanography. of the Adelie Depression. *Deep-Sea Research Part II* , 50, (8–9), 1373–1392.
- Zhao, Z. 2001. Surface Velocities of the East Antarctic Ice Streams from RADARSAT-1 Interferometric Synthetic Aperture Radar Data. Ph.D. Dissertation, The Ohio State University.
- Zwally, H.J., R. Schutz, C. Bentley, J. Bufton, T. Herring, J. Minster, J. Spinhirne, and R. Thomas. 2005. GLAS/ICESat L2 Antarctic and Greenland Ice Sheet Altimetry Data V019. Boulder, CO: National Snow and Ice Data Center. Digital media.
- Zwally, H. J, W. Abdalati, T. Herring, K. Larson, J. Saba, and K. Steffen. 2002. Surface melt-induced acceleration of Greenland ice-Sheet flow, *Science*, 297, 218-222